



ESB-ITA 2023

XII Annual Meeting of the ESB-ITA

# Congress Report

Torino, 18-19 September 2023



**Summary**

Committees	pag. 1
Sponsors	pag. 2
Program at a Glance	pag. 3
Keynote Speakers	pag. 4
Book of Abstracts	pag. 5
<i><u>Day 1 – Thematic Symposium</u></i>	
Integrative biomechanics I – <i>Oral presentations</i>	pag. 6
Integrative biomechanics II – <i>Oral presentations</i>	pag. 12
Integrative biomechanics III – <i>Oral presentations</i>	pag. 18
Integrative biomechanics – <i>Poster presentations</i>	pag. 23
<i><u>Day 2 – General Meeting</u></i>	
Orthopedic and musculoskeletal biomechanics – <i>Oral presentations</i>	pag. 58
Cardiovascular biomechanics – <i>Oral presentations</i>	pag. 63
Medical devices and therapies – <i>Oral presentations</i>	pag. 68
<i>Poster presentations</i>	pag. 73
ESB-ITA Master Thesis Award 2023 – <i>Finalists</i>	pag. 113
Awards Winners	pag. 115



### Local Organizers

Claudio **Chiastra**

Marco A. **Deriu**

Diego **Gallo**

Diana **Massai**

Mara **Terzini**

### ESB-ITA Executive Board

Diana **Massai**, Politecnico di Torino - *President*

Simona **Celi**, Fondazione Toscana G. Monasterio

Alessio **Gizzi**, Università Campus Bio-Medico di Roma

Michele **Conti**, Università degli Studi di Pavia – *ex officio*

Enrico **Dall’Ara**, University of Sheffield – *ex officio*

Bernardo **Innocenti**, Université Libre de Bruxelles – *ex officio*

### Scientific Committee

Arti Ahluwalia, Alessandra Aldieri, Maria Cristina Bisi, Federica Caselli, Gerardo Catapano, Simona Celi, Michele Conti, Luca Cristofolini, Enrico Dall’Ara, Giuseppe De Nisco, Chiara Giulia Fontanella, Gionata Fragomeni, Alessio Gizzi, Bernardo Innocenti, Luigi La Barbera, Sara Mantero, Michele Marino, Francesco Migliavacca, Marco Palanca, Valeria Panzetta, Salvatore Pasta, Giovanni Putame, Andrea Remuzzi, Gianpaolo Serino, Francesco Sturla, Silvia Todros, Giuseppe Vairo, Elisabetta Zanetti

Congress Report designed by Vittoria Civilini, Beatrice Masante, Valentina Mazzi

# ESB - ITA 2023

## XII Annual Meeting of the ESB-ITA

### Sponsors

#### Gold sponsors:



#### Silver sponsors:



#### Bronze sponsors:



#### Award sponsors:



### Patronage



**Politecnico di Torino**  
Department of Mechanical and Aerospace Engineering



**Politecnico di Torino**



**Program at a Glance****18 September 2023 – Thematic Symposium**

<b>8:30-10:00</b>	Welcome and registration
<b>10:00-10:30</b>	Opening
<b>10:30-12:00</b>	Integrative biomechanics I <i>including the perspective talk by Dr. F. Gijsen</i>
<b>12:15-13:45</b>	Poster session I
<b>12:15-13:00</b>	Sponsor Pitch I
<b>12:45-13:45</b>	Lunch
<b>13:45-15:30</b>	Integrative biomechanics II <i>including the perspective talk by Prof. M.T. Raimondi</i>
<b>15:30-16:15</b>	Sponsor Pitch II
<b>15:30-16:15</b>	Coffee break
<b>16:15-17:45</b>	Integrative biomechanics III <i>including the perspective talk by Prof. A. Dogariu</i>
<b>18:00-18:30</b>	Tour Polito <sup>BIO</sup> Med Lab
<b>19:30-00:00</b>	Social dinner and DJ set

**19 September 2023 – General Meeting**

<b>8:00-8:30</b>	Registration
<b>8:30-10:00</b>	Orthopedic and musculoskeletal biomechanics <i>including the perspective talk by Prof. L. Vico</i>
<b>10:00-10:30</b>	Coffee break
<b>10:30-12:00</b>	Cardiovascular biomechanics <i>including the perspective talk by Prof. G. Pedrizzetti</i>
<b>12:00-12:45</b>	ESB-ITA Master Thesis Award 2023
<b>12:45-13:15</b>	Sponsor Pitch III
<b>12:45-14:15</b>	Poster session II
<b>13:15-14:15</b>	Lunch
<b>14:15-15:45</b>	Medical devices and therapies <i>including the perspective talk by Dr. M. Grigioni</i>
<b>15:45-16:15</b>	Coffee break
<b>16:15-17:30</b>	General assembly and Awards



**Keynote Speakers****Frank Gijsen**

*Erasmus MC, Rotterdam, The Netherlands*

“Thrombus mechanics: from micro-structure to outcome prediction”

**Manuela Raimondi**

*Politecnico di Milano, Italy*

“Mechanobiology of cancer progression”

**Aristide Dogariu**

*University of Central Florida, Orlando, FL, USA*

“Using laser light scattering to interrogate cellular and subcellular dynamics and mechanics”

**Laurence Vico**

*SAINBIOSE U 1059, INSERM, Université Jean Monnet, Mines Saint-Etienne, France*

“Our skeleton adapts to the conditions of space flight but the return to the Earth is challenging”

**Gianni Pedrizzetti**

*Department of Engineering and Architecture, University of Trieste, Italy*

“Cardiac fluid mechanics in the clinical scenario: the tale from theoretical models to clinical practice”

**Mauro Grigioni**

*National Centre for Innovative technologies in public health, Istituto Superiore di Sanità, Italy*

“State of the art and challenges for the classification of robotic devices in rehabilitation: Technologies and regulatory issues”



ESB - ITA 2023  
XII Annual Meeting of the ESB-ITA

# Book of Abstracts

Torino, 18 - 19 September 2023





ESB - ITA 2023  
XII Annual Meeting of the ESB-ITA

Day 1  
Integrative biomechanics I  
*Oral presentations*

Torino, 18 September 2023



# MODELLING VASCULAR TONE REGULATION: AN INTEGRATIVE APPROACH FROM MOLECULAR TO SYSTEMIC LEVEL

Michele Marino (1), Bastien Sauty (1,2), Giuseppe Vairo (1)

1. University of Rome Tor Vergata, Italy; 2. Mines Saint Etienne, France

## Introduction

The physiological behaviour of the cardiovascular system is highly affected by the mechanical response of arterial segments, that is in turn dependent from both tissue histological architecture and the contractile tone of smooth muscle cells. The former depends mainly on the different amount and arrangement of constituents (mainly, elastin and collagen fibers), while the latter on chemical drivers of vasoactivity, such as nitric oxide (NO) and reactive oxygen species (e.g., ROS and PN). Moreover, arterial segments undergo a continuous remodelling, that is changes in their structure (e.g., thickening, stiffening, or narrowing). Remodelling is driven by biochemical pathways (involving growth factors – GFs – and enzymes such as matrix metalloproteinases – MMPs) that are activated when the mechanical state (i.e., stresses and/or strains) is non-homeostatic, [1,2]. When remodelling is dysfunctional, pathologies, like chronic hypertension, develop.

It is also noteworthy that the problem is highly multiscale since global hemodynamic conditions (e.g., heart rates, resistance of downstream vasculature) highly affect local flow conditions, and hence the local pressure field and the internal stresses affecting biochemical pathways and remodelling. Detailed high dimensional models (2D or 3D) can generally be used to simulate local hemodynamics of specific arterial sites, while the whole arterial tree is generally described through low dimensional descriptions (i.e., lumped 1D approaches).

## Methods

This work presents a comprehensive multi-scale and multi-field computational framework that accounts for: i) a lumped 1D description of the macroscale arterial tree; ii) a continuum 3D model at the microscale of the local chemo-mechano-biological response of arterial tissues (accounting for passive and active tissue behavior); iii) biochemical-dependent vasoconstriction and vasodilation (the NO-ROS-PN biochemical chain), and biochemical-dependent tissue remodeling (the GFs-MMPs biochemical chain). Simulations from 3D chemo-mechano-biological models drive how parameters of the lumped description vary as function of segment dilation, as well as tissue histology and vasoconstriction. An illustrative representation of the proposed methodology is reported in Fig. 1a.

## Results

The applicative case study investigates the relationship between arterial vasodilation and vasoconstriction with physical exercise. Figure 1b shows the short-term

response of the arterial system during and after 1 hour exercise. The model predicts a release of vasodilators (NO), a decrease of vasoconstrictors (ROS), and a hemodynamic response leading to the maintenance of quasi-homeostatic shear stresses on endothelial cells in the intima.

The obtained numerical results are consistent with available experimental data for normal and spontaneously hypertensive phenomena.

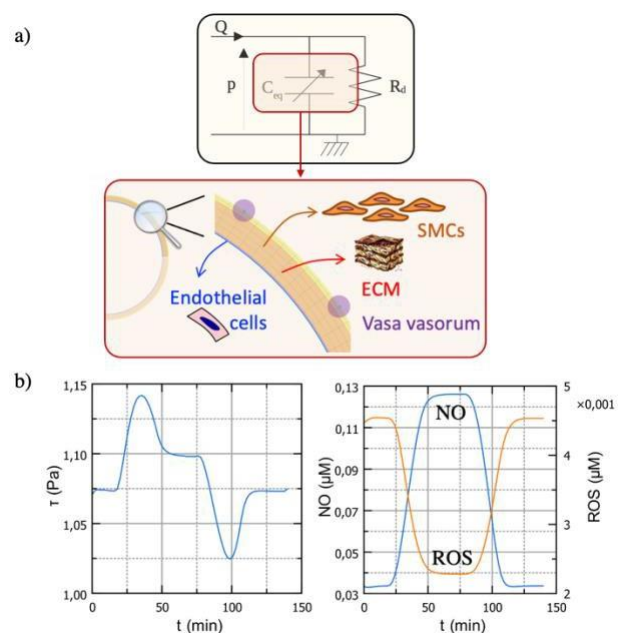


Figure 1: (a) Multi-scale and chemo-mechano-biology rationale. (b) Arterial short-term active response predicted by the model: vasodilation during 1h exercise.

## Conclusions and Future studies

On-going studies are addressing the coupling of the framework with growth and remodeling mechanisms [3], and the reproduction of animal studies [4].

## References

1. Marino et al., J Royal Society Interface 14, 2017.
2. Gierig et al., Biomech Model Mechanobiol; 20:1297,2021.
3. Gierig et al., Comp. Med Biol, doi: 10.1016/j.compbimed.2023.106811, 2023.
4. Nuki et al. J. Cereb. Blood Flow Metab. 29:495-503, 2009.

## Acknowledgements

Funding from Regione Lazio (POR FESR LAZIO 2014; Progetti di Gruppi di Ricerca 2020; project: BIOPMEAT, n. A0375- 2020-36756) is acknowledged.



# VASCULAR WALL VIBRATIONS IN THE ARTERIOVENOUS FISTULA: A NOVEL MECHANOBIOLOGICAL STIMULUS?

**Michela Bozzetto (1), Luca Soliveri (1), Andrea Remuzzi (2), Kristian Valen-Sendstad (3)**

1. Istituto di Ricerche Farmacologiche Mario Negri IRCCS, Bergamo, Italy;  
2. University of Bergamo, Dalmine, Italy; 3. Simula Research Laboratory, Oslo, Norway.

## Background

Native arteriovenous fistula (AVF) is the preferred vascular access for haemodialysis, but it still has high failure rates due to stenosis formation [1]. We recently demonstrated that AVFs harbor transitional flows [2] and the goal of the present study was to investigate whether these hemodynamic conditions could promote aberrant mechanical stresses within the vascular wall.

## Materials and Methods

We generated a 3D patient-specific model starting from non-contrast enhanced fast spin echo magnetic resonance images acquired at 3 days after radiocephalic AVF surgery in a 72-year patient. An external layer with constant thickness of 0.3 mm was added to the AVF to include the vascular wall, that was modeled using three-term compressible Mooney-Rivlin. Robin boundary condition were used to represent the viscoelastic behavior of the surrounding tissues. We imposed pulsatile blood flow waveforms derived from US examination at the proximal and distal artery (Figure 1).

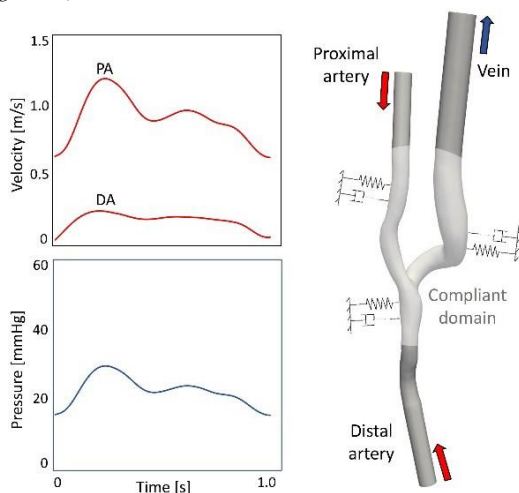


Figure 1: Patient-specific AVF model and velocity and pressure boundary conditions.

A validated and formally 2<sup>nd</sup> order accurate fluid structure interaction solver [3] developed upon FEniCS Finite Element Model library was used to solve for wall deformation and flow field.

## Results

High-fidelity fluid structure interaction simulations revealed the presence of wall vibrations up to 150 Hz and with amplitude of about 10 microns (Figure 2).

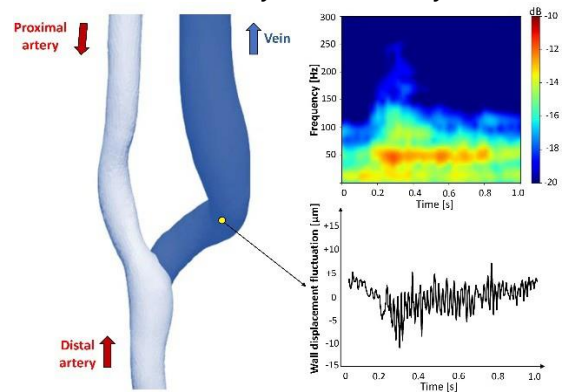


Figure 2: Spectrogram of the wall displacement in the vein (blue colored) and wall displacement fluctuation of a single point on the vein.

Interestingly, the vibrations were predominant at the anastomosis floor and on the inner venous side, locations that correlate with regions where stenosis typically develops (Figure 3).

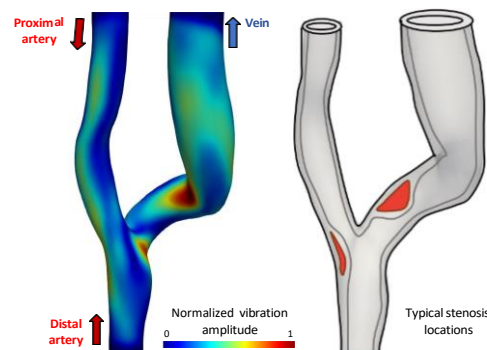


Figure 3: High amplitude vibrations phenotypically collocate with typical stenosis locations.

## Conclusion

The same location of vascular wall vibrations and stenosis may suggest an unknown mechanobiological process linking high-frequency mechanical stresses within the vascular wall and adverse vascular remodeling.

## References

1. Caroli et al, *Kidney Int.* 84: 1237–1245, 2013.
2. Bozzetto et al, *ABME*, 44(8): 2388–2401, 2016.
3. Bergensen et al, *JOSS*, 5(50): 2089, 2015.

## Acknowledgements

The Authors would like to thank Fondazione Dompè for funding.



# MICROMECHANICAL CHARACTERIZATION OF BOVINE PERICARDIUM FOR CARDIAC IMPLANTS

Marta Tosini (1), Andrea T. Lugas (1), Mark Pace Floridaia (2), Mauro Ferraro (2), Alberto L. Audenino (1), Diana Massai (1), Umberto Mobiducci (1), Gianpaolo Serino (1)

1. Polito<sup>BIO</sup> Med Lab and Department of Mechanical and Aerospace Engineering, Politecnico di Torino, Italy.

2. Epygon Italie S.r.l., Colletterto Giacosa (TO), Italy

## Introduction

Biological materials are largely adopted for the fabrication of bioprosthetic heart valves (BHV). BHVs currently available on the market are fabricated using porcine aortic valves, sheets of porcine (PP) or bovine pericardium (BP). BP is an extremely heterogeneous soft tissue, and the process of characterization of its mechanical properties has not yet been defined through a standard protocol [1]. This lack of standardization hampers the optimization of the BHVs manufacturing process, causing a large waste of processed BP. Thus, the identification of tools to test affordably the mechanical behavior of BP samples for BHVs fabrication has become essential. In this context, nanoindentation is one of the most effective techniques for an in-depth characterization of the mechanical response of heterogeneous soft tissues like BP. In a wider perspective, integrating nanoindentation measurements with scanning electron microscopy (SEM) analysis could allow to link the local mechanical response of the tissue to its microstructure. In this study, the local BP mechanical properties were characterized by nanoindentation with the final aim of establishing an affordable pass/fail criterion of BP patches for BHVs fabrication before their treatment and usage.

## Materials and Methods

The samples were cut from a BP patch (provided by Epygon Italie S.r.l) and their thickness was measured with a digital caliper ( $0.51 \pm 0.01$  mm). Stress relaxation tests (Piuma nanoindenter, Optics11) were performed in wet conditions, at  $37^\circ\text{C}$ , controlling the indentation depth ( $\delta$ ). After contact detection, the tests started with a loading phase, where  $\delta = 2500$  nm was reached in 1 s. Then, the set  $\delta$  was held constant for 8 s while recording the load, after which the probe was retracted from the sample. For each sample, two matrices of  $10 \times 10$  indentations (with a distance step size equal to  $500 \mu\text{m}$ ) were recorded. The two matrices were spatially overlapped of  $250 \mu\text{m}$  both in the horizontal (x) and vertical (y) direction. The loading phases of the acquired curves were analyzed applying the Hertz model to obtain the local Effective Modulus ( $E_{eff}$ ), thus estimating the elastic properties of the samples. Data recorded during the holding phase of the tests allowed to estimate the local time-dependent response of the BP samples. The indentation curves were analyzed by applying the Prony series [2], obtaining the relaxation modulus, from which the instantaneous  $G(t=0)$  and equilibrium  $G(t=\infty)$  moduli were calculated. Then the samples were analyzed through a scanning electron microscope.

## Results

A representative relaxation curve is showed in Fig.1A, where the model fits the experimental data. An example of  $E_{eff}$  distribution on a BP sample is presented in Fig. 1B: the  $E_{eff}$  value varies locally in the range 1 - 76 kPa, with an average value equal to  $20.21 (\pm 12.16)$  kPa. The dispersion of the estimated values of the elastic modulus  $E_{eff}$  and of the relaxation moduli are presented in Fig. 1C. Average values of  $G(0)$  and  $G(\infty)$  were  $38.3 (\pm 23.5)$  kPa and  $33.6 (\pm 21.8)$  kPa, respectively, indicating a reduction of  $4.73 (\pm 3.26)$  kPa. Figure 1D shows a SEM image of the tested sample.

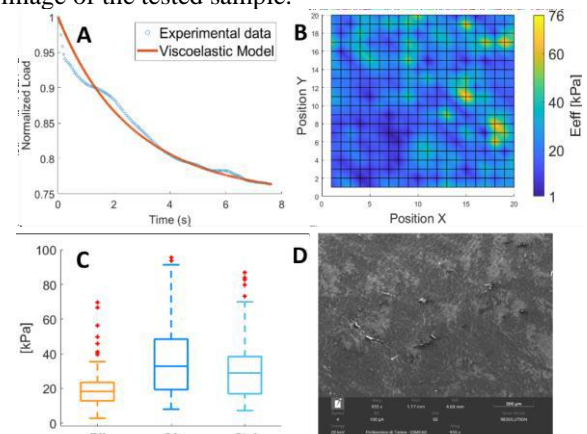


Figure 1: A) Representative experimental and fitted curve; B) Map of the effective modulus  $E_{eff}$  of the tested area; C) Box plot of  $E_{eff}$ ,  $G(0)$ , and  $G(\infty)$ ; D) SEM image of the BP sample.

## Discussion

Combining the nanoindentation map and the surface morphology at the microscale, the proposed approach allowed a proper mapping of the mechanical properties of a representative BP sample. The BP sample behavior is affected by viscous phenomena (Fig. 1A); indeed, the viscoelastic properties are subjected to a reduction of about 13%, on average. The comparison of  $E_{eff}$ ,  $G(0)$  and  $G(\infty)$  indicates that the analysis of the recorded curves performed adopting the Hertz Model, i.e., without considering the viscous effects, could introduce errors in the evaluation of the elastic properties of a BP sample. Furthermore, the high variability of the results (Fig. 1C) is reasonable in relation to the pronounced heterogeneity of the sample, which is also evident at the microscale (Fig. 1D). As a matter of fact, it appears that there is a correlation between the clear spots in the SEM image and the higher  $E_{eff}$  values in the nanoindentation map.

## References

1. Stieglmeier et al, J Mech Beh Biomed Mat, 119, 10443, 2021
2. Mattice et al, J Mater Res, 21(8), 2003-2010, 2006



# IN SILICO EVALUATION OF THE LATERAL TRANSMISSION OF MUSCLE CONTRACTION FORCE

Silvia Spadoni (1), Lorenzo Marcucci (2), Silvia Todros (1), Carlo Reggiani (2), Piero G. Pavan (1,3)

(1) Department of Industrial Engineering, University of Padova, Italy; (2) Department of Biomedical Science, University of Padova, Italy; (3) Fondazione Istituto di Ricerca Pediatrica Città della Speranza, Padova, Italy

## Introduction

Aging represents a physiological condition that is usually associated with the reduction of muscle mass and performance. It has been hypothesized that the decline of contraction capability is due also to the impaired ability of a muscle to laterally transmit the generated force. This may be caused by alterations of the extra-cellular matrix (ECM).

The ECM contribution in the lateral transmission of contraction force is here assessed by a numerical approach based on the Finite Element Method (FEM), also considering the effects of aging.

## Methods

Geometric and mechanical properties of ECM at the level of muscle bundles have been deduced from biopsies of vastus lateralis in young (mean age 21 y.o.) and elderly (mean age 67 y.o.) subjects [1].

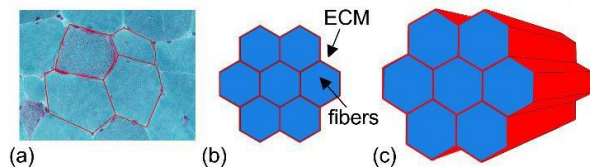


Figure 1: Transverse section of a biopsy sample with ECM outlined in red among muscle fibers (a); Transverse section (b) and 3D view (c) of a simplified geometric reconstruction of a muscle bundle composed of fibers (blue) and ECM (red).

Starting from experimental data, different FE models were built for young and elderly subjects to simulate muscle bundles formed by few fibers connected through the ECM (Fig.1). To describe the contractile behavior of muscle fibers, the three element Hill based formulation developed by Marcucci et al. was adopted [2]. The ECM mechanical behavior was described through an isotropic hyperelastic neo-Hookean constitutive model.

Different numerical analyses were carried out replicating at the scale of a bundle the experimental protocols developed by Huijing et al. [3] and Ramaswamy et al. [4] on whole muscles. These protocols were aimed at assessing the persistence of contraction force transmission following the cut of one or more muscular fibers.

## Results and discussion

The results of the analyses referring to the experimental tests performed by Ramaswamy et al. [4] are reported below. In this simulated experiment, the bundle is fixed

at the proximal side and in an intermediate section using a yoke apparatus (Fig. 2). The fibers are activated, and the amount of contraction force transmitted at the proximal side is evaluated.

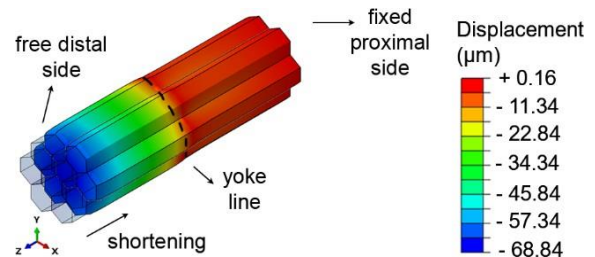


Figure 2: Contour of the longitudinal displacement (z-direction) for the numerical simulation of the yoke apparatus test protocol on a bundle of 1000 μm.

By comparing the results obtained with the FE models for young and elderly subjects, a different drop in the transmitted force is observed, with a higher reduction for the elderly group. The difference is consistent with the maps of the force-length function (Fig. 3), showing that the region of fibers with active stress much lower than the maximum isometric value ( $<0.8$ ) is more extended in the case of elderly than in the case of young bundles. This can be explained by the lower shear stiffness of ECM for elderly bundles, also related to its higher thickness.

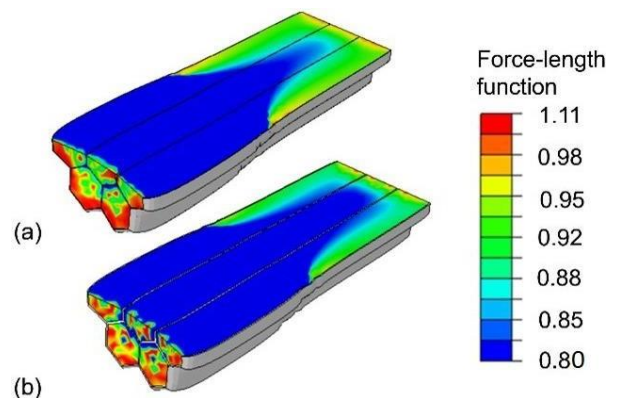


Figure 3: force-length function for young (a) and elderly (b) subjects. The values less than or equal to 0.8 are colored in dark blue.

## References

1. Pavan et al, Int J Mol Sci, 21(11):3992, 2020.
2. Marcucci et al., Biomech Model Mechanobiol, 16:1833-1843, 2017.
3. Huijing et al, J Exp Biol, 201:682-691, 1998.
4. Ramaswamy et al, J Physiol, 589(5):1195-1208, 2011.



# OPTIMIZATION OF PHOTOTHERMAL LASER ABLATION USING AN EXPERIMENTAL-NUMERICAL APPROACH ON AGAROSE PHANTOM

Federica Bianconi (1), Elena De Vita (2), Daniela Lo Presti (1), Carlo Massaroni (1), Daniele Bianchi (1), Agostino Iadicicco (2), Stefania Campopiano (2), Emiliano Schena (1), Alessio Gizzi (1)

1. University Campus Bio-Medico of Rome, Italy; 2. University of Naples "Parthenope", Italy.

## Introduction

Cancer is one of the leading causes of death worldwide. Photothermal therapy (PTT) with laser energy is a minimally invasive cutting-edge technique for cancer removal. Gold nanoparticles (AuNPs) could be injected into the tumor region to enhance the treatment efficacy, preserving surrounding healthy tissue [1]. Fiber Bragg Grating (FBG) technology is an invasive thermometry technique, useful to map the material temperature distribution [2] accurately. *In vitro* verification and validation are required to assess the effectiveness of PTT [3]. The present work focuses on novel agarose-based phantoms and FBG configurations to quantify temperature profiles under PTT procedure. Concurrently, computational modeling was implemented to optimize the procedure and conduct predictive analysis in a combined experimental-numerical approach.

## Methods

The PTT experimental set-up of agarose phantom involves a 3D custom box in polylactic (PLA) to control the FBG arrangement and the reproducibility of the experiments. The NIR laser radiation (wavelength  $\lambda=1064$  nm) was delivered via a quartz optical fiber and 4 FBG arrays were embedded in the phantom. The ablation procedure was performed with a laser power of 3 W for 2 minutes and a total amount of 20 acquisitions were collected. For each experiment, the  $\Delta T$  (with  $T_{ref} = 20$  °C) trends estimated by the 34 FBGs were analyzed and processed in MATLAB®. The computational model was implemented in COMSOL Multiphysics® considering two coupled models [4]: the Optical Diffusion Approximation (ODA) (Eq. 1) to replicate the laser light propagation and Pennes' bioheat equation (Eq. 2) to reconstruct the agarose temperature dynamics:

$$-D \frac{\partial^2 \varphi(z)}{\partial z^2} + \mu_a \varphi(z) = s(z) \quad (1)$$

$$\rho c \frac{\partial T}{\partial t} = \nabla \cdot [k \nabla T] + Q_p \quad (2)$$

In Eq. 1,  $\varphi(z)$  is the light fluence rate,  $s(z)$  the light source, the tissue diffusion coefficient  $D = 1/3(\mu'_s + \mu_a)$  strongly depends on optical properties:  $\mu_a$ , absorption coefficient and  $\mu'_s = (1 - g)\mu_s$ , reduced scattering coefficient,  $g$  is the tissue anisotropy factor and  $\mu_s$  the scattering coefficient. The laser lateral spread was approximated by a bidimensional Gaussian distribution applied to the bottom laser applicator surface. In Eq. 2,  $T$  is the agarose temperature,  $\rho$ ,  $c$  and  $k$  are the density, specific heat and thermal conductivity of agarose, re-

spectively.  $Q_p = \mu_a \varphi(z)$  is the source term due to photon absorption. In the Eq. 2 an addition term  $Q_{pNP}$  should be considered to model the PTT of an agarose-AuNPs phantom [3].

## Results

Temperature profiles over time of six FBGs closest to the laser applicator during laser ablation are displayed in Figure 1 (B). The measured  $\Delta T$  strictly depends on the FBG placements. Temperature progressively decreases starting from the laser tip. A parametric study for material characterization allowed us to obtain well-approximated simulated profiles (dotted lines) with respect to the experimental data (solid lines). Nevertheless, the simulated temperature of A4, A6, C4, and D4 are underestimated. Figure 1 (A) highlights the laser beam shape and the relative positions of the FBGs considered.

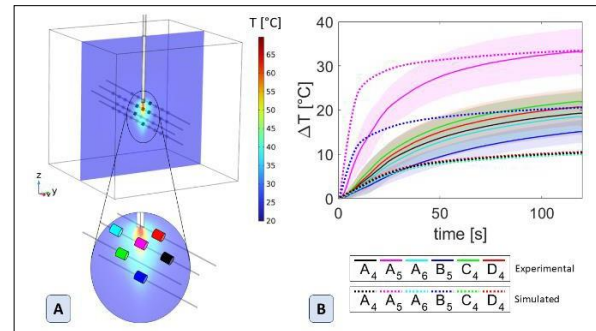


Figure 1: (A) Central slice of temperature distribution in computational domain. Color cubes indicate the six FBGs. (B)  $\Delta T$  evolution of six FBGs. Average temperature (solid line) and variability bands (shadowed bands). Dotted lines indicate the  $\Delta T$  simulated profiles.

## Discussion

Suitable modeling allows us to control the experimental set-up and predict the current temperature distribution. Experimental and simulated data could be combined to refine the computational model. Furthermore, a material experimental characterization could affect the preferential propagation direction of the laser beam. A follow-up study of agarose laser ablation mediated with AuNPs is proposed in parallel with a proper fine-tuned model, including the AuNPs contribution.

## References

1. X. Huang et al, J of Advanced Research, 1:13-28, 2010.
2. L. Bianchi et al, IEEE Sens J, 22(12):11297-11306, 2021.
3. E. Campagnoli et al, Int J Heat Techn 38(3):583-589, 2020.
4. F. J. Reynoso et al, Med Phy, 40 (7), 2015.



Day 1  
Integrative biomechanics II  
*Oral presentations*

Torino, 18 September 2023



# IN-SILICO MODELING OF TUNABLE VISCOELASTIC HYDROGELS FOR THE STUDY OF CELL MECHANOTRANSDUCTION

Nicole Guazzelli (1), Ludovica Cacopardo (1), Arti Ahluwalia (1)

1. University of Pisa

## Introduction

Predicting hydrogel mechanical behaviour is essential to precisely control and guide cell behaviour [1]. Since hydrogel viscoelastic behaviour is strongly related to the interaction of liquid molecules with the solid network, different mathematical models have been proposed to simulate transport phenomena in gels, but they present limitations such as the lack of correlation with gel viscoelastic properties [2]. Here we propose an in-silico model to predict hydrogel viscoelastic behaviour resulting from tuning liquid phase viscosity [3]. The computational tool was used to design the experimental set up for the study of adipose derived mesenchymal stem cells (ADSC) mechanotransduction in response different viscoelastic stimuli. In particular, we focused on the definition of hydrogels with a relaxation time ( $\tau_{rel}$ ) shorter than the time required for the formation of cells focal adhesions ( $\tau_{fak} \in [15 - 60]s$ ) [4].

## Methods

5 mg/mL agarose hydrogels were fabricated with different dextran concentrations in the liquid phase (20, 30, 40 mg/mL) and modelled on Matlab 2022a as a homogeneous porous system. Dextran was considered as a spherical agglomerate linked to the water molecules. The liquid phase movement in the porous matrix was described using the reaction-diffusion equation (1), introducing an apparent diffusion coefficient  $D_{app}$  (2) which adapts the Einstein-Stokes coefficient  $D_0$  through additional coefficients, which considers the obstacle imposed by the porous matrix and the correlation between diffusive and mechanical properties through the average mesh size  $\xi_{avg}$ . A modified Maxwell Standard Linear Solid (mSLS) lumped parameter model was used to describe hydrogel mechanics. mSLS equations in the time domain were implemented in Simulink (fig.1A) and used to fit the experimental data obtained from the hydrogel mechanical characterisation using the epsilon dot method, deriving the instantaneous and equilibrium elastic modulus ( $E_{eq}$ ), and  $\tau_{rel}$  [1]. ADSC ( $50.000 \text{ cell/cm}^2$ ) were cultured for 7 days on the hydrogels and on tissue culture plates (TCP) as control, coated with 50 mg/mL gelatin. YAP, lipidic and calcium deposits were labelled respectively thanks to immunostaining, Oil Red O and Alizarin Red. Confocal and bright field image analysis was used to quantify their distribution.

## Results

Figs.1B-1C show a good correlation between experimental and computational data. Moreover, they also suggest that dextran mainly affect gel viscous properties ( $\tau_{rel}$ ), maintaining a constant  $E_{eq}$ . Cell tests showed that YAP is localised in the cytoplasm in the case of 20 and 30 mg/mL dextran-agarose substrates

(fig.1D), while the 40 mg/mL dextran gels induce the YAP translocation into the nuclei as in the case of TCP controls (fig. 1E).

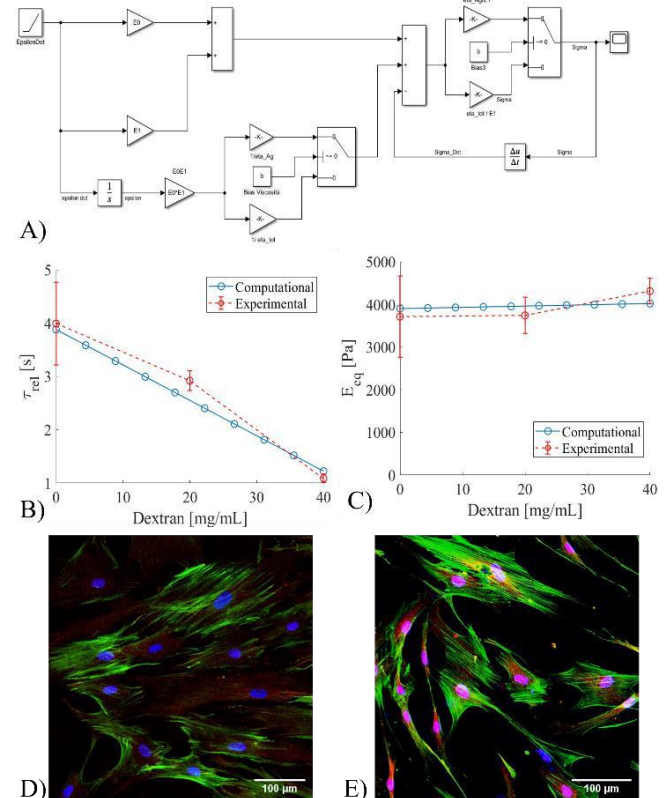


Figure 1. A) mSLS Simulink diagram; B)  $\tau_{rel}$  and C)  $E_{eq}$  of dextran-agarose hydrogels. Confocal images of YAP (red) localization in ADSC on agarose-20 mg/mL dextran hydrogels (D) and on TCP control (E) (green-actina, blue-nuclei).

## Discussion

Cell tests showed that ADSC on gels with dextran < 40 mg/mL preserve their stemness, while 40 mg/mL dextran gels induce ADSC adipogenic differentiation, and in the controls ( $\tau_{rel} \rightarrow \infty$ ) ADSC produced calcium deposits compatible with the osteogenic differentiation.

## Conclusion

The presented computational framework resulted effective in predicting gel mechanical behaviour, providing a useful tool for the identification of the substrates with  $\tau_{rel} < \tau_{fak}$ . Simulations with other materials combinations are ongoing to prove the versatility of the in silico tool for the design of hydrogels for regenerative medicine applications and advanced in-vitro models.

## References

1. Cacopardo et al., Tissue Eng. Part B: Rev., 28:4, 2022
2. Caccavo et al., Chem. Soc. Rev., 47: 2357 -2373, 2018
3. Campbell et al., ACS Biomater. S. Eng. 6:308 – 319, 2020



# ENDOTHELIAL CELLS EXPOSURE TO MECHANICAL VIBRATIONS

Sofia Poloni (1), Elena Carrara (2), Chiara Emma Campiglio (3), Elisa Riceputi (1),  
Michela Bozzetto (2), Andrea Remuzzi (3)

1. Department of Engineering and Applied Sciences, University of Bergamo, Dalmine, Italy; 2. Department of Biomedical Engineering, Istituto di Ricerche Farmacologiche Mario Negri IRCCS, Bergamo, Italy; 3. Department of Management, Information and Production Engineering, University of Bergamo, Dalmine, Italy

## Introduction

The mechanobiology of vascular cells plays a key role in vascular remodelling [1] and evidence showed that turbulent hemodynamics influence endothelial cells (ECs) functions *in vitro* [2]. Recent numerical simulations investigated the effect of mechanical stresses on vessels remodelling [3], but the biological effect on cellular functions remains still unclear. Therefore, this preliminary study aims to investigate the effects of vibrations on ECs exploiting an experimental setup capable of exposing cells to mechanical vibrations obtained by a 50 Hz sound-generated pressure wave.

## Methods

To expose cells to vibrations, an aluminium support structure was built, equipped with a speaker connected with a two-channel digital power amplifier capable of receiving an input sound recording of 50 Hz (Figure 1a). Human umbilical vein endothelial cells (HUVECs) were seeded and cultured in two gelatin-precoated 150 mm cell culture dishes at a density of  $1 \times 10^1$  cells. After 4 days, a cell culture dish was mounted on the support structure to make it receive vibrations and incubated for 48 hours, while the other one was maintained in static conditions as normal control in another cell incubator. The sounds emitted by the speaker and the vibrations of the cells were recorded at the beginning of the experiment, after 24 and 48 hours respectively with an in-house device consisting of an Adafruit Pulse Density Modulation microphone managed by an Arduino Nano 33 BLE board and with an accelerometer (LSM9DS1) mounted on the Arduino platform (Figure 1b), fixed to the plate center. Data were collected with Coolterm and analyzed in MATLAB R2022a. Specifically, sound recordings were analyzed in time and frequency while information of cell culture dish velocity and displacement during time were obtained by the integration of the acceleration data following appropriate high-pass filtering steps.

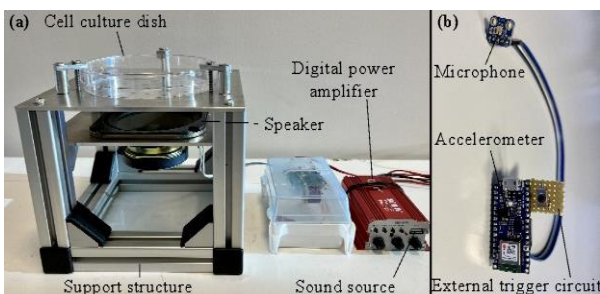


Figure 1: a) Experimental setup. b) Arduino-based device for sound and vibration measures.

At the end of the experiment the morphology of the stimulated and the static control cells was investigated by phase-contrast microscopy. Then, cell counting in the two conditions was performed to evaluate the effect of vibrations and Alamar Blue assay was performed on the samples to determine the HUVECs' viability.

## Results

The sound received by cell culture dish was characterized over time by the main frequency of 50 Hz and its odd harmonics. Assumed a normal distribution of velocity and displacement, mean velocity obtained from acceleration data was 0.04 m/s ( $4\alpha$ ) and the associated  $2\alpha = 71 \mu\text{m}$  indicates the movement of the plate given by vibrations in the direction perpendicular to the dish. The Fourier transform of the acceleration data revealed the same vibration frequency of the sound. Phase-contrast analysis of the stimulated and unstimulated cells showed that sound-induced vibrations changed HUVECs typical morphology and determined their detachment from the substrate (Figure 2). This was confirmed by the number of death cells found in the culture medium of vibrations-exposed HUVECs, about 20% higher than the static control. Alamar Blue assay reported a decrease in cell viability greater than 50% for HUVECs exposed to the mechanical stimulus, suggesting that vibrations importantly affected cell functions.

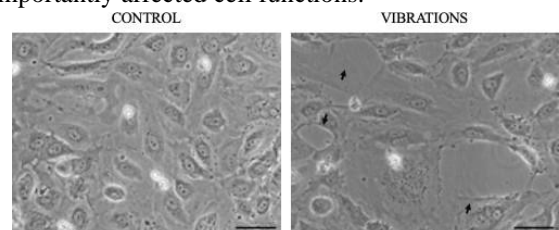


Figure 2: Phase-contrast microscopy magnification 20X, scale bars 50  $\mu\text{m}$ .

## Discussion

Preliminary results underlined a reduction in ECs viability when they are stimulated with a 50 Hz frequency for 48 hours. Our framework showed a great potential for the investigation of vascular remodelling and the related cell dysfunctions responsible for vascular diseases with a simple but reliable system.

## References

1. Koseki et al, Transl. Stroke Res., 11:80-92, 2020.
2. Gimbrone et al, Circ. Res., 118: 620–636, 2016.
3. Souche et al, J. Biomech., 145, 2022.



# ADVANCED PLATFORM FOR IN VITRO STUDYING CELL BIOLOGICAL RESPONSE TO CONTROLLED STRETCH STIMULATION – PERIODONTAL LIGAMENT STEM CELLS APPLICATION

Beatrice Masante (1,2,3), Giovanni Putame (1,3), Andrea T. Lugas (1,3), Marta Tosini (1), Ilaria Roato (2), Mara Terzini (1,3), Federico Mussano (2), Alberto L. Audenino (1), Diana Massai (1,3)

1. PolitoBIOMed Lab and Department of Mechanical and Aerospace Engineering, Politecnico di Torino, Italy; 2. Bone and Dental Bioengineering Lab, CIR-Dental School, Department of Surgical Sciences, University of Torino, Italy; 3. Interuniversity Center for the Promotion of the 3Rs Principles in Teaching and Research, Italy

## Introduction

*In vivo*, mechanical cues are fundamental in promoting cell and tissue development and in maintaining homeostasis [1]. Thus, advanced investigation platforms able to replicate and combine native-like physical stimuli represent essential tools for investigating *in vitro* the biological response of cells under defined mechanical stimuli. In this study, we designed, characterized, and tested an investigation platform, based on a flexible substrate and a stretch bioreactor [2], for exposing adherent cells to controlled uniaxial stretch culture protocols in view of mechanotransduction studies, and we performed explanatory biological tests on human periodontal ligament stem cells (hPDLSCs).

## Methods

The proposed investigation platform is composed of a flexible substrate combined with a previously developed stretch bioreactor [2]. The substrate presents two parallel rectangular wells for enabling test parallelization and optimization of the culture medium volume. To guarantee a planar and uniform uniaxial strain, the substrate design was supported by finite element (FE) analyses (Abaqus, Dassault Systèmes). A uniaxial displacement of 3 mm (15% strain) was imposed at one side of the substrate while the opposite one was fixed, mimicking the bioreactor stretching. Once identified, the optimal substrate design was fabricated in polydimethylsiloxane (PDMS, Sylgard 184). Digital image correlation (DIC) method was adopted (VIC-2D system, isi-sys GmbH) to measure the substrate surface strain under uniaxial stretch (n=3). Explanatory biological tests were carried out on hPDLSCs from healthy donors. After coating with collagen I, the substrates were seeded with hPDLSCs, clamped in the bioreactor (Fig. 1A), and subjected to intermittent cyclic uniaxial stretch (8% constant pre-strain + 7% cyclic strain for 90 s (n=3) or 5 min (n=3) at 1 Hz every 6 h) for 3 days [3]. Cell-seeded substrates were cultured statically as control. Cell alignment was visually inspected by light microscopy and the expression of the osteogenic markers alkaline phosphatase (ALP), collagen type I (COLL 1), osteocalcin (OCN), tenogenic markers tenomodulin (TNM), periostin, and runt-related transcription factor 2 (RUNX2) was quantified by real-time PCR.

## Results

FE and DIC analyses showed similar results (Fig. 1B), with a planar and mostly uniform strain distribution at

the substrate well bottom with a mean strain value along the stretching direction ( $\epsilon_{xx}$ ) of 13.4% and  $14.4 \pm 0.25\%$ , respectively. Biological tests revealed cell alignment and significant over-expressions of OCN and RUNX2 genes with respect to the control when cells underwent the stimulation protocol with cyclic stretch lasting for 90 s. For cells exposed to longer stimulation (5 min), a slight decrease of osteogenic gene expression was observed compared to shorter stimulation (90 s) (Fig. 1C), while 2-fold and 3-fold increase in periostin and TNM respectively was obtained.

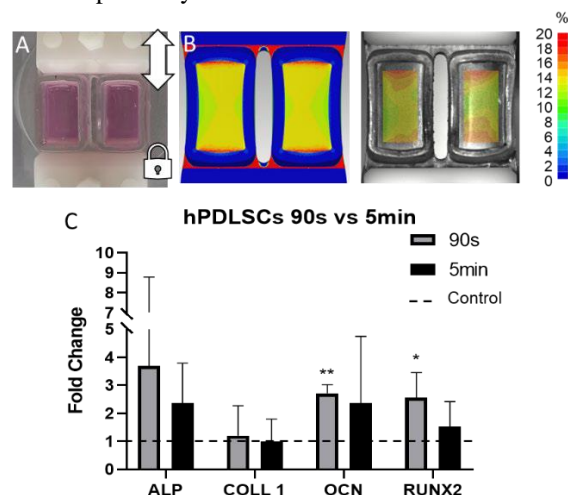


Figure 1: (A) Substrate clamped in the bioreactor; (B) FE (left) and DIC (right) analyses; (C) Genes expression after 3 days of culture under 90 s or 5 min cyclic stretch conditions.

## Discussion

Providing controlled physical stimuli *in vitro* is fundamental for in-depth understanding the cause-effect relationship between the applied mechanical cues and the cellular response. Here, we developed and tested an investigation platform able to provide by stretching controlled planar and uniform strain to adherent cells. Also, the presented platform, allowing for various strain protocols, gives the possibility to separately unravel the effect of each stimulation parameter. Preliminary biological results showed that timing in stimulation can play a crucial role in promoting hPDLSCs alignment and differentiation. Further biological tests are ongoing to confirm the obtained results.

## References

1. Roato et al, Nanomaterials 12(21):3878, 2022
2. Putame et al, Med Eng Phys, 84:1-9, 2020
3. De Jong et al, J Biomater Tissue Eng, 7:1303-1312, 2017



# ARE DECELLULARIZED PORCINE VESSELS SUITABLE GRAFTS FOR VASCULAR SURGERY?

Maria Stefania Massaro (1), Petra Kochová (2), Richard Pálek (1,3), Anna Malečková (1,4), Martina Grajciarová (1,4), Lenka Červenková (1,5), Robert Polák (1,3), Sima Šarčević (1,3), Jan Ševčík (1), Jáchym Rosendorf (1,3), Zbyněk Tonar (1,4), Václav Liška (1,3) and Vladimíra Moulisová (1)

1. Biomedical Center, Faculty of Medicine in Pilsen, Charles University, Czech Republic; 2. New Technologies for the Information Society Center, Faculty of Applied Sciences, University of West Bohemia, Czech Republic; 3. Department of Surgery, Faculty of Medicine in Pilsen, Charles University, Czech Republic; 4. Department of Histology and Embryology, Faculty of Medicine in Pilsen, Charles University, Czech Republic; 5. Department of Pathology, 3rd Faculty of Medicine, Charles University, Czech Republic

## Introduction

Cardiovascular diseases are the leading cause of mortality worldwide, and the need for reliable solutions is still under investigation. Autologous vessels or synthetic grafts are commonly applied, but both present disadvantages [1]. Autologous vessels can cause comorbidities or are not available, while synthetic grafts have compliance mismatch and increased risks of thrombosis [2]. Biologically derived scaffolds are thus being studied for the presence of a natural environment capable of recellularization in vivo. Decellularization, the removal of cells, is leading the research to provide a suitable extracellular matrix (ECM) scaffold.

We investigated decellularized porcine carotid arteries and caval veins using mechanical testing, histological investigation and in vitro functionalization with human endothelial cells (ECs).

## Methods

Both porcine carotid arteries and caval veins were explanted in our surgical facility in aseptic conditions with procedures approved by the ethical committee [3,4]. Vessels were cryopreserved at -80°C in a cryoprotectant (saline + 10% dimethylsulphoxyde). After thawing, perfusion of 1% Triton X-100 and 1% sodium dodecyl sulfate in 4 cycles of 1 hour each was applied. Hematoxylin-eosin (HE) staining was used to determine the efficacy of decellularization, Verhoeff's green trichrome, picrosirius red and Alcian blue with periodic acid Schiff were used to stain elastin, collagen and glycosaminoglycans respectively. Immunofluorescence (IF) stained fibronectin, laminin and vitronectin. Uniaxial tensile testing was applied on both native and decellularized carotid arteries to compare mechanical parameters. Seeding of ECs was performed both statically and dynamically in an in-house developed bioreactor.

## Results

HE staining confirmed the absence of nuclei. Histological staining and IF evidenced the preservation of all the major ECM molecules. Mechanical parameters such as Young's moduli (elastic and viscoelastic), ultimate stress and ultimate strain varied only a little between the native vessel and the decellularized scaffold. This ECM proved to be suitable for ECs repopulation, with better outcome from the dynamic

perfusion where cells were oriented regularly if compared to static seeding where cells were scattered and rounded (Figure 1).

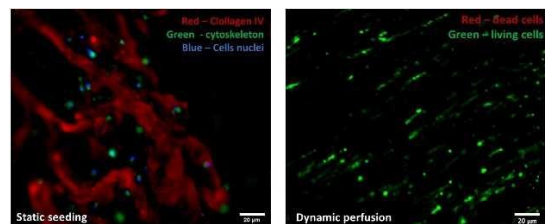


Figure 1: Repopulation of decellularized scaffold with human endothelial cells. Static seeding (left) was stained with immunofluorescence, while dynamic seeding was stained with a live/dead assay (right)

## Discussion

The use of porcine vessels showed promising results for being used as vascular graft both in terms of structure and cells adhesion. The decellularization procedure had little to no influence on the mechanical properties and on the removal of ECM molecules responsible for both strength and cells adhesion. Perfusion of the seeded vessel in a bioreactor lead to a better functionalization of the lumen to limit platelet activation as a consequence of collagen exposure in vivo. Further investigations will involve the proof of function in vivo in a porcine model.

## References

1. Toumpaniari et al., Tissue-engineering Vasc. Grafts, 207:269, 2020.
2. Camasao et al., Mater. Today Bio., 10, 2021.
3. Massaro et al. Front. Bioeng. Biotechnol., 2022.
4. Massaro et al., Biomed. Sci. Eng. 4, 2021.

## Acknowledgements

The study received support from grant START/MED/027 Start Program (No. CZ.02.2.69/0.0/0.0/19\_073/00169 35, Ministry of Education, Youth and Sports, Czech Republic) and projects National Institute for Cancer Research – NICR (Program EXCELES, ID No. LX22NPO5102) - Funded by the European Union - Next Generation EU, Center of Excellence UNCE/MED006 (Charles University “Center of Clinical and Experimental Liver Surgery”) and Cooperation project “Surgical disciplines” (COOPERATION-207043, Charles University).



# SCALING UP OF A PROCEDURE TO PRODUCE 'LIVING' PERICARDIUM MATERIAL FOR PERSONALIZED AORTIC VALVE RECONSTRUCTION

Stefano Rizzi (1,2), Alessia Schiavo (1), Manuele Giuseppe Muraro (3), Sara Mantero (2), Adrien Moya (3), Federica Boschetti (2), Cristina Banfi (1), Maria Laura Bacci (4), Domenico Ventrella (4), Arnaud Scherberich (3), Ivan Martin (3), Maurizio Pesce (1)

1. Centro Cardiologico Monzino IRCCS, Italy; 2. Politecnico di Milano, Italy; 3. Department of Biomedicine, University Hospital Basel, University of Basel, Switzerland; 4. Department of Veterinary Medicine, Alma Mater Studiorum-University of Bologna, Italy

## Introduction

The number of heart valve procedures is expected to triple by 2050 [1], increasing the impact on public health [2]. Mechanical prostheses are still subjected to thromboembolic complications, while biological valves encounter structural deterioration, with recurrence of failure in the mid-long term [2]. Here we introduce the possibility of processing pericardium into a valve. In the present contribution, we describe the results of a small-scale recellularization procedure aiming at obtaining an in-vitro engineered pericardial tissue amenable to adult and pediatric valve surgery and the future experimental program to scale-up recellularization procedure exploiting a custom-designed perfusion bioreactor.

## Methods

The porcine pericardium was decellularized with a complete aldehyde and xenoantigen residue-free procedure previously described [3, 4]. Human adipose-derived stem cells (hADSC) were purchased (Lonza, Switzerland). Decellularized pericardial matrices were recellularized under perfusion flow using  $0.65 \times 10^6$  cells per bioreactor and a flow-rates of 3 ml/min for the first 72 hours and 0.03 ml/min for additional 18 days. Samples were then harvested and prepared for immunofluorescence staining using  $\alpha$ -SMA, Vimentin, and proliferating cell nuclear antigen (PCNA) to evaluate cell phenotype and proliferation. The proteomic assessment was performed after 14 and 21 days of culture. A custom-made bioreactor was designed and prototyped to scale up the procedure using an SLA 3D printer (Form 3B+, Formlabs, USA) with a highly biocompatible resin (Biomed Clear, Formlabs). The system is designed to meet the specifications of a complete standalone bioreactor suitable for clinical employment in a GMP-compliant setting.

## Results

Histology sectioning and immunofluorescence analysis of the recellularized samples indicated increased human valvular-like protein production at late stages of culture. These results were confirmed by untargeted proteomic analysis of recellularized tissues that showed a generalized increase in cellular protein content of the tissue construct over time after the beginning of the culture. The expression of  $\alpha$ -SMA, one of the pathologic markers for VIC was mainly assessed in cells confined in the surface of the recellularized pericardium

but not in cells present in the decellularized matrix. According to PCNA staining, the proliferation rate of the cells penetrating the scaffold was lower than in cells covering the scaffold surface. Conversely, elastin and pro-Collagen I expression was higher in the cells in the inner part of the pericardium.

## Discussion

Our results show that culture conditions described here induce a valve-like phenotype in hADSCs colonizing the decellularized scaffold. We are now in the progress of redesigning the perfusion bioreactor to scale up the recellularization procedure and adapt it to a GMP-compliant setting using autologous stem cells to deliver a fully recellularized pericardial tissue amenable for surgical reconstruction of a patient-tailored aortic valve.

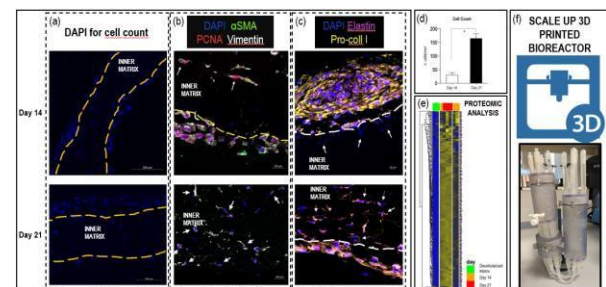


Figure 1: Cell number in the inner part of the scaffold (a,d) denoted a significant increase until day 21, along with protein production (e). Immunofluorescence staining (b) shows reduced  $\alpha$ -SMA expression, while vimentin, elastin, and pro-collagen I (c) confirm the pro-physiological valve-like protein production when proliferation (PCNA) (b), slowed down. The scaled-up bioreactor (f) will allow us to recellularize patches suitable to produce aortic valves.

## References

1. Head et al, Mechanical versus bioprosthetic aortic valve replacement, *Eur Heart J*, 38(28), 2183-2191, 2017.
2. Rizzi et al, Engineering Efforts to Refine Compatibility and Duration of Aortic Valve Replacements: An Overview of Previous Expectations and New Promises, *Front Cardiovasc Med*, 2022, 9
3. Amadeo et al, Aortic valve cell seeding into decellularized animal pericardium by perfusion-assisted bioreactor, *J Tissue Eng Regen Med*, 12(6), 14811493, 2018
4. Amadeo et al, Culture Into Perfusion-Assisted Bioreactor Promotes Valve-Like Tissue Maturation of Recellularized Pericardial Membrane, *Front. Cardiovasc. Med.*, 2020, 7



Day 1  
Integrative biomechanics III  
*Oral presentations*

Torino, 18 September 2023



# NUMERICAL SIMULATIONS OF THE FORMATION PROCESS OF NANOPARTICLES

Marco Bellotti(1), Alessandro Caimi (1), Enrica Chiesa (2), Michele Conti (1), Bice Conti (2), Ida Genta (2), Ferdinando Auricchio (1)

1. Department of Civil Engineering and Architecture, University of Pavia, Via Ferrata 3, Pavia, Italy;

2. Department of Drug Science, University of Pavia, V.le Taramelli 12, Pavia, Italy

## Introduction

Nanoparticles (NPs) are increasingly used as delivery system to carry and release drugs to a specific target; since they prove to be able to protect the payload from degradation, to improve drug solubility and bioavailability and to modify drug pharmacokinetic [1]. Microfluidic production technique is widely used for the NPs manufacture since, through this approach, the NPs size and homogeneity can be easily controlled [2]. Furthermore, the Microfluidic process allows to increase the formulation reproducibility thanks to a deepen control of the fluid dynamic parameters involved in the mixing process [3]. In the proposed work two different techniques are exploited for the production of NPs, passive mixing with herringbone and droplet generation by hydrodynamic flow focusing. Computational Fluid Dynamic (CFD) approach can be exploited to understand which fluidic condition can be adopted and used as boundary conditions to produce NPs. Hence, the present work aims at showing the efficiency of a computational approach to optimize the production of nanoparticles.

## Methods

The geometries of different microfluidic chips are recreated through Autodesk Inventor 2020 and the computational grid is created using Ansys Workbench 2021R2. To mimic the interaction between different fluids (e.g., water-immiscible or miscible) two different multiphase models (i.e., Volume of Fluid and Mixture models) can be exploited.

In order to study the changes in the droplets formation or the mixing processes due to changes in the boundary conditions, data referring the volume fractions of the different phases can be exploited.

## Results

The mixture model was able to capture the macroscopic effect of geometrical and fluid dynamic variations onto the fluids mixing process and consequent NPs production (Fig.1 A). Moreover, in order to preliminary validate the numerical model, experimental results were also collected, and several significant effects were highlighted (Fig.1 B, C) [4].

The VOF in-silico model proved to be able to capture with detail the principal phases of the droplet formation (i.e., separation and elongation) (Fig.1D). and analyze the morphological properties (e.g., bubble length) (Table 1).

## Discussion and conclusions

Although one of the limitations of proposed CFD analysis is the impossibility to capture small scale effect (e.g., molecular dynamics) they are able to highlights the effects of geometry and fluid-dynamic parameters over the NPs mixing zones and droplets morphology. In conclusion, the present approach can be used to identify the fluid-dynamic parameters able to maximize the mixing efficiency and optimize the production parameters.

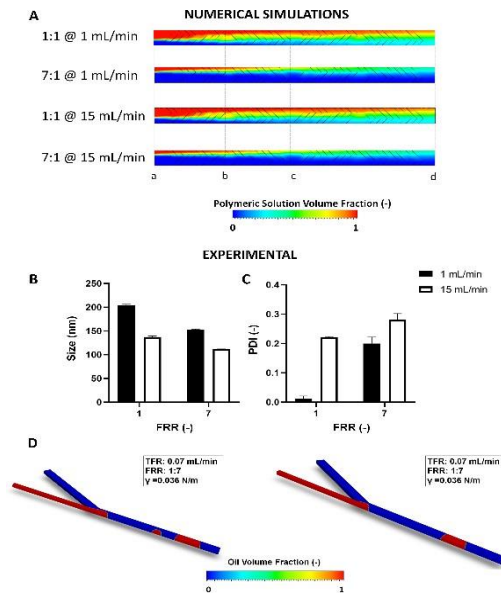


Figure 1: Contour plots of the mixing process with different boundary conditions (A). Distribution of NPs size (B) and polydispersity index (PDI) (C) obtained with a herringbone microfluidic chip with the same numerical boundary conditions. Droplets formation with different boundary condition (D).

FRR	Droplet Volume ( $\text{mm}^3$ )	Droplet Length (mm)	Time of Rupture (s)
1:3	4.26e-3	26.4e-2	2.98e-2
1:7	4.95e-3	31.2e-2	2.13e-2

Table 1: Morphological data and rupture event timing at different flow rate ratio (FRR) condition.

## References

1. Agrahari V. et al, Nanomedicine, 12(8):819-823, 2017.
2. Operti M.C. et al, Pharmaceutics, 14(2):276, 2022.
3. Operti M.C. et al, Int. J. of Pharmaceutics, 550(1-2):140-148, 2018.
4. Chiesa et al., Int. J. of Pharmaceutics, 629,122368, 2022.



# NUMERICAL AND EXPERIMENTAL CHARACTERIZATION OF A PIEZOELECTRIC ACTUATOR FOR MICROFLUIDIC APPLICATIONS

Cristian Brandi (1), Adele De Ninno (2), Enrico Verona (2), Luca Businaro (2), Paolo Bisegna (1), Federica Caselli\* (1)

1. University of Rome Tor Vergata, Italy; 2. CNR Institute of Photonics and Nanotechnology, Italy

## Introduction

Microfluidic impedance cytometry [1] is increasingly used for the high-throughput label-free electrical characterization of single cells. Adding a cell-sorting functionality to impedance cytometry systems represents an attractive opportunity (Fig. 1(a)). This requires the development of tailored approaches for the online processing of impedance signals, coupled with a suitable microfluidic cell sorter. In this work, we present the numerical and experimental characterization of a sorting system based on piezoelectric actuation.

## Methods

As shown in Fig. 1(b-c), the main channel of the microfluidic device is  $150\ \mu\text{m}$  wide, while the width of the three collection channels is  $50\ \mu\text{m}$ . Channels height is  $40\ \mu\text{m}$ . Two lateral regions are designed on the sides of the sorting region. One of them houses the actuator, that consists of a cylindrical chamber (13 mm diameter, 5 mm height) above which a circular ceramic transducer (lead zirconate titanate, PZT) is bonded. The PZT element has a diameter of 15 mm and a thickness of  $110\ \mu\text{m}$ , while its metal substrate (stainless-steel) is 20 mm in diameter and  $100\ \mu\text{m}$  thick.

To analyse the fluid flow and the particles displacement induced by the PZT actuation, a 3D finite element model of the device was implemented (Fig. 1(d)) based on: the linear theory of piezoelectricity, the Navier-Stokes equations for laminar incompressible flow, and the Khan and Richardson's model [2] for particle tracing. Furthermore, an image-based approach was developed for the experimental characterization of particle deviation. Specifically, the time course of the rotation angle of the sample stream was automatically extracted from high-speed video recordings using a custom Matlab script.

## Results

Figure 1(e) shows an example of the simulated displacement of the central point of the metal plate as a function of time, under voltage stimulation at 3 Hz and an inward flow rate of  $10\ \mu\text{l}/\text{min}$  at the main channel inlet (no sheath flows). The overall outward flow rate through the outlets is also reported.

Figure 1(f-g) shows an example of image-based characterization of the rotation angle of the sample stream.

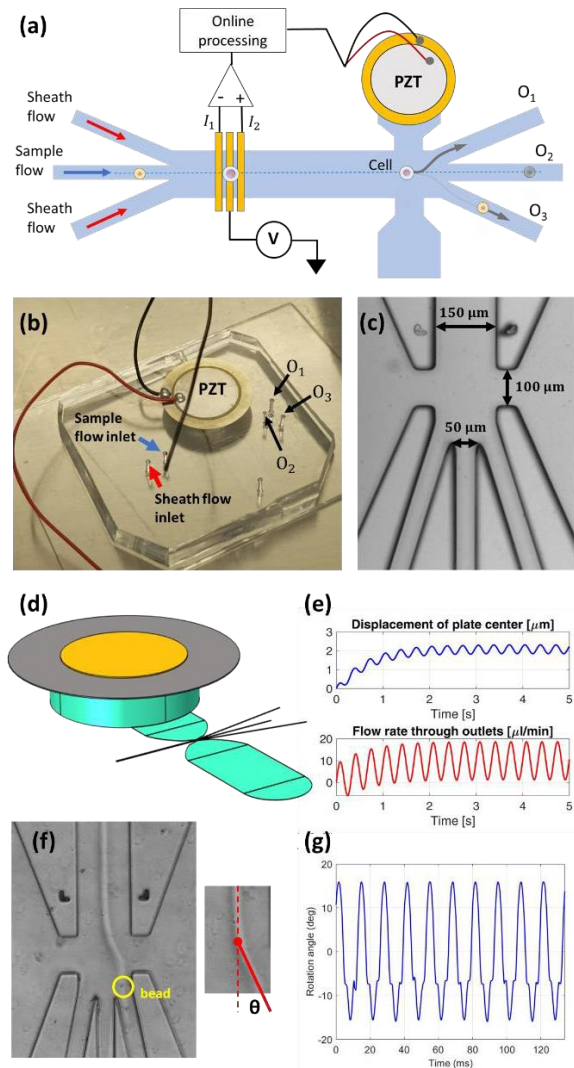


Figure 1: (a) Principle of impedance-based single-cell sorting. (b) Device photograph. (c) Microscopy image of the sorting region. (d) Model geometry. (e) Simulated displacement of plate central point (10 V, 3 Hz). (f) Microscopy snapshot showing an example of particle deviation ( $5\ \mu\text{m}$  bead). (g) Rotation angle,  $\theta$ , of the sample flow upon sinusoidal actuation (5 V, 75 Hz).

## References

1. Honrado et al, Lab Chip, 21(1): 22–54, 2021.
2. Richardson et al, Chemical Engineering, vol. 2. 2013.

## Acknowledgements

This work was supported by Regione Lazio under grant E85F21002390002 (MicroSystemQ, Research Groups 2020).



# MULTISCALE CELL AND TISSUE MECHANICS IN TISSUE MORPHOGENESIS WITH SUBCELLULAR ELEMENT MODELING

Sandipan Chattaraj<sup>1</sup> and Francesco S. Pasqualini<sup>1</sup>

1. Synthetic Physiology Lab, Department of Civil Engineering and Architecture, University of Pavia, Italy

## Introduction

*How do tissues and organs build themselves?* Modeling morphogenetic processes to answer this question is hard. In fact, continuum mechanics deals poorly with non-linear, large deformations caused by individual cells migrating or proliferating. But, discrete Potts models that naturally deal with cellular events fail to capture the underlying multiscale mechanics. We present an enhanced version of the subcellular element modeling (eSEM) framework to tackle this problem. SEM models tissue mechanics by describing cells as ensembles of particles whose interactions are governed by empirically defined potentials. Here, we chose a potential that preserves single-cell rheology to demonstrate how eSEM offers multiscale mechanics in cell proliferation.

## Methods

In eSEM, we model cells with  $N_p$  particles subjected to the overdamped Langevin:  $\eta \dot{\mathbf{r}}_{ijk} = \xi_{ijk} + \mathbf{F}(\mathbf{r}_{ijk})$ . Where  $\mathbf{r}_{ijk}$  is the position of the  $i$ -th particle of type  $j$  in cell  $k$ ,  $\eta$  is the cell viscosity,  $\xi_{ijk}$  is a noise term, and  $\mathbf{F}(\mathbf{r}_{ijk})$  is the net force of all pairwise interactions at  $\mathbf{r}_{ijk}$ . For  $\mathbf{F}(\cdot)$ , we used Morse-like potentials to model adhesion and volume exclusion[1].

By invoking spherical packing, the parameters of these potentials can be linked with values of cell stiffness and viscosity as measured in rheology experiments[2]. Additionally, we modelled the active control of the nuclear intracellular position using spring-like forces that tie the nucleus with the cell's centroid.

To perform simulations, we updated SEM++, a user library[1] for the molecular dynamics solver LAMMPS [3]. We used Ovito[4] for visualization and analysis.

## Results

To verify our potential scalability, we simulated a creep experiment in which a cell formed by  $N_p = [250, 10k]$  particles was stretched to 2.5% strain along the Z-axis in the absence/presence of a larger nuclear particle (Fig. 1). We performed simulations using cells equilibrated in five different initial conditions to account for stochastic effects. As expected, there was a degree of variability around each condition, but no statistically significant differences were observed. Together, these results suggest that whatever the chosen modelling resolution, the particle ensemble will simulate single cell rheology

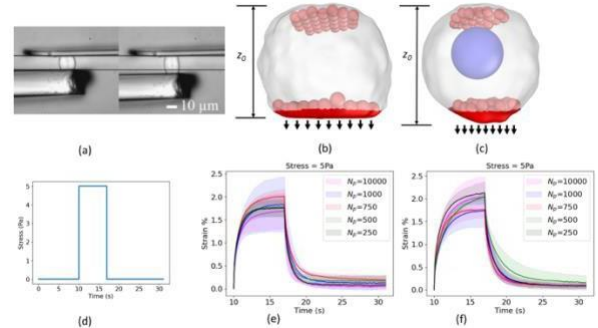


Figure 1: Cell creep simulations varying particle number ( $N_p$ . Example particles in red, grey envelope), type (blue nucleus), and orientation (variance).

In other words, in eSEM cells act as mechanically-sound agents that can be imbued with biologically relevant activity. For example, we simulated three rounds of cell division and demonstrated how eSEM provides descriptions of multi-scale mechanics (Fig. 2).

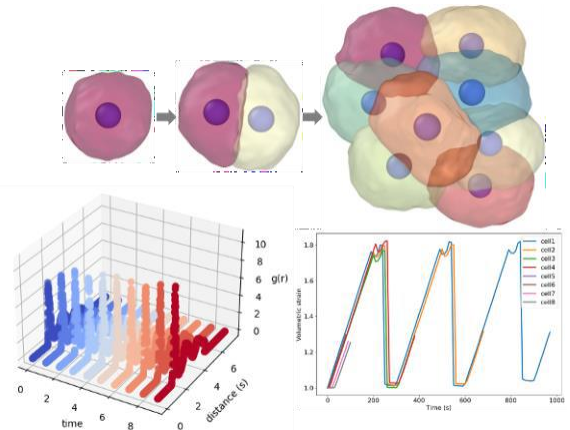


Figure 2: eSEM modelling of cell division (top) showing particle- (bottom left, radial density function) and cell-level mechanics (bottom right) for eight resulting cells.

## Discussions

For eSEM to model morphogenesis, we will work on better modeling (potentials) and computing (GPU).

## References

1. Milde et al, Comp Part Mech 1, 211–227 (2014)
2. Desprat et al, Biophys J, 2224–2233 (2005)
3. Thompson et al, Comp Phys Comm 271 (2022)
4. Stukowski et al, Mod Sim Mater Sci Eng 18 (2010)

## Acknowledgements

This work was supported by grant #852560 from the ERC.



# CELL'S SENSE OF SLOPE

Crescenzo Frascogna (1,2), Valeria Panzetta (1,2), Paolo Antonio Netti (1,2)

1. Centre for Advanced Biomaterial for Health Care, Istituto Italiano di Tecnologia, Napoli, Italy;

2. Dipartimento di Ingegneria Chimica, dei Materiali e della Produzione Industriale, Università degli Studi di Napoli Federico II, Napoli, Italy

## Introduction

Cells have evolved a remarkable ability to sense and respond to their environment. They can detect a wide range of physical and chemical cues, including signals from the extracellular matrix (ECM) that influence their spatio-temporal organization and behavior. These signals play a critical role in guiding essential cellular processes such as morphogenesis, tissue repair, and disease progression. In recent years, the local geometry of the ECM has emerged as an important factor that can affect cell mechanics and signaling [1]. Here, the effects of surface curvature on cellular behavior, including the dynamics of focal adhesions and cytoskeletal rearrangement, have been investigated using a molecular-mechanical model. Then, to validate model formulation, experiments have been carried out to test its predictions. Understanding how cells respond to surface curvature has implications for tissue engineering, regenerative medicine, and the development of new therapeutic strategies.

## Methods

Cells are capable of probing tissue properties via their adhesive molecular machinery, which is commonly referred to as the "molecular clutch". In this work, to better understand the behavior of cells in response to concave and convex substrates, we developed a modified version of the molecular clutch model [2]. This updated model incorporates master equations governing the dynamic evolution of the system, taking into consideration the spatial organization of actin stress fibers in relation to the slope of the substrate. Monte Carlo simulations have been employed to describe the binding and unbinding events of the clutch. In order to investigate the model predictions, single cell analyses on curved PDMS substrate have been carried out coupling immunofluorescence technique and atomic force microscopy. These substrates consisted of microarrays of concavities and convexities with controlled radii of curvature. By characterizing the mechanical identity of NIH/3T3 cells grown on these substrates, we were able to gain a deeper understanding of the role of surface curvature in cell mechanics and mechanotransduction.

## Results

This study investigates the impact of substrate curvature on cytoskeletal activity and cell adhesion using a computational model implemented in MATLAB. Our results reveal that on concave surfaces, the equilibrium condition of the cell, that is associated to the minimum of the actin retrograde flow rate, is characterized by a

lower number of clutches compared to planar surfaces. Conversely, convex substrates show a reversed trend with a higher number of clutches involved in the adhesion process compared to planar surfaces. The model predicts that these slope-dependent changes in clutch dynamics lead to substantial differences in the mean traction forces exerted on curved versus flat substrates. Moreover, our experimental results confirm the model predictions, showing an increase in focal adhesion size and cell Young's modulus on convex substrates compared to concave ones.

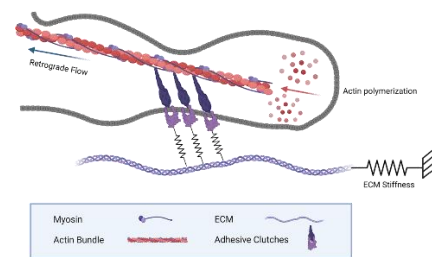


Figure 1: Physical schematization of the molecular clutch model on non-flat substrate.

## Discussion

The concavity induces a softening effect in the cellular perception of substrates with cells adopting a spider-like configuration characterized by a lower number of involved clutches than in the planar case. On the other hand, the convexity induces a stiffening effect that results in cells adopting a snail-like configuration with a higher number of clutches involved in the adhesion and exerting a greater force on the substrate [3]. Cell mechanosensing is not mediated only by substrate stiffness but also the curvature plays a key role in the mechanical response of the cell. Overall, our findings highlight the importance of surface curvature in the way that cells respond to mechanical stimuli and underscore the critical role of the molecular clutch in mechanotransduction. We believe that our molecular clutch model provides a valuable tool for investigating the complex relationship between cell mechanics and ECM architecture and can be applied in a wide range of biological and biomedical studies.

## References

1. Callens et al, Biomaterials, 232:119739, 2020.
2. Bangasser et al, Cell Mol Bioeng, 6(4):449-459, 2015.
3. Werner M et al, Adv Sci, 4(2):1600347, 2016.



Day 1  
Integrative biomechanics  
*Poster presentations*

Torino, 18 September 2023



# DESIGN AND FABRICATION OF AN INTESTINAL PHANTOM TO MIMIC INTESTINAL MOTILITY

P. Signorello, L. Cacopardo, N. Guazzelli, I. Nicolai, A. Ahluwalia  
University of Pisa, Italy

## Introduction

Modelling gut motility is important for the study of gut dysfunctions, which are known to affect nutrient absorption [1]. However current systems are not able to provide a human-relevant model at the macroscale [2]. The aim of this work is thus to engineer a physical twin replicating gut architecture, mechanical features, and dynamics as well as the rheological properties of the luminal content.

## Methods

Polydimethylsiloxane (PDMS) samples were prepared at different monomer - crosslinking agent ratios: 4:1, 5:1, 6:1 and 7:1. Tensile tests were performed at a strain rate of 6 mm/s using a universal testing machine (Zwick-Roell, Z005 ProLine). A 60% maximum deformation was selected corresponding to the limit beyond which the muscle, at a physiological level, remains in the elastic regime [3]. Buffer solutions were obtained by dissolving 0.681% w/v potassium dihydrogen phosphate and 0.022, 0.1164, and 0.187% w/v sodium hydroxide in distilled water, obtaining solutions at pH 6, 7 and 8. pH values were assessed with a pH meter (Hanna, Edge series). Pectin from 0.5 to 5% w/v was then dissolved in the buffer solutions. Viscosity measurements were performed using a Brookfield DV-II+PRO Viscosimeter. The phantom was finally designed using Computer Aided Design (CAD) software (Fusion 360), reproducing the anatomical shape of the bowel.

## Results

Figure 1 shows the technical drawings of the duodenum and the resulting PDMS prototype.

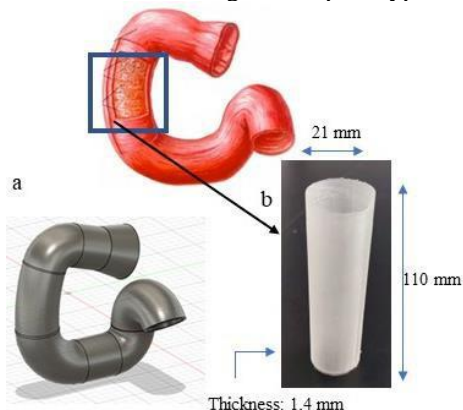


Figure 1: Comparison between physiological duodenum and a) anatomical technical drawings. b) PDMS prototype.

As expected, Figure 2 shows that PDMS apparent elastic moduli decrease with increasing monomer - crosslinking agent ratio and that pectin viscosity increases as a function of concentration and decreases as the pH increases.

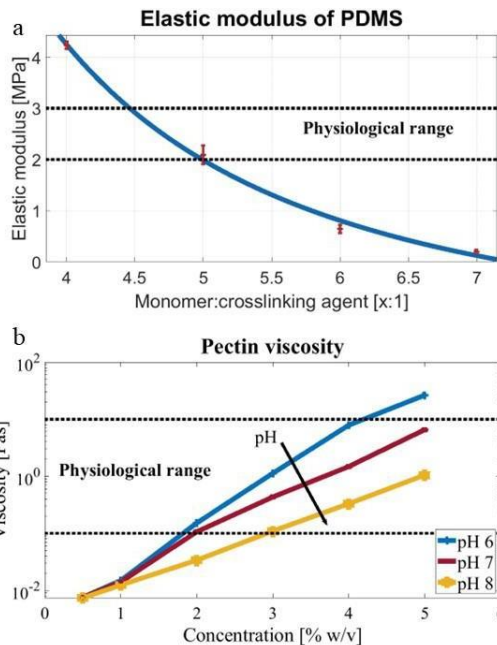


Figure 2: a) Elastic modulus of PDMS at different ratios and b) pectin viscosity in buffer solutions with different pH, plotted in logarithmic scale with respect to pectin concentration.

## Discussion

The 5:1 ratio resulted closer to the desired value of  $2.09 \pm 0.17$  MPa (2-3 MPa [3-4]) and was thus selected for phantom fabrication. Moreover, pectin viscosities resulted within the desired physiological range ( $1-10$  s<sup>-1</sup> [5]) at the different pH values corresponding to physiological pH variations in the gut [6]. Replicating luminal content rheology is indeed fundamental to assess its propulsion within the bowel.

## Conclusions

In this study, materials able to replicate the mechanical and rheological features of the gut and luminal content were defined, enabling the prototyping of a physical twin. Future studies are ongoing to increase the PDMS surface's hydrophilic properties, enabling the coupling with an intestinal mucosal layer. In the future, this model can be used to investigate the efficacy of treatments to restore gut motility.

## References

1. John. et al, *Net. At. Hum. Ph.*, 2002.
2. Li et al. *Comp. Rev. Food Sci. Food Saf.*, 21, 6, 11, 2022.
3. Bourgouin. et al, *Med. Bio. Eng. Comp.*, 50(12), 1279-1288, 2012.
4. Johnson. et al. *Jour. Bio.*, 109, 8, 2020.
5. Hardacre et al, *Jour.The Roy. Soc. Int.* 15, 20180092, 2018.
6. Ovesen et al. *Gastro.* 90, 958 -962, 1986.



# ARE MECHANICAL PARAMETERS OF SURGICAL MESHES RELATED TO STRUCTURE PROPERTIES? A MULTIPLE REGRESSION ANALYSIS

Vittoria Civilini (1)(2), Vincenzo Giacalone (1)(2), Alberto L. Audenino (1)(2), Mara Terzini (1)(2)

1. Department of Mechanical and Aerospace Engineering, Politecnico di Torino, 10129 Turin, Italy;

2. Polito<sup>BIO</sup>Med Lab, Politecnico di Torino, 10129 Turin, Italy;

## Introduction

At present, recurrences after surgical meshes implantation for hernia treatment range from 1.4% to 26.5% [1]. The main causes of failure are often related to a foreign-body reaction and mesh shrinkage due to an incorrect tissue ingrowth during the healing process. Structure (e.g., porosity, thickness, pores dimension and orientation) and mechanical (e.g., mesh elasticity, isotropy, and strength) parameters take part in mesh *in vivo* incorporation and in patient comfort after the implantation [2]. Nonetheless, the correlation between these crucial aspects has only been theoretically analyzed [3]. This study aims to investigate the impact of structural textile characteristics on the mechanical properties of different monofilament polypropylene warp-knitted meshes. In addition, textile porosity and effective porosity are compared as independent variables for the multiple regression analysis.

## Methods

Three quasi-static test methods (i.e., uniaxial tensile test, ball burst test, and suture retention test) were designed in order to extract relevant parameters for the mechanical characterization of synthetic surgical meshes. Therefore, the test protocol was executed on 14 polypropylene meshes with different weights produced by different manufactures. Meanwhile, the structure parameters of textile porosity (ratio between the area occupied by pores and the total area of the mesh) and effective porosity (considers only those pores with diameter greater than 1 mm as effective in reducing scar formation) were obtained through image processing of meshes photos (MATLAB). Additionally, the thickness of each mesh was measured through a thickness gauge (547–321, Mitutoyo). Two multiple regression analyses were conducted to investigate potential correlations between the mechanical properties and two set of structural properties: set I, composed of meshes thickness and textile porosity, and set II, composed of meshes thickness and effective porosity. Variance Inflation Factors (VIF) were also inspected in order to evaluate the severity of multicollinearity in the multiple regression analysis. VIF values greater than 10 are taken as an indication that the multicollinearity should be further investigated.

## Results

The goodness of fit measure for the multiple regression analyses was evaluated through the coefficient of determination,  $R^2$  (Table 1). A strong correlation of

most mechanical parameters with the considered structure properties stands out. Lower values of  $R^2$  are obtained in deformation-related parameters in both uniaxial and ball burst tests, with very low values for dilatational strain at 16 N/cm. The VIF values, lower than 4 in both the analyses, denote a low level of multicollinearity.

### Uniaxial Tensile test

	UTR weak	UTR strong	SR weak	SR strong	k weak	k strong	alfa
I	0.69	0.88	0.13	0.19	0.48	0.85	0.15
II	0.73	0.89	0.29	0.25	0.3	0.83	0.15

### Ball Burst test

	BS	MT	DS	DS16
I	0.85	0.81	0.62	0.11
II	0.88	0.69	0.79	0.05

### Suture Retention test

	SRS weak	SRS strong	
I	0.86	0.87	<i>weak: weaker direction of the mesh</i>
II	0.78	0.89	<i>strong: stronger direction of the mesh</i>

Table 1:  $R^2$  coefficient computed for each mechanical parameter. UTR: uniaxial tension at rupture; SR: strain at rupture; k: secant stiffness; alfa: coefficient of anisotropy; BS: bursting strength; MT: maximum membrane tension; DS: maximum dilatational strain; DS16: dilatational strain at 16 N/cm; SRS: suture retention strength.

## Discussion

The correlation of textile and effective porosity with an exhaustive selection of mechanical parameters derived from surgical meshes testing has been investigated. While previous investigations on the influence of these structure parameters *in vivo* showed that only pores sizes greater than 1000  $\mu\text{m}$  are appropriate for ingrowth of soft tissue in surgical meshes [3], [4], here textile and effective porosities paired with meshes thickness showed up to be related to the mechanical parameters but without substantial differences. Further investigation regarding orientation, shape of pores and loop patterns are ongoing and will enrich the here presented analyses.

## References

1. Köckerling, Front Surg, 6:26, 2019.
2. Zhu et al, World J Gastrointest Surg, 7(10):226-236, 2015.
3. Miao et al, Materials, 8:8148-8168, 2015.
4. Mühl et al., J. Biomed. Mater. Res. B Appl. Biomater, 84:176-183, 2008



# HOW TO SHOW CREDIBILITY OF IN SILICO CLINICAL PROCEDURES: APPLICABILITY ANALYSES

Giulia Luraghi, Sara Bridio, Anna Ramella, Jose Felix Rodriguez Matas, Francesco Migliavacca

Dept. Chemistry, Materials and Chemical Engineering, Politecnico di Milano, Italy

## Introduction

In silico technologies are used to investigate aspects of prevention, diagnosis, follow-up, treatment and outcome of diseases. In particular, cardiovascular and neurovascular clinical procedures can be simulated using detailed -high-fidelity- computational models, but their credibility needs to be assessed. Model credibility is intended as the capability of a computational model to address a given question of interest (QOI) in a specific context of use (COU), through the collection of evidence [1].

The aim of this work is to show an in silico applicability analysis to (i) the thrombectomy and (ii) the Thoracic Endovascular Aortic Repair (TEVAR) procedure in order to deem them credible for use within the frame of in silico medicine.

First, the real environment setting (R-COU) and the physical experimental setting (R-VAL), and the corresponding computational models (M-COU and M-VAL) are described (figure 1 for the thrombectomy case). Then, the central body of the applicability analysis includes equalities and differences between all the described ingredients (R-COU, R-VAL, M-COU and M-VAL). The analysis ends with the conclusion of the credibility assessment.

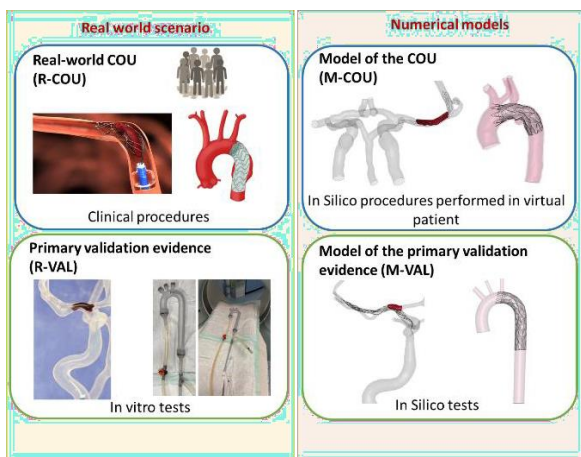


Figure 1: In silico thrombectomy and TEVAR procedures credibility: on the left, the real-world scenario of the context of use and validation evidence. On the right, numerical models of the context of use and validation evidence.

## Credibility of the virtual thrombectomy procedure

Intra-arterial thrombectomy is a minimally invasive procedure for acute ischemic stroke in which the obstructing thrombus (clot) is removed using a

minimally invasive device (stent-retriever). The stent-retriever is inserted from the femoral artery access to the thrombus location in the brain. After the deployment of the stent-retriever, the thrombus is removed by the retraction of the stent-retriever. The virtual procedure can be used as a tool to predict procedure outcome: positive if the clot removal is successful, or negative if the clot remains inside the vessel. In this view, the QOI is: "Is the thrombectomy procedure with a given stent-retriever capable of successfully removing a clot of a given composition, a given volume, from a given location?" [2]. The main validation evidence to demonstrate the applicability of the model is an in vitro thrombectomy performed in a silicone 3D-printed patient-like branch with a specific device and a specific clot analogue.

## Credibility of the virtual TEVAR procedure

TEVAR procedure is a minimally invasive technique for treating aortic pathologies in which a self-expandable stent-graft is inserted and deployed in the pathological region to treat the patient and recreate a more physiological situation. The numerical model is able to simulate the stent-graft deployment and its interaction with the aortic wall. It can be used to predict the TEVAR outcome in a virtual population. In this view, the QOI is: "Will a given stent-graft model be successfully deployed in a given patient-specific aorta in a given position with respect to the location of the pathology (e.g. aneurysm, dissection, PAU)" [3]. As validation evidence, a rigid 3D printed idealized aorta is used to experimentally implant a stent-graft under a CT scan. The stent configuration obtained with the experiment is adopted to validate the simulation results.

## Conclusion

Validation evidence sources are here identified for the specific context of use and adopted to demonstrate the applicability of the numerical procedures replicating thrombectomy and TEVAR procedures, thereby answering the specific questions of interest.

The discussed applicability analyses demonstrated that the developed in-silico models are trustworthy for replicating the clinical procedures in virtual patients.

## References

1. Pathmanathan et al, J Verif Valid Uncert, 2(2), 2017.
2. Luraghi et al, J Biomech, 126, 110631, 2022.
3. Ramella et al, J Biomech, 146, 111423, 2023.



# PERSONALIZED COMPUTATIONAL MODELING OF MYOCARDIAL PERFUSION IN CORONARY ARTERY DISEASE

Giovanni Montino Pelagi (1), Andrea Baggiano (3), Francesco Regazzoni (2), Gianluca Pontone (3), Giovanni Valbusa (4), Christian Vergara (1)

1. LABS, Dip. Chimica, Materiali E Ing. Chimica, Politecnico Di Milano; 2. MOX, Dip. Di Matematica, Politecnico Di Milano; 3. Cardiovasc. Imaging Dept., Centro Cardiologico Monzino, Milan; 4. Bracco Imaging S.p.A., Milan

## Introduction

Quantitative assessment of coronary blood flow and myocardial perfusion is of critical importance in the prognostic stratification of patients suffering from coronary artery disease. Since the most used clinical exams to this aim pose significant burden to the patient, computational approaches could be invaluable in providing relevant information in a non-invasive way. Still, many issues remain to be addressed to use them in a predictive way: tailoring the computational model to a specific patient, capturing the interplay between ventricle contraction and coronary hemodynamics, and accounting for pathological effects. Here, we developed a multiscale framework to run patient-specific simulations of hyperemic coronary blood flow, up to the microvasculature, to predict quantities of clinical interest in individuals with coronary artery disease.

## Methods

Patients anatomy is reconstructed from CT angiographic images using segmentation tools. The multiscale perfusion model features a 3D description of hemodynamics in the epicardial arteries, coupled with a multicompartiment Darcy formulation for the microvasculature, which also includes a treatment for microvessels compliance and ventricular contraction. Tailored pressure boundary conditions, representative of the hyperemic state, are built using routine clinical measures. Blood flow simulations are run in 8 patients using the in-house Finite Elements software LifeX.

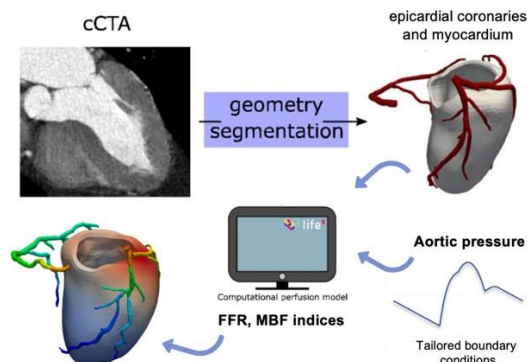


Figure 1: Steps of the personalized blood flow analysis.

Simulation results are post-processed to obtain the Fractional Flow Reserve ( $FFR_{CT}$ ) and the Myocardial Blood Flow ( $MBF_{CT}$ ) indices. The predictive power of the proposed framework is then assessed by direct comparison with measures of FFR and MBF from a

clinical stress test, using a retrospective validation approach.

## Results

In all the patients, the characteristic coronary phasic flow pattern with high arterial inflow in diastole and high venous outflow in systole was recovered. MBF maps show significantly higher values in patients with non-significant coronary stenosis having  $FFR > 0.8$  (mean  $MBF = 289$  ml/min/100g) with respect to patients with at least one lesion having  $FFR < 0.8$  (mean  $MBF = 183,25$  ml/min/100g). Myocardial perfusion defects associated with such lesions were also highlighted in the obtained MBF maps.

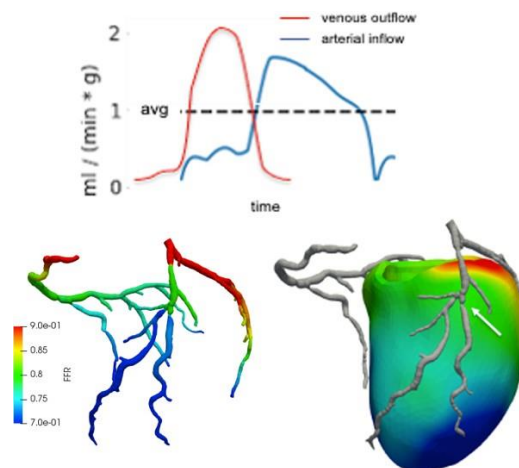


Figure 2: Top: flow patterns in the epicardial arteries and veins. Bottom:  $FFR_{CT}$  results showing significant lesions (left), MBF map with large perfusion defect and culprit lesion identified by the white arrow (right).

## Discussion

$FFR$  results show excellent agreement with the invasive value. Considering the clinical cutoff-based clustering ( $< 0.7$ ,  $> 0.8$  and in range  $0.7-0.8$ ), we achieved a per-vessel sensitivity and specificity of 95.8% and 100% respectively. MBF results show in general a good agreement with values obtained from the stress test, although we notice a slight yet non-negligible tendency in overestimating MBF in the more pathological cases. Indeed, mean MBF shows an absolute accuracy of 91% and 78% for patients without and with significant lesions, respectively. We believe that a more precise parametrization of the myocardium may solve this issue.

# A NUMERICAL MODEL FOR ZEBRAFISH VENTRICULAR ACTION POTENTIAL

Ludovica Cestariolo (1), Jose Maria Ferrero (2), Zachary Long (3), T Alexander Quinn (3), Jose Felix Rodriguez Matas (1)

1. Politecnico di Milano, Milan, Italy; 2. Universitat Politècnica de València, Valencia, Spain;  
3. Dalhousie University, Halifax, NS, Canada

## Introduction

The use of zebrafish in the field of cardiac electrophysiology has grown in the last decades thanks to its action potential (AP) morphology and the functional similarities in cardiac ion channels [1] related to the existence of ~69% human gene orthologues [2]. Considering the exponential growth in using this animal model to help in studying the ionic mechanism involved in the development of cardiac pathologies and the response to pharmacological therapies, it seems to be very helpful the development of an *in-silico* AP model to also allow reducing the number of animals used for the experimentation. Thus, the objective of this work was to develop a mathematical model for the zebrafish ventricular AP.

## Methods

After accurate research to identify individual ion channel experimental data (*i.e.*, by patch-clamp) associated with the main currents responsible for the AP, a detailed AP based on the TenTusscher and Panfilov AP model from 2006 (TP06) [3] was adapted to the adult zebrafish. Therefore, the main currents involved are the: i) fast  $\text{Na}^+$  current,  $I_{\text{Na}}$ , responsible for the rapid depolarization of the AP; ii) T-type  $\text{Ca}^{2+}$  current,  $I_{\text{CaT}}$  (added to the TP06 model), which contributes to the initial AP upstroke; iii) L-type  $\text{Ca}^{2+}$  current,  $I_{\text{CaL}}$ , which maintains the AP plateau and provides the  $\text{Ca}^{2+}$  necessary for contraction; iv) rapid and slow delayed rectifier  $\text{K}^+$  currents,  $I_{\text{Kr}}$  and  $I_{\text{Ks}}$ , involved in repolarization; v) inward rectifier  $\text{K}^+$  current,  $I_{\text{K1}}$ , which contributes to late repolarization and maintains resting membrane potential; and vi)  $\text{Na}^+/\text{K}^+$  pump and  $\text{Na}^+/\text{Ca}^{2+}$  exchanger, essential for restoring ionic balance during the resting phase. The transient outward  $\text{K}^+$  current,  $I_{\text{to}}$ , was removed from the TP06 model since it is not present in zebrafish [1].

The model was implemented in Matlab. To identify the best combination of parameters that fits the recorded AP shape while ensuring model stability, the Monte Carlo method was used with 11000 combinations of 34 parameters. A sensitivity analysis was conducted by varying one parameter at a time for the maximum conductances, the time constants, and the activation and inactivation gating variables.

The newly developed AP model was parameterized by fitting to sharp electrode AP recordings from the ventricle of adult zebrafish isolated hearts maintained in 28°C HEPES-buffered saline solution and paced from the ventricular apex.

## Results

Figure 1 shows a comparison of the numerical against experimental AP recordings for a pacing frequency of 2Hz (left) and restitution behavior of the upstroke for protocol S1-S2 (right), whereas Table 1 gives a detailed comparison of AP morphology for the same stimulation frequency.

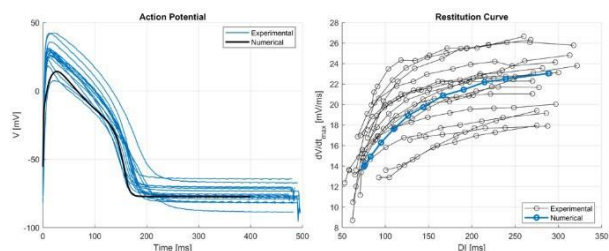


Figure 1: Comparison of ventricular experimental and numerical APs (left) and upstroke restitution curves for S1-S2 protocol (right).

AP marker	Model	Experimental
RMP [mV]	-77.42	-88.42 ÷ -68.48
APA [mV]	91.67	96.27 ÷ 111.20
APD <sub>20</sub> [ms]	74.97	53.06 ÷ 94.48
APD <sub>50</sub> [ms]	138.36	114.92 ÷ 158.07
APD <sub>80</sub> [ms]	156.64	146.88 ÷ 200.25
APD <sub>90</sub> [ms]	162.1	156.48 ÷ 219.66
dV/dt <sub>max</sub> [V/s]	23.12	13.73 ÷ 25.98
V <sub>max</sub> [mV]	14.22	7.85 ÷ 42.56

Table 1: Morphology of ventricular experimental and numerical APs.

## Discussion

This work represents the first attempt to develop an electrophysiological detailed AP model of an adult zebrafish. The model is able to describe in-vitro experimental data from isolated adult zebrafish hearts in both static and dynamic stimulation protocols. However, further examination of the model response to additional stimulation protocols and to drugs is required for further validation of the model.

## References

1. U. Ravens, Prog. Biophys. Mol. Biol., 138:38–44, 2018.
2. K. Howe et al., Nature, 496:498-503, 2013.
3. K. H. W. J. Ten Tusscher et al., Am. J. Physiol. Heart Circ. Physiol., 291, 2006.



# FLUID–STRUCTURE INTERACTION MODELING FOR EVALUATING SENSOR-BASED transcATHETER HEART VALVES

Silvia Puleo, Francesco Scardulla, Salvatore Pasta, Leonardo D'Acquisto,

1. Dipartimento di Ingegneria, viale delle Scienze Ed.8, University of Palermo, Italy

## Introduction

The function of human heart valves is to direct blood flow unidirectionally through the chambers, utilizing a tandem operating mode, towards other organs. Finite-element analysis, computational fluid dynamics (CFD) models and fluid-structure interaction (FSI) models were mostly employed to represent aortic valve hemodynamic and structural mechanics [1]. The complexity of the interaction between blood flow and the relevant anatomical and/or device configurations presents technical challenges requiring the utilize of FSI models [2]. Moreover, different technologies and devices have been studied in literature which allow to obtain in-situ blood pressure measurement for the corresponding monitoring and control [3].

The aim of the study is to carry out a computational framework for the FSI simulation of prosthetic valve with the goal to virtually model the presence of sensors embedded in the valve to measure velocity, blood pressure and vessel deformation for monitoring the deterioration of prosthetic valve leaflets.

## Materials and methods

The CAD tool Rhinoceros (Rhinoceros v.7, McNeel & associates, USA) was used to generate an idealized geometrical model of the aortic root, including the ascending aorta, left ventricular outflow tract and valve leaflets.

The FSI simulation was solved by a partitioned approach with a two-way coupling utilizing the XFlow2022 and Abaqus2021 (Dassault Systemes, Simulia Corp., Providence, RI) solvers for the fluid and structure, respectively. SIMULIA Co-Simulation Engine (Dassault Systemes, Simulia Corp., Providence, RI) managed the data transfer between the solvers. The flow field was discretized with ~1M unity D3Q27 lattices (84×84×155) with high number of degrees of freedom per discrete element of fourth-order spatial discretization. Time-dependent physiological pressure amplitude boundary conditions were imposed on both sides of the domain as outlets pressure boundary conditions. The wall boundary conditions were applied to all other surfaces inside the fluid domain. In addition, following streaming, the bounce-back technique was utilized to impose a no-slip condition close to the walls. For the structural solver, the aortic wall is modeled using an hyperelastic, fiber-reinforced constitutive models, with the distal and proximal ends fixed in the longitudinal direction. For the evaluation of pressure and velocity, two points placed proximally and distally the aortic valve were used to monitor the fluid flow field.

## Results

The flow velocity field evolution using FSI analysis at representative time instants for aortic valve (AV) confirm the ability of FSI model to predict the flow and structural properties of AV.

At the beginning of systole (50 ms), the flow field begins to develop and reaches its peak in the systole peak phase (100 ms), where the flow is characterized as a symmetric central jet flow with a maximum jet velocity of 1.00 m/s. Toward the end of systole (267 ms), a backward flow due to the pressure drop leads to partial to complete closure of the leaflets at the end of systole (300 ms). As the fluid is forced to change direction or stop abruptly, a pressure surge propagates through the valve during this period, and velocity variations are observed. In the diastolic phase of the cardiac cycle (300-870 ms), the velocity decreases toward zero due to decaying small flow fluctuations, especially in mid-diastole (500 ms).

## Discussion

The proposed FSI framework is presented and used for the analysis of transcatheter heart valve. The coupled FSI analysis is very effective and provides good correlations with existing resolved results reported in the literature. We have shown that the FSI model can predict the flow of the transcatheter heart valve.

In future research it would be extremely useful to develop and validate an in-silico simulation that reproduces principle of sensing applied to different valve models for instance simulating electric field in XFlow software. This may help to further optimize the sensor size, shape and positioning according to different prosthesis models, as well as to simulate various altered working conditions for the leaflet.

## References

1. Abbas SS et al., SIMULATION. 2022; 98(1):3-34. doi:10.1177/00375497211023573
2. Le, T.B. et al., Fluids 2022, 7, 94. <https://doi.org/10.3390/fluids7030094>
3. Bailoor S et al., Cardiovasc Eng Technol. 2022 Feb; 13(1):90-103. doi: 10.1007/s13239-021-00553-8.

## Acknowledgements

The study was funded by SiciliAn MicronanOTech Research And Innovation Center SAMOTHRACE" (MUR, PNRR-M4C2, ECS\_0000022), spoke 3 - Università degli Studi di Palermo "S2-COMMs - Micro and Nanotechnologies for Smart & Sustainable Communities".



# TAVI PROGNOSTIC ASSESSMENT COUPLING IMMUNOLOGICAL PROFILE AND HIGH-FIDELITY MODELING

Benedetta Grossi (1,2), Giulia Luraghi (1), Sara Bridio (1), Riccardo Terzi (2), Matteo Sturla (2), Alessandro Villaschi (2), Ottavia Cozzi (2), Anna Ramella (1), Marinos Kallikourdis (2), Josè Felix Rodriguez Matas (1), Gianluigi Condorelli (2), Giulio Stefanini (2), Francesco Migliavacca (1)

1. Politecnico di Milano, Italy; 2. Humanitas Research Hospital, Italy

## Introduction

Transcatheter aortic valve implantation (TAVI) has evolved into the treatment of choice for most patients with severe aortic stenosis (AS) [1]. A close link between inflammatory status and degenerative AS has been established [2] and associated with hemodynamic alterations [3]. In vivo evidence about the benefit of TAVI on the inflammatory background via amelioration of the hemodynamic environment is still lacking. Thanks to advances in computational modelling, such as Fluid-Structure Interaction (FSI) patient-specific simulations, such cause/effect link may be approached using systems biology coupled with in silico modelling. We developed an FSI-based methodology to simulate valve implantation and our preliminary findings showed a robust prediction of procedural success. The aim of this project is to evaluate the inflammatory response after TAVI in patients whose hemodynamic conditions have been evaluated through the employment of FSI models.

## Methods

Using cardiovascular imaging techniques, detailed anatomical and physiological data have been obtained and subsequently analyzed using patient-specific FSI modelling [4]. The in silico model simulates the implantation of the prosthetic valve, the interaction of the device with the patient-specific domain and the hemodynamics during systolic-diastolic cycles after the implantation (Figure 1). In particular, the model considers three components: i) patient-specific anatomical characteristics (e.g., valves calcifications), ii) the TAVI valve and iii) the hemodynamic parameters (pressures) of the patient. The FSI model allows to evaluate and quantify the post-implant aortic regurgitation due to paravalvular leak. The validation of the model has been performed using post-procedural imaging (echocardiography and cardiac MRI). To

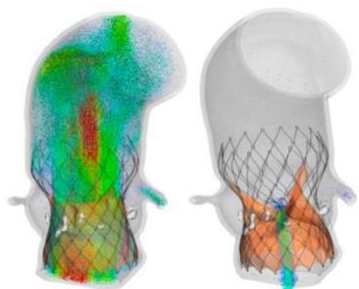


Figure 1: Post-TAVI fluid dynamic simulation: blood velocity representation at systolic and diastolic peaks.

evaluate the link between aortic stenosis treatment and a reduced immune response, the neutrophil-to-lymphocyte ratio (NLR) has been measured at three different treatment stages: pre-operative phase, acute phase (at 3 days) and post-operative phase (at 30 days).

## Results

Twenty patients have been enrolled in the study. In six patients, the NLR was available at all time points. Mean baseline NLR was  $2.27 \pm 0.89$ , which increased to  $3.82 \pm 2.09$  in the acute phase. One month after the procedure, mean NLR was  $1.97 \pm 0.85$ , with an average decrease from baseline of 18% ( $p=0.027$ ) (Figure 2). In five patients, mild aortic regurgitation post TAVI was noted, while in one patient moderate regurgitation (regurgitant fraction = 22%) was observed. FSI simulations are still underway, but the model of this latter patient has already been performed, providing an accurate quantification of the paravalvular leak; of interest, in that single case a lower decrease of NLR (9%) with respect to the pre-operative data was found.

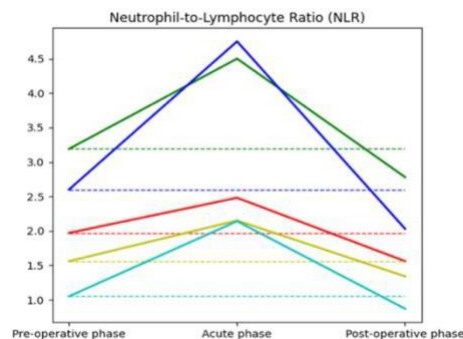


Figure 2: NLR trend in patients with mild regurgitation.

## Discussion

A decrease of the inflammatory response after the restoration of physiological hemodynamic conditions was found in a small subset of patients undergoing TAVI, but such effect may be limited in patients with a suboptimal result. Further analysis will delve deeper into this correlation with the aim of combining biological data with FSI models to create a patient-specific profiling for AS treatment.

## References

1. Mack MJ et al, N Engl J Med. 2019; 380: 1695-1705.
2. Imai K. et al, American heart journal, 156, 713–718, 2008.
3. Baratchi S. et al, Circulation, 142, 1092–1105, 2020.
4. Luraghi G. et al, Expert Rev Cardiovasc Ther. 2021; 19:61-70.

# THE ROLE OF HEMODYNAMICS IN ARTERIOVENOUS FISTULA REMODELLING AND FAILURE

Luca Soliveri (1), Michela Bozzetto (1), Paolo Brambilla (2), Anna Caroli (1), Andrea Remuzzi (3)

1. Department of Biomedical Engineering, Istituto di Ricerche Farmacologiche Mario Negri IRCCS, Italy; 2. Diagnostic Radiology, Papa Giovanni XXIII Hospital - University of Milano-Bicocca, Italy; 3. Department of Management, Information and Production Engineering, University of Bergamo, Italy

## Introduction

Despite its clinical relevance, the mechanism responsible for stenosis development in arteriovenous fistula (AVF) for haemodialysis (HD) remains still largely unknown [1]. This study aims at investigating the relationship between altered hemodynamics and vessel remodelling in a native AVF that failed due to stenosis formation 1.5 years after surgery.

## Methods

Non contrast-enhanced MRI [2] and Doppler Ultrasound (US) examinations were acquired in a 72-year male at 3 days, 40 days, 6 months, 1 year and 1.5 years after surgery at the Unit of Nephrology and Dialysis of Bergamo Hospital. Three-dimensional AVF surface models were reconstructed using the Vascular Modeling Toolkit (VMTK). High fidelity computational fluid dynamic simulations were performed using pimpleFoam (OpenFOAM suit), with a mean timestep of 0.1 ms, setting patient-specific boundary conditions derived from US at the proximal and distal artery. Blood was modelled as Bird-Carreau non-Newtonian fluid and walls were assumed to be rigid.

Vascular lumen cross-sectional areas (CSAs) along the models' centreline were obtained at 0.1 mm intervals in each model to characterize vessel remodelling. Turbulent kinetic energy (TKE) was calculated as

$$TKE = \frac{1}{2} \rho (u'^2 + v'^2 + w'^2) \quad (1)$$

where  $\rho$  is the blood density and  $u'$ ,  $v'$ ,  $w'$  are the fluctuating components of the velocity field [3].

## Results

The AVF was characterized by a successful maturation, with a massive arterial and venous dilatation within the 6 months after surgery and a corresponding increase in blood flow volume.

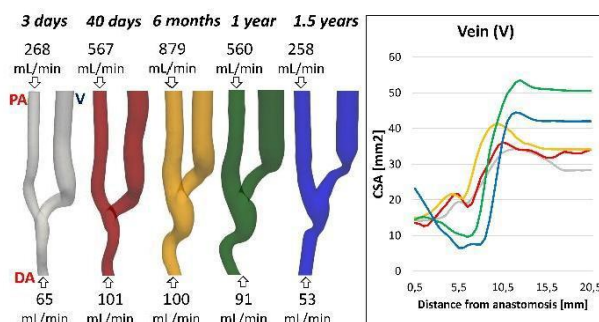


Figure 1: 3D geometrical AVF models, pertinent blood flow rates and vein's CSAs evolution.

Between 6 months and 1 year, a stenosis of the juxta-anastomotic vein caused a CSA reduction of 62.5%, becoming very significant at 1.5 years (-78.8% in CSA). Vessel lumen changes were accompanied by a decrease of the blood flow rate, that did not allow HD.

The development of the stenosis in the venous segment was paralleled by the regularization of blood flow and consequent decrease in the disturbed flow metrics (see Figure 2).



Figure 2: Volume rendering of the mean TKE.

## Discussion

In this longitudinal study, performed on a AVF that developed stenosis after 1.5 year from surgery, we showed the presence of a focal remodelling process in the vein that was paralleled by progressive disturbed flow regularization. Our results, albeit on a single patient, show that local flow instabilities may have induced progressive intimal hyperplasia during time and suggest that inward remodelling could act as a protective mechanism to induce blood flow stabilization.

Future longitudinal studies with an increased number of patients will be required to elucidate the role of disturbed flow in stenosis development, with the final aim of improving AVF clinical outcomes.

## References

1. Remuzzi et al, *CJASN*, 8,12:2186–2193, 2013.
2. Bozzetto et al, *Int J Artif Organs*, 41,11:714–722, 2018.
3. Les et al, *Ann Biomed Eng*, 38,4:1288–1313, 2010.

## Acknowledgements

The Authors would like to acknowledge Valentina Portalupi and Stefano Rota for patient management and Sofia Poloni for fruitful discussion. The Authors would like also to thank Fondazione Dompè for funding.



# PATIENT-SPECIFIC MATERIAL CALIBRATION OF TAVI PATIENTS

Chiara Catalano (1), Stefano Cannata (2), Caterina Gandolfo (2), Salvatore Pasta (1,3)

1. Dipartimento di Ingegneria, Viale delle Scienze Ed. 8, University of Palermo, Italy; 2. Interventional Cardiology Unit, IRCCS ISMETT, Via Tricomi 5, Italy; 3. Department of Research, IRCCS ISMETT, Via Tricomi 5, Italy

## Introduction

As a result of the success of transcatheter aortic valve implantation (TAVI), several complex and accurate in-silico models have been implemented to model this treatment and therefore to assess its structural and hemodynamic consequences. However, the actual material properties of anatomical parts remain unknown and uncertain. This study seeks to provide a calibration of patient-specific constitutive parameters for both the aortic wall and calcific aortic valve using an inverse analysis and electrocardiogram-gated computed tomography (ECG-gated CT) images.

## Methods

Finite Element (FE) models were developed for a group of n.20 patients underwent TAVI with the SAPIEN 3 Ultra transcatheter heart valve (Edwards Lifesciences, USA) with Abaqus\Explicit solver (v.2021hf7, Dassault Systèmes, FR). For each patient CT scans at diastolic phase were segmented in Mimics software (Mimics Innovation Suite v.22, Materialise, BE) to reconstruct the LVOT geometry, calcific plaques, and aortic wall [1]. Given the undetectability of aortic valve leaflets, they were shaped according to a parametric model based on anatomic measurement and landmarks using Rhino software (v.7.1, McNeel & associates, USA) [2]. The inverse approach adopts a quadratic regression model to link the input variables (i.e., the material properties) to the output variables. The regression model consisted of an optimization algorithm to minimize the difference between predicted and CT-based measurements. Specifically, the output variables of interest for the aortic wall and the calcified valve were the peak systolic strain of the aortic root and orifice valve area, respectively. Assuming linear elastic material behaviors for both the aortic wall and orifice area, the Young's modulus is the only parameters to investigate, as the Poisson's coefficient was fixed to 0.475 to account of an incompressible material [3].

For each patient, n.10 simulations of the cardiac beat were carried out varying each time randomly the material properties in their interval of definition [0.8-10 MPa]. For each simulation, the systolic strains (NE) and the nodal coordinates of valve free edges were automatically exported using python scripts. The orifice valve area was then calculated into the Grasshopper plug-in of Rhinoceros. As the solution can lead to two different optimized material parameter sets, the Young's moduli were selected from the solution falling in the interval definition. If both values were contained in the range, these were averaged.

## Results and Discussion

Aortic valve leaflets were found to have a stiff behavior with elastic modulus of  $10.8 \pm 3.0$  MPa, and this is likely caused by the constraining effect of embedded calcifications in severe stenosis condition. The aortic wall behavior was characterized by an elastic modulus of  $5.9 \pm 3$  MPa, also suggesting a stiff behavior of the aorta as compared to literature data when the aortic wall is assumed as linear elastic.

Once the optimal material parameters were achieved, a new analysis was carried out for each patient using the optimized material properties. For the aortic wall, the deformed shape was exported and compared to that from the CT images at systole. The root mean square error (RMSE) was used to quantify the difference between model predictions and CT images. The relative errors for the aortic wall were in the range of 8.6% to 13.6 % with more marked differences in the distal LVOT than in the sinus and ascending aorta. Not any statistical difference was observed between predictions and CT-based measurements ( $p=0.145$ ). The relative errors for the valve between predictions and CT-based measurements were in the range of 0.08% to 11.86%, suggesting a realistic evaluation of the biomechanical response of the stenotic aortic valve.

Given the elderly population of patients undergoing TAVI, the current ex-vivo material descriptors reported in literature are not suitable. In this setting, the major novelty of this study is the development of a non-invasive inverse approach for the assessment of reliable material properties for the aortic root of patients with severe aortic valve stenosis.

Though a linear elastic material behavior was assumed, the present inverse analysis can be extended to the assessment of multiple materials descriptors and thus complex constitutive relationship.

Overall, numerical simulations of the pre-TAVI scenario here presented were found in agreement with CT imaging, thereby leading to a robust non-invasive approach for in-vivo assessment of material properties that could enhance the prediction of TAVI in-silico models.

## References

1. Catalano, C., et al., *Procedia CIRP*, 2022. 110: p. 271-276.
2. Pasta, S., et al., *Artif Organs*, 2017.
3. Bosi, G.M., et al., *Journal of biomechanics*, 2018. 71: p. 236-244.

## Acknowledgements

This project has received funding from the European Union's Horizon 2020 research and innovation programme under grant agreement No 101017523.



# MODELING HOW CHEMICAL ENERGY IS CONVERTED INTO ACTIN-BASED MOTILITY

A. Salvadori(1,2), C. Bonanno(1,2), M. Serpelloni(1,2), M.T. Raimondi(3), E. Jacchetti(3)

1. "The Mechanobiology Research Center, UNIBS", Brescia, Italy

2. Università degli studi di Brescia, Italy

3. Politecnico di Milano, Italy

The chemo-mechanical motor of several physiological and pathological processes in biological systems is a polymerization process, which converts chemical energy into mechanical work. The chief component in this activity is actin, a multi-functional protein forming filament in the cell cytoskeleton. External impulses of a chemical or mechanical nature trigger a chemical reaction, which converts the monomeric form of actin, G-actin, into a polymerized branched-filamentous form, F-actin. Upon polymerization, the cross-linked network acts against the plasma membrane, a pathogenic bacterium, or an endosome, pushing them forward and promoting directional motility.

At the leading edge of cells, actin is organized in an almost bidimensional dendritic array of branched filaments [1]. Binding proteins control actin turnover and filament elongation, mediate the initiation of new filaments as branches on pre-existing filaments and promote (de)branching and (de)polymerization, thus regulating the mechanical response of moving cells.

In a recent publication [2], a thermodynamically consistent continuum-mechanics formulation was proposed, stemming from continuity equations that account for actin chemical kinetics [3]. We have suggested that the volumetric expansion exerted after the phase change from monomeric to a cross-linked network of actin filament ultimately converts chemical energy into motion.

In this note, the formulation in [2] will be extended and unpublished results presented for the first time. The main novelty is the application of Helmholtz free energies with no entropic contributions. Numerical simulations of *Listeria* pathogens, see Fig. 1, with data taken from biological literature, show that the main features of actin-based motility are captured with remarkable accuracy.

The model manifests itself in macroscopic descriptors of biochemical and biological details of the relevant processes, thereby resulting in sufficient generality to be appropriate for several biological systems, targeting cellular motility as a whole.

Fluorescent imaging and quantitative analysis describing the cellular force transducer elements, like the cytoskeleton, will validate our computational models.

Actin fibers and focal adhesion in live cells cultured in different conditions will be stained, to characterize their organization and the dynamic turnover, with the aim to extract quantities of interest (such as number, size, lifetime).

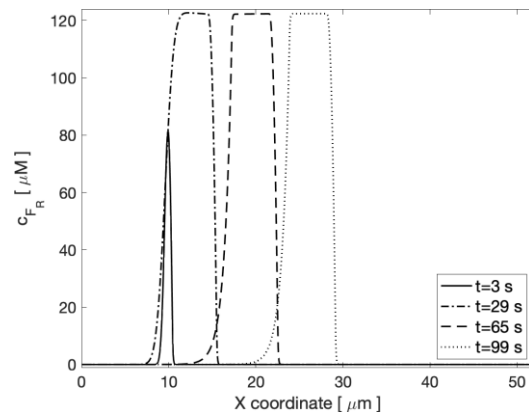


Figure 1: Concentration of F-actin network in *Listeria* pathogens comet tail.

## References

1. L. Blanchoin, R. Boujemaa-Paterski, C. Sykes, and J. Plastino. Actin dynamics, architecture, and mechanics in cell motility. *PHYSIOL REV*, 94(1):235–263, 2022/06/06 2014.
2. C. Bonanno, M. Serpelloni, M. Arricca, R.M. McMeeking, and A. Salvadori. Actin based motility unveiled: How chemical energy is converted into motion. *J MECH PHYS SOLIDS*, 175:105273, 2023.
3. M. Serpelloni, M. Arricca, C. Bonanno, A. Salvadori, Chemo-transport-mechanics in ad-vecting membranes. *INT J ENG SCI* 181:103746, 2022.

## Acknowledgements

We are gratefully indebted with Prof. R. McMeeking for his thoughtful insights and profound discussions. This work was supported by the generous support of Fondazione Ferriera Valsabbia and Comipont. We are grateful to the companies Copan, and Antares Vision that sponsor "The Mechanobiology Research Center, UNIBS".



# UNRAVELING TAXOL EFFECT ON MICROTUBULE MECHANICS THROUGH A MULTISCALE ANALYSIS OF TUBULIN DYNAMICS

Marco Cannariato (1), Eric A. Zizzi (1), Marco A. Deriu (1)

1.Polito<sup>BIO</sup>Med Lab, Department of Mechanical and Aerospace Engineering, Politecnico di Torino, Turin, Italy

## Introduction

The study of microtubule (MT) mechanics and the pathways involved in the transfer of vibrations between tubulins is crucial to understand how MTs are stabilized within the cell. Indeed, the hierarchical organization of MTs is the basis of their stability, mechanics, and function. Modulation of MTs mechanics can alter cell equilibrium and be exploited in therapeutic approaches in cancer [1]: the MT stabilizer Taxol is a clear example. Therefore, this work aims at shedding light on the effect of atomic structure on MT mechanics, and how changes in tubulin induced by Taxol relate to MT properties, through a computational approach connecting different scales, from atom positions to macroscopic observables.

## Methods

We employed a multiscale approach to investigate the mechanics of MTs by integrating all-atom molecular dynamics (MD) simulations and Protein Structure Networks (PSN) with Normal Mode Analysis (NMA) on Elastic Network Models (ENM). All-atom structures of the dimers, in absence ( $MT^{Apo}$ ) and presence ( $MT^{Tax}$ ) of Taxol, were optimized in systems representative of the MT wall in a total of 600ns of MD simulations. In PSN, tubulins were modeled as a graph where amino acids are nodes connected based on their interaction strength. This approach allowed us to obtain information about the propagation of vibrations within the MT, i.e. about mechanical communication between tubulins [2]. MTs of lengths between 250 and 400 nm were built by fitting tubulin rings onto an Electron Microscopy Density (EMD) map and replicating them axially (8.15 and 8.18 nm step for  $MT^{Apo}$  and  $MT^{Tax}$ ) [3,4] (Fig 1A). In ENM, residues are beads connected with springs if closer than 1.2 nm; we obtained MT vibrational frequencies and mechanical properties from NMA of ENM, assuming it as a hollow cylinder of homogeneous isotropic material [5].

## Results

The analysis at the molecular level revealed remarkable differences induced by Taxol. In  $MT^{Apo}$ ,  $\beta$ -tubulins mediate the mechanical communication between protofilaments (PFs) (Fig 1B), while the transfer of vibrations is driven mainly by  $\alpha$ -tubulin in  $MT^{Tax}$  (Fig 1C). These results are interesting since Taxol interacts with residues in  $\beta$ -tubulin M-loop involved in  $MT^{Apo}$  communication path. Moreover, Taxol induces conformational changes in tubulins and loss of structure of the  $\beta$ M-loop, known to mediate the interaction between adjacent PFs. At a higher scale, the persistence length (Lp), bending (Eb), shear (G), and Young's (E) moduli of  $MT^{Apo}$  and  $MT^{Tax}$  have been computed from

NMA vibrational frequencies of 3 MTs, built from MD-derived tubulins. Results highlight that  $MT^{Tax}$  has increased mechanical properties (Fig 1D), in particular the shear modulus, reflecting the atomistic result that Taxol alters the inter-PFs interaction.

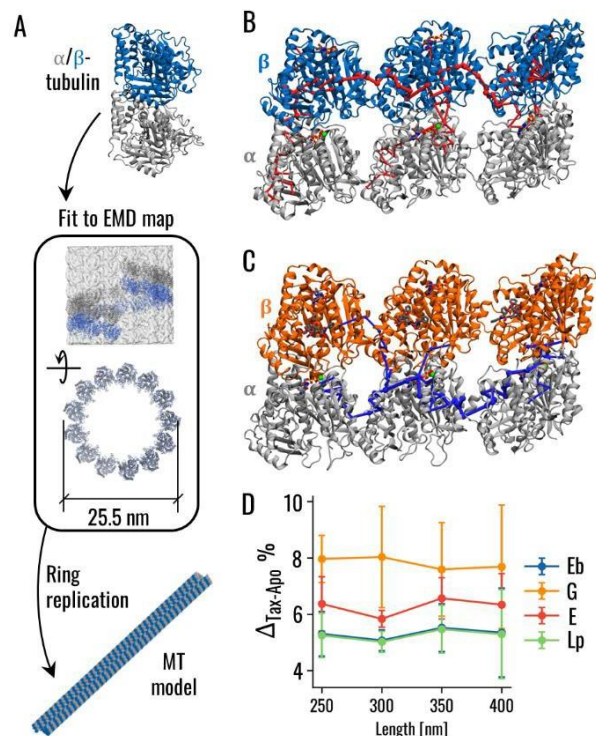


Figure 1: (A) Production of MT models from  $\alpha/\beta$ -tubulins. (B, C) Pathway of communication between PFs in  $MT^{Apo}$  (B) and  $MT^{Tax}$  (C). (D) Difference in mechanical properties driven by Taxol (3 replicas).

## Discussion

Our approach relates microscopic changes induced by Taxol and resulting changes in mechanics with MT stabilization. Taxol interaction alters tubulin conformation,  $\beta$ M-loop structure and inter-PFs communication. This reverberates at a higher scale increasing MT mechanical properties, in particular the resistance to shear forces. Therefore, Taxol can stabilize MTs by strengthening inter-PFs interaction. It will be interesting to analyze how Taxol affects MT dynamical response to an applied stress, providing insights for anti-cancer drug and bioinspired nanomaterials design.

## References

1. Janke et al, Nat Rev Mol Cell Biol, 21:307-326, 2020.
2. Fanelli et al, Methods Cell Biol, 117:43-61, 2013.
3. Sui et al, Structure, 18:1022-1031, 2010.
4. Kellogg et al, J Mol Biol, 429:633-646, 2017.
5. Deriu et al, Biophysical Journal, 99:2190-2199, 2010.



# ADVANCED CONSTITUTIVE MODELLING OF POLYMERS FOR TISSUE BIOPRINTING APPLICATION

Lorenzo Zoboli (1), Daniele Bianchi (1), Giuseppe Vairo (2), Michele Marino (2), Alessio Gizzi(1)

1. Nonlinear physics and mathematical modelling Unit, Campus Bio-Medico University of Rome; 2. Department of Civil Engineering and Computer Science, University of Rome Tor Vergata

## Introduction

Modern 3D bioprinting techniques aim at reproducing a specific tissue composition by extruding a bioink, which is a cluster of stem cells embedded into a hosting gel, into the desired pattern. If the extruded structure is fed suitable nutrients, cell differentiation and growth is initiated. However, prior to activating these processes, the gel must first be converted into a polymer construct to provide support and preferential directions to the successive cellular growth phase. There are many ways to accomplish this melt-to-solid transition, most notably photo-polymerisation. The irradiation of a light with suitable intensity and wavelength triggers chemical processes that induce the cross-linking between polymer chains within the printed material, in a time-evolving scheme of structure formation. Controlling this process holds great importance, since cellular motility and nutrient diffusion are greatly affected by the disposition and orientation of the polymer network. As it currently stands, the 3D printing process briefly described above is well known, but in many instances it is not yet adequately optimised and the influence of a variety of parameters hinders a large-scale production basis. For example, the intensity and direction of the UV light has no standard protocol yet, so the definition of an optimal disposition of the light sources can prove essential in minimising the polymerisation times, hence tissue formation times as a whole. This work intends to ground the choice of selected polymerisation parameters to a rational basis.

## Methods

To achieve the aforementioned objectives, the relevant Physics of what happens after the melted bio-ink is deposited has been represented through multi-physics Finite Element simulations, where the kinetics of polymer cross-linking has been coupled with finite deformation formulations. Specifically, the curing process may be described by evolution equations of the kind:

$$\frac{\partial c_R(x, t)}{\partial t} = \beta m c_I(x, t) I(x, t) - 2k_t c_R^2(x, t) - k_0 c_R(x, t) c_0(x, t)$$

$$\frac{\partial c_O(x, t)}{\partial t} = -k_0 c_O(x, t) c_R(x, t)$$

$$\frac{\partial c_I(x, t)}{\partial t} = -\beta I(x, t) c_I(x, t)$$

In which  $c_R, c_I, c_0$  are the concentrations of radicals, photo-initiators and oxygen respectively, and the light intensity  $I$  follows a Beer-Lambert-like diffusion law.

The behaviour during phase evolution follows a well-

established mechanical model [1, 2] which recasts the non-linear, finite-elasticity problem associated to each time-dependent crosslink formation into a more convenient equivalent phase. Viscoelastic behaviour during polymerisation has also been accounted for. More to the point, the constitutive behaviour of the polymer has been divided into an elastic branch, following a Neo-Hookean law:

$\sigma_{eq} = J_{eq}^{-1} \left( \mu_M J_{eq}^{-\frac{2}{3}} \mathbf{B}'_{eq} + k_M \ln J_{eq} \mathbf{I} \right)$  here  $\sigma_{eq}$  is the Cauchy stress,  $\mathbf{B}'_{eq}$  is the deviatoric part of the left Cauchy-Green deformation tensor, and  $\mu_M$  and  $k_M$  are the shear and bulk modulus of the cross-linked polymer.

To deal with these highly non-linear differential equations representing the problem, a parametrised custom Finite Element variational formulation has been implemented.

## Results

The main results that will be illustrated will address the evolution of the curing (degree of conversion  $p$ ) as a function of light diffusion within the polymer medium (light intensity  $I$ ).

## Figure and Tables

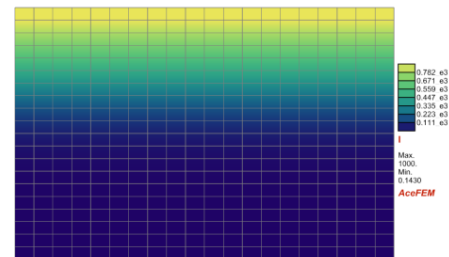


Figure 1: light diffusion inside the medium

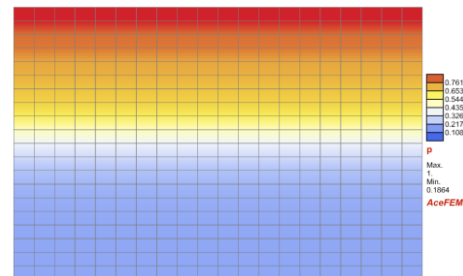


Figure 2: degree of conversion within the analysed medium

## References

1. Wu J. et al, J Mech Phys Sol (2018)
2. Long K. N. et al, J Mech Phys Sol (2009).



# 3D MICROSTRUCTURED SCAFFOLD GEOMETRY DRIVES MESENCHYMAL STEM CELL PHENOTYPE

Emanuela Jacchetti (1), Teresa Baldissera (1), Bianca Barzaghini (1), Letizia Messa (2,3), Cristina Cereda (4), Stephana Carelli (2,4), Manuela Teresa Raimondi (1)

1. Department of Chemistry, Materials and Chemical Engineering, Politecnico di Milano, Italy.
2. Pediatric Research Center "Romeo ed Enrica Invernizzi, University of Milano, Milano, Italy.
3. Department of Electronics, Information and Bioengineering, Politecnico di Milano, Italy.
4. Center of Functional Genomics and Rare Diseases, Buzzi Children's Hospital, Milano, Italy.

## Introduction

Mechanical stimuli from the environment affect mesenchymal stem cells (MSCs) morphology and functionality [1]. We observed an increased stemness maintenance for MSCs grown into a 3D custom-made scaffold [2]. We are now investigating the role of scaffold architecture in maximizing the cell stemness maintenance over the time, and the identification of molecular pathways most significantly deregulated.

## Methods

Custom made organic-inorganic polymeric scaffolds were produced by the two-photon polymerization technique with different dimension of cubic pores ( $15 \times 15 \times 15 \mu\text{m}^3$ ,  $20 \times 20 \times 20 \mu\text{m}^3$ ) or graded pore (Named Nichoid), with a range between 10 and 30  $\mu\text{m}$  transversely and 15  $\mu\text{m}$  in the vertical direction.

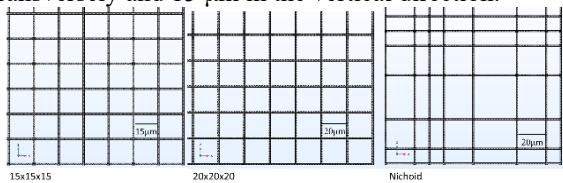


Fig.1: Representative portion of the 3D investigated scaffolds (top view).

Finite element analyses (COMSOL Multiphysics®) were performed to evaluate the displacement ( $d_i$ ) and bending and longitudinal stiffnesses ( $K_i = F_i/d_i$ ) of each pores type. We built the model in stationary condition, and linear elastic and isotropic material properties ( $E = 3.03 \text{ GPa}$ ,  $\nu = 0.49$ ,  $\rho = 1200 \text{ kg/m}^3$ ) were imposed. We tested three load cases ( $|F| = 70 \text{ nN}$ ), one for each direction, placed at half-length of bars for representative pores (Fig.1).

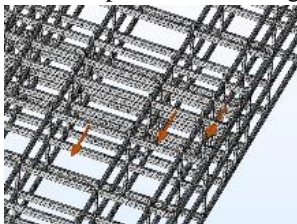


Fig.2: Example of a meshed scaffold composed by graded pores, meshed by COMSOL Multiphysics®.

$10^4$  MSCs were cultured for 24h and 7days, in 3D and 2D samples, using standard culture conditions. As pharmacological control,  $1 \mu\text{m}$  Cytochalasin-D for 1h was used to reduce internal cellular tension.

Fluorescence imaging was performed to investigate cell migration capability in situ and ex situ, nuclear morphology and nucleoskeletal organization. RNA-Seq and Bioinformatic Data Analysis were used to

investigate the gene expression deregulation induced by the different scaffolds.

## Results

RNA-Seq analyses indicate that culture conditions significantly affect gene expression. Among all the 3D conditions tested, cell stemness significantly increased only in Nichoid scaffolds. Computational analysis demonstrates that this condition induces increased gradients in the displacement and stiffness of the microscopic trusses that form the pore microgrid (Fig.2a,b). Fluorescence imaging shows that the 3D scaffold geometry does not affect the organization of several proteins primarily involved in the mechanotransduction pathway; on the contrary, it influences significantly the cell capability to migrate (Fig.2c).

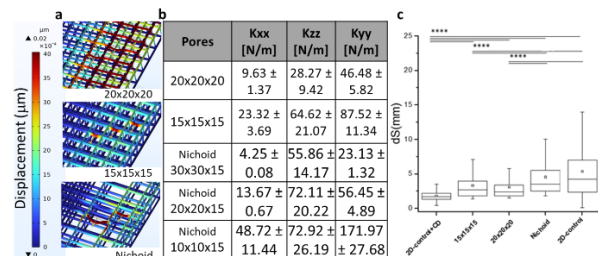


Fig.2: a) Representation of truss displacement under the point load  $F_x = 70 \text{ nN}$ . b) Pore stiffness along the three investigated directions; c) Analysis of MSCs capability to migrate.

## Discussion

MSCs cultured in our 3D scaffolds do not show a significant cell reshaping and remodelling of the main structural proteins; however, it is appreciable a significant gene deregulation. Our hypothesis is that this phenomenon is guided by a modulation of the cell confinement and migration properties.

Our findings reveal novel aspects of the MSCs culture in 3D, representing a step forward in the control of stem cells via purely mechanical conditioning, thus paving the way to new strategies for MSCs translation to clinical applications.

## References

1. Steward AJ et al. J Anat. 2015;227(6):717-31.
2. Remuzzi A. et al. Cells 2020, 9, 1873

## Acknowledgements

ERC, project BEACONSANDEGG, G.A. 101053122; EU, FET-OPEN project IN2SIGHT, G.A. 964481; NICHILD - 101068512 - GAP-101068512



# CHARACTERIZATION OF PANCREATIC DUCTAL ADENOCARCINOMA CELLS MIGRATION AND TRACTION FORCE ON STIFFNESS-TUNABLE SUBSTRATES

Stefano Gabetti (1), Silvia Marino (1), Chiara Vaghi (2), Gianpaolo Serino (1), Marta Tosini (1), Alberto L. Audenino (1), Toshiro Ohashi (3), Alessandra Fiorio Pla (2), Diana Massai (1)

1. PoliToBIOMedLab and Department of Mechanical and Aerospace Engineering, Politecnico di Torino, Italy; 2. Department of Life Sciences and Systems Biology, Università di Torino, Italy; 3. Faculty of Engineering, Hokkaido University, Sapporo, Japan

## Introduction

Pancreatic ductal adenocarcinoma (PDAC) is one of the most aggressive and lethal malignancies [1]. In PDAC, stellate cell activation results in the excessive production of extracellular matrix (ECM), causing a significant increase of tissue stiffness (Young's modulus  $E \sim 1\text{--}4$  kPa in healthy pancreas,  $E \sim 4\text{--}43$  kPa in neoplastic tissue [2]), which affects tissue vascularization and limits chemotherapy effectiveness [3]. Solid stress and cancer-related stiffness are also associated with increased invasive potential. To identify potential candidates for PDAC targeting, it is crucial to understand how PDAC cells respond to tissue stiffness and to detect the key players in the mechanotransduction processes. In this study, we developed stiffness-tunable hydrogels and micropillar arrays and used them to investigate *in vitro* the influence of substrate stiffness on PDAC collective and single cell behavior.

## Methods

To mimic the stiffness of healthy pancreas and PDAC, two polyacrylamide (PAM) substrates (PAM low and PAM high, respectively) were fabricated as thin films bound to coverslips, following a published protocol [4]. The effective modulus  $E^*$  of the PAM substrates, without and with a collagen coating, was characterized by nanoindentation tests (PIUMA, Optics11) performed in wet conditions (PBS) at  $37^\circ\text{C}$ . Human pancreatic cancer cell line (PANC-1) cells were then seeded on the collagen-coated substrates ( $n=3$  for each type), cultured at  $37^\circ\text{C}$  and  $5\%$   $\text{CO}_2$ , and imaged every 10 min for 6 h for random migration assays. The migration rate  $v$  ( $\mu\text{m}/\text{min}$ ) between two consecutive time points was calculated using MtrackJ plugin of ImageJ (NIH). Finally, for characterizing the traction forces exerted by the PANC-1 cells, two polydimethylsiloxane (PDMS) micropillar arrays with different bending stiffness ( $k_L = 72.3$  nN/ $\mu\text{m}$  and  $k_H = 217.2$  nN/ $\mu\text{m}$ ) were designed (Solidworks) and fabricated by soft lithography. PANC-1 cells were then seeded on the fibronectin-coated micropillars, stained with rhodamine phalloidin after 24 h, and after additional 24 h fluorescence images were acquired and analysed (ImageJ, Matlab), measuring pillar deflections, and evaluating traction forces ( $F$ ) as:

$$F = k \cdot x \quad (1)$$

where  $k$  is the pillar bending stiffness (nN/ $\mu\text{m}$ ) and  $x$  is the measured pillar deflection ( $\mu\text{m}$ ).

## Results

The PAM low and PAM high substrates, without and with a collagen coating, exhibited effective modulus

values in the range of pancreatic healthy and tumor tissue, respectively (PAM low:  $E^* = 0.56 \pm 0.36$  kPa and  $E^* = 1.05 \pm 0.76$  kPa w/ collagen; PAM high:  $E^* = 18.79 \pm 5.29$  and  $E^* = 15.98 \pm 5.08$  w/ collagen, Fig. 1A). PANC-1 cells seeded on PAM high substrates showed a higher migration rate ( $v = 0.34 \pm 0.004$   $\mu\text{m}/\text{min}$  for PAM high;  $v = 0.18 \pm 0.003$   $\mu\text{m}/\text{min}$  for PAM low, Fig. 1B). When seeded on micropillar arrays, PANC-1 cells exerted significantly higher mean traction forces on stiffer micropillars ( $F = 14.2 \pm 3.9$  nN for  $k_L$ ,  $F = 32.5 \pm 9.7$  nN for  $k_H$ , Fig. 1C).

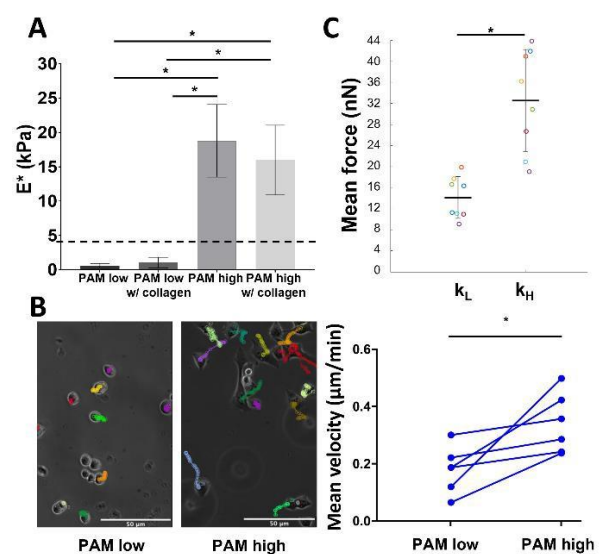


Figure 1: A) Effective modulus of PAM substrates; B) Random migration assay: cell trajectories and mean cell velocity; C) Mean cell traction forces. ( $*p < 0.01$ ).

## Discussion

Nanoindentation tests confirmed the suitability of PAM substrates in mimicking the stiffness of pancreatic healthy and tumor tissue. Biological tests showed that PANC-1 cell migration is faster on PAM high substrates and higher mean traction forces are generated on stiffer micropillars, indicating that the physical environment affects cell behavior. Thus, the proposed approach could provide further insights into PDAC mechano-transduction processes. Tests on co-cultures of PANC-1 and fibroblasts on PAM hydrogels are ongoing, along with further optimization of micropillar arrays.

## References

1. Sarantis et al., World J Gastroint Oncol. 12:173–181, 2020.
2. Nabavizadeh et al., Theranostics, 10:4614–4626, 2020.
3. Hu et al., World J. Gastroenterol., 27:4298–4321, 2021.
4. Tse and Engler, Curr. Protoc. Cell Biol., 47:1–16, 2010.



# A PARAMETRIC CELL STRESSES ANALYSIS DURING EXTRUSION BIOPRINTING PROCESS BASED ON A FSI APPROACH

Gianluca Santesarti (1), Giuseppe Vairo (1), Francesco Viola (2),  
Roberto Verzicco (3), Michele Marino (1)

1. Department of Civil Engineering and Computer Science, University of Rome "Tor Vergata", Italy;

2. Gran Sasso Science Institute, L'Aquila, Italy;

3. Department of Industrial Engineering, University of Rome "Tor Vergata", Italy;

## Introduction

In extrusion bioprinting the cell viability and the quality of the printed scaffold are highly influenced by several process variables, such as the extrusion velocity, the bio-ink properties, and the nozzle dimensions [1, 2, 3]. The introduction of the in-silico (computational) models would allow to reduce the experimental optimization costs and to speed-up the innovation of the bioprinting process. So far, the theoretical and numerical models used are not specific enough to give a quantitative assessment of the main cell damage causes such as the shear stress and exposure time [4]. They often consider very specific fluid behaviors (at most, power laws) and ignore the interaction between cells and the surrounding fluid. The aim of this work is to present a computational model for the extrusion of non-Newtonian hydrogel-based bioinks that explicitly considers the detailed 3D geometry of traditional nozzles used in bioprinting and the presence of cells.

## Methods

To analyze the complex fluid-structure interaction (FSI) occurring in the nozzle between the hydrogel and cells, as well as among cells themselves, we have realized a multi-physics solver based on the immersed boundary technique [5] to accurately reproduce cell extrusion process. The dynamics and deformations of cells are solved using a spring-network structural model based on the Fedosov's interaction potential approach [6].

## Results

The parametric study addresses the cell stress analysis on a standard convergent nozzle geometry with different needle diameters and multiple immersed cells.

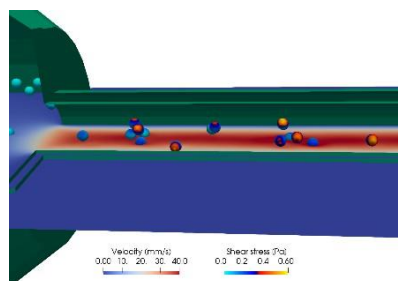


Figure 1: Velocity field along a symmetry plane and shear stress field in the nozzle during the simulation.

In Fig. 1, the computed velocity field of the hydrogel in the convergent area of the nozzle and the shear stresses acting on cell surface are reported. Numerical results demonstrate that cells locally modify the hydrogel velocity field, and that cell shear stresses and deformations are highly influenced by interactions with other cells.

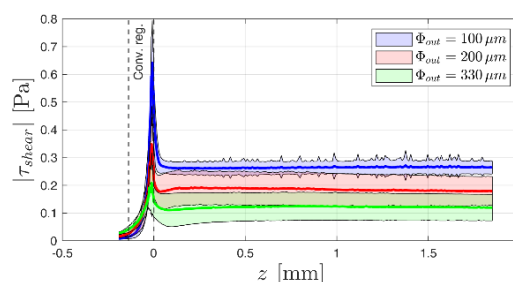


Figure 2: Cell shear stress analysis along the nozzle axis (solid line: mean value; shaded area: standard deviation) for different needle diameters.

In Fig. 2, the probability distribution of the load history of cells for the three diameters considered is shown, which indicates a maximum shear stress peak occurring in the nozzle convergent region.

## Discussion

The planning of a bioprinting protocol requires to find a delicate balance between biological requests and engineering constraints. The proposed in-silico model opens for a systematic virtual optimization of hydrogels material properties, nozzle geometries and cell densities in extrusion bioprinting.

## References

1. Ozbolat, I. T., Hospodiuk, M., Biomaterials, 76, 321-343, 2016.
2. Chang, R. et al., Tissue Eng., Part A 14.1, 41-48, 2008
3. Emmermacher, J. et al., Biofabrication 12.2, 025022, 2020.
4. Ning, L. et al., ACS Biomaterials Science & Eng. 4.11, 3906-3918, 2018.
5. Fadlun, E. A. et al., J. of Comp. Physics 161.1, 35-60, 2000
6. Fedosov, D. A. et al. (2010). Comp. Meth.s in App. Mechanics and Eng., 199(29-32), 1937-1948, 2010.

## Acknowledgements

Fundings from Regione Lazio (POR FESR LAZIO 2014; Progetti di Gruppi di Ricerca 2020; project: BIOPMEAT, n. A0375-2020- 36756)Agency. Support from the INDAM-GNFM group.



# ASSESSING THE PERFORMANCE OF DECELLULARIZATION OF HUMAN TISSUES THROUGH MECHANICAL EVALUATION

Andrea T. Lugas (1,2), Gianpaolo Serino (1,2), Cristina Bignardi (1,2), Giulia Montagner (3), Diletta Trojan (3), Mara Terzini (1,2)

1. Polito<sup>BIO</sup>Med Lab, Politecnico di Torino, Italy; 2. Department of Mechanical and Aerospace Engineering, Politecnico di Torino, Italy; 3. Fondazione Banca dei Tessuti del Veneto Onlus, Italy

## Introduction

Xenografts and allografts are usually crosslinked with glutaraldehyde, which implies cytotoxicity and tissue calcification [1]. An alternative preparation is the decellularization, which limits antigenicity while preserving the integrity of the extracellular matrix structure and thus its mechanical properties [2]. The aim of the present study is the evaluation of the efficacy of new decellularization protocols for human dermis and pericardium in preserving mechanical properties.

## Methods

Human tissues were obtained from cadaver donors following Italian directives and with the proper informed consent. Two testing protocols were developed to evaluate the mechanical performance of the tissues, taking into account the availability of material from which to take samples in the two districts (which is much lower for the pericardium). Therefore, the dermis was uniaxially stretched until failure along multiple directions of sampling (size of specimens:  $40 \times 5 \text{ mm}^2$ ), while the pericardium was equibiaxially stretched up to 20% strain on cruciform specimens cut from  $20 \times 20 \text{ mm}^2$  patches using a custom tool. The thickness of the tissues was determined as the mean of three measurements taken with a thickness gauge (547–321, Mitutoyo, Lainate, Italy) in three points in the central region of each specimen. Uniaxial tensile tests permitted to evaluate the ultimate tensile strength (UTS), strain at break ( $\epsilon_{UTS}$ ) and elastic moduli in the toe region ( $E_{toe}$ ) and in the linear region ( $E_{lin}$ ) of human decellularized (hDD) versus non-treated dermis (control, hCD). Biaxial tensile tests were conducted to simultaneously explore the decellularization treatment effect – comparing human decellularized (hDP) and control (hCP) pericardium patches – and the tissue anisotropy. The  $E_{lin}$  was computed in the two directions. Being the direction of the fibers that compose the extracellular matrix unknown, the loading directions presenting the lowest and highest elastic moduli of each specimen were evaluated separately and will be referred as to D1 and D2 in the following. Three control patches and three decellularized patches obtained from three different donors were analyzed for each tissue.

## Results

Despite the high inter-specimen variability, the hDD resulted significantly stiffer (Figure 1c) and more resistant in terms of UTS (Figure 1a) compared to the control tissue ( $p < 0.05$ ). Moreover, the  $\epsilon_{UTS}$  decreased

after decellularization ( $p < 0.05$ , Figure 1a). The aforementioned properties obtained from the three dermis donors were significantly different ( $p < 0.05$ ). The results obtained from a single donor are shown in Figure 1a and 1c. In contrast, from biaxial tests, no significant differences were highlighted between hDP and hCP, neither along D1 nor along D2, and similar properties were obtained for all the donors (Figure 1b and 1d).

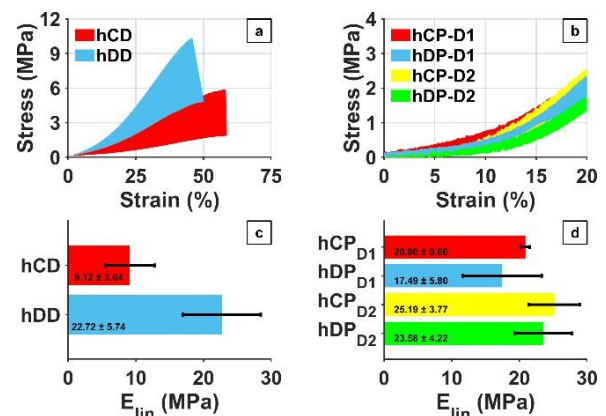


Figure 1: Dispersion of the stress vs. strain curves of human dermis (a) and pericardium (b);  $E_{lin}$  of dermis (c) and pericardium (d): treatment vs. control (mean  $\pm$  SD).

## Discussion

Previous findings confirmed the possibility of an increase of  $E_{lin}$  and UTS in decellularized tissue compared to native one [3]. Moreover, the dispersion of the results on hDD is very close to the variability range of the UTS and  $E_{lin}$  obtained from uniaxial tensile tests on AlloDerm<sup>®</sup>, a widely used acellular dermal matrix for soft tissue applications [4]. Inter-donor variability was expected considering the well-known variability in soft tissues. Nevertheless, the differences that emerged between hDD and hCD could be ascribed to the lack of control in the harvesting orientation and to the variability of fibers direction in the donors' back. On the other hand, although no differences were highlighted between hDP and hCP, the results might have been affected by the tissue anisotropy. Therefore, further studies should be conducted investigating the direction of the fibers in the extracellular matrix prior to testing.

## References

1. Ma et al, Regen Biomater, 1(1):81–89, 2014
2. Montagner et al, Cell Tissue Bank, 2023
3. Bondioli et al, J Tissue Eng Regen Med, 8(4):325–336, 2014
4. Bottino et al, Dent Mater, 25(9), 1109–1115, 2009



# EXPERIMENTAL AND MODELLING ANALYSES FOR UNDERSTANDING OF THE STRUCTURE-MECHANICS RELATIONSHIP OF AORTIC TISSUE

Michela Astore (1), Emanuele Gasparotti (2), Emanuele Vignali (2), Simona Celi (2), Michele Marino (1)

1. University of Rome Tor Vergata, Italy; 2. Fondazione Toscana Gabriele Monasterio, Italy

## Introduction

The analysis of the microstructural characterization of soft biological tissues plays a key role in the understanding of their mechanical response and remodeling. Soft tissues, such as aorta walls, can be regarded as fibrous materials assembled from a ground matrix. Alterations occurring to the embedded collagen fibers have been shown to play a significant role in the pathogenesis of aortic degeneration. Through experimental and modeling analysis, the aim is to study the existing, and yet not well understood, relationship between mechanics and microstructure of healthy and pathological arterial tissues, by combining digital image correlation (DIC), small-angle light scattering (SALS), and multiscale computational modelling.

The study was conducted on pathological tissue samples, specifically affected by aneurysm. An aortic aneurysm is a local bulge of the aorta characterized by segmental weakening of the blood vessel. Irregular hemodynamics have been shown to accelerate the progression of such pathology with a common basis provided by diabetes, male sex, smoking, and hypertension. In addition, imbalance of tissue biochemical pathways results in the onset of pathological remodeling and thus histological changes that affect vascular mechanics [1].

## Methods

To understand the relationship between microstructure and mechanical response of arterial tissue, experimental tests and computational modeling analyses were performed. The experimental mechanical characterization of pathological aortic tissue samples is made through biaxial force-controlled tensile test at different tensile ratios, both along the circumferential and axial direction. Using imaging techniques such as DIC, first the displacement and then the strain field could be accurately identified to reconstruct stress-strain curves  $\sigma$ - $E$ .

A second imaging technique, namely SALS, is used to investigate the microstructure. By performing simultaneously with the tensile test, information on the preferential orientation and dispersion of collagen fibers during mechanical loading could be provided.

At the same time, to perform the modeling analysis, arterial tissue was described a nonlinear hyperplastic material.

Using a micro-macro perspective for the mechanics of crimped fibers. In fact, the straightening of crimped fibers in biological soft tissues is responsible for their nonlinear macroscopic mechanical response.

Therefore, the stress-strain curve takes the characteristic J-shaped curve, by explicitly depending on a set of clearly observable microstructural parameters [2].

A finite element implementation of such multiscale modelling technique is also considered, to reproduce the non homogeneous strain field as obtained from DIC image. For the finite element discretization, quadrilateral elements have been introduced, generated in AceGen. In each material point of the domain the presence of crimped fibers in their undeformed configuration was considered, with different orientations as read from SALS measures. Other microstructural parameters, e.g. radius amplitude and orientation, were calibrated through a process of parametric identification and numerical optimization for a fixed tension ratio 1:1.

## Results

The comparison between the experimental-modeling results demonstrated the validation of the proposed model, showing the relationship existing between microstructure and mechanics in the arterial tissues.

The results obtained are not only representative of the mean mechanical response, but also of the dispersion of strain in the tissue, as obtained from DIC. This correspondence, albeit with different degrees, is maintained even moving away from the calibration condition of the model, defined for the tension ratio 1:1, towards different tension ratios.

Another important result is that the model is also representative of the tissue behavior in terms of collagen fiber realignment, as obtained from SALS measures during mechanical loading.

## Discussions

The present work has shown how a multiscale modelling technique is predictive of the mechanical response but also of the microstructure in terms of fiber thickness, amplitude, and orientation of the collagen fibers, during loading. The strong interconnection between mechanics and microstructure is hence highlighted, developing a predictive tool than can serve in future studies of tissue remodelling.

## References

1. Niestrawska JA, Viertler C, Regitnig P, Cohnert TU, Sommer G, Holzapfel GA. 2016 Microstructure and mechanics of healthy and aneurysmatic abdominal aortas.
2. Micro-macro constitutive modeling and finite element analytical-based formulations for fibrous materials: A multiscale structural approach for crimped fibers Michele Marino, Peter Wriggers.



# TEST BENCH FOR CHARACTERIZING THE PERMEABILITY OF TISSUE ENGINEERING SCAFFOLDS

Simone Israel (1), Stefano Gabetti (1), Beatrice Masante (1,2), Federico Mochi (3), Costantino Del Gaudio (4), Alessandro Schiavi (5), Alberto Audenino (1), Diana Massai (1)

1. Polito<sup>BIO</sup>Med Lab and Department of Mechanical and Aerospace Engineering, Politecnico di Torino, Italy; 2. Department of Surgical Sciences, CIR-Dental School, Università di Torino, Italy; 3. Hypatia Research Consortium, Italy; 4. Italian Space Agency, Italy; 5. National Institute of Metrological Research, Italy.

## Introduction

To create *in vitro* functional tissue substitutes, tissue engineering (TE) approaches rely on the active interaction between cells and porous three-dimensional (3D) scaffolds [1], whose effectiveness is significantly impacted by microstructure. Porosity, pore size, tortuosity, and interconnectivity influence the ability of the scaffold to be permeated by fluids (permeability) and consequently its suitability for cell colonization. Therefore, permeability characterization is essential for a thorough assessment of the scaffold performance [2]. Several approaches were proposed to characterize the permeability of TE scaffolds; however, standardized protocols are missing. Here, we developed a versatile permeability test bench (PTB) for characterizing TE scaffolds and we validated it by testing different bone TE scaffolds and comparing the results with those obtained using a reference test bench (RTB) [3].

## Methods

The proposed PTB is based on the pump method [2]. The permeability chamber (PC), equipped with custom gaskets and grids, allows housing cylindrical samples (height = 1-14 mm, diameter = 8-27 mm). The PC is connected to a closed-loop hydraulic circuit consisting of a reservoir, a peristaltic pump (Masterflex), silicone tubing, two pressure sensors (HJK) upstream and downstream of the PC, and 3-way stopcocks. The sensor signals are collected by a DAQ (National Instruments), which is operated by a computer running a purpose-built LabView interface (Fig. 1A). Tests were conducted using demineralized water. A defined flow rate was imposed to guarantee the laminar flow, consequently, permeability ( $k$ ) was calculated by using the Darcy flow transport model:

$$\Delta P/L = \mu/k*(Q/A) \quad (1)$$

where  $\Delta P$  is the pressure drop across the sample,  $L$  is the sample thickness,  $\mu$  is the viscosity,  $Q$  is the flow rate, and  $A$  is the area of the sample cross-section. For validating the PTB, two 3D-printed PLA scaffolds with a random trabecular microstructure [4] and two commercial biomimetic scaffolds (SmartBone IBI S.A) were tested at 5 mL/min for at least 3 repetitions. Results were then compared with those obtained using the RTB [3].

## Results

Performance tests confirmed watertightness and functionality of the PTB. The permeability values of PLA (P1 and P2) and SmartBone (SB1 and SB2) scaffolds tested within the PTB and the RTB are shown in Table 1. Comparing the results within the same sample for the two test benches demonstrate the reliability of the PTB. The normalized errors between PTB and RTB permeability values were less than 1.

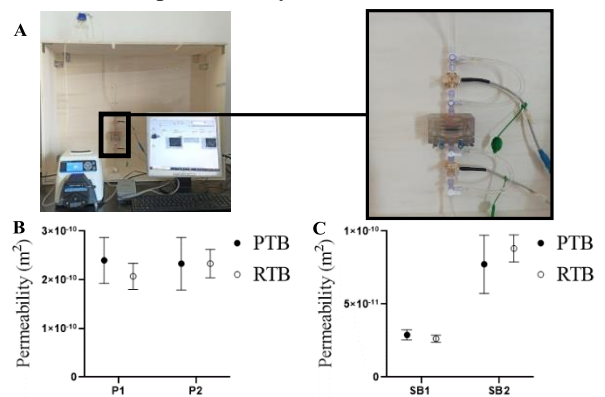


Figure 1: A) Picture of the PTB with focus on the chamber; Permeability test results on PLA (B) and SmartBone (C) scaffolds.

Sample	PTB ( $10^{-10}m^2$ )	RTB ( $10^{-10}m^2$ )
P1	$2.380 \pm 0.570$	$2.070 \pm 0.269$
P2	$2.330 \pm 0.601$	$2.330 \pm 0.290$
SB1	$0.288 \pm 0.034$	$0.263 \pm 0.023$
SB2	$0.772 \pm 0.199$	$0.881 \pm 0.093$

Table 1: Permeability ( $m^2$ ) and confidence interval at 95% of the analyzed samples.

## Discussion

A versatile test bench for characterizing the permeability of TE scaffolds was developed and validated. Despite the measurement dispersion in the PTB tests, the calculated permeability values are in accordance with the results from the reference configuration (RTB). To reduce measurement uncertainty, the PTB data-acquisition system is being optimized. Tests employing soft scaffolds are ongoing for complete validation of the PTB.

## References

1. Amini et al., Crit Rev Biomed Eng 40, 363–408, 2012
2. Pennella et al., Ann. Biomed. Eng., 41:2027-2041, 2013.
3. Schiavi et al., Meas. Sci. Technol., 23:105702, 2012.
4. Pecci et al., J. Mech. Behav. Biomed. Mater., 103, 2020.



# WHAT INFLUENCE DOES THE GEOMETRY OF THE ARTIFICIAL URINARY SPHINCTER HAVE ON THE RISK OF URETHRAL DAMAGE?

Maria Vittoria Mascolini (1,2), Chiara Giulia Fontanella (1,2), Emanuele Luigi Carniel (1,2)

1. Department of Industrial Engineering, University of Padova, Italy  
2. Centre of Mechanics of Biological Materials, University of Padova, Italy

## Introduction

Artificial Urinary Sphincters (AUSs) are prosthetic devices for the treatment of urinary incontinence secondary to sphincteric deficiency. The operating principle can be based on several mechanisms [1] and allows to occlude the urethral lumen ensuring the continence condition. A pressure loading is generally applied around the bulbar urethra through an inflatable cuff and no standardized methods of choice are clinically used for defining the appropriate cuff pressure and size. The long-term efficacy of an AUS has emerged related to the compatibility of the occlusive action, in terms of intensity and distribution, with the urethral tissue health. Tissue erosion and atrophy due to the cuff appear among the most critical complications after AUS implantation, requiring surgical revision [2]. For the identification of the propriety design for device durability, this work aims to evaluate the influence of geometric parameters of the AUS cuff on the stimulation of the urethral tissues through computational mechanics analyses. Models of a novel patented AUS [3] and of the bulbar urethra were developed and different cuff sizes were considered in terms of thickness and length.

## Methods

The 3D CAD model of the AUS cuff was designed as an inflatable cylindrical chamber combined with an external support band. Three different thicknesses (1, 2 and 4 mm) and two different lengths (8.5 and 17 mm) were considered for the chamber to evaluate the impact of the geometry on the performance of the device. An elastomer was assumed composing the AUS and defined through an hyperelastic formulation. On the other hand, the urethral model was developed with a simplified elliptical lumen and mechanically described through a previously identified hyperelastic formulation [4].



Figure 1: Cuff model (in blue), designed by thickness of 2 mm and length of 17 mm, in interaction with the urethral model (in grey).

Models were FE discretized and assembled (Figure 1) by defining the interaction through hard contact in the normal direction and through penalty approach in the tangential one. Computational mechanics analyses

simulated the lumen occlusion through the inflation of the AUS chamber up to 80 cmH<sub>2</sub>O pressure, by means of Abaqus/Explicit 6.14 non-linear dynamic solver.

## Results

Cuffs of different thicknesses involved a different distribution of the occlusive action on the urethra. In reference to the greater length, compressive strain results within the maximum stimulated urethral section are reported in Figure 2. Thicker cuffs exhibited an higher prevalence of strain values in the range 70-80 %, which may induce tissue degenerative phenomena. Similarly, the length of the cuff showed to influence the mechanical stimulation of urethral tissues.

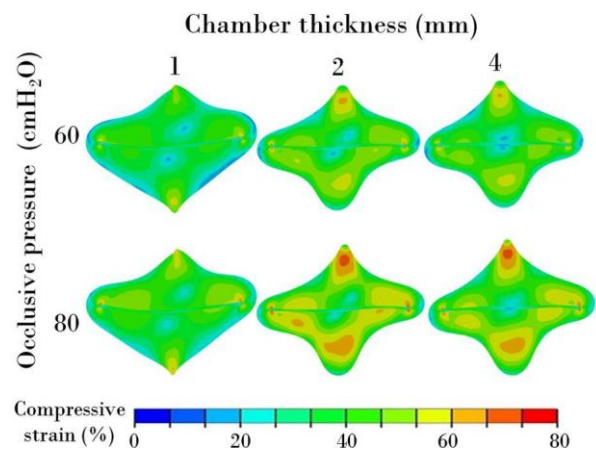


Figure 2: Contours of compressive strain by varying the chamber thickness and the occlusive pressure.

## Discussion

Computational techniques provide valuable tools for designing AUS by enabling the evaluation of the interaction between the device and the biological tissues based on the biomechanical compatibility.

## References

1. Toniolo et al, Artificial Organs,00: 1-23, 2022.
2. Ortiz et al, J Biomech Eng, 204:1027-1032, 2020.
3. Carniel et al, Italian Patent N° 10202000009709, 2020.
4. Natali et al, Exp Physiol, 101:641-656, 2016.

## Acknowledgements

This work was supported by MIUR, FISR 2019, Project n° FISR2019\_03221 (CECOMES: CEntro di studi sperimentali e Computazionali per la ModelliStica applicata alla chirurgia) and by University of Padova, Project FONT\_BIRD2020\_01 "Characterization of Artificial Urinary Sphincters for the identification of new DEVices (AUS-DEV)".

# MECHANICAL CHARACTERIZATION OF PLANTAR ADIPOSE TISSUE

Sofia Pettenuzzo (1), Alice Berardo (1,2), Elisa Belluzzi (3), Assunta Pozzuoli (3), Pietro Ruggieri (3), Emanuele Luigi Carniel (4), Chiara Giulia Fontanella (4)

1. Department of Civil, Environmental and Architectural Engineering, University of Padova, Italy; 2. Department of Biomedical Sciences, University of Padova, Italy; 3. Orthopedics and Orthopedic Oncology, Department of Surgery, Oncology and Gastroenterology (DiSCOG), University-Hospital of Padova, Italy; 4. Department of Industrial Engineering, University of Padova, Italy

## Introduction

The plantar adipose tissue (AT) is composed by adipose chambers and connective septa and it is located between foot bony segments, plantar fascia and skin. Its main mechanical roles are to provide a damping system able to adsorb foot impact and to bear the body weight during static standing [1]. In recent years, different computational models of the foot have been developed to analyse the occurring phenomena, in relation to quantities that are non-obtainable through in vivo studies, e.g., stress and strain fields [2], [3]. Unfortunately, many models still have some limitations, e.g. the lack of information on the proper mechanical characterization of the plantar AT, which changes its microstructural conformation according to the different foot regions. For this reason, the aims of this study are as follows: i) to perform experimental tests on all plantar AT; ii) to define a proper constitutive formulation of the tissue; iii) to develop a computational model of the foot that considers the distribution of the mechanical behaviour of the AT for the plantar region.

## Materials and Methods

Experimental tests were performed on plantar AT collected from four male human donors, ( $56 \pm 18$  years) undergoing amputation due to cancer, at the University Hospital of Padova (CESC Code: AOP2649). Samples were collected from the heel pad (HP), lateral (L), medial (M) and metatarsal (Met) regions (Fig. 1a) and tested with uniaxial unconfined compression tests (Model Match-1, ©Biomomentum). Preconditioning cycles were applied before: 1) loading-unloading (strain rates  $7-70-700\% / s^{-1}$ ) or 2) stress-relaxation (resting time 300s) protocols (Fig. 1b).

A 3D Finite Element model of the foot, composed of plantar AT, bones, ligaments, tendons and plantar fascia, was developed starting from CT data (Abaqus Explicit 2019, Dassault Systemes Simulia Corp., Providence, RI) (Fig. 1c). An almost-incompressible visco-hyperelastic constitutive model was adopted to describe the mechanical response of the plantar AT and the experimental results were used for the evaluation of its parameters. Different numerical analyses were developed to mimic physiological activities, e.g., static standing or gait cycle.

## Results

Experimental results showed a different plantar AT behaviour within the foot regions, with a major elastic

modulus in the M region (about 380 kPa) and a lower in the Met one (less than 30 kPa). Numerical results reported for the stance phase of the gait cycle showed that HP and Met regions, inside the plantar soft tissue, showed the greatest displacement and contact pressure values, while the L and M ones are less stressed (Fig.2).

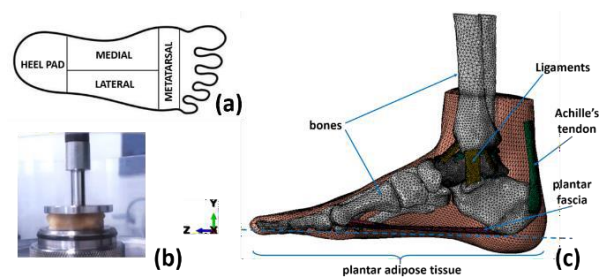


Figure 1: foot subdivision (a), compression test (b), foot Finite Element model (c)

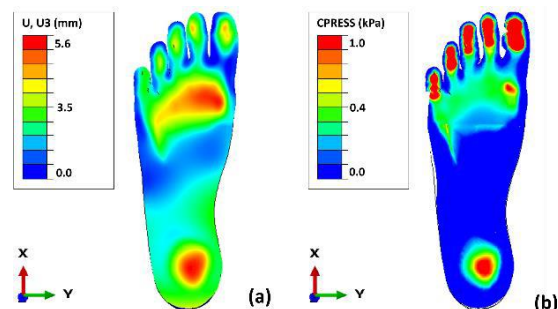


Figure 2: Displacement (a) and contact pressure (b) in the adipose tissue, obtained mimicking the stance phase of the gait cycle by the Finite Element analyses

## Discussion

The computational model considers the real mechanical behaviour of the adipose tissue in the different foot regions, providing information on its mechanical behaviour during physiological loading conditions. A step forward could be the simulation of interactions between foot and footwear, providing information e.g., in the design of specific insoles for sportsmen in order to prevent pathologies such as metatarsalgia.

## References

1. Whittle et al, Gait Posture, 10:264-275, 1999
2. Natali et al, Med Eng Phys, 32:516-522, 2010
3. Fontanella et al, Proc. Inst. Mech. Eng., 228:942-951, 2014.

## Acknowledgements

This work was supported by MIUR, FISIR 2019, Project n° FISIR2019\_03221, titled CECOMES



# AN UNFITTED METHOD WITH ROBIN BOUNDARY CONDITIONS FOR THE ANALYSIS OF HETEROGENEOUS ARTERIAL SECTIONS

S. Gahima (1,2), P. Díez (1,2), M. Stefanati (3), J.F. Rodríguez Matas (3), A. García-González (1,2)

1. Laboratori de Càlcul Numèric, E.T.S. de Ingenieria de Caminos, Universitat Politècnica de Catalunya - BarcelonaTech, Spain; 2 The International Centre for Numerical Methods in Engineering, CIMNE, Spain; 3. Department of Chemistry, Materials and Chemical Engineering "Giulio Natta", Politecnico di Milano, Italy

## Introduction

Ischaemic heart disease is a frequent cause of death globally, with coronary atherosclerosis being the cause of most myocardial infarctions [1]. Typically, a patient presents either stable or unstable plaque. The fast distinction between these two groups is crucial regarding patient treatment. This work proposes an unfitted immersed boundary (IB)-based methodology [2] with a more physical elastic bed boundary condition (BC) to analyze coronary artery sections undergoing uniform pressure in a quasi-static regime.

## Methods

We propose to assume the section to be surrounded by a material along its external boundary. This embedding matrix produces a linear elastic reaction, and it is described with an elastic bed coefficient ( $\alpha$ ) depending on the stiffness. The governing equation for the elastic problem becomes [3,4]:

$$\int_{\Omega} \sigma(\mathbf{u}) : \varepsilon(\mathbf{v}) \, d\Gamma - \int_{\Gamma_R} \alpha \mathbf{u} \cdot \mathbf{v} \, d\Gamma = \int_{\Gamma_N} \mathbf{t} \cdot \mathbf{v} \, d\Gamma \quad (1)$$

where  $\sigma$  is the Cauchy stress tensor,  $\mathbf{u}$  the displacement field,  $\varepsilon$  the strain field,  $\mathbf{t}$  the surface traction, and  $\mathbf{v}$  a virtual infinitesimal displacement.  $\Gamma_R$  represents the elastic-bed BC, equivalent to the well-known Robin BC, while  $\Gamma_N$  the Neumann BC. To improve the computational efficiency, the proposed methodology implements (1) in an IB framework with a generic description of the domain,  $\Omega$ , based on level-sets. The level sets (Fig. 1), defined on a fixed background mesh, provide an implicit description of arterial sections by dividing the domain into subdomains corresponding to different plaque components (e.g., healthy, fibrous, lipid, and calcified core). Without a loss of generality, linear elastic behavior is assumed for all components.

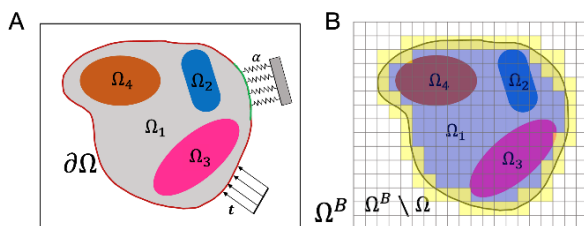


Figure 1: (A) Problem 1 description, with  $\Gamma_N$  in red and  $\Gamma_R$  in green, and (B) background mesh with level-sets.

## Results

To show the accuracy of the methodology, problem (1) is solved using the proposed IB Robin-based (IBR)

model, on a realistic coronary section (Fig. 2A) subjected to an internal pressure  $p = 1e-2$  MPa, and  $\alpha = -1.77e-4$  MPa/mm. Figure 2B shows the displacement field obtained with the proposed IB method, while Figure 2C corresponds to the solution obtained with the classical Finite Element (FE) method. Differences in the average error of the displacement magnitude are found to be less than 0.5% in the section, with a maximum difference of less than 5% (Fig. 2D).

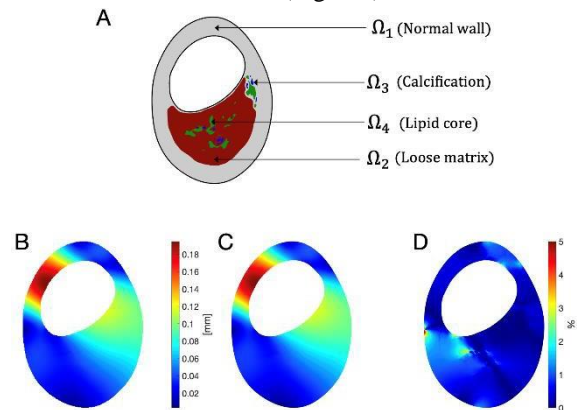


Figure 2: IBR (B) and FE (C) displacement, with real coronary section (A) and the relative local error (D).

## Discussion

The article presents a novel formulation that combines hierarchical level sets (from a 2D arterial segmentation) with an IBR-based formulation to obtain stress and strain fields in arterial sections under physiological conditions of blood pressure. The level-sets allow us to describe the arterial geometries, including plaque component distributions, and use a single background mesh to simulate patient-specific arterial segmentations, avoiding to develop a different conformal FE mesh per geometry. Using the Robin BC (instead of classical Dirichlet) allows to remove the rigid body motion without altering the natural deformation of the arterial section, and to account for the effect of the surrounding tissue on the artery. The results on realistic coronary arterial sections demonstrate that the proposed unfitted IB-based approach provides results equivalent to the standard FE, allowing seamless integration of structural analysis in a medical image processing pipeline.

## References

1. Thygesen et al, J European Heart, 28:2525-2538, 2007.
2. Peskin, Acta Numerica, 11:479-517, 2002.
3. Teng et al, Acta Biomaterialia, 10:5055-5063, 2014.
4. Ebenstein et al, J Biom. Mat. Res., 91A:1028-1037, 2009.



# EFFECTS OF INTERVERTEBRAL DISC DEGENERATION ON THE STRAIN DISTRIBUTION ON THE DISC SURFACE

Giulia Cavazzoni (1), Margherita Pasini (1), Luca Cristofolini (1), Marco Palanca (1)

1. Dept of Industrial Engineering, Alma Mater Studiorum – University of Bologna, Bologna, IT

## Introduction

Intervertebral discs (IVDs) degeneration is defined as “structural failure combined with accelerated or advanced signs of ageing” [1]. Indeed, it implies a tissue weakening primarily due to genetic inheritance, aging, nutritional compromise, and loading history. The structural disruption occurring from injury or fatigue loads leads to the hypothesis that degenerated IVDs are subject to larger deformations.

The effects of the IVDs degeneration can be evaluated experimentally by combining mechanical tests and Digital Image Correlation (DIC) to measure the strain field on the surface of the IVDs.

The aim of this study is to evaluate the strain distribution on the IVDs before and after a mechanically induced IVDs degeneration.

## Materials and Methods

Four T9-L1 human spine segments were obtained through an ethically approved donation program (Ethical approval: Prot.n.113043).

Each specimen was scanned with a 3T Magnetic Resonance Imaging (MRI) and a Computed Tomography (CT) to establish the initial degeneration of the IVDs (Pfirrmann grade = 2 in all specimens) [2] and exclude critical bone pathology. All soft tissues and the anterior ligament were removed without damaging the IVDs. A high-contrast white speckle pattern was prepared on the surface of each specimen.

A four-camera 3D-DIC system (Aramis Adjustable 12M, GOM) was used to measure the surface strain field on the IVDs, at 25 frames per second, with a pixel size of 0.07mm. Mechanical tests were performed using a uniaxial testing machine (Instron 8500, 10kN load cell) to induce flexion, right and left lateral bending, and compression, as defined by [3], on the intact specimens. Each spine segment was loaded until the average minimum principal strain on the central vertebra reached approximately 3000 $\mu\epsilon$  (target to remain in elastic regime without damaging the bone). Ten preconditioning cycles up to half of the load corresponding to the target strain were applied. Then, each specimen was loaded monotonically to reach the target strain in 1s. Artificial IVDs degeneration was mechanically induced (nucleotomy) [4] to simulate a Pfirrmann grade 5 of degeneration [2] in the T11-T12 IVD. Then the degenerated specimens were tested again, following the same loading protocol.

DIC precision was evaluated as the standard deviation of the strain (random error) in zero-strain condition. The minimum principal strains (Eps3) were measured and compared before (intact condition) and after (degenerated condition) the IVD degeneration.

## Results

Random errors were smaller than 100 $\mu\epsilon$ . The Eps3 were larger after IVDs degeneration (Fig.1). In particular, the Eps3 increased by 43% and 57%, in the non-degenerated disc and in the degenerated disc, respectively. 3D strain colour maps allowed to identify the IVD regions which experienced the larger strains. While in the non-degenerated condition the strain distribution was rather uniform, regions with strain concentrations appeared after IVD degeneration (Fig.1).

## Discussion

IVD degeneration leads to an increase in the strains in the degenerated IVD. Due to the change in the load sharing in the spine segment after the degeneration, the non-degenerated IVD experienced larger strain in most cases. Further analyses and mechanical tests are still on going to enlarge the sample to generalize the findings and to extend the analyses on the effects of IVDs degeneration on the adjacent vertebrae.

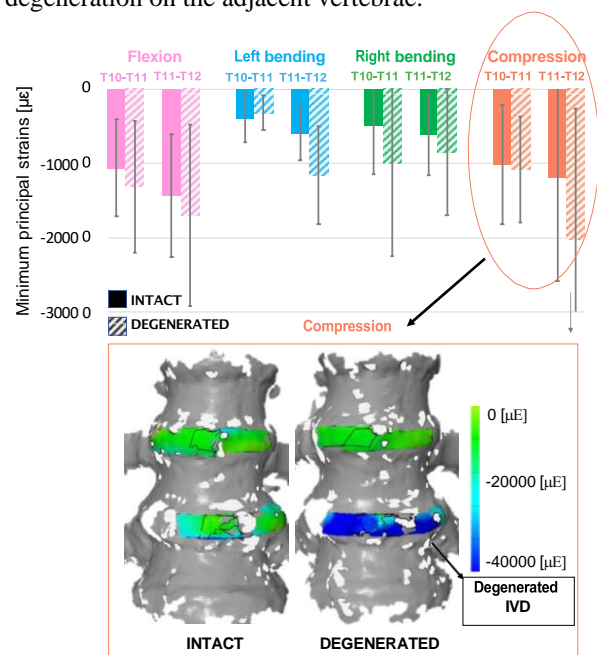


Figure 1: Top: Eps3 averaged on the IVDs surface for each loading condition (median and SD among the sample). Bottom: 3D-strain colour map of the Eps3 on the IVDs surface before and after IVD degeneration.

## References

1. Adams et al. (2006), Spine. 2. Pfirrmann et al. (2001), Spine 3. Palanca et al. (2021), Bone. 4. Techens et al. (2020), MEP

## Acknowledgements

Study partially funded by AOSpine Knowledge Forum Associate Research Award (AOS-KF-TUM-22-003).



# BIOMECHANICAL CHARACTERIZATION OF THE HUMAN FASCIAE OF THE ABDOMINAL REGION: SUPERFICIAL VS DEEP FASCIA

Lorenza Bonaldi (1), Carmelo Pirri (2), Carla Stecco (2, 3), Chiara Giulia Fontanella (3, 4), and Alice Berardo (1, 3, 5)

1. Department of Civil, Environmental and Architectural Engineering, Via F. Marzolo 9, 35131 - Padova, Italy; 2. Department of Neuroscience, Via A. Gabelli 65, 35121 - Padova, Italy; 3. Centre for Mechanics of Biological Material (CMBM), Via F. Marzolo 9, 35131 - Padova, Italy; 4. Italy Department of Industrial Engineering, Via Venezia 1, 35121 - Padova, Italy; 5. Department of Biomedical Sciences, Via U. Bassi 58/B, 35131 – Padova.

## Introduction

The multilayered organization of the fascial system (FS) ensures continuity from the skin to the deepest plane, being a key structure for force transmission. FS substrates have different implications for disorders and, consequently, for treatment planning [1]. Recently, FS biomechanical characterization and variety in accordance with specific anatomical sites are being studied [2]. Historically, the first superficial fascia (SF) to be described in relation to hernias was the abdominal one (known in the lower abdomen as *Scarpa Fascia*). The abdominal deep fascia (DF) is a trilaminar structure known as *rectus sheath* (aponeurotic fascia). Figure 1. Loose connective tissue grants the independent sliding between different layers, excepting along the linea alba where they fuse each other's [1]. Despite the clinical importance, the literature still lacks data on the comparison of mechanical properties of superficial and deep fascia of the abdominal region. Therefore, we have considered this open topic as the focus of this work.

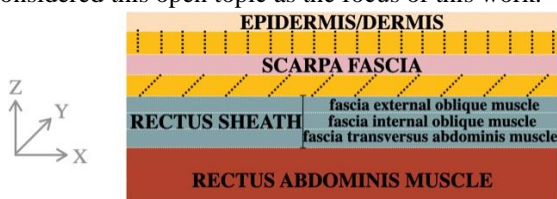


Figure 1: Below the arcuate line.

## Methods

Fasciae patches have been harvested from the abdominal region of a fresh-frozen human donor (male, 86 y/o, no clinical history of fascia alterations), according to Body Donation Program [3]. The patches have been cut into strips (Figure 2a) and tested (Model Match-1, ©Biomomentum) with uniaxial tests. The same orthogonal directions have been considered for both SF and DF, i.e., cranio-caudal (CC, along the  $y$  axis) and latero-medial directions (LM, along the  $x$  axis) Preconditioning cycles were applied before a 1) failure (strain rate: 1%/s) and 2) stress-relaxation protocol (strain rate: 15%/s, resting time: 300s).

## Results

The biomechanical characterization of the SF and DF of the abdominal region was studied in terms of anisotropic

and viscoelastic behavior, highlighting significant differences between the two structures independently from the subject bias (Figure 2b). In particular, DF revealed a clear anisotropy, characterized by an elastic modulus along CC (within the linear region) of about six times lower with respect to the LM direction, while strain at break along LM was about 50% the one obtained from CC samples. Moreover, SF showed a tensile strength up to one order of magnitude lower with respect to DF along the same direction.

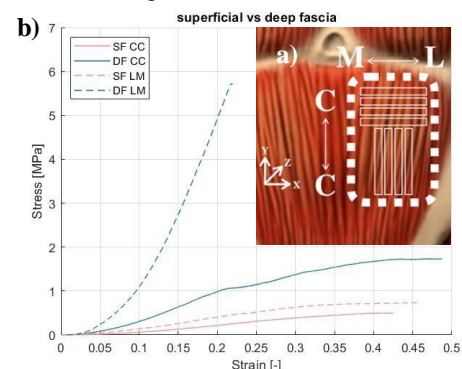


Figure 2: a) Anatomical landmark for the harvested patches and cutting directions b) example of test results.

## Discussion

The variability between SF and DF, according to different directions, is a further proof of their structures and roles. In-depth knowledge of FS mechanical properties has direct applications in tissue engineering and clinical treatment planning (e.g., hernias repair).

## References

1. C. Stecco, Functional Atlas of the human fascial system, Churchill Livingstone, 2015.
2. L. Bonaldi et al, Mechanical Characterization of Human Fascia Lata: Uniaxial Tensile Tests from Fresh-Frozen Cadaver Samples and Constitutive Modelling, Bioengineering, 10(2):226, 2023.
3. A. Porzionato et al, Quality management of Body Donation Program at the University of Padova, Anat Sci Educ, 5(5):264-272, 2012.

## Acknowledgements

This work was supported by MIUR, FISR 2019, Project n° FISR2019\_03221, titled CECOMES (Centro di studi sperimentali e COmputazionali per la ModElliStica applicata alla chirurgia).



# A NANOMECHANICAL ANALYSIS OF THE VISCOELASTIC BEHAVIOR OF BIOLOGICAL TISSUES AND HYDROGELS

Gianpaolo Serino (1), Marta Tosini (1), Torne Tanzer (1,2), Simona Villata (3), Désirée Baruffaldi (3), Valentina Monica (4), Luca Primo (4), Francesca Frascella (3), Alberto L. Audenino (1), Diana Massai (1)

1. *PolitoBIOMed Lab and Department of Mechanical and Aerospace Engineering, Politecnico di Torino, Italy; 2. École Polytechnique Fédérale de Lausanne, Switzerland; 3. PolitoBIOMed Lab and Department of Applied Science and Technology, Politecnico di Torino, Italy; 4. Department of Oncology, University of Torino, Italy*

## Introduction

Cell behavior is strongly influenced by the physical properties of the microenvironment and complex mechanotransduction mechanisms are involved in cell and tissue development, homeostasis and even pathologies [1]. Thus, when developing materials mimicking the extracellular matrix of healthy or pathological tissues their mechanical features should be closely considered. In this context, nanoindentation is a powerful technique for mechanically characterizing biomaterials and hydrogels at the cell-length scale, however, standardized experimental protocols and data analysis techniques are lacking. Here, we propose a methodological approach for quantitatively analyzing and comparing the time-dependent mechanical responses of different samples. As an explanatory study, stress-relaxation nanoindentation tests were performed on human and pig lung samples and on hydrogels in order to quantify and compare their viscoelastic properties.

## Materials and Methods

Three different samples were mechanically characterized by nanoindentation: 1) a human lung sample from a healthy donor, obtained from research-consented organ donors in the framework of the prospective clinical study PROMole; 2) a porcine lung sample, obtained from a slaughterhouse; 3) a gelatin-methacryloyl (GelMa) hydrogel sample, designed for in vitro 3D modelling lung tissue. Stress-relaxation nanoindentation tests were performed (probe stiffness = 0.024 N/m; probe radius  $R = 25.5 \mu\text{m}$ ; Piuma Nanoindenter, Optics11) in wet conditions at  $37^\circ\text{C}$ , setting the indentation mode (max indentation depth  $d_{max} = 1\text{-}5 \mu\text{m}$ ). The imposed indentation depth was reached between 0.1 s and 0.2 s, it was then held constant during load recording, and after 5 s the tip was retracted. For each sample, 10 indentations were performed. The experimental curves were then fitted through a genetic algorithm, imposing 15 sets of initial random parameters and a value of the cost function equal to  $10^{-4}$  as stopping criteria. In detail, the Prony-series that describes the loading history during the holding phase [2] was adopted:

$$P(t) = P(\infty) + \sum_1^N p_K \cdot e^{-\frac{t}{\tau_k}} \quad N = 2 \quad (1)$$

Where  $p_K$  and  $\tau_k$  (the characteristic time constant) are the unknown parameters. The Eq. 2 (where  $\beta_k$  is a parameter used to take into account the non-ideality of the ramp time [3]) based on the  $p_K$  parameters obtained from the fitting procedure and defined as:

$$g_k = \frac{p_k}{16/\sqrt[3]{R} \cdot \sqrt[3]{d_{max} \beta_k}} \quad (2)$$

permits to define the relaxation modulus:

$$G(t) = G(\infty) + \sum_1^N g_K \cdot e^{-\frac{t}{\tau_k}} \quad (3)$$

where  $G(t=0)$  is the instantaneous and  $G(t=\infty)$  is the equilibrium relaxation modulus. Then, for each sample, a set of mean  $p_K$ -parameters was obtained and consequently the mean instantaneous and equilibrium relaxation modulus were calculated, according to Eq. 3.

## Results

Representative experimental and fitted curves for the human lung sample show the accuracy of the fitting method (Fig. 2A). Figure 2B shows the curves obtained using the set of mean parameters for all the samples. Average values of the instantaneous and equilibrium relaxation modulus are reported in Table 1.

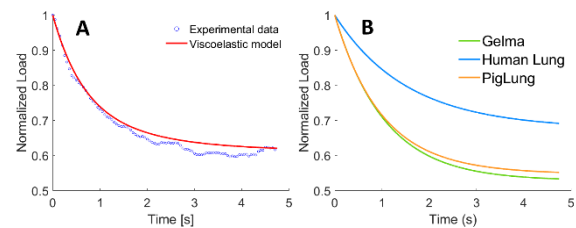


Figure 2: A) Representative experimental and fitted curves for human lung sample; B) Curves from mean parameters set for all samples.

Sample	$G(0)$ (Pa)	$G(\infty)$ (Pa)
HUMAN	$29,4 \pm 23,8$	$22,2 \pm 17,3$
Pig Lung	$35,6 \pm 32,1$	$25,0 \pm 24,1$
GelMa	$117,0 \pm 58,4$	$69,1 \pm 39,7$

Table 1: Average values of instantaneous and equilibrium relaxation moduli for all samples.

## Discussion

The proposed approach allowed comparing the time-dependent behavior of the tested samples. Although the high variability of the results reported in Table 1 due to the heterogeneous nature of the samples, a quantitative measurement of the time-dependent behavior of each sample was provided in terms of instantaneous and equilibrium response, by calculating the relaxation modulus at the onset and at the end of the holding phase. Furthermore, the analysis pointed out the tremendous effect of the time-dependent phenomena on the evaluation of the mechanical properties of the samples.

## References

- Handorf et al, Organogenesis, 11(1):1-15, 2015.
- Mattice et al, J. Mater. Res., 21(8): 2003-2010, 2006.
- Qiang et al, IEEE, 58(7), 1418-1429, 2011



# STRESS RELAXATION OF THE LOWER LIMB TENDONS IN HORSES

Vito Burgio (1), Claudia Tuttobene (2), Mariana Rodriguez Reinoso (3), Valentina Tuveri (4), Marco Civera (5), Cecilia Surace (6)

1.Laboratory of Bioinspired Nanomechanics, DISEG, Politecnico di Torino, Italy

## Introduction

Tendon injuries continue to be a major cause of premature retirement in racehorses. The flexor tendons, especially the superficial digital flexor tendon (SDFT) and the deep digital flexor tendon (DDFT) have the highest incidence according to epidemiological reports present in the literature during practice and race [1].

The anatomical architecture of equine lower limb flexor tendons and joints enable an efficient transfer of energy developed by the muscles favouring rapid locomotion. The Energy-storing tendons, such as Human Achilles tendon and horses' SDFT, are spring-like systems that permit efficient locomotion and reduce muscles workload [2]. The constitutive modelling of ligaments and tendons is important for understanding the soft tissue function, as well as the mechanisms of injury and healing [3]. The most suitable models to represent tendon and ligaments mechanical behaviour is the quasi-linear viscoelastic (QLV) model introduced by Fung [4]. In the QLV model, the stress-strain response is described as a separable function consisting of a stress or strain-dependent function (independent of time) and a time-dependent relaxation or creep function (independent of stress or strain). The time-dependent relaxation or creep function is called the reduced relaxation function ( $G(t)$ ). This work is related to the T-REM3DIE (Tendon REpair MEDical DevIcE) project, whose aim is the developing of cutting-edge technologies for soft tissue repair.

## Methods

The relaxation tests were performed on fresh-frozen tendon specimens, performing uniaxial tensile tests up to 3% and 6% of strain, followed by relaxation at a constant strain level for a hold time of 300 s. Specifically, three types of equine tendons were tested: the common digital extensor (CDET), the DDFT and the SDFT. From the experimental data, stress-time curves were obtained. Then, the fitting of the models was performed and the coefficient of determination was computed ( $R^2$ ). The  $G(t)$  function was defined using the Prony series and the sum of decreasing exponentials in MATLAB environment, to enable the comparison of the results obtained with other tendons and ligaments in literature. In addition, the Percent Lost Stress [5] (PLS) was computed.

## Results

For both the QLV models, higher  $R^2$  values were obtained at 3% of strain compared to 6% of strain (Figures 1-3) and lower PLS as the strain increased.

## Discussion

The application of the QLV model for the characterization of the viscoelastic behaviour of the equine lower limb tendons showed promising results at each percentage of strain tested. These findings are in agreement with the literature where the QLV model was tested on other tendons and ligaments.

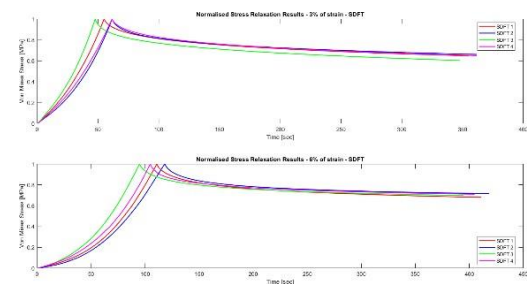


Figure 1: Normalised Stress relaxation of SDFT.

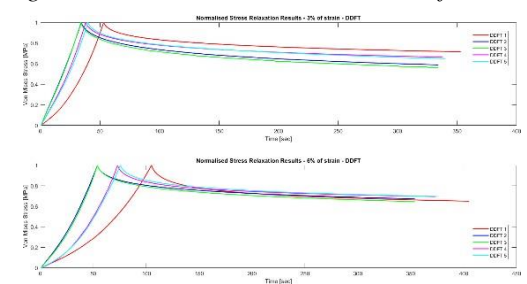


Figure 2: Normalised Stress relaxation of DDFT.

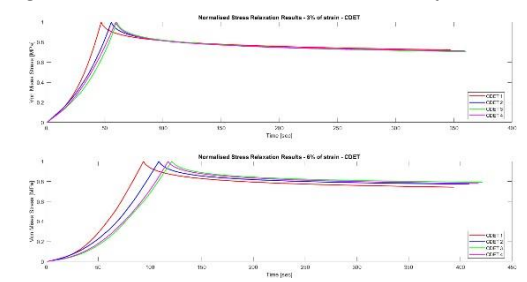


Figure 3: Normalised Stress relaxation of CDET.

## References

- [1] Dabbene et al. *Equine Vet J*, vol. 50, no. 6, pp. 759–765, Nov. 2018.
- [2] Spaas et al. *Sports Medicine*, vol. 42, no. 10, pp. 871–890, Oct. 2012.
- [3] DeFrate et al. *Biomechanics and Modeling in Mechanobiology*, vol. 6, no. 4, pp. 245–251, Jul. 2007.
- [4] FUNG Y.C., *The Meaning of the constitutive equation, Biomechanics: mechanical properties of living tissues*, Springer
- [5] Sylwia et al. *Stress relaxation of porcine tendon under simulated biological environment: experiment and modelling*, *Acta of Bioengineering and Biomechanics*.



# SATISFACTORY MODELLING COMPLEXITY FOR PRK IN-SILICO SIMULATION: AN OPTO-MECHANICAL ANALYSIS

Benedetta Fantaci (1), Miguel-Ángel Ariza-Gracia (3), Begoña Calvo (1,2)

1. Aragón Institute of Engineering Research, University of Zaragoza, Spain; 2. CIBER-BBN, Zaragoza, Spain; 3. ARTORG, University of Bern, Switzerland.

## Introduction

In the last two decades, corneal laser surgery has become a common procedure to correct medium-low refractive defects. It consists of reshaping the corneal surface by means of a laser in order to correct the present vision error. The action of the laser onto the eye causes a modification of the equilibrium among intra-ocular pressure (IOP) and the corneal tissue mechanics, that could cause a mismatch in the actual dioptric correction and, eventually, post-surgical complications, like ectasia. In this work, we present an in-house developed automatized finite element (FE) methodology to simulate Photorefractive Keratectomy (PRK), analysing the minimal modelling requirements for obtaining a reliable opto-mechanical presurgical evaluation of the surgery outcome.

## Methods

A top-down approach was used, by building three corneal models with growing complexity: conic, biconic [1] and patient-specific (PS) models. Our automatized methodology starts by receiving as input patient's topographic data (radius and asphericity values or directly the surfaces point clouds for the PS model), in order to build the geometry point clouds. Due to the lack of peripheral surface data, in PS geometry corneal surface reconstruction is performed by means of Zernike's polynomials [12]. Then, the point clouds are directly meshed with the software ANSA pre-processor by BETA-CAE v22.0.1. A non-linear anisotropic Holzapfel-Gasser-Ogden constitutive model was chosen to model the behavior of corneal tissue, including in-plane and out-of-plane dispersion of the collagen fibers [3]. The effect of three different boundary conditions (BC) was tested: fixed BC at the base of the cornea; symmetric BC at the base of the sclera (only in this case sclera was considered); sliding boundary condition at the base of the cornea, where only radial displacements are allowed. A pre-stretch iterative algorithm was used to compute the stress-free configuration and the patient's IOP of 15 mmHg was applied to the corneal posterior surface. A PRK laser surgery was simulated by removing corneal tissue from the anterior surface. The ablation profile was calculated using conic and biconic equations [4] for the analytical models and wavefront calculation [5] for the PS model, aiming at correcting -4 D, as indicated by the topography of the patient. All mechanical simulations were calculated using ABAQUS. Corneal optics was calculated using an in-house algorithm.

## Results

From the mechanical analysis, a concentration of stresses and strains (Figure 1.a - only strains are shown)

arises in the optical zone ( $R = 3$  mm), induced by the surgery, where the ablation is performed, in all the models. From an optical point of view, if we look at the pre- and post-surgical sagittal curvature maps (Figure 1.b), it can be noticed how the surgery performs a decrease and a smooth regularization of the surface refractive power, especially in the PS case.

## Discussion

Although the PS model is the most representative of patient's real corneal state, simpler model can be used to have an esteem of the opto-mechanical effect of laser surgery onto the structure. While conic model is not able to replicate both myopic and astigmatic defect, the biconic model is a valid approximation to analyze the opto-mechanical changes.

This methodology could become a useful tool for the clinicians to anticipate the surgery outcome, given that it allows to consider the optics and the mechanics of the cornea, both necessary to have a complete evaluation of the clinical state of the patient's eyes. Clinical validation will follow on a larger patients' database.

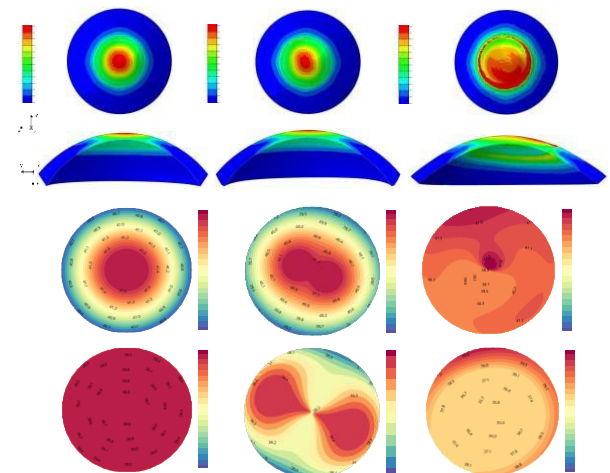


Figure 1.a. Strain Differences caused by the ablation; b. Pre- and post-surgical sagittal curvature maps.

## References

1. Navarro, J Optom, 2:3-18, 2009
2. Lakshminarayanan et al, J Modern Optics, Vol. 58, 2011.
3. Wang et al, J Biomech Eng, 143(3), 2021.
4. Jiménez et al, J Refr Surg, 2003
5. Du, R. et al, International Ophthalmology, 2021.

## Acknowledgements

This project has received funding from the European Union's Horizon 2020 research and innovation programme under grant agreement No 956720.



# FINITE ELEMENT ANALYSIS OF HEMIPELVIC CUSTOM-MADE RECONSTRUCTIONS IN THE LONG-TERM FOLLOW-UP

Giulia Fraterrigo (1,2), Cristina Cattellino (1,2), Giulia Visonà (1,3), Massimiliano De Paolis (4), Davide Donati (1), Fulvia Taddei (1), Enrico Schileo (1)

1. IRCCS Istituto Ortopedico Rizzoli, Bologna, Italy; 2. Politecnico di Torino, Torino, Italy; 3. Università di Padova, Padova, Italy 4. IRCCS Policlinico di Sant'Orsola, Bologna, Italy

## Introduction

Pelvis reconstruction after primary bone tumour resection surgery is still very challenging today. Custom-made 3D printed pelvic prosthesis are increasingly used to restore patient anatomy and physiological load transmission. They significantly shortened surgery, and are clinically successful in the short-term, but their long-term biomechanical risk, and consequent possible need of structural customization of the design have not been studied yet.

Our study belongs to a larger project that studied the mechanical behaviour of 3D printed custom-made hemipelvis. Results on six patients analysed at  $32 \pm 18$  months of follow-up through motion analysis and musculoskeletal models reported a good functional recovery [1] but a concurrent asymmetry of the internal loads between limbs [2].

To evaluate the prosthesis safety and the risk of bone fracture or resorption in the long term, we built subject-specific finite element (FE) models, and we quantitatively estimated prosthesis stress and bone strain distribution in the force peak instants of walking (most frequent, monopodal task) and squat (demanding bipodal task).

## Methods

FE models of six patients (2 females and 4 males, age= $31 \pm 7$  yrs, BMI  $22.6 \pm 2.9$  kg/m<sup>2</sup>, follow-up time= $32 \pm 18$  months) were built starting from CT-images [3]. A 10-node tetrahedral mesh was generated to model bone, prosthesis, and cartilage components, whereas tensile-only trusses were used for ligaments (Figure 1).

Bone was considered isotropic and inhomogeneous, and properties were mapped from CT-data using validated relationships [4]. Material properties for prosthesis [5], cartilage [6] and ligaments [7] were taken from the literature.

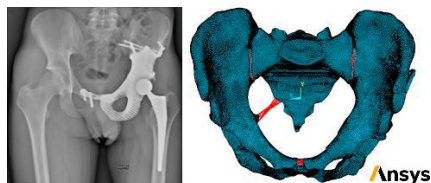


Figure 1: The RX of patient #3 and the corresponding FE model derived from CT-data.

Loads were extracted from personalized musculoskeletal models, considering hip and muscles (19 muscles per side) forces, and distributed over

anatomical attachment areas. Three patients were classified as symmetric, and three as asymmetric according to peak values of hip reaction forces in the intact and operated hemipelvis during walking.

Results were analysed in terms of Von Mises stress in the prosthesis and principal strain in the bone.

## Results

Von Mises stresses in the prosthesis body were  $< 50$  MPa for both walking and squat simulations.

Linkage elements (screws and screwed flaps) showed higher stresses, which were below the usually assumed fatigue limit for titanium alloys (400 MPa) but revealed an unwanted bending condition in sacroiliac screws, and possible concerns for sizing of pubic flaps, where stress was maximum at 300 MPa.

The distribution of strain in both motor tasks did not overcome 3000  $\mu$ strain, regarded as a physiological limit [8]. Corresponding highly strained areas (e.g., greater sciatic notch) of intact and operated side showed similar values in symmetric cases, while the operated hemipelvis was strained 50-70% less than the intact one in asymmetric cases, pointing to a possible risk of bone resorption over time.

## Discussion

FE results indicated that the prosthesis body, currently personalized upon anatomy, is safe and does not require a structural customization. Positioning and sizing of linkage elements may deserve attention during planning/design phases, to limit flexural stresses in the screws and excessive stresses in the flaps.

The reduction of strain in the operated limb might suggest a risk of bone resorption, which would be however entirely due to asymmetric unloading of the operated limb, and not to prosthesis strain-shielding. An effort should be therefore directed towards an efficient post-operative rehabilitation of the operated limb to balance load distribution between the two limbs.

## References

1. Valente G., et al., *Gait & Posture*, 97:73-79, 2022.
2. Valente G., et al., *Gait & Posture*, 102:56-63, 2023.
3. De Paolis M., et al., *Orthopedics*, 45(2): e110-e114, 2022.
4. Leung A.S.O., et al., *JEIM*, 223(8):965-79, 2009.
5. La Barbera L., et al., *IJAO*, 42(10):575585,2019.
6. Toyohara R., et al., *Sci Rep*, 10:13683, 2020.
7. Zheng N., et al., *Med Biol Eng Comput*, 35:77-82, 1997.
8. Milgrom C., et al., *Am. J. Phys. Med. Rehabil.* 80:433-438.,2001.

# MORPHOLOGICAL AND MATERIAL CHARACTERIZATION OF SLM Ti6Al4V THIN SAMPLES FOR ORTHOPEDIC IMPLANTS

Francesca Danielli (1), Francesca Berti (1), Adelaide Nespoli (2), Valentina Lo Presti (1), Edoardo Sironi (1), Davide Ninarello (2), Tomaso Villa (1), Lorenza Petrini (3)

1. CMIC, Politecnico di Milano, Italy; 2. CNR-ICMATE, Lecco, Italy; 3. DICA, Politecnico di Milano, Italy

## Introduction

The advantages of Additive Manufacturing (AM) in orthopedics are nowadays recognized. A new generation of devices mimicking bone is an example: lattice structures characterized by thin struts (in the order of hundreds of  $\mu\text{m}$ ) are conceived to resemble bone trabeculae. Contrary to traditional manufacturing processes, AM allows to produce custom devices fitting complex anatomies. Unlike mass-production devices, there are no defined methodologies to assess safety and quality of custom implants, given their unique shape and dimension. Finite Element (FE) modeling of implantable devices can be a valid option, as long as the model reliability is verified, in terms of geometry and material description. As for the latter, the characterization of thin struts involved in bone implants is an open issue: their final geometry and mechanical properties are affected by their dimensions approaching AM accuracy, as suggested by [1,2]. Thus, morphology and mechanical behavior of AM struts should be investigated together. The current study aims to provide an exhaustive morphological and material characterization of Ti6Al4V thin struts produced by Selective Laser Melting (SLM), coupling a pure experimental approach adopted in literature with FE analyses. The results will be used to design a safe and efficient device for talus substitution, as discussed in [3].

## Materials and Methods

**(i) AM production.** Cylindrical samples (0.6 mm of diameter, approaching the thickness of bone trabeculae) were manufactured (SLM technique and Ti6Al4V ELI powder) in three different directions w.r.t. the build plane ( $45^\circ$ ,  $60^\circ$ ,  $90^\circ$ ), chosen based on the struts inclinations of the trabecular cells commonly used for orthopedic devices and compatibly with AM limits (Fig. 1a). **(ii) Morphological characterization.** The quality of the as-built samples was investigated by performing: 1) density analysis to assess the presence of internal pores w.r.t. a machined Ti6Al4V, 2) global geometry evaluation to assess mismatches of AM samples from the nominal ones (Fig. 1b), 3) local geometry evaluation of the surface texture. **(iii) Material characterization.** Static uniaxial tensile tests were performed under displacement control on three samples for each batch (Fig. 1c). To measure strains, extensometers could not be applied, given the samples small dimensions. Thus, experiments were coupled with FE analyses: samples FE models were developed considering the actual cross-section areas derived from the morphological characterization. Finally, fatigue tests were performed under force control (stress ratio 0.1, mean force 40 N)

until either sample failure or runout ( $5 \cdot 10^5$  cycles). To date, three load levels were considered and five samples for each level and for  $60^\circ$ - and  $90^\circ$ - batches were tested (Fig. 1d). The runout was chosen based on the final application of the talus prosthesis. Considering the walk activity as a cycling load and assuming an average of  $10^6$  steps/year, the time to guarantee an osseointegrated implant is about half a year ( $5 \cdot 10^5$  cycles), during which the device is the only element bearing the body weight.

## Results

The underrated cross-section area (5%-20% difference w.r.t. the nominal one, Fig. 1b) and the surface roughness led to a reduction in the effective load-bearing section. In the static tests, a decrease of about 40% and 7% was found for the elastic modulus and for the yield stress, respectively. In the fatigue tests, a 20%-40% reduction of the limit stress within the cycles range  $4 \cdot 10^4$ - $10^5$  was observed w.r.t. to the literature results for bulk Ti6Al4V samples (diameter 3-6 mm, [4]) (Fig. 1d). The introduced parameters were not affected by the print direction, with the exception of the cross-section area.

## Discussions

AM peculiarities in the production of thin struts are currently an open issue. A deep insight into their morphological and material properties is fundamental in view of correctly describing and predicting the mechanical behavior of AM lattice-based prostheses exploiting a FE approach.

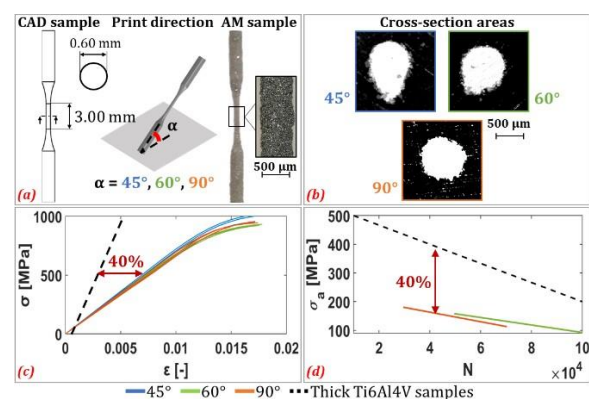


Figure 1: a) SLM-manufacture of Ti6Al4V samples, b) Cross-sections of the samples, c) Stress-Strain curves from static tests, d) Stress-Number of cycles curves from fatigue tests.

## References

1. Murchio et al, J Mech Behav Biomed Mater, 2021.
2. Hossain et al, Addit Manuf, 2021.
3. Danielli et al, J Mech Sci, 2023.
4. Pegues et al, Int J fatigue, 2018.



# COMPARISON OF PHANTOM-BASED AND PHANTOMLESS CT CALIBRATION ON FE MODELS TO PREDICT HIP FRACTURE

Julia A. Szyszko (1, 2), Alessandra Aldieri (3,2), Antonino A. La Mattina (1,2), Marco Viceconti (1,2)

1. Department of Industrial Engineering, Alma Mater Studiorum – University of Bologna, Bologna, Italy; 2. Medical Technology Lab, IRCCS Istituto Ortopedico Rizzoli, Bologna, Italy; 3. PolitoBIOMed Lab, Department of Mechanical and Aerospace Engineering, Politecnico di Torino, Torino, Italy

## Introduction

Finite element (FE) models built from computed tomography (CT) images have largely been employed as digital twins to predict bone fracture [1] [2]. These models rely on the definition of elastic properties assigned heterogeneously to the bone based on the CT Hounsfield Units (HU). This involves primarily the assessment of a HU-density relation through a calibration procedure. Traditionally, that is done by placing a calibration phantom inline or scanning it offline with the same CT parameters. However, a phantom-based calibration might result rarely feasible in the clinical practice. In this perspective, CT phantomless calibration, i.e., a calibration performed taking advantage of the patient's tissues visible in the CT, could represent a viable alternative. This study aimed to compare the outcomes of CT-based FE models developed from phantom-based and phantomless calibration procedures.

## Methods

This study was based on a cohort of 101 women aged 55 years or older (mean age of 68 years) with CT scans available from Rizzoli HipOp collection. The CT images were calibrated adopting phantom-based and phantomless procedures as explained in the following. The phantom-based calibration involved scanning the European Spine Phantom, consisting of 5 components with varying densities. Average HU values were computed for each component, and a linear regression performed against the known densities. The phantomless calibration instead was based on the methodology reported in [3], where air, adipose, and muscle tissues were employed to carry out calibration using reference density values ( $\rho_{QCT}$ ) of -840, -80 and 30  $\text{mg}/\text{cm}^3$ , respectively. A custom MATLAB script allowed to select a 9 slices-wide region of interest (ROI) centred at the middle point between the femoral head and knee centres, and which included air, adipose, and muscle tissues. The reference HU values for selected tissues were extracted by identifying the peaks from the HU distribution within the ROI and patient-specific calibration lines identified through linear regression between the HU and known  $\rho_{QCT}$ . For both methods, Young's modulus was assigned elementwise (*Bonemat*, IOR, Bologna, Italy) using validated density-modulus relationships [4] [5]. The FE simulations run (Ansys Inc., PA, USA) replicated a sideways fall loading scenario: a 1000N load was applied at femur head centre and a rigid frictionless contact plane perpendicular to the load direction was created at the greater trochanter.

Twenty-eight different FE simulations were performed varying the femur's impact pose [2]. Principal strains (tensile:  $\epsilon_1$ ; compressive:  $\epsilon_3$ ) were considered to compare the two calibration procedures.

## Results

Principal strains comparison between the two calibration procedures is shown in Fig. 1 for one of the impact poses simulated (femur aligned to its own anatomical reference system). Average relative differences of 5.8% for  $\epsilon_1$  and 5.45% for  $\epsilon_3$  were found. Considering all the impact poses, average differences of 5.68% ( $\epsilon_1$ ) and 5.52% ( $\epsilon_3$ ) were obtained.

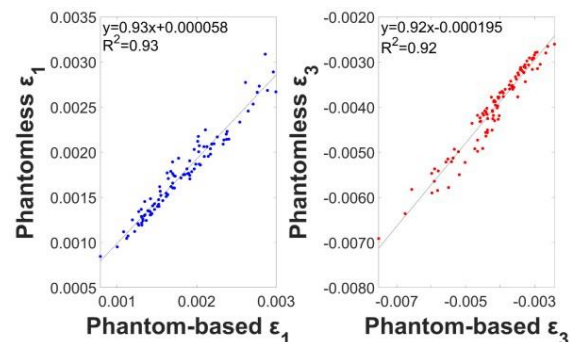


Figure 1: Highest  $\epsilon_1$  (left) and lowest  $\epsilon_3$  (right) values got from the phantom-based and phantomless FE simulations for the whole cohort.

## Discussion

This study compared FE outcomes obtained from a CT phantomless calibration with those coming from a phantom-based calibration. A good agreement was found between the two, which encourages, when needed, the adoption of phantomless calibration. A reliable and standardized phantomless calibration procedure might in fact support the use of opportunistic CT images to implement digital twins solutions.

## References

1. Altai et al., *Clin Biomech*, 2019
2. Bhattacharya et al., *Biomech Model Mechanobiol.*, 2019.
3. Eggermont, F. et al., *PLOS ONE*, vol. 14, no. 7, 2019.
4. Schileo, E. et al., *J Biomech*, vol. 41, pp. 2483-2491, 2008.
5. Morgan, E. et al., *J Biomech*, vol. 36, pp. 897-904, 2003.

## Acknowledgements

This study was supported by the European Commission through the H2020 project "In Silico World: Lowering barriers to ubiquitous adoption of In Silico Trials" (topic SC1-DTH-06-2020, grant ID 101016503).



# MECHANICAL BEHAVIOR OF NERVE CONDUITS BASED ON OXIDIZED POLYVINYL ALCOHOL AND CARBON NANOTUBES

Marta Confalonieri (1), Elena Stocco (2), Silvia Barbon (2), Silvia Todros (1), Ludovica Ceroni (3), Enzo Menna (3), Andrea Porzionato (2), Piero G. Pavan (1)

1. Department of Industrial Engineering, University of Padova, Italy; 2. Department of Neurosciences, Section of Human Anatomy, University of Padova, Italy; 3. Department of Chemical Sciences, University of Padova, Italy.

## Introduction

Nerve conduits (NCs) based on bioresorbable polymers represent a promising alternative to nerve autografts, being currently the gold standard in the treatment of severe peripheral nerve injuries. Since the outcomes associated with commercially available devices are not fully satisfactory, there is interest in designing innovative NCs to overcome their limitations. To this purpose, NCs based on oxidized polyvinyl alcohol (OxPVA) already proved their ability in sustaining axonal regeneration in pre-clinical studies [1]. In the present study, OxPVA was combined with multi-walled carbon nanotubes (CNTs) to confer enhanced electrical properties that are expected to encourage material-neuron interactions and promote nerve regeneration [2]. Possible modifications in the mechanical properties, due to the CNTs incorporation, were here investigated analyzing the OxPVA+CNTs NCs tensile behavior through uniaxial tensile test. Indeed, NCs should be able to bear sutures, to provide anti-compression protection, but also to have suitable ability to withstand the strain generated during limb activities, thus protecting the new axons.

## Material and methods

OxPVA solution was obtained through a partial oxidative reaction (oxidation degree: 1%) in accordance with a previously published protocol [1]. Hence, once the CNTs were covalently functionalized with benzenesulfonate groups to allow their dispersibility in water, the hybridization with OxPVA solution occurred through mechanical embedding (0.1 wt% of CNTs).

The NCs were fabricated by cast-molding technique (Figure 1A). Briefly, the hydrogel solution was sucked into a stainless-steel cylindrical mold (internal diameter: 2.1 mm) and a coaxial stainless-steel plunger (external diameter: 1 mm) was placed into to create the internal lumen of the conduit. Cross-linking of the polymer occurred by six freeze-thawing (FT) cycles (F at  $-20^{\circ}\text{C}$  for 6 h and T at room temperature (RT) for 1 h).

For uniaxial tensile tests, samples of OxPVA and OxPVA+CNTs NCs (4 samples/group) with a free length of 1 cm were let thaw for 1 h at RT, immersed in phosphate buffer saline solution. The tests were performed at strain rate of  $0.5\% \text{ s}^{-1}$ , up to 50% strain in hydrated conditions using the Bose ElectroForce® Planar Biaxial Test Bench instrument (TA Instruments, New Castle, USA). In view of future *in vivo* trials, the same test was performed on 4 samples of sciatic nerve

excited from two Sprague-Dawley rats (Authorization n. 837/2019-PR, 09 December 2019) used as controls.

## Results and discussion

The results of preliminary uniaxial tensile tests are shown as nominal stress  $\sigma_n$  vs. nominal strain  $\epsilon$  for two NC samples (OxPVA and OxPVA+CNTs) and for one sciatic nerve sample (Figure 1B). It can be observed that the curves  $\sigma_n$ - $\epsilon$  of OxPVA and OxPVA+CNTs NCs have almost superimposable trend. Moreover, the NCs are able to withstand deformation in the physiological strain range [3] without fracturing.

Although many studies reported an increase in the polymer stiffness due to CNTs inclusion, no differences were detected here comparing the mechanical behaviour of OxPVA and OxPVA+CNTs. This feature may descend from the low CNTs concentration within the hydrogel. Previous preclinical studies demonstrated that OxPVA NCs guarantee structural support *in vivo*, resisting to suture and physiological loads, and allowing morpho-functional regeneration/recovery of the nerve in animal model of disease (gap: 5 mm) [1]. According to the data in the present study, the absence of significant difference in tensile behaviour after the addition of CNTs allows us to assume that also OxPVA+CNTs NCs would be able to provide for an adequate mechanical behaviour *in vivo*.

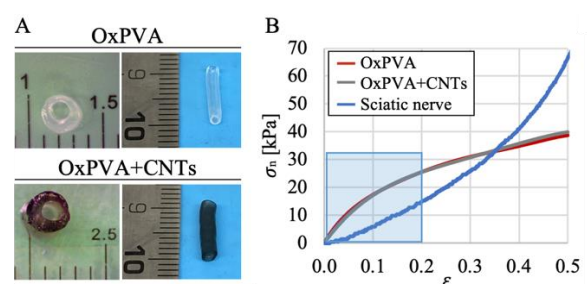


Figure 1: (A) NCs optical microscope images: cross-sectional and lateral views; (B) Uniaxial tensile behavior of two samples of OxPVA and OxPVA+CNTs NCs and of a sample of sciatic nerve. The blue square highlights the range of rat sciatic nerves physiological deformations.

## References

1. Stocco E et al, Sci Rep, 8(1):604, 2018
2. Homaeigohar S et al, Carbohydr Polym, 224:115112, 2019
3. Boyd BS et al, J Orthop Res, 23(4):764-70, 2005



# ENGINEERING SPHERICAL MEMBRANES FOR INHALATION TESTS IN THE PRESENCE OF SYNTHETIC MUCUS

Ludovica Cacopardo, Nicole Guazzelli, Paolo Signorello, Federico Pratesi, Alessandro Corti, Arti Ahluwalia

University of Pisa, Italy

## Introduction

Inhalation tests are fundamental for assessing drug and substance absorption. Standard in-vitro models are based on flat 2D semipermeable membranes at the air-liquid interface. Only recently some studies attempted to replicate the spherical alveolar geometry [1, 2] or the presence of a mucus layer [3]. However, they still lack lung properties such as stretchability. To this end, we developed spherical membranes which replicate the alveolar architecture in a more accurate manner.

## Methods

2D and 3D Agarose-Gelatin (AgGel) membranes were fabricated by cast-drying 1%-5% w/v agarose-gelatin solutions in custom moulds. Mechanical tensile tests were performed at a constant strain rate ( $0.2 \text{ s}^{-1}$ ). A549 cells were seeded ( $100.000/\text{cm}^2$ ) on the membranes and in PET Transwells as control. Transcellular and paracellular transport was investigated with FITC-dextran and rhodamine. Transepithelial electric resistance (TEER) and Alkaline Phosphatase (ALP) release were also evaluated. The spherical membranes were then interfaced with fluidic compartments (Fig.1) fabricated by stereolithographic printing. Different artificial mucus formulations based on alginate with high and low molecular weight (Alg H and L) and pectin were characterised with a Brookfield viscosimeter to mimic mucus rheology. Neutrophils ( $1.4 \text{ million/mL}$ ), derived from healthy donors, were encapsulated in the solutions or suspended in medium as control. Their viability was assessed with the Alamar Blue assay.

## Results

The membranes resulted highly transparent and elastic in the range of pathophysiological strains (5-17%) [1] with an apparent elastic modulus =  $1.07 \pm 0.35 \text{ MPa}$  and failure stress =  $0.13 \pm 0.03 \text{ MPa}$ . Fig. 1 shows that cells adhered forming an uniform monolayer on AgGel membranes. Moreover, AgGel3D presented lower TEER, FITC and ALP values with respect to AgGel2D and PET controls (Fig. 2). Alg H was selected for its ability to mimic mucus rheology at low concentrations [3]. In this condition, the viability of encapsulated neutrophils was equal to  $60.12 \pm 6.09\%$  with respect to controls. Preliminary tests assessed the suitability of the device to mimic dynamic flow and breathing conditions.

## Discussion

Results suggested that curved substrates provide physiological culture conditions for lung epithelial cells. Indeed, in conventional cultures, A549 typically presents not-physiological high TEER values and ALP is known to be overexpressed in cancer [3,4]. The fluidic device can be also connected in different configurations replicating lung hierarchical structure and allowing the study of substance

passage and deposition from a cellular to an organ level. Moreover, the feasibility of encapsulating patient-derived immune cells in synthetic mucus may increase the relevance of the model. Indeed, it is known that they can affect substance absorption and mucus viscosity due to the formation of neutrophil extracellular traps during inflammation [3].

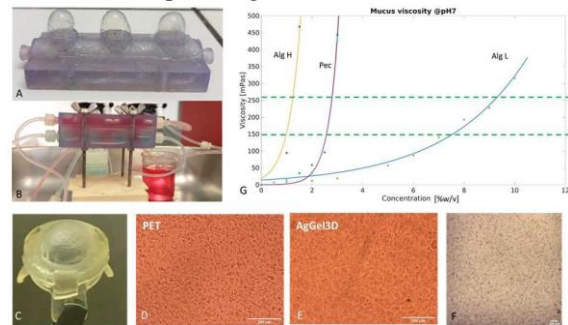


Fig.1 Spherical membranes interfaced with A-B) fluidic compartments and C) cell-crown inserts. D-E) A549 cells on PET and AgGel3D membranes, F) Neutrophils in synthetic mucus, G) viscosity of different materials as a function of their concentration. Green dotted lines indicate pathophysiological viscosity range.

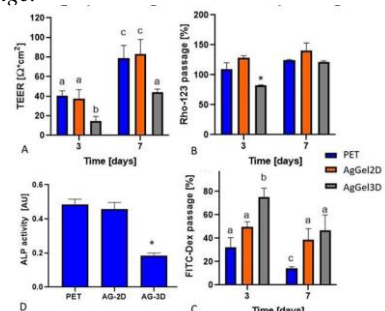


Fig. 2: A) TEER measurements, B-C) FITC and P-gp passage, D) ALP release. Different letters and \* indicate statistical differences ( $p < 0.05$ )

## Conclusion

This work presents preliminary results toward the definition of multiscale human-relevant in-vitro inhalation systems alternative to animal tests. Further tests are ongoing to refine the model and investigate substance absorption in dynamic conditions and in the presence of immune cells encapsulated in synthetic mucus with different viscosities replicating healthy and diseased conditions (e.g., lung cystic fibrosis).

## References

1. Nossa et al, J Tissue Eng, 12:1-28, 2021
2. Baptista et al, Biomat, 266: 120436, 2021
3. Butnarusu et al, Mol Pharm, 19:34, 2022
4. Gaur et al, J Cancer Res, 16(4):839-842, 2020
5. Srinivasan et al, J Lab Aut, 20(2) 107-126, 2015

## Acknowledgements

This project has received funding from the Italian Ministry of Health for Alternative In-vitro Methods



# DESIGN AND VALIDATION OF AN IN VITRO PLATFORM FOR LYMPHOCYTES RECIRCULATION IN CANCER IMMUNOTHERAPY APPLICATIONS

Paolo Ritter (1,2), Stefania Oliveto (2,3), Claudio Conci (1), Emanuela Jacchetti (1), Stefano Biffo (2,3), Manuela Teresa Raimondi (1)

1. Department of Chemistry, Materials and Chemical Engineering “Giulio Natta”, Politecnico di Milano – piazza Leonardo da Vinci 32, Milan, Italy; 2. National Institute of Molecular Genetics “Romeo ed Enrica Invernizzi” - INGM – via Francesco Sforza 35, Milan, Italy; 3. Department of Biosciences, University of Milan – via Giovanni Celoria 26, Milan, Italy

## Introduction

In recent years, the development and validation of immunotherapy models played an increasingly relevant role in biological research. As compared to traditional therapies such as surgery, chemotherapy, and radiotherapy, immunotherapy is expected to be one of the most promising approaches to tumor treatment. [1]. In addition, the introduction of three-dimensional (3D) cellular models is assisting in lowering high failure rates in research. The primary causes of these failures include partial translation and a failure to confirm experimental conclusions gained from two-dimensional (2D) *in vitro* models during *in vivo* animal research. In this regard, our research seeks to develop a predictive and experimental *in vitro* model capable of providing a controlled environment for the interaction of cancer and immune cells. To that purpose, we developed an ad-hoc millifluidic device (MOAB-Nichoid) that combines the primary features of two well-established culturing supports: the Nichoid, a nanostructured polymeric scaffold [2], and the MOAB, a miniaturized optically accessible bioreactor [3].

## Methods

The MOAB-Nichoid was realized by two-photon polymerizing (2PP) the Nichoid scaffolds. These were then embedded into the chambers of the MOAB with a gluing procedure.

The design and realization of the MOAB-Nichoid was accompanied by the development of a hydraulic circuit that, coupled with a syringe pump, would allow the recirculation of suspended cells through the bioreactor. This circuit required the insertion of a dual check valve and a custom-made reservoir to collect the cells suspension and allowing its recirculation.

Finite element modelling was setup by means of COMSOL Multiphysics software using the laminar flow and particle tracing physics to assess the behavior of the circulating cells inside bioreactor chamber. First we retrieved parameters such as flow velocity, pressure, and shear stress in the bioreactor chamber; then these were used to simulate the flow of immune cells by means of particle tracing.

## Results

We realized 14 samples of the MOAB-Nichoid platform consisting in three independent chambers each (Fig.1e-f). These allowed to perform both a functional and a

biological validation, confirming the feasibility and reproducibility of immune cell recirculation experiments through the developed bioreactor.

The first step of the validation process focused on the assessment of the adequate functioning of the hydraulic circuit. Further *in vitro* analyses evaluated the immune cells recirculation capability of the setup, confirming and completing the predictions made on the basis of the *in silico* model.

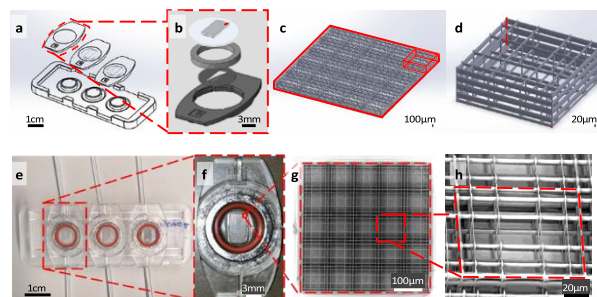


Figure 1: a. CAD of the bioreactor; b. CAD of the lid of the single chamber with the array of Nichoids; c. CAD of Nichoid block; d. CAD of the single niche; e. Picture of the MOAB Nichoid; f. Picture of the lid of the single chamber with the polymerized scaffold; g. SEM image of the Nichoid block; h. SEM image of the single niche.

## Discussion

The *in vitro* model called MOAB-Nichoid was demonstrated to be suitable for immune cells recirculation. Furthermore, it will allow for the culture of cells derived by solid cancers, standing as an optimal candidate for an animal-free patient-specific platform for testing the efficacy of cancer immunotherapies, increasing the effectiveness of cancer treatment.

## References

1. De Ponte Conti et al, eLife, 10, 2021.
2. Testa et al, Frontiers in Bioeng and Biotech, 10, 2023.
3. Perottoni et al, Lab on a Chip, 21, 2021.

## Acknowledgements

This work was supported by: European Research Council (ERC, projects BEACONSANDEGG, G.A. 101053122 and NICHILD, G.A. 101068512); European Commission (EU, FET-OPEN project IN2SIGHT, G.A. 964481 and fIMAGIN3D, G.A. 101073507); NC3Rs (project MOAB, G.A. NC/C019201/1); AIRC (IC 2022 27021 to S.B.).



# ENGINEERED MODELS OF FIBROTIC CARDIAC TISSUE AS PREDICTIVE PLATFORMS FOR PRECLINICAL VALIDATION

**Mattia Spedicati (1,2,3), Gerardina Ruocco (1,2,3), Alice Zoso (1,2,3), Irene Carmagnola (1,2,3), Andrea LAPINI (4,5), Leonardo MORTATI (4), Valeria Chiono (1,2,3).**

1 Department of Mechanical and Aerospace Engineering, Politecnico di Torino, Torino, Italy

2 POLITO BioMedLab, Politecnico di Torino, Torino, Italy

3 Interuniversity Center for the promotion of the 3Rs principles in teaching and research, Italy.

4 Istituto Nazionale di Ricerca Metrologica (INRIM), Torino, Italy

5 Department of Chemical, Life and Environmental Sustainability Sciences, University of Parma, Parma, Italy

## Introduction

Myocardial infarction (MI) is the main cause of mortality and morbidity worldwide. After MI, a stiff cardiac fibrotic tissue (CFT) forms, causing a decrease in cardiac ejection fraction [1]. *In vitro* models of pathological cardiac tissue are under development, mainly exploiting cellularized hydrogels, as predictive platforms for preclinical validation of new therapies [2, 3]. However, these models are unable to faithfully reproduce the mechanical properties of CFT. In this work, 2D and 3D models of early-stage human fibrotic tissue were prepared through bioartificial scaffolds with biomimetic architecture, chemical composition and stiffness.

## Methods

Polycaprolactone (PCL) was used as scaffold bulk material to reproduce tissue stiffening. CFTs with low and high thickness were engineered from 2D random membranes fabricated by solution electrospinning and 3D square-meshed scaffolds prepared by melt-extrusion additive manufacturing, respectively. Type A Gelatin (G) was grafted on PCL scaffolds surface after 3,4-Dihydroxy-DL-phenylalanine polymerization (PolyDOPA), to obtain biomimetic properties. Scaffolds physico-chemical properties were thoroughly investigated. Ventricular human cardiac fibroblasts (v-HCFs) were cultured on scaffolds up to 3 weeks. Immunofluorescence analysis and two-photon microscopy were used to evaluate the activation into fibrotic cell phenotype and the deposition of pathological cardiac ECM on scaffolds.

## Results

Electrospun 2D scaffolds random mats showed defect-free nanofibers with  $127 \pm 33$  nm diameter and  $< 1$   $\mu$ m average pore size. 3D PCL scaffolds (0.7 mm thickness) with square mesh size of 150  $\mu$ m showed high shape fidelity and porosity degree. Scaffold stiffness was higher than healthy cardiac tissue as measured by surface AFM analysis in wet and dry conditions. Immunostaining showed that scaffold surface mechanical properties and architecture triggered the activation of myofibroblast phenotype and fibrotic-like ECM deposition. Moreover, SEM and two-photon

excitation fluorescence showed ECM homogeneous distribution on 2D and 3D scaffolds.

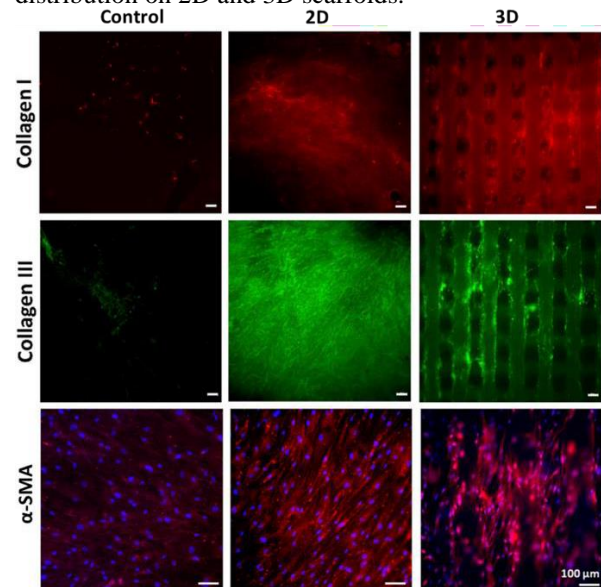


Figure 1: Immunostaining for Collagen -I, -III and  $\alpha$ -SMA on v-HCFs cultured for 3 weeks on PCL/polyDOPA/G scaffolds and G-coated glass (control). Nuclei were stained in blue with DAPI.

## Discussion

2D and 3D bioartificial PCL scaffolds surface functionalized with polyDOPA/G were prepared, provided with CFT-like surface composition and stiffness. They supported long-term culture of v-HCFs, and triggered their fibrotic activation and pathological ECM deposition. Such *in vitro* models can reproduce patient-specific features of human cardiac fibrosis for the testing of new regenerative therapies.

## References

1. Shirani, J. et al., J. Am. Coll. Cardiol. 35, 36–44 (2000).
2. Sadeghi, A. H. et al., Adv. Healthc. Mater. 6, 1–14 (2017).
3. Conant, G. et al., Stem Cell Rev. Reports 13, 335–346 (2017).

## Acknowledgements

This project is funded by the European Research Council under European Union's Horizon 2020 research and innovation programme grant agreement No-772168.



# TOPOLOGY OPTIMIZATION FOR THE DESIGN OF NOVEL FEMORAL ARTERY STENTS

Dario Carbonaro (1), Francesco Mezzadri (2), Nicola Ferro (3), Giuseppe De Nisco (1), Alberto Luigi Audenino (1), Diego Gallo (1), Claudio Chiastra (1), Umberto Morbiducci (1), Simona Perotto (3)

1. PoliTo<sup>BIO</sup>Med Lab, Department of Mechanical and Aerospace Engineering - Politecnico di Torino, Italy;
2. Department of Engineering "Enzo Ferrari" - University of Modena and Reggio Emilia, Italy;
3. MOX, Department of Mathematics - Politecnico di Milano, Italy

## Introduction

Self-expandable femoral stents are employed in diseased femoropopliteal arteries to provide mural support and prevent vessel obstruction after intervention [1]. The state-of-the-art in femoral stents design is represented by contributions that rely on minimum modifications of a limited number of stent geometries. This results in high costs due to the conventional trial-and-error design pipeline. In order to overcome the limitations of such approaches, we propose a novel computational framework for designing from scratch innovative self-expandable femoral stents by resorting to mathematically sound optimization techniques.

## Methods

A stent can be considered as a hollow cylindrical device whose exterior surface is generated through the repetition of a 2D unit cell. Stents typically present differences in such a unitary geometry, which, in turn, characterizes the devices with diverse physical properties.

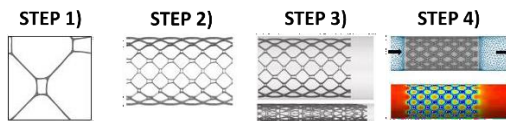


Figure 1: Stent design workflow.

The workflow in Fig. 1 follows 4 steps, namely:

- 1) the use of an *ad hoc* inverse homogenization topology optimization enhanced by an anisotropic mesh adaptation procedure [2]. This phase drives the design of customized 2D unit cells that retain some desired mechanical properties, while imposing the minimization of the contact area between the stent and the vessel;
- 2) the generation of a 3D stent geometry starting from the optimized 2D unit cell;
- 3) the evaluation of structural mechanics performance of the new stent in terms of peak maximum principal strain, radial force, foreshortening and crimpability into the catheter [3];
- 4) the assessment of the stent hemodynamics performance, by quantifying the blood flow disturbances induced by the stent inside the vessel in terms of Time-Averaged Wall Shear Stress and Topological Shear Variation Index [3].

## Results

The design workflow is tested onto five proof-of-concept stent designs. The obtained layouts in Fig. 1 are characterized by high heterogeneity in the topology of the unit cells and differ from the state-of-the-art shapes employed in stenting clinical practice.



Figure 2: Optimized unit cells for stent design.

All the generated stents feature a desirable low contact area between stent and vessel, and are characterized by diverse structural and fluid dynamics properties.

## Discussion

By a critical examination of the results, we conclude that the new computational workflow is disruptive, cost- and time-effective and capable of generating novel and functional stent designs. In more detail, the finite element analyses suggest that only two designs meet the minimum requirements for usability in terms of device crimpability into the catheter, although they differ in terms of mechanical and fluid dynamics features. In particular, the first design (see Fig. 2, left) exhibits: a low value of the peak maximum principal strain at the catheter diameter, corresponding to high safety in terms of structural integrity; high radial force; an adequate foreshortening at the implantation diameter. Conversely, the fluid dynamics simulations highlight that the last design (see Fig. 2, right) is subject to a low risk of in-stent restenosis. As a consequence, these two stents turn out to be promising, yet some further explorations are needed in order to determine the best candidate. With this regard, it is possible to pave the way to future enhancements, such as the inclusion of structural and fluid dynamics criteria directly in the design step 1), the introduction of manufacturability constraints for production purposes, as well as the optimization of the material employed for the subsequent production phase.

## References

1. Shlofmitz E, et al., *Circ Cardiovasc Interv*, 12: 1–8, 2019.
2. Ferro N, et al., *Lect Notes Comput Sci Eng*, Springer Cham, 132: 211–221, 2020.
3. Chiastra C, et al., *J Biomech Eng*, 144: 061002, 2022.



Day 2

Orthopedic and musculoskeletal  
biomechanics  
*Oral presentations*

Torino, 19 September 2023



# BIOLOGICAL EVALUATION OF BONE-LIKE SCAFFOLDS IN SIMULATED MICROGRAVITY

Federico Mochi (1,2), Eleonora Zenobi (1,2), Elisa Scatena (1,2), Luca Panizza (3), Raffaella Pecci (4), Mario Ledda (5), Antonella Lisi (5), Costantino Del Gaudio (6)

1. E. Amaldi Foundation, Rome, Italy; 2. Hypatia Research Consortium, Rome, Italy; 3. Studio E Roma srl, Rome, Italy; 4. National Center for Innovative Technologies in Public Health, Italian National Institute of Health, Rome, Italy; 5. Institute of Translational Pharmacology, National Research Council, Rome, Italy; 6. Italian Space Agency, Rome, Italy.

## Introduction

Bone mass loss is a well-known consequence to microgravity exposure which implies an alteration of bone homeostasis, a decrease in bone mineral density, an increase in fracture risk, and a premature osteoporotic phenotype [1]. The modifications induced by weightlessness show similarities with known hallmarks of aged bone and it is becoming widely accepted that microgravity induces bone phenotypic changes comparable to those of bone-related disorders experienced on Earth [1]. In this regard, space could be considered an accelerated model to investigate the mechanisms that play a key role in skeletal affections, with the aim to refine existing therapeutic protocols and develop new countermeasures [2].

An experimental strategy to further elucidate the results collected so far and to provide innovative models for space research is highly recommended, especially if referred to long-term space missions (e.g. Moon, Mars) [3]. In this work, an innovative 3D biomimetic platform composed of engineered bone-like scaffolds [4], osteoblastic cell model [5], and a bioreactor capable of simulating microgravity is proposed to analyze the scaffold-cell interaction.

## Methods

Three CAD models were designed (Meshmixer, v.2018, Autodesk, San Rafael, CA, USA) with different degrees of porosity to resemble the physio-pathological morphology of human trabecular bone (Table 1). Bone-like scaffolds were then 3D printed employing the fused deposition modeling (FDM) technique processing a polylactic acid (PLA) filament, an approved FDA material, and characterized by means of micro-computed tomography (micro-CT). Human osteosarcoma (SAOS-2) cells were seeded on the scaffolds to evaluate the biological response in simulated microgravity, investigating the metabolic activity and the inflammatory response. Microgravity was simulated by means of a rotary cell culture system (RCCS; Synthecon, Inc., Houston, TX, USA).

## Results

The micro-CT analysis showed that 3D printed scaffolds resemble the physio-pathological microarchitecture of human trabecular bone from different anatomic sites. The biological assays confirmed the bioactivity and biocompatibility of the tested scaffolds, without inflammatory response, where

the most porous model showed the best cell-scaffold interaction (Figure 1).

	S1	S2	S3
Design	53.8%	72.9%	83%
micro-CT	44.7%	62.3%	80.5%

Table 1: Comparison of designed and micro-CT evaluated scaffold porosity

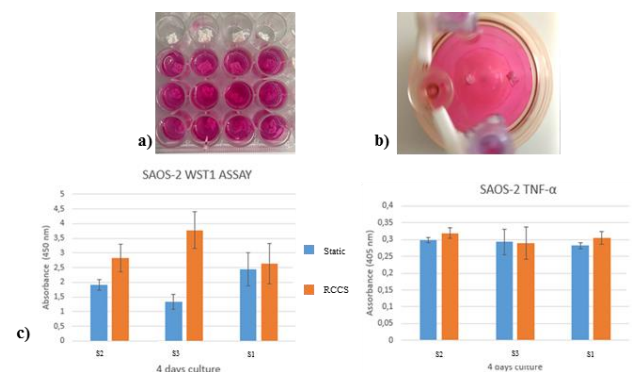


Figure 1: a) Static cell culture; b) RCCS bioreactor with seeded scaffolds; c) results of metabolic activity (left panel) and ELISA biological assay (right panel).

## Discussion

The results demonstrated that cell response is directly related to scaffold morphology, being enhanced if dealing with the most porous one. Moreover, simulated microgravity further supported cell adhesion, viability and proliferation. These findings suggest that biomimetic scaffolds and microgravity culture conditions deserve a detailed investigation as an instructive approach to assess cell osteoactivity.

## References

1. Juhl, IV, O. J. et al. *npj Microgravity*, 7(1), 28, 2021.
2. Avitabile, E. et al. *Front Bioeng Biotechnol*, 8, 722, 2020.
3. Mochi, F. et al. *npj Microgravity*, 8(1), 45, 2022.
4. Ledda, M. et al. *Int J Mol Sci*, 23(10), 5383, 2022.
5. Pecci, R. et al. *J Mech Behav Biomed Mater*, 103, 103583, 2020.

## Acknowledgements

This work was supported by the research project “Dispositivi biomimetici realizzati mediante stampa 3D per il trattamento di patologie del sistema scheletrico (BioBone3D)” – Gruppi di Ricerca 2020 POR FESR LAZIO 2014-2020.



# OSSEOINTEGRATED CURVED STEM PROVIDES GOOD IMPLANT STABILITY IN TRANSFEMORAL AMPUTEES

Giulia Galteri (1), M. Palanca (1), V. Betti (1), K. Morellato (2), E. Gruppioni (2), L. Cristofolini (1)

1. Dept of Industrial Engineering, Alma Mater Studiorum - University of Bologna, Bologna, IT
2. Centro Protesi INAIL, Vigorso di Budrio, Bologna, IT

## Introduction

The direct connection between the external prosthesis and the patient's bone makes osseointegrated prostheses for transfemoral amputees more advantageous than the socket prostheses, which are currently the *gold standard*. However, similarly to other uncemented prostheses, the osseointegrated ones are at risk of stress-shielding and aseptic loosening. How the implant influences the bone strain in specific regions of the femur was experimentally investigated only for straight-stemmed implants [1],[2].

In order to better match the physiological curve of the femoral canal, OTN implant offers a curved stem. However, the influence of the curved implant influences on femoral bone strain has not been investigated yet. Thus, the aim of the study was to evaluate the implant stability and the load transfer of OTN implant with Digital Image Correlation (DIC).

## Material and Methods

One human cadaveric femur was obtained through an ethically approved donation program. CT scans (slice thickness=0.6mm, in plane resolution=0.5mm) were performed to assess the dimension of the femoral canal and choose the correct size of the implant. An osteotomy was performed 200mm from the condyles. An OTN implant size 17 (Badal X<sup>tm</sup>, OTN) was implanted after reaming the femoral canal to guarantee the optimal press-fit. The proximal femur was embedded into a metal pot, tilted as to load the femur like in the heel strike during gait. A speckle pattern was prepared on the surface of the femur for DIC measurements, while to track stem-bone micromotions, set of markers was placed on the distal end of the prosthesis.

Mechanical tests were performed using a uniaxial testing machine (Instron 8500, 10kN load cell). One hundred load cycles (80N-880N), corresponding to a bending moment of 30Nm at the osteotomy level, were delivered (Fig. 1a) [3]. A 4-camera 3D-DIC system (Aramis Adjustable 12M, GOM, 10 fps, measurement spatial resolution 2mm) was used to measure the displacement and strain fields on the femur and prosthesis. A zero-strain analysis was performed to measure the DIC precision.

The maximum principal strains ( $\epsilon_1$ ) were measured in two regions of interest: close to the osteotomy (ROI1) and close to the stem tip (ROI2) during the peak load of each cycle. The elastic micromotions were measured as the inducible displacement of the stem with respect to the bone within each cycle. The permanent migrations accumulated throughout the test were measured.

## Results

The random error was smaller than  $100\mu\epsilon$ . Maximum principal strains in ROI1 were smaller than those found close to the stem tip ROI2:  $320\pm 97\mu\epsilon$  vs  $1300\pm 220\mu\epsilon$ , respectively (Fig.1b). Inducible micromotions along the longitudinal axis were around  $100\mu\text{m}$  and stable throughout the test. Permanent migration of  $2\mu\text{m}$  was measured along the longitudinal axis.

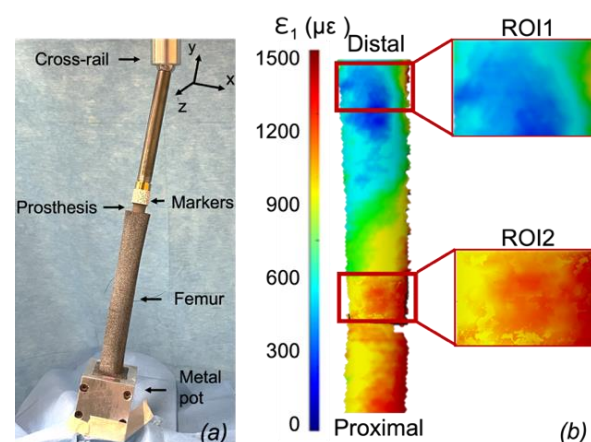


Figure 1:(a) Experimental setup (front view, with the femur mounted upside-down). (b) Color map showing the distribution of maximum principal strains ( $\epsilon_1$ ) on the femur, in ROI1 and ROI2.

## Discussion

The 3D strain distribution showed how the insertion of the OTN implant leads to a high strain-shielding at the distal region of the femur and a strain concentration proximally (at the stem tip level). The strain distribution obtained is comparable to those reported in a previous study of straight-stemmed implants [1]. The inducible micromotions and permanent migrations were both lower than the micromotions critically inducing fibrous tissue formation [4]. This suggests that this prosthesis reached a satisfactory press-fit condition and the primary stabilization. In order to generalize the findings, further mechanical *in vitro* tests will be carried out.

## References

- [1] P.K.Tomaszewski et al. (2013), *J.M.B.B.M.*
- [2] Ahmed et al. (2020), *Ann. Biomed. Eng.*
- [3] W.C.C. Lee et al. (2008), *Med. Eng. Phys.*
- [4] R.M.Pilliar et al (1986), *Clin. Orthop.*

## Acknowledgements

Study funded by INAIL (PR19-CR-P5-OsteoCustom). The authors thank G.Cavazzoni for the valuable support.



# OSTEOSYNTHESIS OF THE PUBIC SYMPHYSIS: EXPERIMENTAL-NUMERICAL COMPARISON BETWEEN TWO FIXATION SYSTEMS

Alessandra Aldieri (1), Dario Carbonaro (1), Alessandro Aprato (2), Mara Terzini (1), Cristina Bignardi (1)

1. Polito<sup>BIO</sup> Med lab, Department of Mechanical and Aerospace Engineering, Politecnico di Torino, Torino, Italy; 2. Department of orthopaedics and traumatology, University of Turin, CTO, Torino, Italy.

## Introduction

Pelvic fractures, which often result from high-energy trauma, can involve disruption of the pubic symphysis. In these cases, adequate reduction and fixation of the symphysis are crucial for restoring stability and alignment of the pelvic ring [1]. Open reduction and internal fixation with plates has become the preferred standard of care due to its lower rate of complications compared to the other possible approaches [2]. Nevertheless, implant failure rates between 12% and 31%, loss of reduction of 7% to 24%, and revision rates of 3% to 9% have been reported in the literature [3]. Recently, a dynamic fixation approach employing the Endobutton CL device (Smith & Nephew, Memphis, TN, USA) has been proposed for reduction of pubic symphysis diastasis [4]. The aim of this study was to compare the efficacy of the Endobutton CL and the plate reduction techniques for the treatment of open-book pelvic fractures. Experimental tests were conducted to measure the performance of the devices and to assess the validity of a finite element (FE) model developed within this study.

## Methods

A total of nine Sawbones pelvis samples were tested: three in a non-reduced open book fracture configuration, three with the Endobutton CL reduction, and three with the plate fixation. The boundary conditions for the tests are shown in Fig. 1a. A compressive uniaxial load was applied on the sacrum under displacement-controlled conditions at 1 mm/min speed up to 3000 N. Nine markers were placed on the specimens' surface and their displacements tracked during the test (GOM Correlate). FE models were developed to reproduce the experimental tests. Elastic isotropic mechanical properties were assigned to trabecular and cortical bone (0.155 and 10 GPa respectively), and to the 316L steel plate (210 GPa). The sacroiliac joints and the experimental boundary conditions at the acetabula were replicated through kinematic constraints and spring elements properly calibrated based on the experimental tests. The Endobutton device was modelled by means of rigid spheres connected by springs.

## Results

The Endobutton reduction allowed the highest pubic symphysis opening at the maximum load of 3000 N, with an average of  $5.76 \pm 0.15$  mm. While the fractured specimens yielded an opening of  $9.02 \pm 0.76$  mm, the plate reduction showed a very limited symphysis opening ( $0.61 \pm 0.30$  mm). Pelvis stiffness, computed as the ratio between the force registered at the sacrum

and the crosshead displacement, was only slightly higher in the case of plate fixation than in the case of Endobutton fixation ( $682.46 \pm 65.27$  N/mm against  $612.56 \pm 28.97$  N/mm) when computed at 500 N. Nevertheless, the former showed a 75% increase of stiffness at 2000 N, while the latter showed a more modest stiffness increase, equal to 44%. The FE models achieved a good agreement with the experiments when looking at the displacement of nodes equivalent to the markers tracked experimentally (Fig 1b).

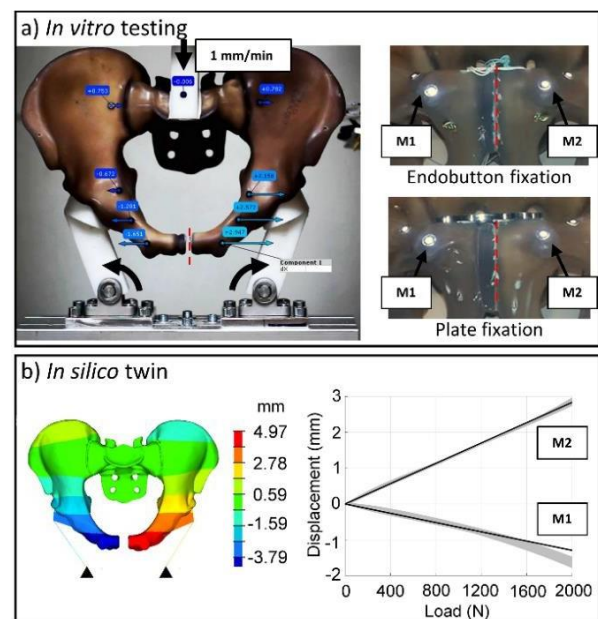


Figure 1. a) *in vitro* testing of fractured and fixated pelvis; b) horizontal displacement of fractured FE model with comparison of numerical (black lines) and experimental displacements (gray bands) of the two symphysis markers (M1 and M2).

## Discussion

The Endobutton fixation allowed a much higher degree of mobility compared to plate fixation. For relatively low loads it proved to be stiff enough to guarantee the diastasis stability. Nevertheless, as the load increased it allowed increased flexibility compared to the plate fixation. The validated FE model will be employed to reproduce more complex physiological loading conditions in order to further compare the two fixation techniques.

## References

1. Sagi et al., *J Orthop Trauma*, 18(3):138–143, 2004
2. Mason et al., *Injury*, 36(5): 599–604, 2005
3. Morris et al., *Clin Orthop Relat Res*, 470(8): 2154–2160, 2012
4. Chen et al., *Acta Orthop Belg*, 79(1):54–59, 2013

# PROXIMAL FEMUR FRACTURE RISK ASSESSMENT USING FINITE ELEMENT METHOD SIMULATIONS

Ariel F. Pascaner (1), Francesca Rotini (1), Stefania Marconi (1), Amir Sternheim (2)(3), Zohar Yosibash (4), Alessandro Reali (1), Michele Conti (1), Ferdinando Auricchio (1)

1. Civil Engineering and Architecture Department, Università degli Studi di Pavia, Pavia, Italy; 2. National Unit of Orthopaedic Oncology, Tel-Aviv Medical Center, Tel-Aviv, Israel; 3. Tel-Aviv University, Sackler Faculty of Medicine, Ramat Aviv, Israel; 4. Computational Mechanics and Experimental Biomechanics Lab, School of Mechanical Engineering, The Iby and Aladar Fleischman Faculty of Engineering, Tel-Aviv University, Ramat-Aviv, Israel.

## Background

Bones' tumor metastasis is a disease with very high incidence (approximately one third of all cancers), being the proximal femur the most common site. Osteolytic metastases may cause pathological fractures of the bone, in which case life expectancy is less than one year following the fracture [1]. This work aimed at developing a framework for the assessment of patient-specific risk of fracture using finite element method (FEM) simulations, which would assist in surgical planning and optimized prosthetics design.

## Materials and methods

Left and right femurs of a female patient (age: 57 years old, weight: 60 kg) with a proximal bone tumor were automatically segmented from the CT scan using Simfini Software [2] (Figure 1, left). High-order volumetric tetrahedral meshes were generated from the segmentations (approximately 70k elements each) and material properties were computed from the CT Hounsfield Units (Figure 1, center). For each geometry, we performed a FEM simulation with the Mechanical APDL modulus of Ansys 2022 R2, using the following boundary conditions. The most distal slice of the mesh was fixed by imposing 0 displacement on all the degrees of freedom of all nodes. A force was applied on the femoral surface in the direction defined between the head center and the intercondylar notch. The magnitude of the force was computed as 2.5 times the weight of the patient (1470 N) and it was distributed among the nodes within an 11 mm diameter circle on the top of the femoral head. Maximum total displacement and

maximum compression strain (E3) were assessed, being the latter an indicator of fracture risk.

## Results

Simulations were performed using an Intel Core i7-11370H processor @3.30 GHz, with 32 GB of RAM. Table 1 shows the maximum total displacement and maximum compression strain (E3) for the left and right femurs. An increased maximum compression strain was observed on the right femur (-4414  $\mu$ S vs -3863  $\mu$ S), corresponding to the location of the tumor, evidencing a high risk of fracture. The obtained values are consistent with the literature [3], where *ex-vivo* validation of the FEM simulations was conducted.

Femur	Max. displacement [mm]	Max. compression strain (E3) [ $\mu$ S]
Left	5.58	-3863
Right	5.84	-4414

Table 1: Maximum total displacement and compression strain (E3) obtained for both femurs.

## Conclusion

In this work, we performed FEM simulations of the femurs of a patient with bone cancer, showing an increased compression strain on the tumorous femur, which is a sign of high fracture risk. Adequate surgical planning is crucial in these types of tumors, given the short survival after pathological fractures. The information extracted from a CT scan allows the generation of 3D bone models, which can be then used to simulate virtual implantation of prosthetics, assisting surgeons in the decision-making process. Further work should be done to achieve optimized patient-specific prosthetics design, allowing the fabrication of long lasting implants.

## References

1. M. J. Parker et al, Hip Hint: J Clin Exp Res Hip Pathol Ther, 21(5):526-530, 2011.
2. Z. Yosibash et al, Comput Math, 80(11):2417-2432, 2020.
3. Y. Katz et al, Clin Biomech, 77:1-11, 2020.

## Acknowledgements

This work was supported by "AIO – AI for Orthopedics" project, funded by MAECI (Italy) and MOST (Israel).

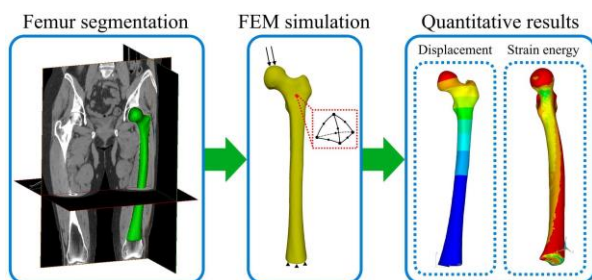


Figure 1: Workflow consisting of: femur automatic segmentation from the CT scan, generation of the 3D high-order tetrahedral mesh and FEM simulation to obtain quantitative results.

Day 2  
Cardiovascular biomechanics  
*Oral presentations*

Torino, 19 September 2023



# SEGMENTATION OF THORACIC AORTA 3D PC-MRI DATASET THROUGH SYNTHETIC DATA AUGMENTATION

Simone Garzia (1,2), Martino Andrea Scarpolini (1,3), Marilena Mazzoli (1,2), Simona Celi (1)

1. BioCardioLab, Fondazione Toscana G. Monasterio, Massa, Italy; 2. Department of Information Engineering, University of Pisa, Pisa, Italy; 3. Department of Industrial Engineering, University of Rome "Tor Vergata", Roma, Italy

## Introduction

Phase contrast magnetic resonance imaging (PC-MRI) is a modern non-ionizing imaging technique, capable of providing functional and morphological information, as well as supporting computational modellings. Segmentation of 3D PC-MRI is usually a complex and time-consuming process. In the literature, several studies leveraged neural networks (NN) to perform segmentation by using large image datasets [1]. However, the complex data post-processing and limited availability of patients' images for research purposes make the training of the NN challenging. This work aims investigating the feasibility of a pipeline for generating synthetic thoracic aorta PC-MRI data to expand the limited dataset of patient-specific images, thus improving the accuracy of neural NN even with a small real dataset.

## Materials and Methods

Synthetic high-resolution (HR) 4D velocity images were created by analysing 250 computational fluid dynamic velocity (CFD) maps from two different scanners (Philips and GE). To generate high-fidelity low resolution (LR) images, a specific pipeline was developed. First, a statistical shape model [2] was used to synthesize new artificial geometries so that improving data numerosity and variability. Secondly, transient CFD simulations were performed in OpenFOAM by prescribing patient-specific boundary conditions: a 2D velocity profile at the inlet, and a 3-element Windkessel model at each outlet. Next, a fast Fourier transform (FFT) was performed with a high-frequency truncation and addition of zero-mean white gaussian noise [3]. Finally, an inverse FFT was applied to revert data to the spatial domain and final volumes were obtained using the PC magnetic resonance angiography (PC-MRA) formula. A specific 3D U-Net was set up and trained with different combinations of real and synthetic data namely *Synth<sub>40/50</sub>*, *Synth<sub>40/100</sub>*, *Synth<sub>40/250</sub>*, with respect to the only real data case (*No\_Synth*). A total of 10 real PC-MRA were used as the test set and the effect on the DICE score (DS) was evaluated.

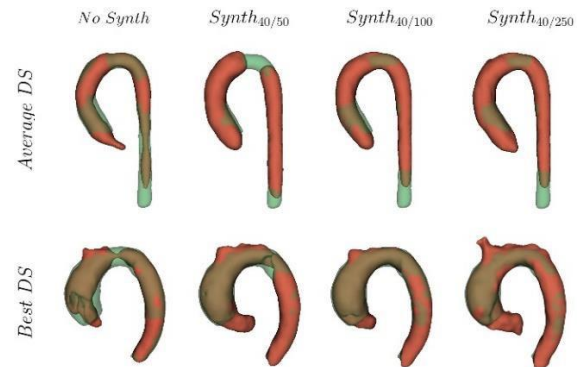


Figure 1: Comparison among different experiment reporting the average, and best results. The ground truth is displayed in green, and the predicted segmentation is in red.

## Results

Table 1 shows a DS value of 0.83 for synthetic augmented experiment with respect to the *No\_Synth* case (DS = 0.65) and a significative reduction in the standard deviation (SD). A higher accuracy and a better target reconstruction are also visible in Figure 1.

Method	Volume_R	Volume_S	DS	SD
<i>No_Synth</i>	40	0	0.65	0.10
<i>Synth<sub>40/50</sub></i>	40	50	0.81	0.05
<i>Synth<sub>40/100</sub></i>	40	100	0.83	0.03
<i>Synth<sub>40/250</sub></i>	40	250	0.82	0.02

Table 1: DICE scores. N.B: *Volume\_R* = Real volumes, *Volume\_S* = Synthetic volumes

## Discussion and Conclusion

Results suggest the advantages of adopting synthetic data augmentation for the 3D U-Net such as the ability to increase the dataset in terms of numerosity and variability, thus improving the segmentation accuracy.

## References

- Berhane et al, Magn Reson Med, 84(4): 2204-2218, 2020.
- Scarpolini MA et al, ESB-ITA, p. 13, 2022.
- Ferdian, E et al, Front. Physics 138, 2020.

## Acknowledgements

This work was supported by the MeDiTaTe Project from the European Union's Horizon 2020 research and innovation programme under Grant Agreement 859836.



# A NEW 3D-DERIVED INDEX TO PREDICT THE DEFORMATIONAL BEHAVIOR OF AORTA IN FENESTRATED EVAR

Laura Cercenelli<sup>1</sup>, Stefano Deidda<sup>1</sup>, Antonino Logiacco<sup>2</sup>, Barbara Bortolani<sup>1</sup>, Camilla Gironi<sup>1</sup>, Mauro Gargiulo<sup>2</sup>, Emanuela Marcelli<sup>1</sup>

1. eDIMES Lab-Laboratory of Bioengineering, Department of Medical and Surgical Sciences, University of Bologna, Italy; 2. Vascular Surgery Unit, IRCCS Azienda Ospedaliero-Universitaria di Bologna, Italy

## Background

The introduction of fenestrated endografts (fEVAR) enabled endovascular treatment of short-necked, juxtarenal, and suprarenal abdominal aortic aneurysm (AAAs) [1]. Endograft implantation in the target visceral vessels (TVVs) influences arterial angle and curvature after fenestrated EVAR positioning [2]. This altered anatomy could potentially kink the stented target vessel and strain the endograft, thus leading to post-operative complications that require reinterventions [3]. The exact influence of endograft implantation on aortic anatomy and the endograft changes after complex endovascular treatments remain unknown [4].

The aim of the study is to analyze the morphological changes of the aortic and TVVs anatomy after fEVAR endografting, using three-dimensional (3D) virtual modeling and a novel index computed on 3D anatomical reconstructions.

## Materials and Methods

For the study, a total of 11 patients who underwent fEVAR at IRCCS Azienda Ospedaliero-Universitaria di Bologna were selected. The cases were divided into: “Instability” group (n=6): patients presenting post-EVAR type III endoleak verified at follow-up imaging; “Control” group (n=5): patients free from type III endoleak at follow-up.

Computed Tomography Angiography (CTA) scans of the patients were digitally processed to generate 3D reconstructions of the aortic anatomy using D2P® software (Oqton, San Francisco, California, US). For both groups, the 3D model was reconstructed at the pre-operative stage (T<sub>-1</sub>), at the immediate post-operative stage (T<sub>0</sub>), and at 3-12 months follow-up (T<sub>1</sub>). The central lumen line (CLL) for the aorta (AO) and the TVVs were automatically extracted from the 3D model (Figure 1).

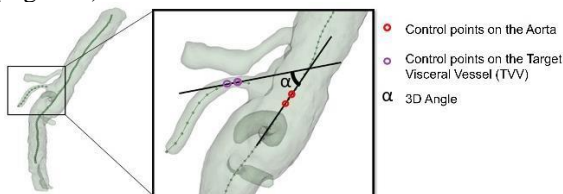


Figure 1: 3D model reconstruction with extracted CLL for AO and TVVs, and the calculated AO-TVV angle.

Then, each CLL was sampled via control points, identified with x,y,z spatial coordinates. All automatic processing was implemented in 3DSlicer software. The angle between the AO and the TVV of interest (AO-

TVV angle,  $\alpha$ ) was calculated between two straight lines passing through two selected control points of the AO and TVV (Figure 1), for all 11 patients at T<sub>-1</sub>, T<sub>0</sub>, T<sub>1</sub>.

## Results

The endograft implantation introduces a variation in the amplitude of the AO-TVV angle. In the Control group, an increase in amplitude from the pre-operative (T<sub>-1</sub>) to the immediate post-operative stage (T<sub>0</sub>) is always followed by a further increase in amplitude at follow-up (T<sub>1</sub>). Similarly, a decrease at T<sub>0</sub> always corresponds to a further decrease at T<sub>1</sub> (Figure 2a). Conversely, in the Instability group, a variation in AO-TVV angle amplitude from T<sub>-1</sub> to T<sub>0</sub> is always followed by a variation in the opposite direction at T<sub>1</sub> (Figure 2b).

The percentage variations of the AO-TVV angle obtained for all patients in the two groups are reported in Figure 2.

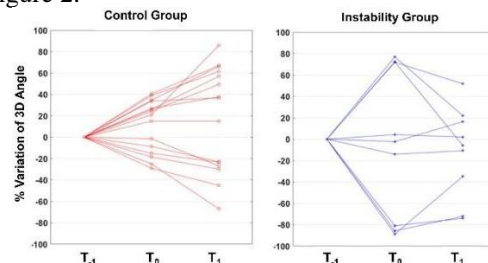


Figure 2: Percentage variations of the AO-TVV angle from T<sub>-1</sub> (reference) to T<sub>0</sub> and T<sub>1</sub>.

## Discussion

This work has defined a new method of evaluating the deformational behavior of the aortic anatomy after fEVAR. We have introduced the automatic calculation of the angle between the AO and TVVs starting from 3D reconstructions obtained from patient imaging. The new 3D-derived angle is attributable to a clearly different behavior for the two groups: a monotonous ascending or descending trend for the Control group, and an inverting trend over time for the Instability group. These findings suggest the role that the AO-TVV angle may have in predicting instability, therefore in optimizing patient surveillance protocols. As major limitations: the study report results from a small sample size; only one type of fEVAR endograft was considered; and time for follow-up CTA is not standardized for all patients.

## References

1. De Niet A. et al, Surg Technol Int 29: 220–230, 2016.
2. Keschenau PR. et al, J Endovasc Ther, 27(3):445–451, 2020.
3. Gallitto E. et al, J Vasc Surg, 74(6):1808–1816, 2021.
4. Oshin O.A. et al, J Endovasc Ther, 18(4):569–575, 2011.



# BEYOND THE STANDARD: HOW DO THE CHARACTERISTIC OF THE AORTIC CONDUIT AFFECT THE PERFORMANCES OF HEART VALVES

Arianna Callera (1), Marco Contino (1), Roberto Frassine (1), Maria Laura Costantino (1), Francesco De Gaetano (1)

1. Department of Chemistry, Material and Chemical Engineering, Politecnico di Milano, Milan, Italy

## Introduction

When approaching the design and testing of a new heart valve prosthesis, the first step is the ISO 5840:2021[1]; in this Standard all needed information for pre-clinical and clinical trials is provided. In particular a pulsatile test is required to assess the hydrodynamic performances of the valve. While several requirements are listed there isn't a guide on which characteristics the conduits replicating the vessels should have. In the authors opinion this could be particularly inappropriate for the conduit downstream the aortic valve that should model the aorta but is often reduced to a straight and rigid conduit. This work concerns itself with modifying this conduit to introduce first the geometry, characterized by the Valsalva sinuses, and then the ascending aorta's compliance.

## Methods

To obtain the aortic phantom 3D printing was exploited. In order to print a physiological-like conduit a complete characterization was performed on the selected Elastic 50 A resin from Formlabs. The characterization included but was not limited to: tensile tests on samples differently oriented during printing, cyclic test, swelling and aging tests.

A previously developed pulse duplicator (Figure 1) [1], was modified implementing three different types of conduit downstream of the aortic valve: rigid and straight conduit, rigid conduit with Valsalva sinuses, compliant conduit with Valsalva sinuses. The pulsatile tests were performed on these three different set-ups; in each set up a mechanical, a polymeric, and a biological valve were tested.

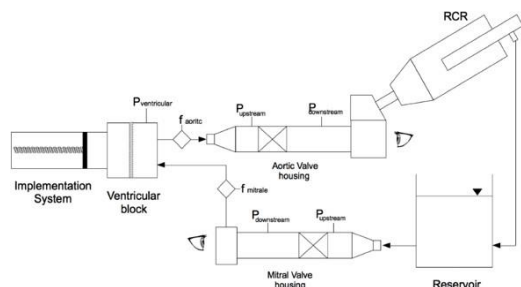


Figure 1: Schematic representation of the pulse duplicator used in this work

## Results

From the material characterization we found that a conduit with 1.82 mm thickness would show the correct compliance; this conduit would also be able to withstand

the pulsatile test. From the aging test we concluded that tests should be carried out in 5 days maximum to avoid the alteration of properties.

From the pulsatile test emerged that the introduction of the Valsalva sinuses led to a decrease in regurgitation (Table 1), and an increase in MSPD. The compliance instead provoked a decrease in the MSPD and, consequently, of the EOA (Table 2), but led to an increase in regurgitation.

Regurgitation	Mechanical	Polymeric	Biological
Standard	14.49	6.46	12.65
Rigid sinuses	8.60	5.57	13.50
Compliant sinuses	19.77	8.93	18.49

Table 1: Regurgitation results for each of the tested conditions

EOA	Mechanical	Polymeric	Biological
Standard	$0.79 \pm 0.09$	$1.35 \pm 0.21$	$1.13 \pm 0.23$
Rigid sinuses	$0.57 \pm 0.01$	$1.47 \pm 0.29$	$1.08 \pm 0.08$
Compliant sinuses	$0.90 \pm 0.11$	$1.10 \pm 0.11$	$1.04 \pm 0.36$

Table 2: EOA results for each of the tested conditions.

## Discussion

We proved the feasibility of fabricating an aortic phantom with 3D printing even if the time-dependent behavior remains a major drawback of this material.

The presence of the Valsalva sinuses introduced, as expected from theory, the formation of vortices that aid the closure of the valve, reducing regurgitation. The increase in MSPD can be explained by the fact that, in order to keep the diameter downstream the sinuses at 34 mm and respect the anatomical ratios, the diameter upstream the sinuses is of 27 mm. When the compliance is introduced, the effect is mitigated from the deformability of the conduit. Since the conduit deforms and recoils at each cycle, during recoil a backflow is generated, increasing regurgitation of the valves

## References

1. F. De Gaetano et al, International Journal of Artificial Organs, vol. 38, n. 11, 2015..



# VORTICITY TRANSPORT IN ABDOMINAL AORTIC ANEURYSMS WITH FOLLOW UP

Valentina Mazzi (1), Karol Calò (1), Christian Vergara (2),  
Maurizio Domanin (3), Diego Gallo (1), Umberto Morbiducci (1)

1. Polito<sup>BIO</sup>Med Lab, Department of Mechanical and Aerospace Engineering, Politecnico di Torino, Italy;  
2. Labs, Dipartimento di Chimica, Materiali e Ingegneria Chimica "Giulio Natta", Politecnico di Milano, Milan, Italy; 3. Unit of Vascular Surgery, I.R.C.C.S. Fondazione Cà Granda Policlinico Milano, Milan, Italy.

## Introduction

Local blood flow disturbances play a key role in progression of the Abdominal Aortic Aneurysm (AAA), because they alter transport of biochemicals and fluid-wall interactions [1]. Therefore, a multitude of hemodynamic quantities has been proposed over the years to provide biomechanical markers of AAA evolution. However, these proposed quantities often fail in predicting aneurysm wall pathophysiology and remodeling, and in discriminating rupture risk based on hemodynamics. These results suggest that a different perspective to explore richness of fluid structures in AAAs is needed. Starting from the observation that the dynamics of large-scale vortices dominates the AAA hemodynamics, we propose a thorough characterization of the complex vortex structures produced and transported in the AAA, aiming at identifying vorticity-based quantities to be tested as potential markers of AAA progression, based on longitudinal data.

## Methods

The lumen and the intraluminal thrombus (ILT) of three AAAs with their two years follow-up were reconstructed from CT-scan data. CFD was used to numerically solve the governing equations of fluid motion, using the finite element open-source code SimVascular [2]. The results from CFD simulations were used to quantify the vorticity transport equation:

$$\frac{D\boldsymbol{\omega}}{Dt} = (\boldsymbol{\omega} \cdot \nabla)\mathbf{u} + \nu\Delta\boldsymbol{\omega} \quad (1)$$

where  $\mathbf{u}$  is the velocity vector,  $\boldsymbol{\omega}$  is the vorticity vector and  $\nu$  is the kinematic viscosity. The material derivative of the vorticity is given by the contribution of a stretching term (first term on the right side), quantifying the vortex lengthening due to velocity gradients, and of a term quantifying vorticity diffusion due to viscosity (second term on the right side). The vortex dynamics was here analyzed also in terms of the local swirling strength ( $\lambda_{ci}$ ).

## Results

Examples of instantaneous volumetric maps of the vorticity stretching term after systolic peak and at mid-diastole are presented in Figure 1 together with the time-histories of the volume-average values of the stretching term and of the swirling strength for one explanatory model and its two-years follow-up model. Both at baseline and at follow up, the AAA inflow jet rolls up

into vortex rings transported inside the expansion region by the experienced pressure-gradient. Such vortex rings undergo stretching and tilting along the systolic deceleration phase and break-up in smaller vortical structures in diastole in the distal part of AAA sac in correspondence of the greatest ILT growth over time (gray arrows in Figure 1A). The vorticity in the AAA at baseline exhibits higher stretching and swirling strength than at follow-up, suggesting that those quantities may have contributed to AAA growth (Figure 1B).

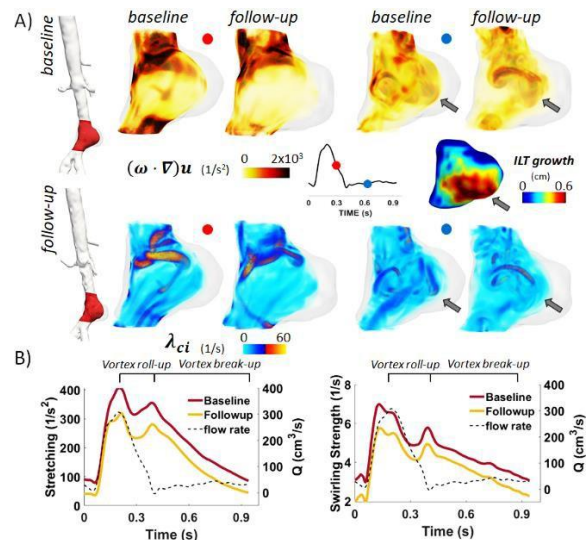


Figure 1: A) Volumetric maps and B) time-histories of the volume-average value of swirling strength and stretching in a AAA model and its two-years follow-up.

## Discussion

In this study, a vorticity transport-based analysis is proposed on computational hemodynamics models of AAA, aiming at deciphering their intricate hemodynamics in a longitudinal investigation. A deeper understanding and interpretation of vorticity transport in AAAs could contribute to elucidate the role of flow disturbances in ILT formation, platelets dynamics, and inflammatory mechanisms [3], and in general of those hemodynamics-driven processes underlying AAA progression, potentially improving risk assessment and the clinical management of AAA patients.

## References

1. Arzani, A et al., Phys Fluids, 24(8), 2012
2. Updegrave et al, Ann. Biomed Eng, 45(3):525-541, 2016
3. Biasseti, et al., J. R. Soc. Interface, 8:1449-1461, 2011



Day 2  
Medical devices and therapies  
*Oral presentations*

Torino, 19 September 2023



# TOWARD A NEW PRINTABLE AND CUSTOMIZABLE AIRWAY STENT

Jusús Zurita Gabasa (1), Carmen Sánchez Matás (2), Cristina Díaz Jiménez (3), José Luis López Villalobos (4), Mauro Malvè (1)

1. Public University of Navarre (UPNA), Pamplona, Spain; 2. Department of Thoracic Surgery, University Hospital 'La Paz', Madrid, Spain; 3. Asociación de la Industria Navarra (AIN), Pamplona, Spain; 4. Department of Thoracic Surgery, University Hospital 'Virgen del Rocío', Sevilla, Spain

## Introduction

Tracheobronchial stents are tubular scaffolds used for enlarging a constricted airway. However, their placement is affected by several clinical problems. These prostheses should be easy to be inserted and eventually removed; they should avoid migration and be biocompatible [1]. Additionally, they should adapt to the airway and possibly be customizable to the patient [2]. In this sense, the three dimensional (3D) printing offers new opportunities that could help the clinics allowing rapid prototyping and fabrication of image-based and patient-specific anatomical shapes [1]. The goal of this work is to simulate and fabricate a new customizable and printable tracheobronchial prosthesis. With this aim, we proposed a parametric numerical tool capable of analysing the importance of each single parameter.

## Methods

The baseline stent model created with the in-house tool is shown in Figure 1a and 1b. The outer surface of the tube was designed with an additional upward reinforcing structure that is similar to the typical X-pattern of the metallic stents. The geometry of the stent has been parameterized in order to study the effect of each single geometrical feature on the mechanical properties. Through modulating the different parameters in fact, the radial stiffness and the mechanical strength of the stent can be manipulated. Briefly, the inner radius, the stent thickness, the dimensions of the reinforcing fibres and their orientation can be changed. The in house code produces an input file for Ansys Mechanical (Ansys Inc., Canonsburg, PA, USA) in which the numerical analysis is carried out (Figure 1b).

## Results

In Figure 1b, the stiffness of selected prosthesis configurations is compared. The plotted curves illustrate that different radial stiffness can be obtained, modulating the different parameters in which the prosthesis has been designed. For example, for a fixed configuration of the external fibres, the stiffness of the prosthesis with a thickness of 0.75 mm (black line with squares) can be obtained with a reduced thickness of 0.5 mm and a thicker fibre bottom width of 2 mm. Additionally, the same stiffness could be also obtained using a fibre bottom width of 3 mm and a ratio between upper and bottom fibre thickness of 0.5 (green line with triangles). The computational results were

validated by means of a parallel experimental work that includes the production of selected stent configurations using the 3D printing technology (Figure 1c and 1d), their compressive test using an Advanced Digital Force Gauge (Mecmesin, Slinfold, UK) and their numerical simulation.

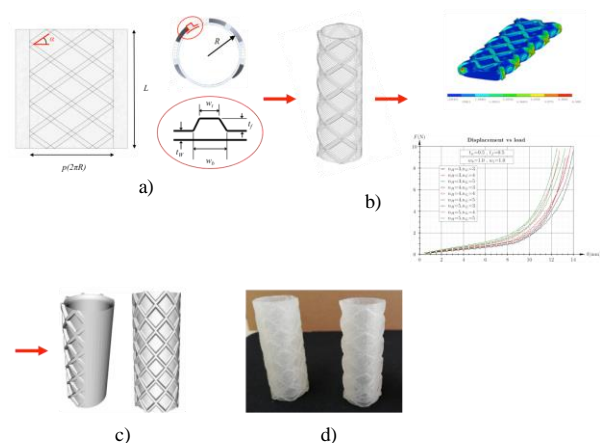


Figure 1: a) and b) baseline model and main parameters; b) numerical analysis for obtaining the mechanical properties; c) optimized geometrical models; d) 3D printed prostheses.

## Discussion

Progress towards the customization of commercial airway stents has been made in the recent years. However, the offered personalization is related only to few dimensions under request to the fabricant. In many cases, the use of customized commercial prosthesis could be a good compromise, but frequently this is not sufficient [1]. The methodology proposed in this study offers the possibility of addressing some of these limitations. For instance, the thickness of the stent can be reduced by adequately increasing the external fibres thickness. This aspect has important applications to the stent design, as the obstruction and mucus plugging is one of the more frequent problems after the surgery and it is caused by the thickness of the prosthesis.

## References

1. Guilbert, N. et al., *Respirology*, 25:953-962, 2020.
2. Xu, J. et al., *Drug Dev. Ind. Pharm.*, 45:1-10, 2019.

## Acknowledgements

The authors are supported by grant PID2021-125731OB-C31 from MCIN/AEI/10.13039/501100011033/ and FEDER ('A way to build Europe').



# MULTISCALE MODELING TO SIMULATE VASCULAR ADAPTATION PROCESSES

Anna Corti (1), Matilde Marradi (1), Jose F. Rodriguez Matas (1), Claudio Chiastra (2)

1. LaBS, Dept. of Chemistry, Materials and Chemical Engineering "Giulio Natta", Politecnico di Milano, Milan, Italy; 2. PoliTo<sup>BIO</sup>Med Lab, Dept. of Mechanical and Aerospace Engineering, Politecnico di Torino, Turin, Italy

## Introduction

The thorough understanding of vascular adaptation processes in atherosclerosis and restenosis is lacking. Multiscale agent-based modeling frameworks, integrating both continuum and discrete approaches, have recently emerged as promising mechanobiological models to capture the multiscale and multifactorial network of events underlying those diseases, which are characterized by the interplay between biomechanical forces, cellular behavior, and molecular pathways [1]. Our research group has recently developed a multiscale agent-based modeling framework, which has been used to study atherosclerosis [2], restenosis after percutaneous transluminal angioplasty (PTA) and in-stent restenosis [3,4]. Herein, a novel patient-specific framework of restenosis after PTA is proposed to capture the remodeling process in response to the PTA-induced damage and perturbed hemodynamics.

## Methods

Figure 1 shows the main steps of the developed multiscale framework of restenosis following PTA, applied to a patient-specific diseased femoral artery for a follow-up time of 2 months.

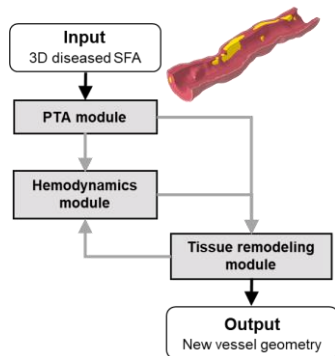


Figure 1: Multiscale framework

The framework consists of a PTA, a hemodynamics, and a tissue remodeling module. Within the PTA module, a finite element analysis of balloon expansion was performed and the post-PTA arterial configuration and damage were determined. Hyperelasticity was considered to model the arterial wall tissues [5] and a damage model with element deletion strategy was implemented to simulate the damage and arterial wall laceration experienced during the intervention. Within the hemodynamics module, steady-state computational fluid dynamics simulations were performed and the wall shear stress (WSS) was computed. Within the tissue remodeling module, (i) a 2D agent-based model (ABM)

of 11 evenly-spaced cross-sections simulated cellular dynamics driving the arterial wall remodeling in response to the PTA-induced wall damage and post-operative WSS, and (ii) the 3D arterial lumen geometry was reconstructed from the ABM outputs. After 1 month, the hemodynamics and tissue remodeling modules were coupled to update the WSS input to the cellular activities.

## Results

Figure 2 shows details of the damage and WSS maps at day 0, driving the 2-month ABM evolution of 3 explanatory vessel planes. The ABM at day 0 embedded the damage-induced laceration. At month 2, the intimal growth was mainly observed at regions with elevated damage levels and low WSS: the lacerations were filled and a median restenosis of 25% was obtained at 2 months, with the greatest reduction in lumen area occurring during the first post-operative month.

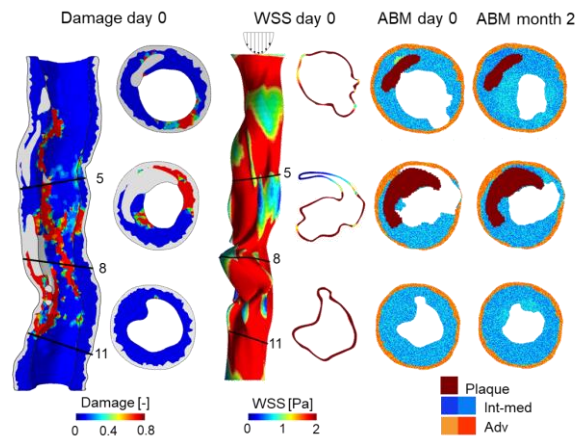


Figure 2: Arterial wall remodeling following PTA

## Conclusions

By showing the application of the framework to the study restenosis following PTA in a patient-specific scenario, this work demonstrates the potentiality of this hybrid, multiscale, multifactorial and systems biology approach to capture the mechanobiological mechanisms underlying vascular adaptation.

## References

1. Corti et al., Front Bioeng Biotechnol, 9:744560, 2021.
2. Corti et al., Comput Biol Med. 118:103623, 2020.
3. Corti et al., J R Soc Interface. 19(188):20210871, 2022.
4. Corti et al., J R Soc Interface. 20:20220876, 2023.
5. Cunnane et al., Acta Biomater. 11, 295–303, 2015.



# TRANSCATHETER HEART VALVE IN TRANSCATHETER HEART VALVE: A COMPUTATIONAL STUDY

Roberta Scuoppo (1), Stefano Cannata (2), Caterina Gandolfo (2), Salvatore Pasta (1,4)

1. Dipartimento di Ingegneria, viale delle Scienze Ed.8, University of Palermo, Italy

2. Interventional Cardiology Unit, IRCCS ISMETT via Tricomi, 5, Italy

3. Department of Research, IRCCS ISMETT via Tricomi, 5, Italy

## Introduction

Transcatheter aortic valve implantation (TAVI) is increasingly used to treat patients with severe aortic stenosis (AS) who are deemed inoperable or at high risk for surgical aortic valve repair. Thus, even in the absence of concerns about transcatheter aortic valve (TAV) durability, a substantial proportion of contemporary TAVI patients are expected to live sufficiently long to experience the degeneration and failure of TAV. In the case of device's failure, the therapeutic option for the treatment of structural TAV degeneration are limited to open-heart surgery and redo-TAVI (or TAV-in-TAV) [1].

This study aimed to develop a computational framework to simulate TAV-in-TAV as clinically performed in one patient with early failure of the implanted device. Patient-specific computational modelling was carried out to determine structural metrics of delivered devices while a parametric analysis of the implantation depth of the second TAVI procedure was performed to assess the impact of the relative device position [2].

## Materials and methods

A 68-years old gentleman with severe AS was initially treated with a 23-mm SAPIEN 3 Ultra TAV at IRCCS ISMETT in 2019. After 3-year from TAVI, the device failure was treated by redo-TAVI with a 29-mm Evolut Pro device.

Pre-TAVI CT images were processed in Mimics (v.21, Materialize, Belgium) to reconstruct the aortic root anatomy and calcific plaques using semi-automatic thresholding. Since native valve leaflet were not clearly visible at CT scan, a parametric modelling approach was adopted generate the leaflet geometry using anatomic measurements and the CAD tool Rhinoceros (Rhinoceros v.7, McNeel & associates, USA). Once segmented regions were obtained, they were meshed using ICEM meshing software (v2021, ANSYS Inc., USA). Neo-Hookean models were adopted for both the aortic valve and native valve leaflets. The calcification had a linear-elastic model. Geometrical models of 23-mm SAPIEN 3 Ultra and 29-mm Evolut PRO device frames were obtained by reverse engineering of micro-CT images. Numerical analysis of the redo-TAVI procedure was developed in Abaqus/Explicit (v2021hf7, Dassault Systèmes, USA) using mass-scaling.

A parametric analysis of the TAV-in-TAV procedure was carried out by varying the implantation depth and device size with respect to the baseline model. Eccentricity and expansion indexes were calculated

from both TAVI CT and redo-TAVI CT images and then compared to those predicted by computational analysis.

## Results

Expansion index was used to quantify the level of agreement between FEA and CT images. Predictions of expansion index were in good agreement with CT-based measurements (ie, ie,  $120.8 \pm 10\%$  for CT-based measured of S3 versus  $96.5 \pm 14\%$  for numerical-based measured of S3, while  $90.6 \pm 13\%$  for CT-based measured of Evolut Pro versus  $79.2 \pm 21\%$  for numerical-based measured of Evolut Pro).

Figure 1 illustrates the TAV-in-TAV deformed configurations for the four scenarios with different implantation depth or device overexpansion.

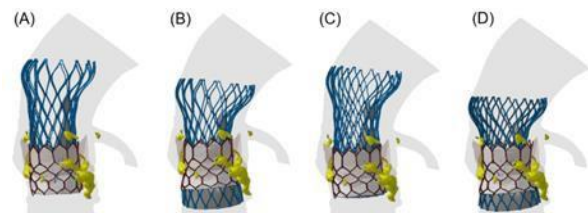


Figure 1 (A) reference TAV-in-TAV as done clinically, (B) low redo-TAVI, (C) high redo-TAVI and (D) TAV-in-TAV overexpansion.

## Discussion

To the best of our knowledge, this is the first computational study evaluating the structural mechanics of TAV-in-TAV. We first simulated the TAV-in-TAV according to the implantation depth and device size indicated by the Heart Team, and then carried out a parametric analysis varying these device parameters. Future computational flow studies will be undertaken to explore whether the parametrically-derived TAV-in-TAV shapes may lead to coronary flow obstruction and thus adverse events.

Moreover, simulations were used to explore the efficacy and safety of TAVI in young and high-risk patients, which are not conventionally treated with TAVs.

## References

1. Gallo M et al, European Journal of Cardio-Thoracic Surgery, 61(5): 967-76, 2022.
2. Pasta S et al, Artif Organs, 41(9): E92-E102, 2017.

## Acknowledgements

This project has received funding from the European Union's Horizon 2020 research and innovation programme under grant agreement No 101017523.



# USE OF HIGH-FIDELITY PATIENT-SPECIFIC NUMERICAL SIMULATIONS TO PREDICT SHORT-TERM TEVAR OUTCOME

Anna Ramella (1), Francesco Migliavacca (1), Jose F Rodriguez Matas (1), Tim J Mandigers (2), Daniele Bissacco (2), Maurizio Domanin (2,3), Robin H Heijmen (4), Santi Trimarchi (2,3), Giulia Luraghi (1)

1. Politecnico di Milano, Italy; 2. Fondazione IRCCS Ca' Granda Ospedale Maggiore Policlinico, Milan, Italy; 3. Università degli Studi di Milano, Italy; 4. Radboud University Medical Center, Nijmegen, Netherlands

## Introduction

Thoracic Endovascular Aortic Repair (TEVAR) is a minimally invasive technique used to treat various thoracic aortic pathologies, such as aneurysms, ulcerations, or dissections. It has demonstrated superior patient outcomes in comparison to open surgical repair since the Food and Drug Administration (FDA) authorized the first stent-graft in 2005 [1].

In the literature, computational models are widely adopted to analyze the behavior of stent-grafts in the post-TEVAR scenario, as they can provide valuable insights into device performance and aid clinicians in their decision-making. This study aims to employ a validated finite element (FE) methodology to reproduce the TEVAR procedure with a commercial stent-graft on patient-specific aortic anatomies. The outcomes of the simulations are also compared with short-term (<3 months) postoperative CT data.

## Methods

Based on a previously validated methodology from our laboratory [2], FE models of commercial Valiant Captivia stent-grafts (Medtronic Inc.) were generated. Experimental crimping tests were performed on the device to calibrate the shape memory Nitinol (stent) and fabric PET (graft) material parameters and to validate the device models. The stent was discretized with beam elements and the graft with triangular membrane elements. The TEVAR procedure was validated in idealized and patient-specific rigid aortas by comparing the FE simulation results with an ad-hoc experimental set-up (performed under CT). The same numerical methodology was then applied to reproduce the stent-graft implantation in four patient-specific aortic anatomies segmented from preoperative CT images [3]. The aorta is modelled as an isotropic hyperelastic material, and the wall prestress due to blood pressure is considered. The vessel was discretized in ANSA (BETA CAE System) with three layers of tetrahedral elements. Postoperative CT images were used to determine the appropriate device size and landing zone for each patient. As further validation to assess the quality of the simulation, a comparison of the simulation results with the stent segmented from short-term postoperative CT scan was performed.

The simulations were carried out using the explicit FE LS-Dyna solver (Ansys Inc.).

## Results

Fig.1-a. shows the four aortic anatomies reconstructed from preoperative CT images using VMTK (Orobix Srl.). For each anatomy, the last instant of the patient-

specific FE simulations (deployed configuration) and the comparison between the stent reconstructed from CT images and the simulated one are reported in Fig.1-b. and 1-c., respectively.

Globally, the opening area errors between the simulated and segmented stent configurations are below 10%, lower with respect to other literature studies in which errors reached 30% [4].

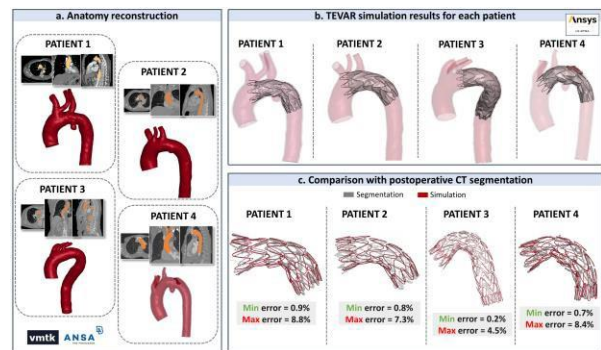


Figure 1: (a.) aortic anatomies segmented from preoperative CT images; (b.) TEVAR simulation outcomes for each anatomy; (c.) Overlap of the simulation results (red) with stent segmented from postoperative CT (grey). Max and min errors in opening areas of each stent strut are reported.

## Discussion

The proposed methodology follows the V&V40 guidelines to develop high-fidelity stent-graft models and TEVAR simulations: after proper material calibration and simulation validation, the applicability of the model for patient-specific simulations is proved [3]. The comparison of the simulation results with the stent reconstructed from postoperative CT images reveals that the numerical model can predict the short-term outcome of the TEVAR procedure with good accuracy, given the uncertainties of the biological and clinical data. This suggests that the numerical model can be employed during the preprocedural planning phase as it can help in understanding the outcomes of the procedure in a realistic scenario before the actual clinical intervention.

## References

1. Daye et al, Cardio Diagn & Ther, 8:S138, 2018.
2. Ramella et al, Ann Biomed Eng, 50(12):1941-1953, 2022.
3. Ramella et al, J Biomech, 146:111423-111429, 2023.
4. Perrin et al, J Biomech, 48:1868-1875, 2015.

## Acknowledgements

This project has received funding from the MIUR FISRFISR2019\_03221 CECOMES



Day 2  
General Meeting  
*Poster presentations*

Torino, 19 September 2023



# STANDARDIZING SURGICAL MESHES POROSITY ASSESSMENT WITH A NOVEL IMAGE ANALYSIS PROTOCOL

Vincenzo Giacalone (1,2), Vittoria Civilini (1,2), Mara Terzini (1,2)

1. Department of Mechanical and Aerospace Engineering, Politecnico di Torino, 10129 Turin, Italy.

2. Polito<sup>BIO</sup>Med Lab, Politecnico di Torino, 10129 Turin, Italy

## Introduction

Since the introduction of surgical meshes for the treatment of abdominal wall hernia, these devices have proved to be more reliable than direct suture repair [1,2]. Nevertheless, many questions still arise on how the properties of surgical meshes influence the outcome of the surgical procedure. Among them, morphological properties (i.e. pore size and porosity) play a crucial role in the processes of host integration and mesh encapsulation [3,4]. Several methods have attempted to calculate these parameters, however, computational techniques appear hopeful as they are non-destructive and do not deform meshes during measurements, despite computing a 2D porosity [5].

By presenting a precise and reproducible image analysis protocol, this work aims to standardize the computation of textile and effective porosity of surgical meshes.

## Methods

An experimental set-up was designed to acquire images with a sufficient quality for the subsequent postprocessing step (Figure 1). A holder and a bubble level maintain the camera perpendicular to the mesh; a ring light allows constant lighting conditions; a calibration column is used to calibrate the system and a mesh support distances the mesh from the background to enhance the contrast. The last two components were 3D printed for ease of reproducibility.

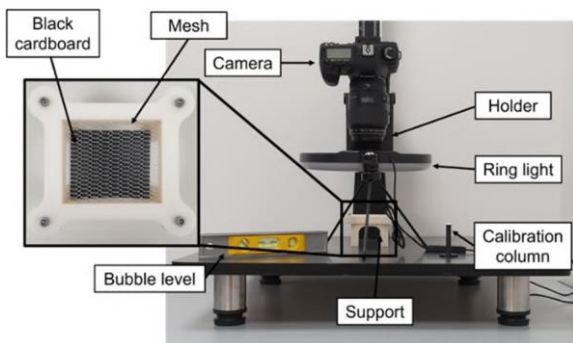


Figure 1 Experimental set-up for image acquisition.

The algorithm for subsequent postprocessing was coded on MATLAB (version R2021b) and includes four phases: (1) calibration, (2) image binarization (Figure 2a) and optimization (sequence of dilatation and erosion functions, Figures 2b and 2c), (3) manual cropping and mask correction (Figure 2d), (4) textile (ratio between the area occupied by pores and the total area of the mesh) and effective (considers only those pores with Feret diameter greater than 1 mm as effective in

reducing scar formation) porosity computation. The algorithm was embedded in a free to use software (*poreScanner*) and tested on meshes from different manufacturers. The computing parameters were tuned using one heavy mesh and one light mesh, because of the different exposure conditions between the two mesh types. Seven samples were finally acquired from 22 different surgical meshes (7 heavy, 6 medium, 9 light) and the intrasubject coefficients of variation (CVs) were computed.

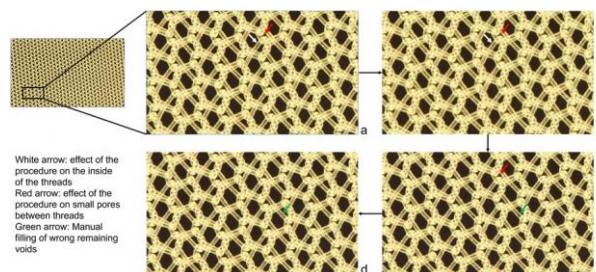


Figure 2 Binarization of the image (a) and processes of dilatation (b), erosion (c) and manual correction (d).

## Results

The intrasubject CVs computed on 22 meshes of different grammage varied between 0.23% and 6.44%, with a median of 1.16%, confirming the protocol repeatability. Additionally, a usability test was conducted on the *poreScanner* software by selecting five individuals who were instructed to read the manual and calculate the porosities of two specific images. The intersubject CV ranged from 0.52% to 1.75%.

## Discussion

The lack of international standards and shared protocols among researchers presents a major challenge in studying surgical meshes. Therefore, it is crucial to establish new methodologies that are easy to replicate, enabling research groups to compare their results effectively. This work aims to meet this need by proposing a reproducible protocol for textile and effective porosity assessment, supported by a MATLAB-based software that is available for free.

## References

1. Aldridge AJ et al, Br J Surg, 88(3):471, 2001.
2. Larson GM et al, Am J Surg, 135(4):559-563, 1978.
3. Conze J et al, Hernia, 8(4):365-372, 2004.
4. Raptis et al., J Surg Res, 169(1):1-6, 2011.
5. Mühl T et al, J Biomed Mater Res – Part B Appl Biomater, 84(1):176-183, 2008.

# MULTI-OBJECTIVE OPTIMIZATION OF BIORESORBABLE WIRE-BRAIDED STENTS

Agnese Lucchetti (1)\*, Dario Carbonaro (2)\*, Thomas Gries (1), Alberto L. Audenino (2), Claudio Chiastra (2), Ted J. Vaughan (3)

1. Institut für Textiltechnik of RWTH Aachen University, Germany; 2. Polito<sup>BIO</sup>Med lab, Politecnico di Torino, Italy; 3. Biomechanics Research Centre (BMEC), School of Engineering, University of Galway, Ireland.

\* The two authors have equally contributed to the study.

## Introduction

Bioresorbable stents are a promising alternative to permanent metallic devices since they naturally degrade and provide vessel support only for the required time, thus avoiding drawbacks in the long-term. Despite the promising results, several design improvements still need to be addressed due to the lower mechanical properties of polymeric bioresorbable stents in comparison to metal devices [1]. Mathematical models were investigated for characterizing the mechanical behavior of metal braided stents, however these models were inadequate to predict the properties of polymer stents due to the excessive simplification of the model assumptions [2]. In this setting, a finite element (FE) based framework is presented for the optimization of the geometry of bioresorbable braided stents in relation to their mechanical performance and associated clinical effectiveness.

## Materials and Methods

The procedure applied for the stent optimization consisted of the following steps: (i) parametric FE modelling of the stent [3] by considering four geometric parameters (i.e., number of wires  $n$ , diameter of the stent  $D_s$ , diameter of the wire  $d$  and braiding angle  $\alpha$ ) (Fig 1a); (ii) FE analysis of the stent crimping with Abaqus/Explicit (Fig 1b) and evaluation of three outputs to measure the device mechanical performance: the radial force at implantation diameter, to determine the stent scaffolding capability, the foreshortening, as indicator for the precise device placement, and the peak maximum principal stress, as a measure for the risk of structural failure of the device; (iii) design parameter sampling simulations using the central composite design scheme; (iv) generation and validations of polynomial surrogate models of the three outputs; (v) identification of optimal stents design candidates by conducting a multi-objective optimization (non-dominated sorting genetic algorithm II) with respect to the four design parameters and three FE outputs. The optimization can be mathematically summarized as:

$$\left\{ \begin{array}{l} \max_{x \in D} f_{RF}(x) \\ \min_{x \in D} f_F(x) \\ f_{MPS}(x) < 150 \text{ MPa} \\ x = [n, d, D_s, \alpha] \\ n \in [24, 48] \text{ with } n \in \mathbb{N} \\ d \in \{0.05 \text{ mm}, 0.075 \text{ mm}, 0.10 \text{ mm}\} \\ D_s \in [4.5 \text{ mm}, 5.5 \text{ mm}] \\ \alpha \in [60^\circ, 70^\circ] \end{array} \right\} \text{ s. t. } D =$$

where the radial force  $f_{RF}$  and the foreshortening  $f_F$  are the two contrasting optimization objectives;  $x$  is the vector of the design parameters; the maximum principal stress  $f_{MPS}$  is accounted as a constraint related to the material yield limit [2];  $D$  is the design space, accounting for the manufacturing constraints.

## Results

Fifteen optimal design candidates were identified, lying on the pareto-front represented in Fig. 1c. Feasible stress values below the yield limit were obtained for all the optimal design candidates. Radial force values of the FE simulations showed a good agreement with experimental studies conducted on the same polymeric bioresorbable stents [2], thus proving the reliability of the numerical model and optimization approach.

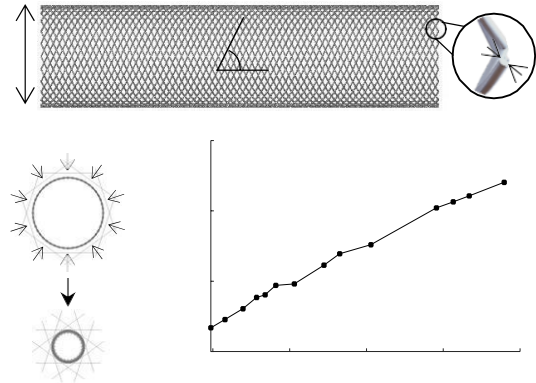


Figure 1: (a) Stent geometry parameters; (b) crimping simulation; (c) pareto-optimal design solutions.

Optimal design	$n$	$D_s$ (mm)	$d$ (mm)	$\alpha$ (°)
1	44	4.5	0.1	60
15	48	4.7	0.1	69

Table 1: Geometrical features of two optimal candidates

## Discussion

A validated computational framework for the optimization of the mechanical performance of bioresorbable braided stents was developed within this study, contributing both to accelerate the device design phase and to increase the effectiveness of the treatment.

## References

1. Wu et al, Expert Rev Med Devices, 18: 351–65, 2021.
2. Lucchetti et al., J Mech Behav Biomed Mater, 138: 105568, 2023.
3. Zaccaria et al, J Biomech, 107: 109841, 2020.



# UNRAVELING THE BIOMECHANICS OF NITINOL BONE STAPLES: A COMBINED EXPERIMENTAL AND NUMERICAL INVESTIGATION

Dario Carbonaro (1), Claudio Chiastra (1), Federico Bologna (1), Alberto Audenino, Mara Tezini (1)

1. Polito<sup>BIO</sup>Med Lab, Department of Mechanical and Aerospace Engineering, Politecnico di Torino, Italy

## Introduction

Nitinol bone staples showed to be a safe and effective option for internal fixation, demonstrating even superior characteristics in terms of usability, surgery time and post-surgery recovery time compared to traditional stainless-steel staples [1]. Nitinol staples recover their initial shape after being inserted into the predrilled holes, either owing to the super-elastic or to the shape-memory proprieties of Nitinol (i.e., super-elastic and shape-memory Nitinol staples, respectively) to pull the fractured bones together and apply a compressive force [2]. Despite the promising clinical results of both types of staples, most biomechanical investigations have focused on shape-memory devices. Few studies have been conducted on super-elastic staples. In this context, this study combines experimental tests and finite element (FE) analysis to assess the mechanical performance of commercially available Nitinol staples and determine their unique super-elastic properties, which are influenced by specific thermo-mechanical processing operations [3]. The ultimate goal is to develop a better understanding of the mechanical characteristics of these devices for successful treatment.

## Methods

The two commercially available super-elastic Nitinol bone staples (Arthrex, USA and Johnson & Johnson, USA) shown in Fig. 1A (staples 1 and 2) were investigated. An experimental four-point bending test was conducted at 37°C to characterize their mechanical response by fixing each staple within two blocks (Fig. 1B), according to the standard ASTM-F564-17 for the testing of metallic bone staples. The tensile testing machine E3000 (Instron, USA) was adopted to apply three cycles of displacements (rate 0.5 mm/s) and to measure the generated force. Fig. 1C shows the adopted experimental set up, indicating (1) the custom-made temperature-controlled bath, (2) the four-point bending apparatus and (3) the staples fixing blocks. Geometrical models of the staples were obtained by micro computed tomography. FE models replicating the experimental tests were implemented in Abaqus Standard (Dassault

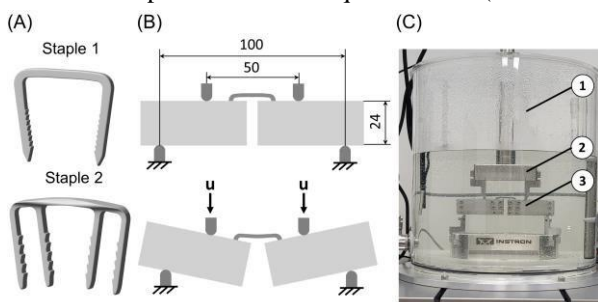


Figure 1: (A) Two commercially available staples; (B) Testing scheme; (C) Experimental set-up.

Systèmes, FR). The super-elastic constitutive model was adopted for the Nitinol and in absence of material data a FE-based material calibration framework was developed to deduce the values of the constitutive model parameters.

## Results

Fig. 2 shows the four-point bending test curves obtained both experimentally and numerically (using the material calibration framework). The forces of staples 1 and 2 in the implantation configuration (legs and the bridge forming an angle of 90°) were experimentally found to be 68.4 N and 84.8 N, respectively (Fig. 2). The FE model approximated well the experimental curves ( $R^2 > 0.99$ ) and the obtained Nitinol parameters differed between the two staples, indicating a different thermo-mechanical processing and chemical composition [3].

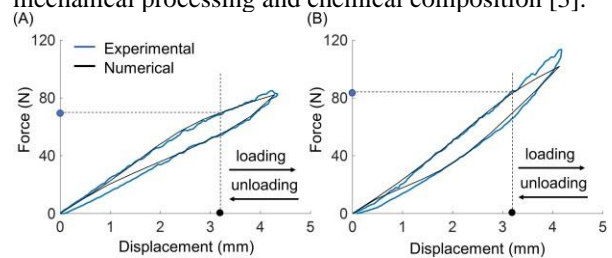


Figure 2: Experimental and numerical four-points bending curves of (A) staple 1, (B) staple 2.

## Discussion

The results of this study highlighted the different mechanical response of the two investigated staples, which are attributed to a combination of different geometry and material characteristics. In the future, the calibrated FE staple models can be used to support device design, avoiding time and cost associated with prototype manufacturing and testing, and to optimize the geometry and material characteristics, improving the effectiveness of the treatment.

## References

1. Malal et al, Foot Ankle Surg 45:113–17, 2006.
2. Russel et al, J Mater Eng Perform, 18:831–835, 2009.
3. Carbonaro et al, J Mech Behav Biomed Mater, 138:105623, 2023.

## Acknowledgements

This work has been supported by Piedmont Region (POR FESR PiTeF 2014-20 351-96, Nitoliera).



# A COMPUTATIONAL APPROACH FOR MANUFACTURING OPTIMIZATION OF 3D PRINTED FLEXIBLE INSOLES

Daniele Bianchi (1,2), Lorenzo Zoboli (1), Cristina Falcinelli (3), Alessio Gizzi (1)

1. University Campus Bio-Medico of Rome, Italy;

2. Medere srl, Italy;

3. G. D'Annunzio Chieti-Pescara University, Italy.

## Introduction

In recent years, innovative materials have been developed to mimic the lightweight and strong characteristics found in biological systems like bones, honeycombs, sponges, and wood. These materials are characterized by a porous microstructure that alternates between solid and void. At the same time, the emergence of innovative manufacturing techniques, such as 3D printing, has facilitated the production of cellular materials in various fields especially in healthcare [1,2] where the additive manufacturing is emerging as an efficient production method from different point of view (e.g., cost, environment) [3]. On the other hand, the 3D printing manufacturing can take a long time for production depending on material (e.g., rigid or flexible), infill pattern and printing parameters. The proposed study defines a computational approach based on FEM to optimize the infill pattern, the printing parameters and material distribution with the aim to reduce the production time.

## Materials and Methods

A computational tool has been developed integrating a numerical homogenization and a topological optimization implemented in ANSYS Academic Research Mechanical. In detail, a computational homogenization has been implemented to simulate the mechanical properties of the infill of the insoles. Different infills have been investigated in terms of mechanical properties and printing performance (e.g., speed and accuracy). The calculated constitutive properties have been assigned to the insoles geometries and different loading scenarios have been analyzed regarding therapeutic and use framework. With the results of these structural simulations, several topology optimization analyses have been performed, aiming at minimizing the compliance of the frontal part of the insole, while reducing its mass under a specified threshold. The objective of this study was to find a possible distribution of mass that allows to minimize the material use and printing time while retaining an acceptable structural response during the insertion phase of the insole into the shoe.

## Results

Since the aim of this work is to optimize the production of 3D printed insoles, the distributions of material are evaluated addressing different loading conditions. Nevertheless, the main result concerns the production

time of the insoles. As an example, in Fig. 1 depicts the optimal material distribution for a loading condition replicating the insertion of the insole in the shoes.

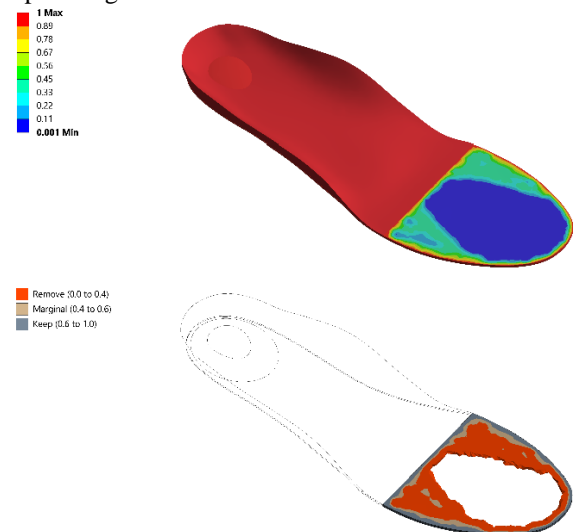


Figure 1: Optimal material distributions for a loading condition replicating the insertion of the insole in the shoes.

## Discussion

In this work, a computational procedure is developed in order to investigate different infill patterns on the mechanical performance of 3D printed flexible insoles. Moreover, the printing time can be reduced optimizing the material distribution in the insoles. The developed computational tool can be used for different orthopaedic devices making more effective the 3D printing production.

## References

1. Sun, Y., et al. 2019 IEEE int. conf. ROBIO (2019).
2. Auricchio, F., et al EFORT open reviews 1.5 (2016): 121.
3. Ferro, N., et al., Struct Multidiscipl Optim, 65.3 (2022): 79.

## Acknowledgements

Daniele Bianchi and Cristina Falcinelli acknowledges the funding by the Italian Ministry of University and Research (MUR) within the PON "Ricerca e Innovazione" 2014–2020 (azione IV.6) - FSE-REACT EU.

# SAFETY OF PORTACATH IMPLANTATION IN EVERYDAY'S LIFE: A FINITE ELEMENT STUDY

Vittorio Lissoni (1), Federica Campagna (1), Giulia Luraghi (1), Filippo Spreafico (2), Jose Felix Rodriguez Matas (1)

1. Politecnico di Milano, Milan, Italy; 2. Fondazione IRCCS Istituto Nazionale dei Tumori, Milan, Italy

## Introduction

Chemotherapy is a significant therapeutic option in oncology. Usually, patients are subjected to this treatment for a mean time of 6 to 9 months during which chemotherapy cycles are administered every three weeks [1]. Due to the continuous venous access, throughout this time vessel integrity may be compromised by repeated venous access [2], [3]. To prevent this complication, in the last years total implantable venous access port have been developed; among these devices, one of the most used is Port-a-cath which is implanted subcutaneously under the clavicle. This device is composed by a reservoir from which drugs are delivered through a catheter into a big vein, such as the subclavian. Drugs are periodically loaded in the reservoir through subcutaneous injections without the requirement to locate a vein. Due to its position, the device is visible through the skin. This fact raises concerns in patients about the risk of damaging the device or the surrounding tissues during the practice of sport. The aim of this study is to simulate the interaction between the Port-a-cath and the surrounding tissue during normal implantation and under the impact of a ball during the practice of exercise to evaluate the safety of the device and the possibility of lesions in the surrounding soft tissue.

## Methods

A patient-specific human torso model was obtained through segmentation process of CT-scans of a patient who received port-a-cath implantation. Within the torso, parts corresponding to skin, muscle, bones, cartilage, whereas internal organs were neglected. A cad model of the port-a-cath was created with the software Solidworks and correctly positioned inside the torso in correspondence with the CT images of the patient post-implantation as shown in Figure 1a.

The torso was discretized with tetrahedral elements and the components modelled as linear elastic materials with mechanical properties obtained from literature [4]–[7]. On the contrary, the port-a-cath was considered as rigid. The simulation was performed in two steps. In the first step, the implantation of the device was simulated by considering the interaction of the device with the muscle and the skin. In a second step, an impact with a soccer ball at 20 m/s recreating a shut of a young football player [4] was considered. Different impact angles were investigated ranging from a direct frontal impact to a shallow angle impact. [8]. All simulations were performed as explicit using the Finite Element software ANSYS-LsDyna

## Results

The results indicate that the area of influence of the port-a-cath after the implantation is limited to a small region around the port-a-cath, with the maximum stress located at the muscle (see Figure 1b). A frontal impact of the ball increases the peak stress around the porta by a factor of 16 and was found to be located at the muscle. The simulations also show that other tissues, such as bone and cartilage, were not excessively stressed by the impact of the ball even in presence of the portacath.

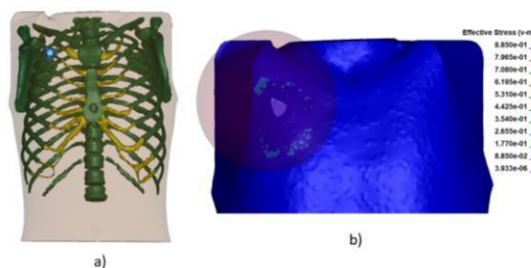


Figure 1: a) Torso with different parts and the port-a-cath; b) von Mises stresses [MPa] during the hit of the ball

The average stress in the muscle surrounding the device was extracted during the impact phase, resulting in a maximum peak stress of 0.22 MPa, which results lower than the threshold of 0.26 MPa for muscle damage [9].

## Discussion

The results showed no damage to the tissues around the device on a patient-specific geometry giving proof of the safety of the device implanted in everyday life's activities.

## References

1. Bow EJ, et al. *J Clin Oncol* 1999;17(4):1267.
2. Bernaerts, G. et al. *Int J Nurs Stud* 2000 Apr;37(2):101-10.
3. Tomford JW. et al. *Intern Med* 1984;144(6):1191-4.
4. Nakashima D, et al. *Exp Ther Med.* 2018 Apr;15(4):3225-3230.
5. Albert DL, et al. *J Mech Behav Biomed Mater.* 2021 Oct;122:104668
6. Muñoz MJ, et al. *J Biomech.* 2008;41(1):93-9.
7. Abe, et al. *Data Book on Mechanical Properties of Living Cells, Tissues, and Organs.* 1996.
8. Valente M, et al. *Scuola dello sport CONI Liguria*, 2011
9. Singh G, et al. *Biomed Mater.* 2021 Oct 19;16(6).

## Acknowledgement

Work developed within the MUSA – Multilayered Urban Sustainability Action – project, funded by the European Union – NextGenerationEU, under the National Recovery and Resilience Plan (NRRP) Mission 4 Component 2 Investment Line 1.5: Strengthening of research structures and creation of R&D “innovation ecosystems”, set up of “territorial leaders in R&D”

# UPPER LIMB JOINT KINEMATICS OPTIMIZATION IN REAL-TIME THROUGH A CONSTRAINED ISB-CONSISTENT MODEL

Marco Caruso (1), Elisa Digo (1), Laura Gastaldi (1), Stefano Pastorelli (1), Andrea Cereatti (1)

1. Politecnico di Torino, Italy

## Introduction

Real time robust upper limb joint kinematics description is a central point for several applications such as telerehabilitation and clinical evaluation. The use of wearable sensors (IMUs) together with state-of-the-art sensor fusion algorithms represents a convenient solution to unobtrusively monitor the subject performance in real-world environments. However, for long acquisitions (e.g., ~10 minutes), errors in joint angle estimates increase with time due to orientation drift thus affecting joint kinematics reliability. The aim of this work is two-fold: i) to propose a multi-segmental model of the upper limb compliant with the guidelines of the International Society of Biomechanics (ISB), ii) to propose a real-time optimization framework for the IMU-based joint kinematics estimation by setting *ad-hoc* model constraints based on both the physiological joint limits and the knowledge of the performed movement. The accuracy of the shoulder and elbow constrained kinematics was tested on one subject equipped with two IMUs during a 10-minute exercise.

## Methods

A three-segment chain was designed following the Denavit-Hartenberg robotic convention to model the upper limb including the trunk, the upper arm (UA), and the forearm (FA). The shoulder and elbow joints were modeled as three ( $\theta_1, \theta_2, \theta_3$ ) and two ( $\theta_4$  and  $\theta_6$ ) degrees of freedom, respectively, following the ISB axis sequence. The carrying angle  $\theta_5$  was modeled as a fixed and subject specific parameter. One healthy subject was equipped with two IMUs on the UA and FA and asked to draw a continuous path with a pencil over a printed page on a horizontal surface while seated. Four reflective markers were also placed on each IMU to provide the orientation reference. IMU and marker data were recorded for ten minutes at 100 Hz. Before this, the offset of each gyroscope was subtracted from angular velocity readings. Experiments were repeated eight times with eight pairs of IMUs to test the method robustness to different IMU noise. For each time-step, the joint angles were obtained in an optimization framework by minimizing the difference between the orientation predicted using the upper limb model and the corresponding orientation computed using the sensor fusion algorithm [1] without magnetometer whose parameter was optimally tuned [2]. In addition, the optimal ( $\theta_1, \theta_2, \theta_3, \theta_4$ , and  $\theta_6$ ) solution had to satisfy two set of constraints. The first defined the extreme values for each  $\theta$  based on the physiological joint limits. The second was determined exploiting the a priori task-specific knowledge. In fact, during the entire recording

the elbow and wrist positions remained on a limited portion of space. Errors were computed as root mean square differences between the reference joint angles and those obtained through the optimization framework with and without applying the constraints, respectively.

## Results

Average errors (deg) for  $\theta_1, \theta_2, \theta_3, \theta_4$ , and  $\theta_6$  obtained with (without) the constraints over the eight repetitions amounted to 10.9 (13.0), 6.4 (7.5), 3.9 (3.9), 14.4 (16.4), 5.4 (5.7), respectively. The average execution time to perform ~62000 iterations amounted to 9.42 ms.

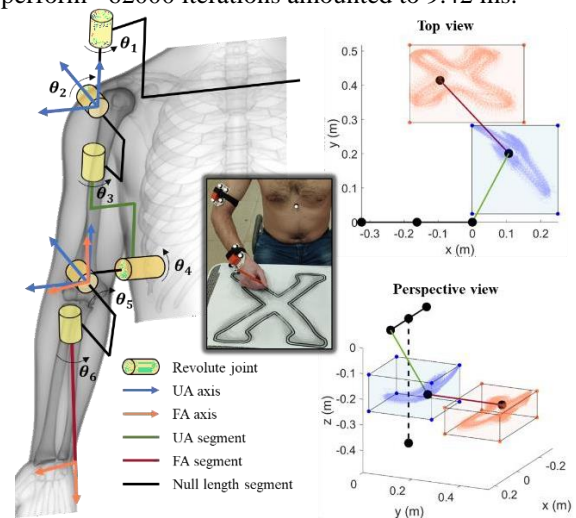


Figure 1: (left) the ISB upper limb model. (right) the boxes represent the elbow and wrist volume constraints; the point clouds represent the corresponding elbow and wrist positions estimated during the trial.

## Discussion

By exploiting the knowledge of the performed movement, the constraints application allowed to reduce both shoulder and elbow angular errors by around 12% and 11%, respectively, thus limiting the impact of the IMU orientation errors on the estimated joint angles. The execution time lower than the sampling period is suitable for a real-time joint kinematics computation.

## References

1. Madgwick et al, ICORR, 2011.
2. Caruso et al, Sensors, 2021.

## Acknowledgements

This abstract is part of the project NODES which has received funding from the MUR – M4C2 1.5 of PNRR with grant agreement no. ECS00000036. Part of DoMoMEA project funded by Sardegna Ricerche with POR FESR 2014/2020.



# POSE ESTIMATION METHODS FOR GENERAL MOVEMENTS ASSESSMENT IN INFANTS: OPEN METHODOLOGICAL ISSUES

Rita Stagni (1), Tommaso Doto (1), Arianna Tomadin (1), Alessandra Sansavini (2), Arianna Aceti (3), Luigi Tommaso Corvaglia (3), Maria Cristina Bisi (1)

1. DEI, Unibo, Italy; 2. PSI, Unibo, Italy; 3. DIMEC, Unibo, Italy

## Introduction

General Movements Assessment (GMA) is a non-invasive reliable assessment for identifying risk of neurological impairment in infants [1]. General Movements (GMs) are spontaneous movement patterns evident up to 20 weeks of age; they involve the whole body in a variable sequence of arm, leg, neck and trunk movements. GMA is performed through direct or video observation by a licensed operator, resulting in a qualitative description of motor performance of the infants. These aspects limit widespread objective and quantitative evaluations [1].

Recently, technological approaches aiming at automated or technology-assisted GMA have surfaced [2]. Video-based approaches remain authentic to the non-intrusive character of the classic GMA and guarantee potential easy and widespread clinical applications [2].

Video-based automatic GMA generally consists of i) automatic tracking of body segment kinematics, ii) metrics extraction, and iii) performance classification. The proper initial tracking of segmental kinematics is the prerequisite for reliable metrics extraction and resulting classification; unfortunately, when comparing the few available studies [2], exploiting mainly state-of-the-art open source software for automated tracking [2], no standard can be identified for video acquisition and processing.

The present work aims to fill this gap, investigating the influence of video acquisition settings (i.e. frame rate and resolution) and processing (e.g. reconstruction model, accuracy thresholding, filtering, and interpolation) on resulting kinematics, as well as on a set of assessment metrics from previous studies [3].

## Methods

**Experimental protocol:** As part of an ongoing research study, 81 infants at risk of neurodevelopmental impairment (preterm newborns with gestational age <32 weeks and/or birth weight <1500 g) were recruited at the Neonatal Unit of IRCCS AOU Bologna (ethical approval n° EM1229-2020\_76/2013/U/Sper/AOUBo). Videos of GMs were collected at term equivalent age, using, ease of use in a clinical setting by clinical staff, a commercial video camera (GoPRO Hero 9), at 240fps, and 1920x1080p resolution. Video collection was performed following GMA guidelines [1].

**Data analysis:** Kinematics of body segments was extracted using OpenPose [2] (predefined Body25, 25 landmark5, and MPI, 15 landmarks, models) and DeepLabCut [2] (ad-hoc defined 14 landmark model), having been used in previous studies. For the

implementation of DeepLabCut *ad-hoc* model, influence of the number of training iterations was tested for 200k, 400k, 600k, 800k, and 1M iterations.

Computational time and percentage of missing reconstructed points were analysed for basic performance assessment.

Percentage of points with confidence above 95%, distance of marker trajectories for increasing number of training iterations, and spectral analysis were performed to assess influence of video resolution and sampling frequency, and model training iterations on trajectory reconstruction.

Influence of model training iterations, filtering, and interpolation on resulting evaluation metrics (i.e. range, covered distance, velocity and jerk mediated over 1s windows) was tested for processing assessment.

## Results

Due to double processing time and low performance in trajectory reconstruction Open-Pose was excluded from further analysis after basic performance assessment.

After 400K iterations reconstructed trajectories resulted to reach a plateau in terms of stability, completeness, and number of values above 95% confidence.

Both filtering and interpolation resulted to critically affect evaluation metrics.

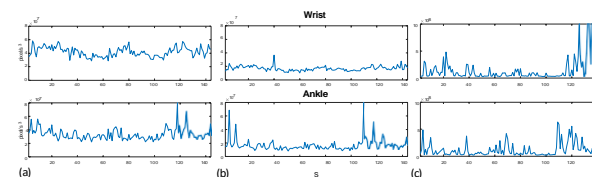


Figure 1: trajectory jerk mediated over 1s window over time: a) for raw trajectory over 95% confidence; b) 60Hz filtered trajectory over 95% confidence; c) linearly interpolated trajectory over 95% confidence.

## Discussion

Preliminary analysis highlighted the critical role of video acquisition settings and processing on reconstructed kinematics and, even more, on the resulting evaluation metrics. The finalization of the analysis will provide evidence-based criteria for the definition of a reliable methodologic approach for the automatic assessment of GMs.

## References

1. Tsuji et al., Scientific Reports 10: 1422, 2020.
2. Silva et al., Res. Dev. Disabil 110: 103854, 2021.
3. Moro et al., Comput Methods Programs Biomed. 226: 107119, 2022



# WALL SHEAR STRESS AND ATHEROSCLEROTIC PLAQUE PHENOTYPES IN FOCAL AND DIFFUSE CORONARY ARTERY DISEASE

Maurizio Lodi Rizzini (1), Alessandro Candreva (1,2), Valentina Mazzi (1), Daniel Munhoz (3), Jean Paul Aben (4), Claudio Chiastra (1), Carlos Collet (3), Diego Gallo (1), Umberto Morbiducci (1)

1. Dept. of Mechanical and Aerospace Engineering, Politecnico di Torino, Italy; 2. Dept. of Cardiology, USZ, Switzerland; 3. Cardiovascular Center Aalst, Belgium; 4. Pie Medical Imaging BV, The Netherlands.

## Introduction

Translesional pressure gradient during hyperemia is a fundamental clinical parameter to evaluate the functional severity of coronary artery disease (CAD), being associated with adverse clinical events [1]. Its measurement is performed in the distal part of the coronary artery, thereby reflecting the cumulative pressure losses along the whole vessel [2]. Automatic pullback pressure measurements allow quantifying pressure losses along the vessel, differentiating the CAD functional pattern in focal or diffuse [2]. In addition to pressure gradients, wall shear stress (WSS) profiles are associated with plaque progression and destabilization [3], and with adverse clinical events [4].

In this study, a combination of (1) invasive pressure pullback measurement, (2) angiography-based WSS obtained with computational fluid dynamics (CFD) simulations, and (3) plaque phenotype characterization based on optical coherence tomography (OCT) was adopted to unveil possible relationship between CAD functional patterns, WSS, and plaque phenotype.

## Methods

A total of 105 coronary arteries with flow limiting lesions, identified by distal fractional flow reserve (FFR) lower than 0.80, underwent pressure pullback measurement and angiography-based WSS analysis. A subset of 51 vessels was analyzed with OCT pullback. FFR motorized pullback tracings (Volcano R100, Volcano Corporation) during maximal hyperemia were used to obtain the pressure pullback gradient (PPG), a non-dimensional continuous quantity, ranging from 0 (diffuse CAD) to 1 (focal CAD) [2]:

$$PPG = \frac{1}{2} \left[ \frac{MaxPPG_{20mm}}{\Delta FFR_{vessel}} + \left(1 - \frac{L_{FD}}{L_{TOT}}\right) \right] \quad (1)$$

where  $MaxPPG_{20mm}$  was defined as the maximum PPG over a 20 mm length,  $\Delta FFR_{vessel}$  as the difference between FFR values obtained at the ostium of the vessel and at the most distal anatomical location, the length of functional disease  $L_{FD}$  as the length with FFR drop  $\geq 0.0015$  per mm, and the total vessel length  $L_{TOT}$  was derived from the motorized pullback pressure tracing. 3D vessel models were reconstructed from two angiographic projections at least  $30^\circ$  apart. Lesions and mid segment (i.e., the segment of the lesion where the severity is maximal) were identified using an automatic approach. The anatomic severity was characterized in terms of percentage area stenosis (%AS). Then, CFD simulations were performed on reconstructed 3D vessel models using a finite element-based code (CAAS Workstation WSS software, Pie Medical Imaging). WSS vector field was characterized in terms of time-

average WSS (TAWSS) and topological shear variation index (TSVI) [4], which accounts for variability of WSS contraction/expansion action on the endothelium along the cardiac cycle. TAWSS and TSVI values were averaged over the mid segment of the lesion [4]. Finally, plaque composition analysis [5] was performed acquiring OCT pullbacks of 75 mm length. For the statistical analysis, odd ratios (OR) were obtained from the exponential of the standardized correlation coefficients of generalized linear models.

## Results

Focal lesions (PPG above median value of 0.67) presented significantly lower distal FFR, higher %AS, TAWSS and TSVI ( $p < 0.001$  for all). Focal lesions presented a lower fibrous cap thickness with respect to diffuse ones ( $p = 0.005$ ). PPG was associated with the presence of thin-cap fibroatheroma (OR 2.85,  $p = 0.029$ ) and plaque rupture (OR 4.94,  $p = 0.002$ ). A significant association emerged between TAWSS and the presence of macrophages (OR 1.15,  $p = 0.018$ ), TSVI and plaque rupture (OR 1.01,  $p = 0.024$ ), TSVI and the presence of cholesterol crystals (OR 1.01,  $p = 0.041$ ).

## Discussion

The findings of this study, schematized in Fig. 1, support the hypotheses that: (1) the hemodynamic profile is different in patients presenting with focal and diffuse CAD; (2) this different hemodynamic profile is also associated with different plaque phenotype; (3) focal CAD and higher TAWSS and TSVI are associated with high risk plaque phenotypes. These results, combined with previous observations [2,4], make focal lesions the favourite candidates to revascularization interventions.

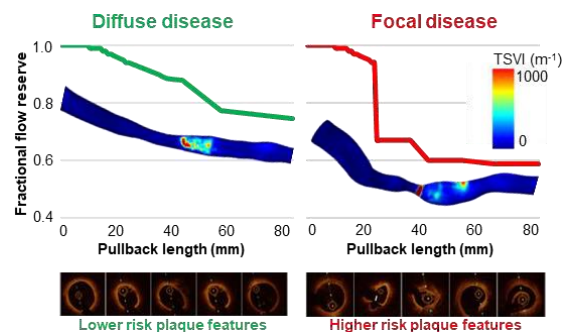


Figure 1: interplay between coronary hemodynamics and plaque composition in diffuse vs. focal lesions.

## References

1. Pijls et al., *J Am Coll Cardiol*, 56(3):177-184, 2010.
2. Collet et al., *J Am Coll Cardiol*, 74(14):1772-1784, 2019.
3. Wentzel et al., *Cardiovasc. Res.*, 96:234-243, 2012.
4. Candreva et al., *Atherosclerosis*, 342:28-35, 2022.
5. Jang et al., *Circulation*, 111(12):1551-1555, 2005.



# IMPACT OF DIFFERENT PATIENT-SPECIFIC BOUNDARY CONDITIONS ON HAEMODYNAMIC MARKERS IN PERIPHERAL ARTERIAL DISEASE

Federica Ninno (1), Claudio Chiastra (2), Monika Colombo (3), Alan Dardik (4), David Strosberg (4), Janice Tsui (5), Stavroula Balabani (1), Vanessa Diaz-Zuccarini (1)

1. University College London, UK; 2. Politecnico di Torino, Italy; 3. Aarhus University, Denmark; 4. VA Connecticut Healthcare Systems, USA; 5. Royal Free Hospital, UK

## Introduction

Peripheral arterial disease (PAD) is the third cause of cardiovascular morbidity [1]. Surgical (i.e. bypass) and/or endovascular approaches (i.e. stenting) are employed to restore impaired blood flow resulting from the pathology. Restenosis, i.e. an abnormal re-narrowing of the treated blood vessels, is a common negative outcome of these procedures. Altered haemodynamics plays a role in its progression. The integration of haemodynamic variables, arising from computational fluid dynamic (CFD) simulations, and routinely collected information has the potential to predict when re-occlusion occurs. However, the accuracy of such predictive tools relies on the quality of the clinical data. Data availability (i.e. computed tomography (CT) scans and Doppler ultrasound (DUS) images) tends to be fragmented, as the timings of DUS and CT imaging may differ. In this work, we assess the impact of applying different (in time) patient-specific boundary conditions (BCs) - obtained from the DUS images - on haemodynamic indices and hence ascertain that reliable information is obtained to predict restenosis occurrence.

## Methods

CT scans and DUS images of three patients suffering from PAD who underwent bypass or stenting were obtained from VA Connecticut Healthcare Systems, West Haven, USA. DUS images acquired at the same time and at heterogeneous time points with respect to CT scans acquisition were considered as inlet BCs. Patients' vessels were reconstructed and patient-specific CFD analyses were performed following Colombo et al. workflow [2]. Haemodynamic indices related to restenosis (i.e. Time-Averaged Wall Shear Stress (TAWSS), Oscillatory Shear Index (OSI), Relative Residence Time (RRT) and Topological Shear Variation Index (TSVI)) were computed. The differences in the haemodynamic indices with respect to those obtained when CT scans and DUS match in time were quantified, and the ability to capture regions subjected to altered haemodynamic values was assessed.

## Results

Fig.1(a) shows the % differences in spatially averaged TAWSS index along the bypass length with respect to the reference case for one patient. Fig.1(b) shows the regions subjected to low TAWSS (restenosis marker). These were identified by imposing as critical threshold the 1<sup>st</sup> tertile of the TAWSS distributions for every applied BC. The TAWSS index may be underestimated or overestimated along the bypass length. However, no

significant differences were observed in the depicted critical regions for restenosis [3].

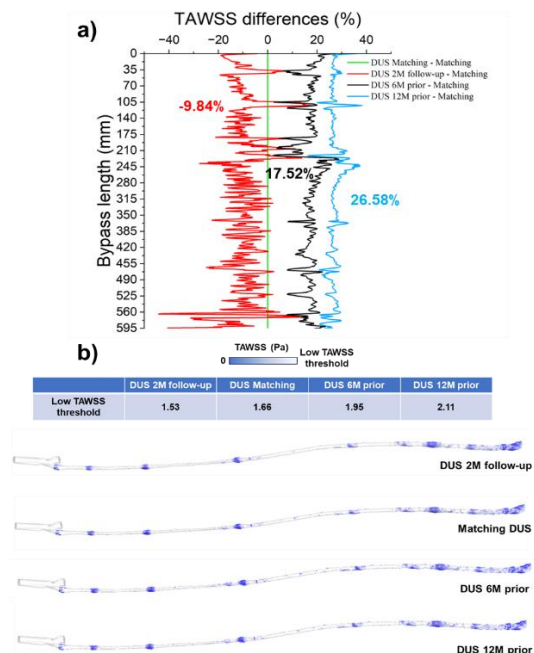


Figure 1: a) Differences (median value in bold) in TAWSS indices with respect to the reference case along the bypass length when 2-months (2M) follow-up, 6- and 12-months (6M, 12M) prior DUS to CT scan acquisition are applied; b) luminal regions subjected to low TAWSS for examined inlet BCs.

## Discussion

In summary, potential critical areas for restenosis can be identified even from fragmented data if critical thresholds are computed based on single distributions. Although the haemodynamic values along the bypass may be incorrectly estimated when DUS images do not match CT scans in time, critical areas for restenosis are still reliably identified. Further analysis of the entire dataset is currently in progress to support these findings.

## References

1. Fowkes et al., The Lancet, 2013.
2. Colombo et al., Med Eng Phys, 2020.
3. Colombo et al., Ann Biomed Eng, 2021.

## Acknowledgements

This work was supported by funding from UCL EPSRC CDT i4health [EP/S021930/1]. This study was ethically approved with approval number AD0009 from VA Connecticut Healthcare Systems, West Haven, CT, USA.



# A MESH MORPHING TOOL FOR MOVING BOUNDARIES CFD SIMULATIONS AND WALL STIFFNESS ESTIMATION OF THE AORTA

Francesca Dell'Agnello (1, 2), Emanuele Vignali (1), Martino Andrea Scapolini (1, 3), Katia Capellini (1), Emanuele Gasparotti (1), Filippo Cademartiri (4) and Simona Celi (1)

1. BioCardioLab, Fondazione Toscana Gabriele Monasterio, Italy; 2. Department of Information Engineering, University of Pisa, Italy; 3. Department of Industrial Engineering, University of Rome "Tor Vergata", Italy; 4. Clinical Imaging Department, Fondazione Toscana Gabriele Monasterio, Italy

## Introduction

Computational Fluid Dynamics (CFDs) is a well-established technique to analyze blood flow of the thoracic aorta (TA) and its correlation with pathological conditions [1]. However, standard CFD simulations are based on the rigid wall hypothesis, so vessel structural properties are neglected. The mechanical behavior of the arterial tissue is an important indicator of the functional and structural changes within the vessel wall [2]. In this perspective, Fluid-Structure Interaction (FSI) simulations consider wall compliance, but demand extensive computational resources and additional information on the vessel wall difficult to be defined in-vivo. Recently, mesh morphing techniques are presented as promising tools to cope with the aorta wall changes [1, 3]. Nevertheless, they are limited to the ascending aorta and show some intrinsic discontinuities. The aim of this work is to develop and implement a new tool which employs mesh morphing techniques to set up moving boundaries CFD simulations for the assessment of the hemodynamics of the TA and estimate the aortic stiffness from in-vivo patient-specific images.

## Methods

From ECG-gated CT images of five subjects we performed a segmentation process through a U-net deep neural network [4]. This allowed to reconstruct, for each patient, ten 3D models of the TA, corresponding to different phases of the cardiac cycle. Then, we applied an in-house non-rigid registration algorithm to morph the baseline mesh on the geometries of the other phases. Firstly, the morphed meshes, together with a spline interpolation, were used to obtain the TA wall displacement for the whole cardiac cycle. This displacement was included in the setup of a moving-boundary CFD simulation (CFD<sub>morph</sub>) in Ansys Fluent® and used by the solver to handle the volume mesh. In addition to the developed procedure, we performed a standard CFD simulation (CFD<sub>0</sub>) for the baseline configuration of the TA to compare hemodynamic results. Secondly, the meshes were employed in a workflow for the assessment of the aortic wall stress, strain and stiffness [5]. We evaluated the circumferential strain as the ratio between sectional contour lengths. The vessel wall behaviour was assumed as membranous and linearized under the physiological pressure load. Under these assumptions, the circumferential Young's modulus ( $E_{\theta}$ ) was obtained according to Laplace assumption and Hooke's law.

## Results

The proposed tool replicated the TA patient-specific deformations and wall motion throughout the cardiac cycle, without significantly decreasing mesh quality. Velocity ( $v$ ) distributions showed differences between the two simulation strategies (Figure 1a), as well as the main wall shear stress based hemodynamic parameters. Moreover, the CFD<sub>morph</sub> was able to model flow waveform shift occurring along the aortic lumen. Finally, the presented method revealed heterogeneous stiffness distributions, with differences between ascending and descending districts (Figure 1b).

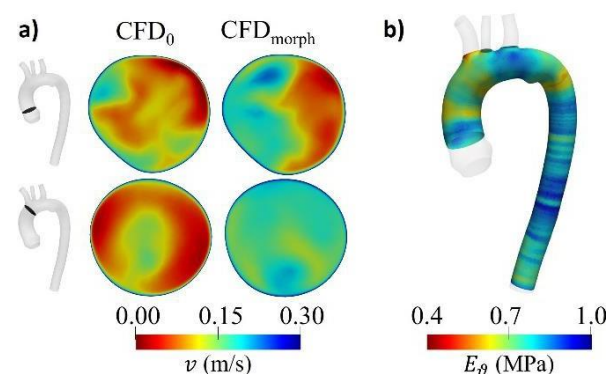


Figure 1: Velocity magnitude at different TA sections at maximum acceleration time (a) and  $E_{\theta}$  distribution (b)

## Discussion

The mesh morphing tool represents a worthwhile strategy for moving boundaries patient-specific CFD simulations, overcoming the main limitations of standard CFD and FSI approaches. Additionally, it is a valid method for the non-invasively local estimation of the aortic wall mechanical properties.

## References

1. Capellini et al, J Biomech Eng, 140(11), 2018.
2. Cavalcante et al, J Am Coll Cardiol, 57(14):1511-22, 2011
3. Capellini et al, Med Eng Phys, 91:68-78, 2021.
4. Scapolini et al, ESB-ITA, 2022
5. Celi et al., Front Bioeng Biotechnol, 11:1096196, 2023

## Acknowledgements

This work was supported by the MeDiTaTe Project from the European Union's Horizon 2020 research and innovation programme under Grant Agreement 859836.



# DEVELOPMENT OF ARTERY MODELS FOR PATIENT-SPECIFIC SIMULATIONS OF CORONARY STENTING: A SIX-CASE STUDY

Luca Antonini (1), Gianluca Poletti (1), Lorenza Petrini (2), Giancarlo Pennati (1)

1. LaBS – Dept. of Chemistry, Materials and Chemical Engineering, Politecnico di Milano, Milan, Italy;  
2. Dept. of Civil and Environmental Engineering, Politecnico di Milano, Milan, Italy.

## Introduction

In recent years, *in silico* analyses have gained increasing attention as a powerful tool to support clinical decision-making. In the context of coronary stenting, simulations can be used to predict the effects of complex treatments, furnish supplementary comprehension regarding post-treatment hazards, and reduce the need for animal and clinical studies during the development and assessment phases of a new device. As a result, computational studies have become an essential part of medical research, opening the issue of establishing the credibility of stent and coronary artery models used in simulations. Various studies have explored different strategies to mechanically describe arterial tissues, ranging from simple homogeneous approaches [1, 2] to more complex fiber-reinforced models [3]. In this work, we aim to discuss different modeling methods, including the representation of arterial tissue softening due to damage at high deformations, and assess the ability of these models to reproduce the stenting procedure of six patient-specific cases. Specifically, it is intended to evaluate the models' abilities to replicate clinical outcomes such as postoperative vessel lumen area and prediction of the presence of any malapposition.

## Materials and Methods

The arterial models of each patient were obtained through reconstructions based on clinical images (OCT and angiographies). Through the analysis of these images, it was possible to differentiate the adventitia and media layers in the model, as well as different components of atherosclerotic plaque, such as calcifications, lipid pools, and generic plaque. The mechanical description followed the approaches proposed in a previous literature work [4], with the additional incorporation of a phenomenological damage model that can replicate the gradual mechanical deterioration of arterial tissues under high deformations. All the simulations were carried out in Abaqus/Explicit, with the hypothesis of working in quasi-static regime and faithfully replicating the stent deployment procedure adopted for the treatment of each patient.

## Results

In comparison with post-stenting clinical data (Figure 1), the developed damage model was demonstrated to be effective in replicating what was observed in correspondence with high values of lumen gain, where the reference model (NoDamage) fails to predict the post-treatment lumen area. As reported in Figure 2, the

approach proposed in this study has also proved to be effective in predicting areas of stent strut malapposition.

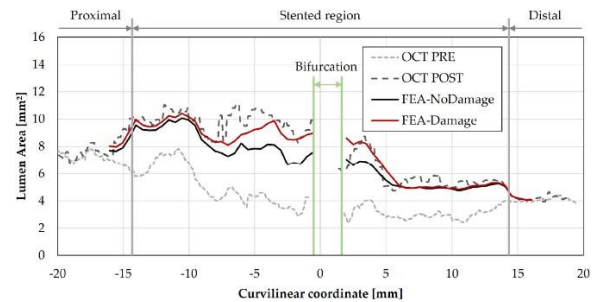


Figure 1: Comparison between the computational results (with and without the damage model), with respect to lumen area values acquired from OCT slices.

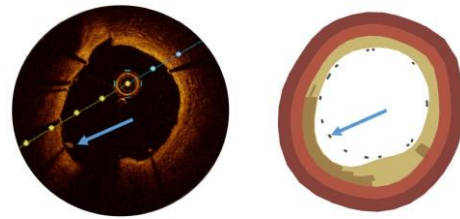


Figure 2: Detection of malappositions: comparison between OCT slice (on the left) and simulation cross-section (on the right).

## Discussion

Despite using a phenomenological approach, the mechanical description of arterial walls has demonstrated to be robust and valid in reproducing, with good approximation, the results observed in six clinical cases. Incorporating the damage description, the previous model's capability to accurately reproduce the behavior at low deformations was preserved, providing also realistic performance even when high lumen gain values were encountered.

## References

1. Chiastra, C. et al, J Biomech, 49:2102–2111, 2016.
2. Zhao, S. et al, Scientific Reports, 11, 2021.
3. Mortier, P. et al, Ann of Biomed Eng, 38(1):88–99, 2010.
4. Poletti et al, Electronics, 11(3):502, 2022.

## Acknowledgements

This project has received funding from the European Union's Horizon 2020 research and innovation programme under grant agreement no 777119. This article reflects only the authors' view and the Commission is not responsible for any use that may be made of the information it contains.



# WALL SHEAR STRESS TOPOLOGICAL SKELETON VARIABILITY PREDICTS PLAQUE PROGRESSION IN HUMAN CORONARY ARTERIES

Giuseppe De Nisco (1), Eline Hartman (2), Elena Torta (1), Diego Gallo (1), Claudio Chiastra (1), Joost Daemen (2), Jolanda Wentzel (2), Umberto Morbiducci (1)

1. PoliTo<sup>BIO</sup>Med Lab, DIMEAS, Politecnico di Torino, Italy; 2. Department of Cardiology, Biomedical Engineering, Erasmus MC, Netherlands

## Introduction

Although low wall shear stress (WSS) has become the consensus hemodynamic mechanism for coronary atherosclerosis, the exact biomechanical stimulus affecting atherosclerosis evolution is still undetermined [1]. Aiming at bridging this gap of knowledge, recently the WSS topological skeleton (TS) is receiving increasing interest, because of (1) its link with flow features associated with vascular dysfunction [2], and (2) its capability to concur to the description of the complex biomechanical stimulus affecting atherosclerosis evolution [3]. Briefly, the WSS TS is composed by fixed points, where the WSS vanishes, and unstable/stable manifolds connecting them, where WSS exerts a contraction/expansion action on the endothelium [4]. Here we test the ability of WSS TS, solely or synergistically with plaque phenotypes, to predict the temporal evolution of coronary artery plaque atheroma volume (PAV), a hallmark of atherosclerosis development, in 38 patient-specific computational models of human coronary arteries.

## Methods

A non-culprit coronary segment for 37 hemodynamically stable patients was imaged at baseline (T1) and at 1 year follow-up (T2). Vessel geometries were reconstructed at T1, and computational hemodynamic simulations were carried out prescribing patient-specific boundary conditions. Widely adopted descriptors of WSS magnitude and multidirectionality were tested (i.e., TAWSS, OSI, RRT, and transWSS). Additionally, a Eulerian method was applied to analyse the WSS TS [4], identifying WSS contraction/expansion regions at the coronary luminal surface by the divergence of normalized WSS vector field ( $DIV_{WSS}$ ). The amount of variation in WSS contraction/expansion action along the cardiac cycle T was quantified by the Topological Shear Variation Index (TSVI) [2]:

$$TSVI = \left\{ \frac{1}{T} \int_0^T [DIV_{WSS} - \overline{DIV_{WSS}}]^2 dt \right\}^{1/2} \quad (1)$$

Plaque progression was evaluated as the difference between PAV measurements ( $100 \times \text{plaque volume} / \text{total vessel volume}$ ) at T2 and T1 averaged over  $3\text{mm}/45^\circ$  luminal sectors. Additionally each sector was classified as lipid rich, fibrous or plaque free based on OCT images. Hemodynamic descriptors were averaged over  $3\text{mm}/45^\circ$  luminal sectors and divided into artery-specific low, mid and high tertiles to perform a statistical analysis on the associated  $\Delta PAV$ , solely or in combination with plaque phenotype.

## Results

The luminal distribution of TAWSS, TSVI and  $\Delta PAV$  are reported in Figure 1A for an explanatory case. Overall, sectors exposed to high TSVI at T1 exhibited  $\Delta PAV$  in the T2-T1 time interval significantly higher than sectors exposed to low or mid TSVI at T1 (figure 1B). A clear trend emerged also for the exposure to low TAWSS at T1 and high  $\Delta PAV$ . Plaque phenotype acted synergistically with TAWSS or TSVI regarding plaque progression: at low TAWSS or high TSVI sectors in combination with lipid rich plaque,  $\Delta PAV$  values were significantly higher ( $p < 0.01$ ) than expected based on the individual contribution of hemodynamics.

Low values emerged for OSI ( $< 0.01$ ) and transWSS ( $< 0.15\text{Pa}$ ) suggesting a minor role of WSS multidirectionality in promoting aggravating biological events.

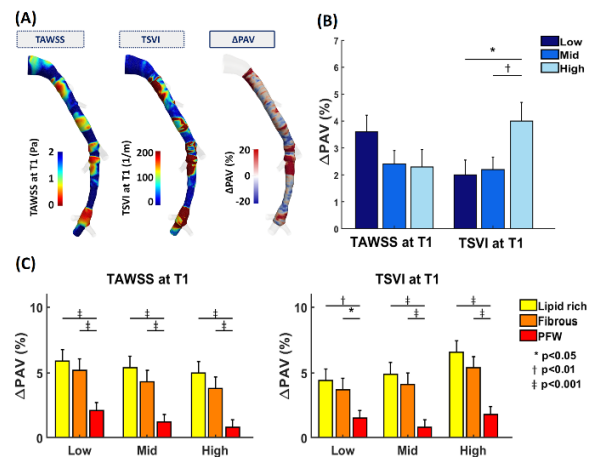


Figure 1: (A) TAWSS, TSVI and  $\Delta PAV$  luminal maps; (B) TAWSS and TSVI vs. estimated PAV; (C) solely; (C) in combination with OCT-derived plaque phenotypes.

## Discussion

Here we demonstrate that luminal exposure to high TSVI, solely or combined with lipid rich plaque phenotype, was associated with plaque progression. Physically, TSVI quantifies WSS contraction/expansion action variability on the endothelium, describing a different hemodynamic stimulus with respect to low TAWSS. This study confirms recent findings on TSVI as biomechanical marker of vascular disease, encouraging further trials for its translation to clinics.

## References

1. Brown AJ et al., Nat Rev Cardiol, 13:210-220, 2016.
2. Morbiducci U et al., Ann Biomed Eng, 48:2936-49, 2020.
3. Candreva A et al., Atherosclerosis, 2021.
4. Mazzi V et al., Biomech Model Mec, 19(5):1403-23, 2020.



# VIRTUAL BENCH TESTING OF MECHANICAL HEART VALVES: A PRELIMINARY FLUID-STRUCTURE INTERACTION STUDY

Mariachiara Arminio (1), Dario Carbonaro (1), Sara Zambon (1), Alessandro Scattina (1), Lorenzo Peroni (1), Umberto Morbiducci (1), Diego Gallo (1), Claudio Chiastra (1)

1. Department of Mechanical and Aerospace Engineering, Politecnico di Torino, Italy

## Introduction

Aortic valve disease is a highly impactful condition. A primary treatment approach consists in replacing the native valve with a prosthetic one. According to recent guidelines [1], surgical mechanical prosthetic valves should be the first choice in patients under 50 years of age with no contraindication to anticoagulation therapy and they may be considered in patients up to 65 years of age. Over the last years, computational models have emerged as a powerful tool for the study of these devices. Fluid-structure interaction (FSI) simulation is currently the most exhaustive approach as it accounts for both the solid domain mechanics and blood flow dynamics [2]. In this context, this work presents a computational framework for the FSI simulation of mechanical aortic valves, aiming at providing a robust and affordable tool supporting their design and optimization, potentially replacing *in vitro* tests recommended by the standard ISO 5840:2021.

## Methods

An idealized geometrical model of the aortic root including a portion of the ascending aorta and the left ventricular outflow tract was created using HyperMesh (Altair Engineering, MI, USA) [3]. A geometrical model of a commercial mechanical bileaflet aortic valve (St Jude Medical Regent bileaflet valve, Abbott Laboratories, IL, USA) with a size of 25 mm was generated using SolidWorks (Dassault Systèmes, FR) (Fig. 1A). The two models were assembled by placing the valve cuff in supra-annular position. The resulting model was meshed in HyperMesh. The fluid volume enclosed by the aortic root was discretized with ~931k hexahedral elements, valve leaflets were discretized with ~2,7k quadrilateral shell elements each, and valve frame and cuff were discretized with ~28k and ~26k tetrahedral elements, respectively. FSI simulations were performed using LS-DYNA 971 R13.0 (Ansys Inc., PA, USA), with an “operator split” Lagrangian-Eulerian approach, to model the interaction between the fluid domain and the valve. Physiological pressure waveforms were imposed at the inlet and at the outlet of the fluid domain (Fig. 1B). The no-slip condition was applied at the solid-fluid interface. The aortic root was assumed as a rigid wall boundary.

## Results

The contour maps of the velocity magnitude confirm the capability of the FSI approach in replicating the expected kinematics of valve opening/closure and the

resulting fluid dynamics (Fig. 1C). Regarding the latter, the FSI model appropriately replicates: (1) the three distinct jets configuration characterizing systolic flow, a consequence of the three-orifices configuration of the bileaflet mechanical valve; (2) the flow field during valve closure, when blood flow is accelerated across the closing leaflets; (3) the low velocities in the aortic root along late diastole, despite the expected minor leakage. The FSI simulation enabled the *in silico* evaluation of the effective orifice area (EOA), which for the case under study was equal to 2.46 cm<sup>2</sup>, thereby satisfying the EOA requirement indicated by ISO 5840:2021.

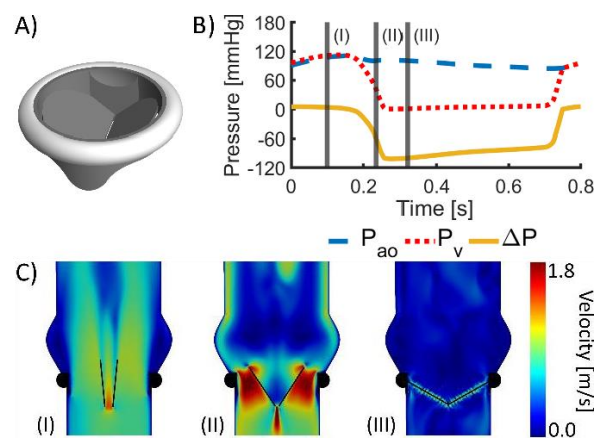


Figure 1: A) CAD model of the valve; B) Aortic pressure ( $P_{ao}$ ), ventricular pressure ( $P_v$ ), and transvalvular pressure drop ( $\Delta P$ ) waveforms; C) Velocity magnitude contours on a long-axis section during the systole (I), valve closure (II) and diastole (III).

## Discussion

The preliminary results of this work suggest that the proposed FSI framework, based on a Lagrangian-Eulerian formulation, is capable of successfully capturing the kinematics and fluid dynamics features of a mechanical heart valve. In future research, this simulation approach will be adopted to study various scenarios with different anatomical aspects (e.g., aortic wall curvature, presence of the coronary arteries), methodological aspects (e.g., aortic wall distensibility, different blood rheological model), and mechanical valve designs.

## References

1. Otto et al, Circulation, 143:e35-e71, 2021.
2. Nobili et al, J Biomech, 41:2539-2550, 2008.
3. Carbonaro et al, Struct Multidiscip Optim, 64:1825-1842, 2021.



# MODELING OF BICAVAL TRANSCATHETER SYSTEM IN SEVERE TRICUSPID REGURGITATION

Fabrizio Crasci (1,3), Stefano Cannata (2), Caterina Gandolfo (2), and Salvatore Pasta (1,3)

1. Dipartimento di Ingegneria, viale delle Scienze Ed.8, University of Palermo, Italy;

2. Interventional Cardiology Unit, IRCCS ISMETT via Tricomi, 5, Italy;

3. Department of Research, IRCCS ISMETT via Tricomi, 5, Italy

## Introduction

Tricuspid regurgitation (TR) is a type of heart valve disease in which tricuspid valve (TV) does not close properly [1]. Consequently, blood leaks backward into the right atrium increasing atrial pressure and leading to heart dilatation. The development of non-invasive therapeutic strategies of the replacement of the TR has gained a remarkable attention. TR can be indirectly treated by caval valve implantation using device implanted in the caval anatomy to alleviate congestive signs of heart failure and the hemodynamic impairment [2]. To perform caval valve implantation, the transcatheter bicaval system (TricValve) is the first type clinically-used device to treat TR by reducing caval pressure and improve the functional status at the 8-week follow-up [3, 4]. The TricValve system is composed of two valves, one implanted in the superior vena cava (SVC) and the other one in the inferior vena cava (IVC). The aim of the study is to carry out a computational analysis of the structural and hemodynamic performance of the TricValve system in patient-specific model.

## Materials and methods

The case of a 72-yrs old gentlemen with severe TR and sings of heart failure was investigated. The simulation performed consisted of a) delivering both the IVC and SVC devices in the human host, followed by an elastic recoil, b) computational fluid dynamic analysis of post-TricValve deployment. A 3D model was created from the patient's computed tomography (CT) images [5]. Patient's geometry was then meshed with triangular shell element (S3) and uniform thickness of 1.5 mm. The model of the two valves was developed from a single wire replicated in polar series and then wrapped on a primitive surface. The devices were then positioned in the patient vena cava anatomy with the support of CT images. Both SVC and IVC devices were meshed with size 0.5 mm resulting in 149939 and 167729 hexahedral-structured elements, respectively (C3D8).

## Results

Figure 1 shows a comparison between the final deformed shape of TricValve in the anatomic part and the fluoroscopic image taken during the intervention. We also found high velocities magnitude at the two systolic peaks rather than the diastole. During diastole (0.44 s), when the valve leaflets of both SVC and IVC devices are closed, the velocity drastically reduces.

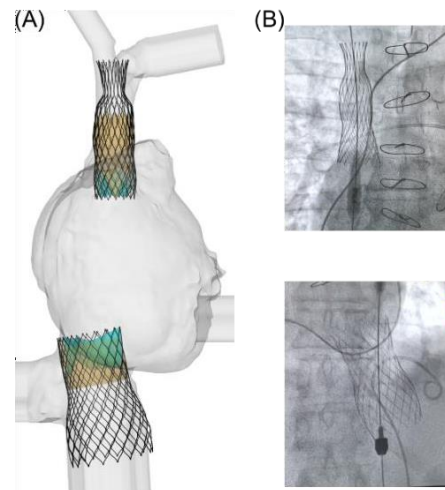


Figure 1: (A) Final deformed shape of TricValve; (B) fluoroscopic images

## Discussion

To the best of our knowledge, this is the first study describing the biomechanical performance of the new TricValve system to treat severe TR. The most striking findings are the contact pressure as indicator of the risk of stent frame migration and the low flow velocity alleviating the hemodynamic impairment during diastole. Computational flow analysis has allowed us to quantify the flow velocity during the cardiac beating. We speculate that the low flow velocity seen in diastole may allow to outflow the cardiac flow in a larger time period with respect to the pre-TricValve hemodynamic conditions. This may reduce the hemodynamic impairment with the left heart and then the pressure into the right atrium, thereby portending remodeling of the right atrial chamber. This study can bring new insights on the biomechanics of the TricValve system to better understand device positioning and flow hemodynamic. Findings may also be used to improve the design of novel transcatheter heart valve for the treatment of severe TR in the context of complex clinical conditions.

## References

1. Kadri AN, et al. Heart; 105(23): 1813-17, 2019.
2. Altisent OAJ, et al. Journal of clinical 10(19):4601, 2021,
3. Lauten A, et al. Journal of the American College of Cardiology, 59(13): E2046-E46, 2012
4. Lauten A, et al. Eur Heart J 2010; 31(10): 1274-81.
5. D'Ancona G, et al. Interactive cardiovascular and thoracic surgery, 17(3): 576-8, 2013

## Acknowledgements

Fabrizio Crasci thanks the IRCCS ISMETT and the PNRR for supporting his research.



# BLOOD DYNAMICS IN THE LEFT HEART TO ASSESS TURBULENCE FOR MITRAL REGURGITATION: A COMPUTATIONAL STUDY BASED ON MULTI-SERIES CINE-MR IMAGES

Lorenzo Bennati (1), Vincenzo Giambruno (2), Francesca Renzi (1), Venanzio Di Nicola (2), Caterina Maffei (1), Giovanni Puppini (3), Giovanni Battista Luciani (2) and Christian Vergara (4)

1. Department of Surgery, Dentistry, Pediatrics, and Obstetrics/Gynecology, University of Verona, Italy;

2. Division of Cardiac Surgery, Department of Surgery, Dentistry, Pediatrics, and Obstetrics/Gynecology, University of Verona, Italy;

3. Department of Radiology, University of Verona, Italy;

4. LaBS, Dipartimento di Chimica, Materiali e Ingegneria Chimica Giulio Natta, Politecnico di Milano, Italy

## Introduction

Mitral valve regurgitation (MVR) is a condition leading to a formation of a regurgitant jet in the left atrium during the systolic phase due to an incomplete closure of the mitral valve leaflets. The formation of the regurgitant jet may give rise to: i) turbulent atrial flow leading to hemolysis in the atrium and ii) washing out of stagnant blood in the atrium preventing the formation of thrombi.

In this respect, computational methods represent a non-invasive way to better understand the left heart pathophysiology and to predict the outcomes of surgical interventions. Among different models, we focus on Computational Fluid Dynamics (CFD) with imposed motion, where the displacement of the left heart (LH) internal wall surfaces (left atrium, left ventricle and aortic root) and valves is provided from kinetic medical images.

The aim of this work is to perform a fully patient-specific image-based CFD simulation with imposed motion of the whole heartbeat on a healthy subject and, for the first time, on patient with MVR to compare, between the subjects, the occurrence of turbulence, risk of hemolysis and thrombi formation. To do this, we reconstruct the geometry and displacement of the left heart internal wall surfaces and valves from multi-series cine-MRI images.

## Methods

To reconstruct the geometry and displacement of the LH internal wall surfaces, we combine two different reconstruction techniques used for the left ventricle and for the left atrium and aortic root, respectively.

Concerning the valves, we reconstruct the patient-specific mitral valve in its fully open and fully closed configuration by using the method proposed in [1]. For the aortic valve, instead, we deform a template geometry to match its annulus with the annulus detected from the cine-MRI images.

For CFD, we consider the Navier-Stokes equations in the Arbitrary Lagrangian-Eulerian framework with a LES model for transition to turbulence [2] and a resistive method to manage the valve dynamics [3] that has been modeled in an on-off modality, where the reconstructed

leaflets opened and closed instantaneously according to the pressure drop across the valve and the flow rate through the valve plane, respectively.

## Results

In Figure 1, we report the velocity standard deviation (SD) at a representative time instant of the systolic phase for the healthy scenario H (left) and for the regurgitant patient R (right). We notice that the regurgitant jet in the MVR case leads to a larger amount of transition to turbulence especially in the left atrium resulting also in a higher risk of formation of hemolysis. Moreover, we observe that MVR promotes a more complete washout of stagnant flows in the left atrium during the systolic phase and in the left ventricle apex during diastole. Our results are supported by the validation with echo color Doppler velocity measures in the healthy subject and by a qualitative comparison with a cine-MRI flow pattern in the MVR case highlighting a good agreement and thus the ability of our method to give clinically significant information.

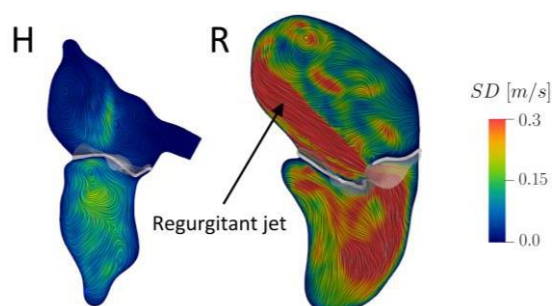


Figure 1: velocity standard deviation (SD) at a representative time instant for H (left) and R (right).

## References

1. Stevanella, M. et al, Cardiovascular Engineering and Technology, 2, 66–76, 2011.
2. Nicoud, F. et al, Physics of Fluids, 2011.
3. Fedele, M. et al, Biomechanics and Modeling in Mechanobiology, 2017.



# ANALYSING WALL SHEAR STRESS PROFILES AND STRUCTURAL BEHAVIOR IN CAROTID BIFURCATIONS

Sara Zambon (1), Mariachiara Arminio (1), David A. Steinman (2),  
Claudio Chiastra (1), Umberto Morbiducci (1), Diego Gallo (1)

1. Polito<sup>BIO</sup>Med Lab, Department of Mechanical and Aerospace Engineering, Politecnico di Torino

2. Biomedical Simulation Lab, Department of Mechanical & Industrial Engineering, University of Toronto

## Introduction

Near-wall hemodynamics and structural stress of the vasculature might be involved in the initiation of atherosclerosis at the carotid bifurcation [1,2]. Most of the literature has generally focused on either structural or hemodynamic quantities, although their coupling can be implemented in fluid-structure interaction (FSI) approaches. In this regard, rigid-wall simulations have recently shown that the intra-cycle variability of wall shear stress (WSS) topological skeleton is associated with intima-media thickening after carotid endarterectomy [1]. Here, fully coupled two-way FSI simulations accounting for arterial wall prestress, vessel anisotropic material properties, and external tissue support are performed to explore the nature of the relationship between hemodynamic and wall structural quantities.

## Methods

Seven healthy carotid bifurcations models were reconstructed from magnetic resonance (MR) angiography [1] including 15 radii of the common carotid artery (CCA). Arbitrary Lagrangian-Eulerian formulation-based FSI simulations were carried out, modelling the vessel wall as a fiber-reinforced anisotropic nonlinear material (Holzapfel-Gasser-Ogden model). The initial loading state and the fibers orientations were obtained through wall vessel prestress [4]. Subject-specific flow rates from MR measurements [1] were used for the CCA inflow boundary condition (BC) and for tuning three-element Windkessel models at the external and internal carotid artery (ECA and ICA) outflow sections. Viscoelastic support from external tissues was accounted imposing a Robin-type BC [3]. All simulations were carried out in SimVascular [3]. The near-wall hemodynamics was characterized in terms of the canonical WSS-based quantities time-average WSS (TAWSS) and oscillatory shear index (OSI). In addition, the WSS topological skeleton was characterized in terms of variability of the WSS contraction/expansion action on the endothelium, by the topological shear variation index (TSVI) [1]. Wall mechanics was characterized in terms of cycle-averaged maximum principal stress ( $\sigma_1$ ) and strain ( $\epsilon_1$ ). Model-specific 20<sup>th</sup> percentile (TAWSS) and 80<sup>th</sup> percentile ( $\sigma_1$ ,  $\epsilon_1$ , OSI, and TSVI) values were used to quantify the relative surface area (SA) below (TAWSS) or above ( $\sigma_1$ ,  $\epsilon_1$ , OSI, TSVI) threshold values. The relationship of WSS-based and structural quantities was evaluated in terms of (i) co-localization of SAs, and (ii) a sector-

based statistical analysis, where hemodynamic descriptors were averaged over 1.5mm/30° luminal sectors and divided into model-specific low, mid, and high tertiles to perform a statistical analysis (Student's t test) on the associated structural quantities.

## Results

SI values for the couplets of hemodynamic and structural quantities are reported in Table 1, highlighting a moderate co-localization: SAs of hemodynamic descriptors were mainly located at the carotid bulb, while the highest  $\sigma_1$  and  $\epsilon_1$  were located around the bifurcation apex. Sectors exposed to low TAWSS values exhibited the highest  $\sigma_1$  (Figure 1). Sectors exposed to high OSI exhibited higher  $\sigma_1$ , but not  $\epsilon_1$ , than sectors exposed to low OSI. Conversely, sectors exposed to high TSVI exhibited higher  $\sigma_1$  and  $\epsilon_1$  values than low TSVI sectors.

SI	TAWSS	OSI	TSVI
$\sigma_1$	0.33±0.07	0.31±0.07	0.29±0.08
$\epsilon_1$	0.24±0.05	0.25±0.06	0.29±0.07

Table 1: SIs (mean±SD) between hemodynamic and structural quantities

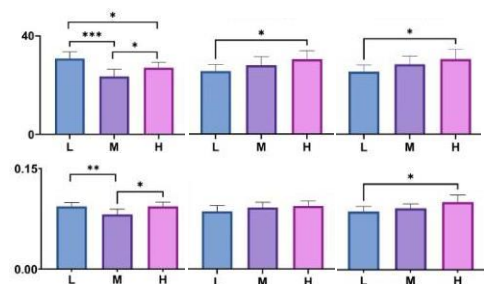


Figure 1: Model-specific hemodynamic vs. structural quantities. Histograms represent model-specific tertiles (L: low tertile; M: mid tertile; H: high tertile).

## Discussion

The present findings suggest a complex relationship between hemodynamic and structural quantities, with model-specific differences deserving further investigations.

## References

1. Morbiducci et al, Ann Biomed Eng, 48:2936–2949, 2020
2. Tang et al, J Biomech, 41:727–736, 2008.
3. Bäumlner et al, Biomech Model Mech, 19:1607–28, 2020.
4. Hariton et al, J Theor Biol, 248:460–470, 2007.



# ADVANCED CMR-BASED STRATEGY FOR FINITE ELEMENT ANALYSIS OF MITRAL VALVE PROLAPSE BIOMECHANICS

Davide Tondi (1), Francesco Sturla (2,1), Mateo Marin-Cuartas (3), Ricardo Spampinato (3), Maja-Theresa Dieterlen (3), Alberto Redaelli (1), Michael A. Borger (3), Emiliano Votta (1,2)

1. Politecnico di Milano, Milano, Italy; 2. IRCCS Policlinico San Donato, San Donato Milanese, Italy;  
3. Leipzig Heart Center, Leipzig, Germany

## Introduction

Degenerative mitral valve prolapse (MVP) affects up to 3% of the population and carries the risk of serious secondary complications [1]. MVP biomechanics has already been investigated through finite element (FE) models based on cardiovascular magnetic resonance (CMR) imaging [2]. However, a dedicated approach to reconstruct 3D MV geometry is required since CMR data consist in stacks of 2D images. Also, chordae tendineae cannot be clearly identified and uncertainty in their definition in the FE model may heavily impact on the reliability of numerical analysis. Based on cardiovascular magnetic resonance (CMR) imaging, we aimed to provide additional insight into MVP biomechanics by advancing our FE modeling strategy.

## Methods

A 45-year-old male subject with healthy MV and a 57-year-old male patient with severe MVP-induced regurgitation underwent CMR exam on a Philips Ingenia 1.5T scanner (Philips Medical System). CMR images were acquired on 18 evenly distributed radial planes [2], and on a stack of short-axis planes encompassing the entire MV. Under the hypothesis of pixel-intensity similarity along their intersections, CMR planes were realigned by optimizing their normalized cross correlation [3]. After manual tracing of MV annulus, leaflets and papillary muscle (PMs) tips at end diastole, the stress-free MV leaflets geometry was reproduced using Fourier and NURBS fitting functions (Fig. 1.a) and discretized ( $\Omega_{ED}^{GRID}$ ). A functionally equivalent model of chordae tendineae was included with insertions uniformly distributed over the leaflet surface (15 insertions/cm<sup>2</sup>); in MVP case, chordal density was locally reduced in the prolapse region based on a Gaussian function. To calibrate initial chordal length  $\Omega_{ED}^{GRID}$  was morphed onto the mid-systolic leaflet surface reconstructed from CMR data ( $\Omega_{MS}^{CMR}$ ): i) MV annulus and free edge were displacement-controlled to match the corresponding  $\Omega_{MS}^{CMR}$  profiles, ii)  $\Omega_{ED}^{GRID}$  was drive to contact  $\Omega_{MS}^{CMR}$  by a 5 mmHg pressure load, yielding the new position of chordae insertion, iii) simulating the chordae as inextensible, the MV model was pressurized to 120 mmHg, extracting the true force distribution in the chordae to infer their initial length at ED [4]. MV closure was finally simulated from ED to MS in Abaqus/Explicit (Dassault Systèmes) applying a 120 mmHg pressure load; anisotropic and hyperelastic mechanical response of MV tissues [4] as well as annular and PMs motion from CMR data were included.

## Results

As tested on both the models, chordal length calibration allowed for consistency between the MV configuration simulated at MS and ground-truth CMR data (Fig. 1.b-c), reporting a mean Euclidean nodal distance from  $\Omega_{MS}^{CMR}$  equal to 0.96 mm and 1.50 mm in normal and MVP model, respectively. As compared to ED design, in the healthy MV, calibration made 95% of chordae longer by 4.2 mm (+12.3%) and 5% shorter by 0.6 mm (-1.4%), on average. In the MVP model, 19% of chordae were extended by 3.1 mm (+13.4%) while 81% were shortened by 4.0 mm (-12.5%), on average.

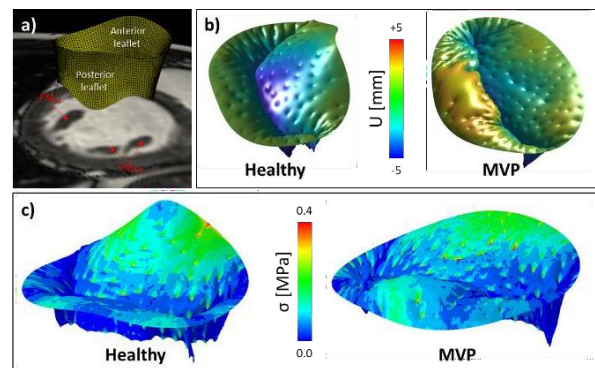


Figure 1: a) MV model at ED, b) relative leaflets displacement above the annulus, c)  $\sigma_1$  on MV leaflets

At MS, maximum principal stress ( $\sigma_I$ ) markedly increased on a large portion of the prolapsing posterior MV leaflet if compared to healthy MV model (Fig. 1.c). Force transferred by chordae to PMs reached 20.7 N and 25.4 N in the normal and MVP model, respectively.

## Discussion

Advances to our CMR-based MV modeling strategy effectively improved MV model reliability on a patient-specific basis, thus offering a deeper insight into biomechanical derangements associated with degenerative MVP.

## References

1. Morningstar *et al*, J Am Heart Assoc 2021, 10: e022332
2. Sturla *et al*, JTCVS 2014, 148: 1025-34
3. Carminati *et al*, Comput Biol Med 2014; 46: 42-50
4. Khalighi *et al*, Ann Biomed Eng 2019; 47(1): 60-74

## Acknowledgements

IRCCS Policlinico San Donato is a clinical research hospital partially funded by the Italian Ministry of Health.



# A SURROGATE MODEL OF THE THROMBECTOMY PROCEDURE FOR IN SILICO STROKE TRIALS

Sara Bridio, Giulia Luraghi, Jose Felix Rodriguez Matas, Francesco Migliavacca,  
for the INSIST investigators (www.insist-h2020.eu)

LaBS-CompBioMech, Dept. of Chemistry, Materials and Chemical Engineering, Politecnico di Milano, Italy

## Introduction

*In silico* trials (ISTs) consist in virtually simulating a medical procedure on a cohort of virtual patients, and aim at supporting the development and evaluation of new medical devices, procedures, or drugs, reducing the risks, time and cost of clinical trials [1]. Endovascular thrombectomy (EVT) is a minimally-invasive mechanical treatment for acute ischemic stroke, aiming at removing the thrombus occluding a cerebral artery with a stent-retriever and/or aspiration catheters. In this work, a surrogate model of the (EVT) procedure is developed and integrated in a framework to run the first proof-of-concept *in silico* stroke trials [2].

## Methods

One hundred cerebrovascular anatomies were reconstructed from images of stroke patients within the INSIST European project (www.insist-h2020.eu). Thrombi of different length and composition were modeled (Fig.1A), following distributions found in stroke patients. Finite-element (FE) analyses of EVT with stent-retriever were run with the settings described in [3]. A simulated EVT procedure is successful if the thrombus is removed from the vessels, unsuccessful otherwise (Fig.1B). A geometric characterization of the vascular anatomies was performed as described in [4], and an analysis was conducted to identify the most important parameters for the determination of the virtual EVT outcomes. A total of 8 parameters (6 anatomic and 2 thrombus characteristics) were identified and chosen as inputs for the surrogate EVT model. The chosen surrogate model is a binary classifier, using a logistic regression algorithm, trained on the realizations from the FE simulations. The final model, given as input the 8 parameters describing a new patient, provides the probability of successful recanalization.

The surrogate model was integrated in an event-based framework for IST for stroke treatments, developed by INSIST partners [2]. The first step of the framework generates the virtual population of stroke patients, from which the required set of 8 input parameters is derived. The surrogate EVT model is interrogated for each virtual patient, providing population-based results on the effectiveness of the treatment. First, a *Validation trial* is run to verify the reliability of the model, by comparing the IST results with a real clinical trial [5]. Then, a *Thrombus composition trial* is run to compare the treatment outcomes in different subpopulations, followed by a *Device comparison trial* demonstrating the use of the IST for comparing the performance of different devices.

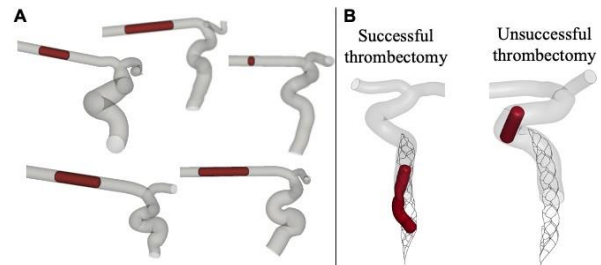


Figure 1: A) Examples of cerebrovascular models. B) Successful and unsuccessful virtual EVT procedures.

## Results

The *Validation trial* showed that the surrogate EVT model was able to produce a similar success-rate as the real clinical trial. The *Thrombus composition trial* reported higher success-rate for the subpopulation with soft thrombi (with high content of red blood cells), with respect to hard thrombi (rich in fibrin). The *Device comparison trial* showed improved recanalization results with a newer stent design, although these results are only exploratory as the surrogate model for the newer device lacks data for validation.

## Discussion

This work presented the development of a surrogate model of the EVT procedure. The model was integrated in a framework for *in silico* stroke trials and its reliability was proven by comparison with the results of a real clinical trial with the same inclusion criteria. Two other exploratory ISTs were run, demonstrating the use of the IST platform for the selection of subpopulations for the real clinical trials, or for a preliminary assessment of the performance of new devices, which can save the costs and risks of traditional clinical trials.

## References

1. Viceconti et al, Int J of Clinical Trials, 3(2):37-46, 2016.
2. Miller et al, CMPB, 228:107244, 2023.
3. Luraghi et al, Interface Focus, 11(1):20190123, 2021.
4. Bridio et al, Front Med Technol, 3:719909, 2021.
5. Berkhemer et al, New Engl J Med, 372:11-20, 2015.

## Acknowledgements

This project has received funding from the European Union's Horizon 2020 research and innovation programme under grant agreement No 777072 and from the MIUR FISRFISR2019\_03221 CECOMES.



# A STATISTICAL SHAPE MODELING FRAMEWORK TO CORRELATE MORPHOLOGY AND HEMODYNAMICS OF COMPLEX GREAT VESSELS

Marilena Mazzoli (1,2), Martino A. Scarpolini (1,3), Benigno M. Fanni (1), Simona Celi (1)

1. BioCardioLab, Fondazione Toscana Gabriele Monasterio, Italy; 2. Department of Information Engineering, University of Pisa, Italy; 3. Department of Industrial Engineering, University of Rome "Tor Vergata", Italy.

## Introduction

Statistical Shape Models (SSMs) are well-established tools for assessing the variability of vascular geometries. Starting from a heterogeneous population, SSMs can provide useful biomarker information, in terms of geometrical features (i.e. size, curvature, orientation). This technique is based on a non-rigid registration, which may be challenging to perform with complex anatomies. In the context of vascular anatomies, several studies have been presented [1,2], mainly focused on the aorta with the exclusion of the supra-aortic branches. To overcome this limitation, which is also reflected in the subsequent Computational Fluid Dynamics (CFD) clustering studies, we developed a non-rigid registration algorithm. The purpose of this work is to demonstrate the potentiality of this novel algorithm as applied to a different great vessel, the pulmonary artery. Moreover, a correlation study between the morphological and hemodynamic features is reported, obtained from SSMs and CFD simulations, respectively.

## Methods

A total of 21 segmented pulmonary arteries and 28 aortas were considered, originated from MRI and CT images respectively. All the pulmonary arteries were affected by Tetralogy of Fallot. The dataset of thoracic aortas included both healthy and aneurysmatic cases. All the datasets were segmented in 3D-Slicer using a region-growing algorithm. The segmented geometries were used to develop the SSM, by registering a template geometry on all the other target geometries of the dataset. Starting from previous work [3], we developed an in-house algorithm for the non-rigid registration based on (i) a modified second order gradient descent approach, (ii) a loss function based on the minimization of chamfer distance and (iii) four steps of remeshing. The second step was performed to achieve the dimensionality reduction of the problem to few meaningful geometric features through the application of Principal Component Analysis. The first principal components (or modes), significant for about 98% of the total variance, were used to reconstruct 5 new geometries by varying the most significant mode from -2 to +2 standard deviation (SD). A progression in the shape was observed for both pulmonary artery and aorta and the resulting geometries were used to assess the effects of morphological variability on the correspondent CFD models. Simulations were carried out using ANSYS Fluent, considering the fluid as Newtonian and a laminar flow. For the hemodynamic analysis the wall shear stress, its related indexes (i.e.

OSI, TAWS) and the flow split (only for the pulmonary arteries) were evaluated. Finally, an analysis of correlation was performed between the morphological and the hemodynamic features to derive a relationship between shape, fluid dynamics and pathology.

## Results

Although most of the target geometries presented very peculiar shapes, different from source mesh one, a maximum error of 0.7 mm in the registrations was obtained by applying the proposed novel algorithm. By varying the first mode, a progression in the shape from a short, straight and corrugated to a long and curved pulmonary artery was observed; meanwhile, for the thoracic aortas it was noticed a progression from healthy to completely aneurysmatic aorta. All these results were in perfect agreement with the composition of our initial datasets. Moreover, significant correlations between the variation of the first mode, and hence the variation in size, and hemodynamical parameters were discovered (example on OSI variation reported in Figure 1).

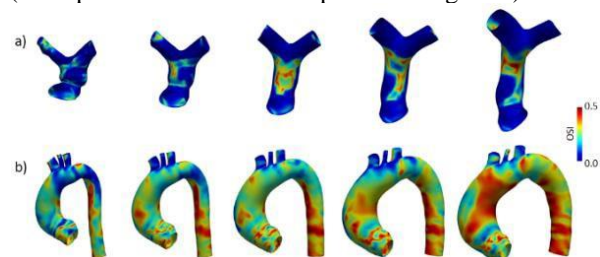


Figure 1: OSI values on geometries generated by the variation of the first mode from -2 (left) to +2 (right) SD for pulmonary vessel (a) and aorta (b).

## Discussion

In this work we aimed to highlight the potential of SSMs to generate new realistic vascular anatomies for CFD simulations and the versatility of the presented novel algorithm. In fact, good non-rigid registration results were achieved not only over widely different geometries but also between different vascular districts.

## References

1. Bruse et al, J Thor Cardiovasc Surg, 153.2: 418-427, 2017.
2. Sophocleous et al, EJCTS, 55.4: 704-713, 2019.
3. Nicolet et al, ACM Trans Graph, 40(6):1-13, 2021.

## Acknowledgements

This work was supported by the MeDiTaTe Project from the European Union's Horizon 2020 research and innovation programme under Grant Agreement 859836.



# APPLICATION OF MACHINE LEARNING TECHNIQUE IN THE PREDICTION OF THE HEMODYNAMIC PARAMETERS OF AN ATHEROSCLEROTIC PLAQUE

Sohrab Jafarpour (1), Hamed Farokhi (2), Mohammad Rahmati (3), Alireza Gholipour (4)

1-3. Department of Mechanical and Construction Engineering, Northumbria University, United Kingdom 4. Sydney Medical School & School of Health Sciences, Faculty of Medicine and Health, University of Sydney, NSW, Australia

## Introduction

Risk assessments of atherosclerotic plaques require reliable evaluation of changes occurring in hemodynamic parameters during the progression of plaque [1]. Fluid-structure interaction (FSI) modelling is the most reliable method to study hemodynamic parameters [2]. However, FSI modelling is a costly process and yet it is not considered an efficient way in clinical settings. Meanwhile, the machine learning (ML) technique offers a promising method for creating mathematical models with a large decrease in processing costs and increased simplicity [3]. The aim of this study is to develop a tool with which the hemodynamic parameters of an unstable plaque can be assessed both reliably and efficiently and it can assist the practitioner in the vulnerability assessment of plaque. For this purpose, deep neural network algorithms (DNNs) are implemented to develop surrogate models from the corresponding FSI models of plaque. Three separate feed-forward networks are designed to predict the changes in the hemodynamic parameters namely, the maximum of wall shear stress signal (WSS), time-averaged wall shear stress (TAWSS), and the maximum velocity in a cardiac cycle.

## Methods

To train the DNNs, a design-of-experiment method is implemented to generate sampling data that are appropriately distributed across the design and analysis space. The current analysis space is made of the geometric risk factors i.e., the stenosis ratio ( $25 \leq \%St \leq 70$ ), the plaque shoulder length ( $2.5 \text{ mm} \leq l_{plq} \leq 8 \text{ mm}$ ), and the fibrous cap thickness ( $0.025 \text{ mm} \leq f_c \leq 0.1 \text{ mm}$ ). Then, the corresponding FSI models of data are developed based on a 3-D idealised geometry of negatively remodelled plaque. The surrogate models take the three geometrical parameters as input to predict the intended hemodynamic parameter.

## Results

The optimum architectures for DNNs are obtained based on the absolute relative error depicted in Eq.1. Each network is trained 10000 times and the best models are provided in Table 1.

$$RE = abs\left(\frac{\hat{\chi} - \chi}{\chi}\right) \times 100, \quad (1)$$

In which  $\hat{\chi}$  is the predicted value of the desired hemodynamic parameter via DNN and  $\chi$  is derived from the FSI model. In Figure 1, the effect of changes in the stenosis ratio and the plaque shoulder length on the WSS is obtained via network A and is compared with FSI models.

Network	Output	Maximum RE	Architecture
A	Peak of WSS	3.22 %	(5 5 5)
B	TAWSS	3.46%	(5 5 5)
C	Velocity	3.66%	(3 3 3)

Table 1: Details of the optimum DNNs.

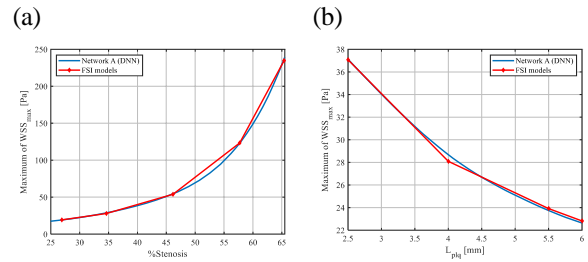


Figure 1: The performance of network A (DNN) versus the FSI models. (a) The effect of stenosis ratio ( $l_{plq} = 7 \text{ mm}$  and  $f_c = 0.045 \text{ mm}$ ). (b) The effect of plaque shoulder length ( $\%St = 34.62$  and  $f_c = 0.045 \text{ mm}$ ).

## Discussions

The networks provided excellent performance with an absolute relative error of less than 4%. According to the results, machine learning techniques can reliably help practitioners in clinical risk assessment procedures.

## References

- Pandey, R., et al., *Numerical approach*. Computer Methods and Programs in Biomedicine, 2020. **187**: p. 105243.
- Carpenter, H.J., et al., *International Journal of Engineering Science*, 2020. **147**.
- Quer, G., et al., *JACC State-of-the-Art Review*. Journal of the American College of Cardiology, 2021. **77**(3): p. 300-313.



# IMPACT OF VESSEL MORPHOLOGY ON HEMODYNAMICS OF LENTICULOSTRIATE ARTERIES DURING ATRIAL FIBRILLATION

Francesco Tripoli (1), Andrea Saglietto (2,3), Jaco Zwanenburg (4), Geert Jan Biessels (5), Gaetano Maria De Ferrari (2,3), Matteo Anselmino (2,3), Luca Ridolfi (1), Stefania Scarsoglio (1)

1. *PolitoBIOMed Lab, Politecnico di Torino, Turin, Italy*; 2. *Div. of Cardiology, Cardiovascular and Thoracic Dept., "Città della Salute e della Scienza" Hospital, Turin, Italy*; 3. *Dept. of Medical Sciences, University of Turin, Turin, Italy*; 4. *Dept. of Radiology, University Medical Center Utrecht, Utrecht, The Netherlands*; 5. *UMC Brain Center, University Medical Centre Utrecht, Utrecht, The Netherlands.*

## Introduction

Lenticulostriate arteries (LSAs) are small perforating arteries mainly departing from the middle cerebral artery (MCA) and, less frequently, from the anterior cerebral artery (ACA). These arteries are responsible for supplying blood to important deep brain structures such as the basal ganglia. LSAs are susceptible to small vessel disease, which is one of the main mechanisms of subcortical vascular dementia development [1]. In addition, there is growing evidence that an alteration of deep cerebral hemodynamics due to atrial fibrillation (AF) increases the risk of vascular dementia and cognitive impairment [2]. In this complex context, an important role could be played by the almost orthogonal branching of these vessels. The purpose of this study, which combines CFD analysis of LSAs with 7T high-resolution magnetic resonance imaging (MRI), is to investigate the impact of different LSAs morphologies on cerebral hemodynamics during AF events.

## Methods

High-resolution 7T cerebral MRI data of 10 subjects were used for the reconstruction of the vasculature geometry leading to a total of 17 segmented LSAs. To perform 3D CFD simulations, a validated 0D cardiovascular-cerebral model [3], which simulates the cerebral hemodynamics in AF and sinus rhythm (SR), was used to obtain inlet and outlet conditions. By the Vascular Modeling Toolkit (VMTK) a number of subject-specific geometric characteristics (tortuosity, radius, bifurcation angles) were extracted. Relationships between wall shear stress (WSS) pattern in LSAs inlets and morphological features were assessed by multiple regressions. In particular, the hemodynamic variable investigated was the  $\Delta WSS$ , which was defined as the difference between the WSS magnitude obtained in correspondence of the 95<sup>th</sup> percentile of  $p(Q_{max})$  and the one obtained at the 5<sup>th</sup> percentile of  $p(Q_{min})$ , where  $p(Q_{max})$  and  $p(Q_{min})$  are respectively the probability density functions of the maximum and minimum values per beat of the MCA flow rate time series, which was 5000 beats long.

## Results

During AF the LSAs proximal regions were exposed to an increased range of WSS compared to SR (see Fig. 1). Moreover, regressions revealed a statistically significant correlation between some of the geometric characteristics and the 90<sup>th</sup> percentile values of the WSS range ( $\Delta WSS$ ).

## Discussion

The present study shows how the local hemodynamics of lenticulostriate arteries may be affected by their morphologies, such as different MCA or ACA radii in the bifurcation proximity or different in-plane bifurcation angles. This suggests that LSAs with particular morphologies may be more prone to vascular disease.

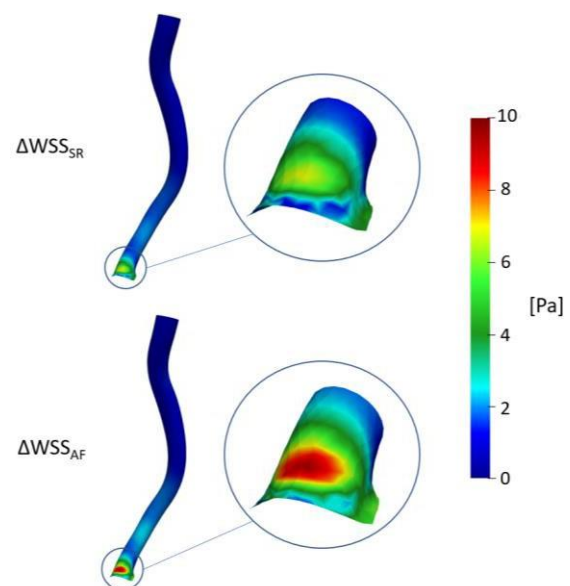


Figure 1: CFD model of a representative LSA displaying local  $\Delta WSS$ : SR (top) and AF (bottom).

## References

1. Román, G. C., Erkinjuntti, T., Wallin, A., Pantoni, L., & Chui, H. C. (2002). Subcortical ischaemic vascular dementia. *The Lancet. Neurology*, 1(7), 426–436.
2. Anselmino, M., Scarsoglio, S., Saglietto, A., Gaita, F., & Ridolfi, L. (2016). Transient cerebral hypoperfusion and hypertensive events during atrial fibrillation: a plausible mechanism for cognitive impairment. *Scientific reports*, 6, 28635.
3. Saglietto, A., Scarsoglio, S., Ridolfi, L., Gaita, F., & Anselmino, M. (2019). Higher ventricular rate during atrial fibrillation relates to increased cerebral hypoperfusions and hypertensive events. *Scientific reports*, 9(1), 3779.



# AORTIC ARCH ANGULATION INCREASES BLOOD PRESSURE IN AN EX-VIVO PORCINE MODEL

Ariel F. Pascaner (1), Tim Mandigers (2)(3), Martina Schembri (1), Sonja Jelic (1), Maurizio Domanin (2)(4), Ferdinando Auricchio (1), Santi Trimarchi (2)(4), Michele Conti (1)

1. Civil Engineering and Architecture Department, Università degli Studi di Pavia, Pavia, Italy;
2. Department of Vascular Surgery, Fondazione IRCCS Cà Granda Ospedale Maggiore Policlinico, Milan, Italy;
3. Department of Vascular Surgery, University Medical Centre Utrecht, Utrecht, The Netherlands;
4. Clinical and Community Sciences Department, Università degli Studi di Milano, Milan, Italy.

## Background

It is well established that increased central blood pressure has major effects on cardiovascular risk and disease manifestation. However, the relationship between aortic geometry and hemodynamics has not been completely elucidated yet. This study explored the impact of severe aortic arch angulation on blood pressure in an *ex-vivo* porcine model.

## Materials and methods

We harvested the aortas of 20 pigs (commercial hybrid, near 12 months old, 160 to 180 Kg), and prepared them by removing the surrounding tissue and clamping all ramifications between the aortic root and the celiac artery. The animals were raised and sacrificed for commercial use only at a local abattoir and not for the purpose of this study. Therefore, authorization of a local ethics committee was not requested.

Two cases of aortic arch angulation were studied; namely Type I and Type III arch [1]. To emulate these arch geometries the aortas were placed into custom-made guides, which were virtually designed and subsequently 3D-printed (Figure 1). The aortas were connected into a mock circulatory loop endowed with a pulsatile pump [2]. For each aorta, the experimental workflow was the following. We first connected the aorta using the Type I arch guide and configured the circuit parameters to achieve: 4.5-5.5 L/min of cardiac output at 75 beats per minute and 70-80 mmHg – 115-125 mmHg of diastolic and systolic pressure, respectively. Pressure and flow waveforms were registered at 1 KHz for at least 20 seconds (Honeywell

40pc015g series, Morristown, NJ, U.S.A. and Em-tec, Finning, Germany, respectively). After the acquisition, we placed the aorta into the Type III arch guide and reconnected it to the circuit. To emulate the compensatory mechanisms of the heart, after changing the geometry, the stroke of the pump was adjusted to reach the same cardiac output as under the Type I geometry. Similarly, pressure and flow were registered using the Type III arch guide.

For each experiment flow and pressure data were automatically separated into individual heartbeats for post-processing. For each heartbeat, we extracted: mean flow (Q), diastolic (Pd), systolic (Ps) and mean (Pm) pressures and then averaged among the available cardiac cycles. Data were compared with paired t-tests after normality confirmation using Shapiro-Wilk test.

## Results

Table 1 shows the obtained values of mean flow and pressures for the Type I and Type III configurations. Mean flow was similar for both types of aortic arch consistently with the experimental workflow. All pressures resulted higher in a Type III arch with respect to the Type I arch ( $p < 0.001$ ).

Parameter	Type I	Type III	p
Q [L/min]	$4.73 \pm 0.41$	$4.74 \pm 0.39$	0.14
Pd [mmHg]	$73.6 \pm 1.6$	$82.5 \pm 5.7$	<0.001
Ps [mmHg]	$122.0 \pm 2.2$	$134.1 \pm 11.1$	<0.001
Pm [mmHg]	$89.7 \pm 1.5$	$98.8 \pm 6.5$	<0.001

Table 1: Results of mean flow (Q), diastolic (Pd), systolic (Ps) and mean (Pm) pressures for Type I and Type III arch geometries.

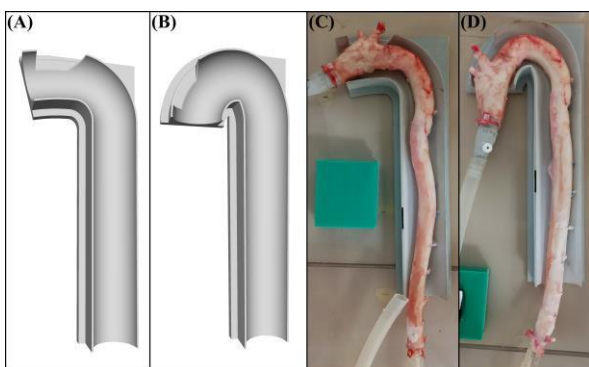


Figure 1: (A) and (B): CAD models of the Type I and Type III guides, respectively. (C) and (D): Example of aorta placed under the Type I and Type III arch guides, respectively.

## Conclusion

Our study showed that an increased angulation of the aortic arch results in higher blood pressure levels, which is a main factor for the progression of cardiovascular disease. Further studies are needed to translate these observations to *in-vivo* human arteries and to assess its impact on cardiovascular risk.

## References

1. S. Madhwal et al, J Invasive Cardiol, 20(5), 2008.
2. H. de Beaufort et al, Ann Vasc Surg, 43:302-308, 2017.

# COMPUTATIONAL PREDICTION OF THE DEGENERATION OF TRANSCATHETER AORTIC VALVE IMPLANTATION

Luca Crugnola (1), Ivan Fumagalli (2), Laura Fusini (3), Gianluca Pontone (3), Christian Vergara (1)

1. LaBS, Dipartimento di Chimica, Materiali ed Ingegneria Chimica "Giulio Natta", Politecnico di Milano, Italy;
2. MOX, Dipartimento di Matematica, Politecnico di Milano, Italy
3. Department of Perioperative Cardiology and Cardiovascular Imaging, Centro Cardiologico Monzino IRCSS, Italy;

## Introduction

Transcatheter Aortic Valve Implantation (TAVI) is a minimally invasive technique for the treatment of severe aortic stenosis (AS). Since the first procedure in 2002, TAVI has revolutionized the management of AS and become the standard of care for patients with AS at prohibitive surgical risk, and the preferred treatment for many intermediate and high-risk elderly patients [1]. Moreover, the results of recent clinical trials suggest that TAVI might be the preferred option for AS treatment even in low-risk, younger patients [2]. However, Structural Valve Deterioration (SVD), an irreversible degenerative process typical of bio-prosthetic leaflets tissue, can drastically reduce the long-term durability of the implanted valve [3]. The exact mechanisms underlying SVD are not completely understood, thus there is an increasing interest in studying this phenomenon.

Computational Fluid Dynamics (CFD) models have been mostly employed in the TAVI framework to study paravalvular leakage [4], whereas, to the best of our knowledge, only few authors tried to study SVD using a CFD approach [5].

The aim of this study is to employ a CFD model to numerically simulate post-TAVI hemodynamics inside patient-specific aortic roots and ascending aortas starting from pre-operative images, in order to identify correlations with SVD.

## Methods

The available clinical data, thanks to our collaboration with Monzino Cardiology Center, Milan, is a dataset of pre-TAVI Computed Tomography (CT) scans, balanced between patients who have experienced a premature onset of SVD after TAVI (degenerated cases) and patients who did not (non-degenerated cases). Starting from such CT scans the patient-specific aortic geometries, together with calcifications, have been reconstructed in order to generate post-TAVI computational domains by virtually implanting the valve in those geometries. In particular, in this study we considered the Edwards Sapien TAVI valves. CFD simulations are then carried out inside the generated computational domains and the results are post-processed in order to identify quantities that allows us to differentiate between the two subsets of patients.

## Results

CFD results showed that the presence of the TAVI valve gives rise to a high velocity jet in the ascending aorta and to the generation of vortical structures around this jet, as shown in Figure 1. Such structures collide with the aortic wall generating great shear stresses on the endothelium and a highly disturbed flow inside the aorta. We found that patients with degenerated TAVI present higher shear stresses and flow disturbances with respect to the non-degenerated ones, providing a clear separation between the two groups.

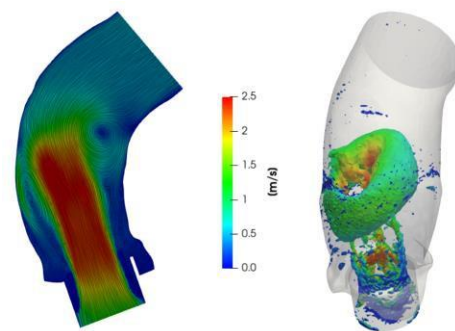


Figure 1: Left: Velocity streamlines on a longitudinal section; Right: Vortical structures, colored by velocity, quantifying flow disturbances.

## Discussion

These results suggest a correlation between a premature onset of SVD and great shear stresses and flow disturbances in the ascending aorta. High shear stresses on the aortic wall can damage both the endothelial and the blood cells, whereas the highly disturbed flow generated by the collision of the vortical structures on the aortic wall allows particles to remain inside the aortic root during the whole cardiac cycle. Thus, we think that blood-dynamics inside the ascending aorta could in principle have an impact on SVD.

This is an ongoing project, indeed we aim at employing the presented CFD approach to a wider population in order to support our findings.

## References

1. T J Cahill et al, Eur Heart J, 39(28):2625–2634, 2018.
2. M Guglielmo et al, Eur Radiol, 32(9):6017-6027, 2022.
3. A E Kostyunin et al, JAHA, 9(19), 2020.
4. M Bianchi et al, Biomech Model Mechanobiol, 18(2):435-451, 2019
5. I Fumagalli et al, Int J Num Meth Biomed Eng, to appear.



# The Effect of Early Progressive Resistive Exercise Therapy on Balance Control of Patients with Total Knee Arthroplasty

Razieh Yousefian Molla (1), Heydar Sadeghi (2), Taian Vieira (3), Amir Hossein Kahlaee (4)

1. Department of Physical Education and Sports Sciences, Faculty of Physical Education and Sport Sciences, Islamic Azad University of Karaj, Karaj, Iran; 2. Department of Biomechanics and Sports Injuries, Faculty of Physical Education and Sport Sciences, Kharazmi University, Tehran, Iran; 3. Polito<sup>BIO</sup>Med Lab and LISiN, Politecnico di Torino, Turin, Italy; 4. Department of Physiotherapy, Faculty of Rehabilitation, University of Social Welfare and Rehabilitation Sciences, Tehran, Iran;

## Introduction

Total knee arthroplasty (TKA) is a commonly accepted surgical procedure recommended for severe OA characterized by radiographic evidence of joint damage, moderate to severe persistent pain, and clinically significant functional limitations affecting the quality of life when conservative treatments fail [1]. Rehabilitation following TKA is crucial to the success of the surgery. Most studies recommend that rehabilitation be initiated immediately after discharge from the hospital [2]. The aims of this study were thus to investigate whether an early progressive strengthening exercise program could improve static, dynamic, and semi-dynamic balance compared with routine physical therapy in patients with TKA. We hypothesized that (i) a 6-week rehabilitation program after TKA would improve balance and (ii) the addition of early progressive resistive exercise to routine physical therapy after TKA would yield greater improvement in balance.

## Methods

In this double-blind randomized controlled trial study, 40 patients with severe osteoarthritis, sampled by a simple convenient method, were randomly assigned into either control group or early resistive exercise group. After TKA surgery, both groups attended a routine rehabilitation program while the experimental group received extra early resistive exercises. Static, semi-dynamic, and dynamic balance were assessed by the Sharpened Romberg (SRBT), Star Excursion (sebt), and berg (BBT) balance tests prior to surgery, after the rehabilitation process (seventh weeks), and at a 2-week later follow up time (ninth week).

## Results

At the end of the seventh and ninth weeks, in both groups all 3 balance scores were significantly enhanced comparing the baseline scores ( $p < 0.001$ ). The experimental group had significantly higher scores than the control group in SRBT, SEBT, and BBT after the intervention and at the follow-up time ( $p < 0.001$ ).

## Discussion

The findings of this study showed that rehabilitation following TKA is accompanied by balance (static, semi-dynamic, and dynamic) improvement, and this improvement is greater among patients participating in and early resistive exercise regimen. Early progressive resistive exercise in addition to routine physical therapy may lead to better balance performance than routine physical therapy and might be incorporated into the postoperative physical therapy of these patients. Further studies with longer follow-up periods are needed to confirm these results.

## References

1. American Academy of Orthopaedic Surgeons. Treatment of Osteoarthritis of the Knee (Non-Arthroplasty). Rosemont, IL: American Academy of Orthopaedic Surgeons; 2008.
2. Artz N, Elvers KT, Lowe CM, Sackley C, Jepson P, Beswick AD. Effectiveness of physiotherapy exercise following total knee replacement: systematic review and meta-analysis. *BMC Muscu- loskelet Dis.* 2015;16(1):15-36.



# SHORT INTER-ELECTRODE DISTANCES UNDERMINE THE SENSITIVITY OF SURFACE ELECTROMYOGRAMS

Taian Vieira (1,2), Alberto Botter (1,2), Kohei Watanabe (3), Andrew Vigotsky(4)

1. LISiN-DET, Politecnico di Torino, Italy; 2. PoliTo<sup>BIO</sup>Med Lab, Politecnico di Torino, Italy; 3. Laboratory of Neuromuscular Biomechanics, Chukyo University, Japan; 4. Departments of Biomedical Engineering and Statistics, Northwestern University, United States

## Introduction

With surface electromyography (sEMG), there is an inherent tradeoff between sensitivity and specificity. While specificity is generally acknowledged in the sEMG literature (e.g., crosstalk), only recently has the sensitivity been systematically studied (1, 2). The existence of Type II errors in surface EMG has been formalized (3), but their practical importance has not yet been documented. Specifically, of broad biomechanical interest, how much does sensitivity affect inferences regarding muscle excitation when using bipolar sEMG?

## Methods

In this study, we used a dense array of surface electrodes to systematically assess this issue for two muscle geometries. With this array, we were able to compute bipolar EMGs for progressively greater inter-electrode distances (IEDs)—from 5 mm to 50 mm, with greater IEDs having greater spatial sensitivity—with all pairs of electrodes being centered roughly at the same skin region over biceps brachii (BB; Figure 1) and gastrocnemius medialis (GM) of 20 healthy subjects. Using these signals, we investigated how much the onset of muscle excitation, the quality of surface EMGs (signal-to-noise ratio; SNR), and the coherence between EMG and joint moment were affected by IED. Non-parametric statistics and a Bayesian hierarchical model were used to test the hypothesis that excessively reducing IEDs limits the biomechanical and physiological validity of sEMG signals.

## Results

Our results revealed a significant influence of IED on the onset of muscle excitation, quality of the detected signals (SNR), and the association between EMG amplitude and joint torque. The greater the IED, the more sensitive the bipolar signal was to changes in joint torque. In contrast, IEDs shorter than 30 mm resulted in EMG descriptors of dubious validity: physiologically unplausible onset values, spuriously low SNR values, and weaker EMG-force associations.

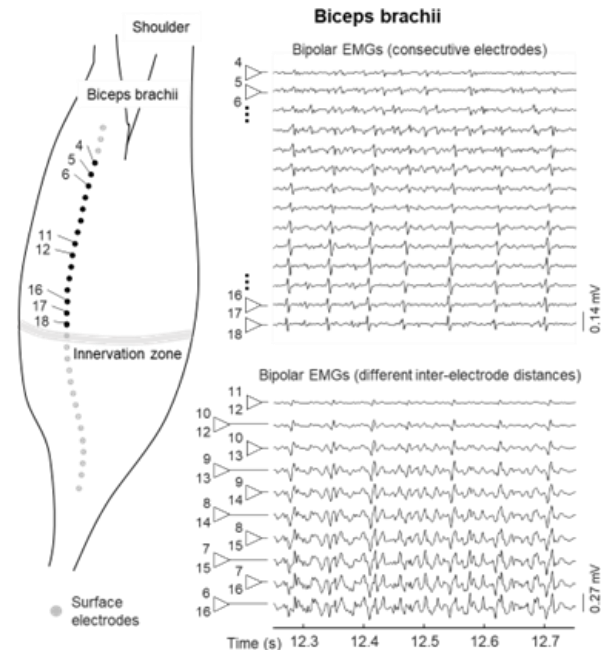


Figure 1: Inter-electrode distance (IED) and surface EMGs. Bipolar EMGs detected by 15, consecutive pairs of surface electrodes (IED = 5 mm) from the biceps brachii muscle are shown on top biceps brachii. Bipolar EMGs detected for progressively greater IED are shown at the bottom, from 5 mm to 50 mm.

## Conclusion

Inter-electrode distance imposes a biophysical constraint on EMG sensitivity. Short IEDs yield EMG descriptors of dubious physiological validity, including the inflation of Type II errors. Owing to sEMG's ubiquitous use, our findings are of general biomechanical and physiological interest. We propose a potentially valid procedure for defining the most appropriate IED to help balance sensitivity and specificity in single bipolar sEMG recordings.

## References

1. Vieira et al, Sci Rep 7: 1–11, 2017.
2. Munneke et al, J Electromyogr Kinesiol 40: 23–31, 2018.
3. Vieira and Botter, Exerc Sport Sci Rev 49: 23–34, 2021.



# EMG-ASSISTED METHOD AND UNCONTROLLED MANIFOLD THEORY TO EXPLORE SUBOPTIMAL CONTROL IN CHILDREN

Alex Bersani (1,2), Giorgio Davico (1,2), David G Lloyd (3), Christopher P Carty (3), Claudio Pizzolato (3), Marco Viceconti (1,2)

1. Alma Mater Studiorum – University of Bologna, Bologna, Italy; 2. Medical Technology Lab - IRCCS Istituto Ortopedico Rizzoli, Bologna, Italy; 3. Griffith Centre of Biomedical and Rehabilitation Engineering (GCORE), Menzies Health Institute Queensland - Griffith University, Gold Coast, Australia

## Introduction

Commonly, biomechanical simulations employing musculoskeletal models assume that to perform simple locomotor tasks the central nervous system selects a neural strategy that minimises the metabolic cost, i.e. optimal control. This is likely not valid for pathological populations with neuromuscular disorders (e.g., cerebral palsy, CP) who tend to adopt suboptimal control strategies. Alternative methods, such as the EMG-assisted [1] and probabilistic [2] approaches, have been developed and tested to the purpose.

In this work we explored different ways to model the muscle activation patterns in children with CP and typically developing (TD) age-matched controls. Specifically, we compared the knee joint contact forces estimated through standard static optimisation, an EMG-assisted method and a probabilistic approach.

The aim was to evaluate differences among methods and to understand whether the EMG-assisted solution could be explained as a stochastic variation from optimal solution for healthy and pathological subjects.

## Methods

Subject-specific musculoskeletal models were developed using nmsBuilder [3] for three children with CP (GMFCS I-II, age:  $8.35 \pm 2.01$  years, height:  $1.25 \pm 0.12$  m, mass:  $23.30 \pm 5.33$  kg) and three age-matched TD children (age:  $7.98 \pm 1.75$  years, height:  $1.23 \pm 0.10$  m, mass:  $24.47 \pm 6.02$  kg). Bone geometries, muscle paths and muscle maximal isometric forces were personalised using magnetic resonance images. Biomechanical simulations of ten walking trials were performed in OpenSim (v4.1) [4] using static optimisation and EMG-assisted approaches (CEINMS [1]). A probabilistic approach was used to estimate  $2e5$  plausible solutions combining Bayesian statistics and Markov Chain Monte Carlo algorithm (Metabolics [5]) to explore the solution space within a 5% and 10% variation from the optimal solution (i.e., static optimisation).

## Results

For the TD children, the static optimisation and EMG-assisted approaches produced similar knee contact force profiles. Only few discrepancies were observed, of relatively small magnitude (less than 1 BW). In all three cases, the EMG-assisted solutions fell tendentially within a 5% manifold (variation from the optimal solution) generated by the stochastic approach.

For the CP children, a common trend was not observed. The discrepancies between EMG-assisted and static optimisation estimates were generally larger than in the TD cohort. In one case, in particular, the EMG-assisted solution fell outside of the 5% manifold (but within 10% variation from the optimal solution) (Figure 1).

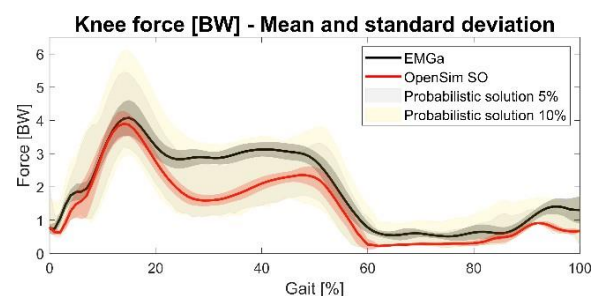


Figure 1: Knee contact force predictions for a CP child, expressed in bodyweights (BW). Comparison of EMG-assisted (black), static optimisation (red) and probabilistic solutions (grey shaded area for 5% variation and yellow shaded area for 10% variation).

## Discussion

The purpose of this study was to compare three different methods to model suboptimal muscle activation patterns. These preliminary findings suggest that for healthy individuals the EMG-assisted and static optimisation methods produce similar results, which are contained in a narrow manifold. However, the same does not hold true for children with CP, for whom EMG-assisted predictions may largely deviate from an optimal solution. Further work is warranted to support these results.

## References

1. Pizzolato et al., J Biomech 48, 3929–3936, 2015.
2. Martelli et al., J Biomech 46, 2097–2100, 2013.
3. Valente et al., Comput Methods Programs Biomed 152, 85–92, 2017.
4. Seth et al., PLoS Comput Biol. 2018.
5. Heino et al., Comput Methods Programs Biomed 97, 151–167, 2010.

## Acknowledgements

This study was partially supported by EU H2020 project “Mobilise-D”, and by the Ricerca Finalizzata ForceLoss funded by the Italian Ministry of Health. This project has received funding from the European Union’s Horizon 2020 research and innovation programme under grant agreement No 101016503.



# DEVELOPMENT AND VALIDATION OF A MORPHABLE ARTICULATED TOTAL BODY

Giulia Pascoletti (1), Elisabetta M. Zanetti (1)

1. Department of Engineering, University of Perugia, ITALY

## Introduction

Articulated total body models, known as ATBs, are implemented in multibody codes, allowing for the acquisition of kinematic and dynamic information on the human body with minimal computational effort for subject-specific analyses, such as forensic biomechanics or for safety design. The most common ATB models are made up of articulated bodies having simple geometries [1] (such as spheres or ellipsoids), with the dimensions and inertial properties calculated through regression equations based on the subject's gender, height, and weight. More refined anthropomorphic models can be created using outer geometries obtained through laser scanning or other reverse engineering techniques and calculating inertial properties from a given density value. This article presents a novel method for developing an anthropomorphic ATB by segmenting a 3D parametric human geometry and morphing it based on up to 24 subject-specific measurements.

## Methods

The anthropomorphic model's external geometry was obtained using specialized software [2], developed at Delft University of Technology. This software can generate the outer subject geometry for up to 24 anthropometric measurements, morphing a 'standard' geometry. Anatomical landmarks have been identified on this geometry and they were used to segment the whole body to identify 17 volumes corresponding to limbs, trunk sections, the head and the neck [3] (Figure 1).

The 17 volumes were articulated to one another through joints simulating the respective articulations. For each anatomical joint the ranges of motion, along with passive stiffness properties, were established for each degree of freedom, based on literature data.

The model has been validated against 5 cadaver tests performed at the laboratory of applied biomechanics of the Faculty of Medicine North, in France [4], aimed at replicating and investigating real-world pedestrian-car collisions.

## Results and Discussion

Figure 2 reports the kinematic comparison between experimental results and numerical results for one of the tests: overall, there was a satisfactory qualitative agreement observed across all tests.

The qualitative comparison was followed by a quantitative one focused on time histories of velocities and displacements measured at the head center of mass; for example, Table 1 reports results obtained at the instant of time where the head impacts the ground: the absolute error could reach 0.8 m/s and the percentual error kept below 16%.

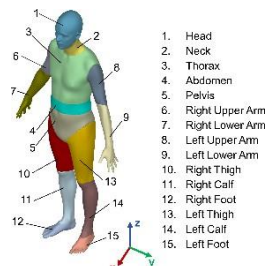


Figure 1: Morphable mesh of a male subject, segmented in 17 volumes.

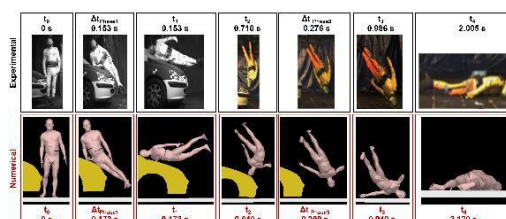


Figure 2: Kinematic comparison between experimental tests on cadavers (1<sup>st</sup> row) and numerical data (2<sup>nd</sup> row).

Test #	Experimental Head velocity [m/s]	Numerical Head velocity [m/s]	Absolute Error [m/s]	Percentual Error [%]
1	5.1	4.3	-0.8	-16
2	2.6	2.5	-0.1	-4
3	5.1	4.3	-0.8	-16
4	3.9	3.3	-0.6	-15
6	5.5	5.6	0.1	2

Table 1: Comparison of head velocity at time of contact to the ground.

The analysis confirmed the good predictive ability of the model; nonetheless, its accuracy could be improved adopting subject-specific stiffness behavior since it was evident that standard values actually do not exist. Future tests to study this aspect will be focused on living subjects, disturbed from their equilibrium condition.

## References

- Haug, E et al, Computational Models for the Human Body, Elsevier, Amsterdam (2004)
- Huysmans, T et al, Tijdschrift voor Human Factors, 45 (2020)
- Pascoletti, G et al., In C. Rizzi, et al., Design Tools and Methods in Industrial Engineering II – Proc. 2nd Int Conf on Design Tools and Methods in Industrial Engineering, ADM 2021, Springer (2022)
- Shang S et al, Kinematics and dynamics of pedestrian head ground contact: A cadaver study, Safety Sci, 127 (2020).

## Acknowledgements

This work was supported by grants "Ricerca di base 2019" and "Ricerca di base 2020" from Università degli Studi di Perugia.



# MUSCULOSKELETAL MODELLING OF A PROTHESIZED HIP ALLOWS TO DETERMINE HIP CONTACT LOADS AND LOCATIONS

Giovanni Putame (1,2), Federico A. Bologna (1,2), Alberto L. Audenino (1,2), Mara Terzini (1,2)

1. Polito<sup>BIO</sup>Med Lab, Politecnico di Torino, Turin, Italy

2. Department of Mechanical and Aerospace Engineering, Politecnico di Torino, Turin, Italy

## Introduction

Due to the rising of the average population longevity and the concurrent decrease of the age at which arthroplasty is performed, an important increase in revision surgery for total hip arthroplasty (THA) has been estimated by the year 2030 [1]. Based on these forecasts, a better understanding of the loads to which implants undergone during daily activities, together with insights of how such loads are related to the implant geometrical features, can provide valuable information in order to extend implants lifespan, hence reducing the necessity of revision surgeries. In this context, *in silico* musculoskeletal modeling represents an effective and flexible approach able to estimate articular loads [2]. In this study, a multibody (MB) model of the lower limb, including a parametrized hip prosthesis, is exploited to assess the impact of the implant geometry on hip contact force and contact point location on the femoral head during normal walking activity.

## Methods

A MB model of a lower limb (Fig. 1A) was created (Adams View MSC Software, USA) including scaled bony geometries (from pelvis to tibia), main muscles, and a parametrized hip prosthesis (Fig. 1B). Muscle actuators are implemented through a set of feedback controllers having the muscle lengthening as controlled variables. Motion and ground reaction forces for a normal walking activity were derived from the OrthoLoad datasets [3] and used as inputs to perform inverse kinematics followed by muscle-driven forward dynamic simulations for which average external forces and torques were directly applied to the ankle joint while the pelvis kinematics was prescribed. Also, 1 DoF knee joint was considered, beside a contact pair was defined between femoral and acetabular cup. Simulations were repeated by varying the implant geometry. Specifically, the influence of different prosthesis neck lengths ( $L$ ) was investigated (ref = 38, long = 42, short = 34 mm), thus, the obtained hip contact force, expressed in body weight (BW), and the contact location on the femoral head were compared.

## Results

Numerical analyses revealed a contact force variation of roughly  $\pm 0.1$  BW (Fig. 1C), during mid and terminal stance phases, where the shorter neck length produced the highest force. Looking at the contact location, a negligible alteration in the contact point trajectory was observed among the different configurations. In general,

the contact point moves along an arc path located apically on the femoral head (Fig. 1D).

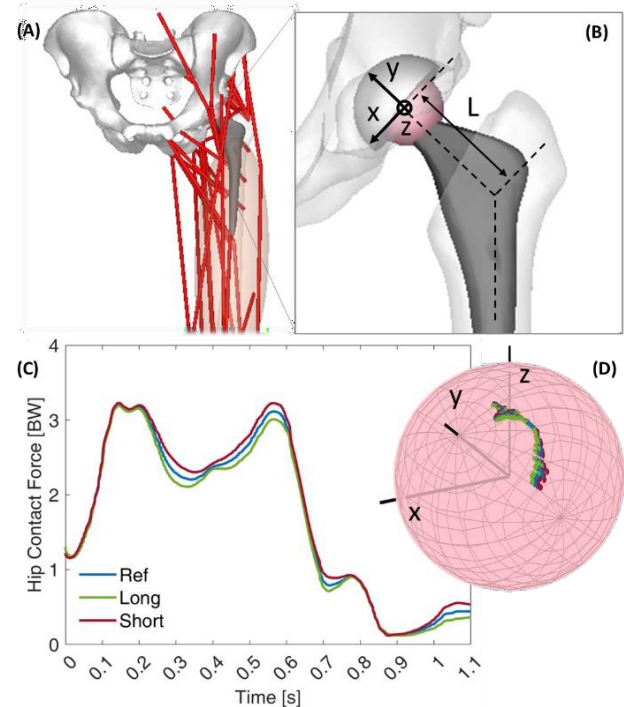


Figure 1: (A) multibody model of the THA; (B) hip prosthesis with the parametrized neck length ( $L$ ), and the head reference system ( $x, y, z$ ); Explanatory results showing (C) hip contact force and (D) contact location on the femoral head during walking for different  $L$ .

## Discussion

The presented musculoskeletal model can find applicability in a variety of outstanding scenarios, spanning from advanced patient-specific preoperative planning to *in silico* testing of novel hip prosthesis designs. Indeed, the outputs attainable from the model, e.g., loads and related points of application, undeniably constitute a plus for more reliable loading conditions in finite element modeling. In the next future, the model capability will be further enhanced by including additional motion activities, e.g., knee bending, and other settable geometrical implant parameters.

## References

1. Kurtz et al, J Bone Jt Surg Am, 89(4):780–785, 2007
2. Tomasi et al, Biomech Model Mechanobiol, 2022.
3. Bergmann et al, J Biomech, 34:859–871, 201.

## Acknowledgements

Research supported by MIUR PRIN 2017 “BIONIC” project.



# DEVELOPMENT OF A MUSCULOSKELETAL MODEL FOR THE EVALUATION OF THE DOG'S SPINAL BIOMECHANICS

Martina Pedroli<sup>1</sup>, Edoardo Bori<sup>2</sup>, Francesca Berti<sup>1</sup>, Luigi La Barbera<sup>1</sup>, Luca Ciriello<sup>1</sup>, Bernardo Innocenti<sup>2</sup> and Tomaso Maria Tobia Villa<sup>1</sup>

1. Politecnico di Milano, Italy; 2. Université Libre de Bruxelles, Belgium

## Introduction

Some of the most common problems and diseases in dogs are related to the spine. Like humans, dogs are subject to herniated discs, vertebral fractures and degenerative diseases, and in most cases surgery is required [1].

The use of a 3D musculoskeletal model could be very useful to study and define how to intervene in case of necessity. Up to now, there is not a valid model of large dogs, because most of the studies are done on small dogs, as beagles [2]. Therefore, the aim of my work is based on the development of a 3D musculoskeletal model of a dog's spine.

## Methods

I started my work from the analysis of CT scans of a German Shepherd dog provided by Prof. Vandeweerd, from University of Namur, and Dr. Kayser, from CHU UCL Namur.

I started by segmenting the complete spine of the dog with 3D Slicer software, obtaining every single vertebra. I also added other bones of the body that would be useful for my studies, in order to have a complete model.

After this, I introduced the most important muscles that allow the dog's body to move and recreate some basic movements, using Opensim software.

Starting from the study of the dog's anatomy, I defined which muscles are most involved during movement. The model will obviously be simplified compared to the dog's real body because there are too many muscles involved, so I am concentrating on those most implicated and necessary to perform the movements.

I am currently completing my work by looking for some kinematic data of the dog's motions to recreate and obtain a model close to reality.

## Results

Using the Opensim software, I want to reproduce the movements performed by the dog based on the available data to have a correctly functioning model of a German Shepherd dog. The completed model will then be characterised by the most important muscles of the spine, also connected to the fore and the hindlimbs.

This will allow simulations very similar to reality to be obtained and canine movements to be studied.

## Discussion

Since large dogs have many spinal problems and there are no musculoskeletal spine models available at the moment, my work will be very useful.

This model will be able to help vets as it will provide information that can be necessary before surgery, so that they can work in the best possible way, minimising the risk of failure.

In addition to being a support for veterinarians, it will also be helpful for the engineers themselves. Indeed, when a spinal fixator is created, it is important to test if what has been designed can be fitted correctly on the spine and if it can perform all the functions for which it has been designed.

A model like this will be able to define the correct points in which the fixators should be placed, simulating their behaviour on the dog's body and making it possible to understand which forces need to be applied to avoid damage to the skeleton, encourage bone regrowth and help the dog in its movements.

## References

1. <https://www.animalpedia.it/malattie-della-colonna-vertebrale-del-cane-cause-e-trattamento-3968.html>
2. Stark, H., Fischer, M.S., Hunt, A. et al. A three-dimensional musculoskeletal model of the dog. *Sci Rep* 11, 11335 (2021)



# AN *IN SILICO*-*IN VIVO* FRAMEWORK FOR THE ACUTE OCULAR AND CARDIOVASCULAR RESPONSE TO 6° HEAD-DOWN TILT

Matteo Fois (1), Ana Diaz-Artilles (2), Syeda Yasmin Zaman (2), Luca Ridolfi (3) and Stefania Scarsoglio (1)

1. Department of Mechanical and Aerospace Engineering, Politecnico di Torino, Turin, Italy; 2. Department of Aerospace Engineering, Texas A&M University, College Station, Texas (USA); 3. Department of Environmental, Land and Infrastructure Engineering, Politecnico di Torino, Turin, Italy

## Introduction

Ensuring the healthiness of astronauts undergoing long-term missions in space is of primary importance for the aerospace community. Spaceflight associated neuro-ocular syndrome (SANS) has been widely acknowledged to cause severe ocular disorders in astronauts returning from long permanence in weightlessness [1].

In this context, head-down tilt (HDT) has gained large popularity to resemble the cardiovascular response to microgravity, as well as to study SANS [2].

We propose a novel multiscale numerical framework to simulate the acute response to 6° HDBR – with *in vivo* validation – to help shed light on SANS onset.

## Methods

We developed a new cardiovascular model integrating our previously validated *in silico* framework [3] with a lumped model of the eye [4] and of the cerebrovascular circulation [5]. The global model presents a 1D description of the arterial tree combined with 0D analogues of the remaining vasculature, accounting for short-term homeostatic control and for the action of gravity during posture changes. Using this model, we simulated a tilt maneuver between 80° head-up tilt (HUT) and 6° HDT.

*In vivo* measures were taken at the Bioastronautics and Human Performance (BHP) Laboratory at Texas A&M University (TX, USA). Six healthy male subjects were positioned upright (80°) on an inversion table, tilted down to -6° HDT for approximately 10 minutes and eventually tilted back upright to 80°. Subjects' arterial pressure, heart rate, cardiac output, stroke volume, and intraocular pressure measures were collected at each position. Seated baseline measures of the same parameters were also acquired.

## Results

The model results in response to acute 6° HDT – and tilt back to 80° – are shown in Figure 1. The corresponding *in vivo* mean and standard deviation ( $\mu \pm \sigma$ ) of subjects' parameters are also depicted in Figure 1.

## Discussion

The model results reproduce the *in vivo* acute ocular and cardiovascular response to 6°HDT. In addition, the model offers novel insights into the hemodynamic mechanisms related to intraocular pressure and

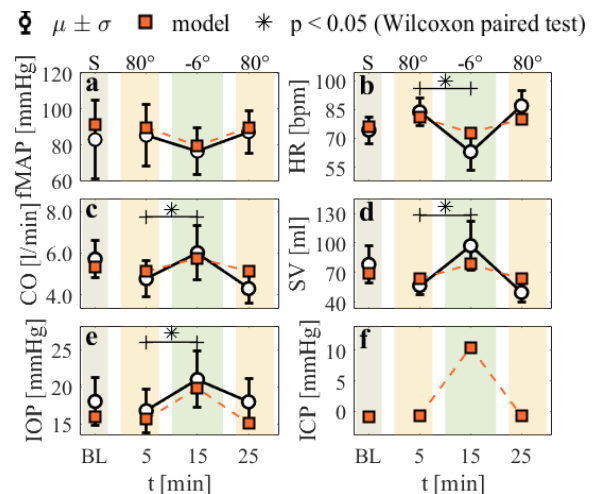


Figure 1: Model results and experimental data for finger mean arterial pressure at brachial level (fMAP, panel a), heart rate (HR, panel b), cardiac output (CO, panel c), stroke volume (SV, panel d) and intraocular pressure (IOP, panel e). ICP (panel f) is the simulated intracranial pressure. S: baseline seated.

intracranial pressure – in terms of average and pulsatile values – both at steady-state and during the transient dynamics.

As also observed upon entering microgravity, the initial fluid shift associated with 6° HDT leads to a sudden increase in SV and CO accompanied by a drop in HR. While arterial pressure does not show wide variations, IOP rises by 4.2 mmHg (model) compared to 80° upright ( $21.0 \pm 3.8$  at 6° HDT vs.  $18.0 \pm 3.2$  at 80° HUT). In addition, the model simulates an ICP increase of 11.3 mmHg in response to 6° HDT [6-7] which is much larger than the observed IOP increase. As a result, our model predicts that the transmural pressure IOP-ICP is markedly reduced during acute HDT (-43%) [6-8]. These results may contribute to the understanding of SANS among astronauts experiencing analog ocular and vascular responses upon long-term space missions.

## References

1. Mader et al, Ophthalmology, 118.10: 2058-2069, 2011.
2. Ong et al, Front Neurol, 12:648958, 2021.
3. Fois et al, Front Physiol, 13:826989, 2022.
4. Petersen et al, J Appl Physiol, 132(1):24-35, 2022.
5. Ursino & Giannessi, Ann Biomed Eng, 38:955-974, 2010
6. Lawley et al, J Physiol, 595: 2115-2127, 2017.
7. Laurie et al, Physiol Rep, 5(11):e13302, 2017
8. Zhang and Hargens, Physiol Rev, 98(1):59-87, 2017



# DEVELOPMENT OF A NOVEL NITINOL CORNEAL IMPLANT FOR THE TREATMENT OF KERATOCONUS

Graziana M. Ragonese (1), Andrea T. Lugas (1), Ramon Gloor (2), Sara Zambon (1), Dario Carbonaro (1), Moses Kakanga (3), Claudio Chiastra (1), Michael de Wild (2), Diego Gallo (1), Emiliano Lepore (3)

1. Polito<sup>BIO</sup>Med Lab, Department of Mechanical and Aerospace Engineering, Politecnico di Torino, Italy;

2. School of Life Sciences, FHNW, Switzerland; 3. Recornea srl, Italy;

## Introduction

Keratoconus (KC) is a progressive corneal ectatic disorder that causes stromal thinning and collagen weakening, resulting in a cone-like protrusion of the cornea and significant loss of vision and quality of life. Current treatment options suffer from major limitations [1]. Contact lenses and spectacles are only effective in early KC stage. Reductive laser corrective surgery is of limited use as KC corneas are thinner than healthy ones. Corneal transplant is invasive and expensive. Ring-shaped implants offer scarce remodelling support to the cornea leading to poorly predictable clinical results. The GROSSO<sup>®</sup> implant is the world's first Nitinol corneal implant aiming at remodelling the whole cornea by virtue of a dome-shaped design.

Here, we assess experimentally and computationally the mechanical performance of the GROSSO<sup>®</sup> implant in two potentially critical situations. The first situation consists in a 90° bending of two opposite edges of the implant occurring in its minimally invasive implantation in the patient's intracorneal pocket. The second one is a vertical crushing of the device to test its strength and provide information on possible impacts occurring in daily use. Moreover, a thermal colouring process of the Nitinol through heat-treatment is being developed to obtain coloured implants matching the iris colour of patients and minimise the visibility of the implant.

## Methods

The computational model of the GROSSO<sup>®</sup> implant was reconstructed from micro-computed tomographic acquisitions (Phoenix v|tome|x m, resolution: 1 µm) of the actual GROSSO<sup>®</sup> implant. The mechanical behavior of the Nitinol alloy was modelled by implementing a super-elastic constitutive law with non-linear material parameters obtained from experimental tensile tests, which also determined pseudoelastic behaviour and the strain value at which permanent plastic deformation occurs. Finite element analysis of the bending and crushing tests were performed in Abaqus (Dassault Systèmes Simulia Corp.) to obtain the reaction force (RF) exerted by the device, its maximum principal stress and maximum principal strain, verifying the absence of permanent deformations.

Heat treatment in an inert atmosphere at specific temperatures was used to control the thickness of the oxide layer and thus the interference color.

## Results

The maximum principal strain reached by the filigree connectors of the device in the bending simulation is 6.9% (Fig. 1A), while the maximum principal stress is

620 MPa, and the RF is 0.19 N. The crushing simulation indicated a maximum principal stress value of 519 MPa, a maximum strain value of 3.8% and an RF of 0.71 N. The developed computational tool is currently being validated through experimental replication of the bending and crushing simulations. Preliminary experimental results on the bending of the device confirmed the order of magnitude of the RF. Thermal treatments show promising color changes on polished Nitinol discs (Fig. 1B).

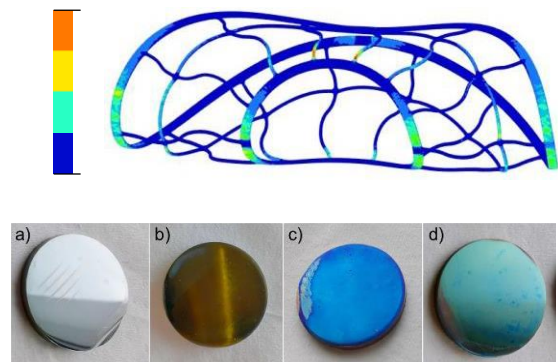


Figure 1. A: Maximum Principal Strain reached by the implant during bending. B: Polished Ø25 mm nitinol disks (56.0 wt% Ni,  $A_f = -14.1^\circ\text{C}$ ) a) as-polished, b) after heat-treatment at 400°C, c) 450°C and d) 500°C.

## Discussion

The GROSSO<sup>®</sup> implant is expected to offer mechanical stability without any risk of permanent deformation either during implantation or during daily use. These results appear promising in view of providing a predictable clinical outcome to KC patients. The developed computational tool allows exploring different device designs, cost-effectively predicting the mechanical properties at the macroscale, and the compliance to relevant standards or regulatory requirements. Moreover, the established anodization process allows achieving colour specificity to match the most common colours of the human iris. As next steps, surface modifications induced by the anodization process will be characterized. Moreover, the interaction between the device and corneal tissues will be modelled by digitally generating KC corneal anatomies to evaluate the anatomical fitting and the reshaping effect.

## References

1. Atalay et al, Ther Adv Ophthalmol, 13: 1-13, 2021.

## Acknowledgements

Horizon 2020 project HUMANeye (GA 878719) is acknowledged.



# PREDICTING BONE PLATES RUNOUT USING TENSILE STRENGTH AND GEOMETRIC PROPERTIES TO REDUCE REGULATORY TESTING

Federico Bologna (1,2), Alberto Audenino (1,2), Mara Terzini (1,2)

1. Department of Mechanical and Aerospace Engineering, Politecnico di Torino, Turin, Italy

2. Polito<sup>BIO</sup>Med Lab, Politecnico di Torino, Turin, Italy

## Introduction

Mechanical tests on bone plates are mandatory for regulatory purposes and, typically, the ASTM F382 standard [1] is used, which involves a four-point bending test setup to evaluate the bending stiffness, structural stiffness, bending strength, and cyclic bending fatigue performance of the bone plate. These test campaigns require a considerable financial outlay and long execution times; therefore, an accurate prediction of experimental outcomes can reduce test runtime with beneficial costs cut for manufacturers [2].

Hence, an analytical framework is here proposed for the direct estimation of the maximum bending moment of a bone plate under fatigue loading, to guide the identification of the runout load for regulatory testing.

## Methods

A complete test campaign was carried out according to ASTM F382 to evaluate the static and fatigue bending properties of eleven bone plates pending certification. The bone plates involved in the study were designed for different anatomical regions and manufactured from steel and titanium alloys. An analytical prediction of the maximum bending moment was then implemented starting from the ultimate tensile strength ( $\sigma_{UTS}$ ) specified in the raw material certification and the plate geometry. The section of each plate with the minimum moment of inertia in the bending direction was detected with an automatic procedure. In this section, the width and thickness of the plates, as well as the diameter of the screw hole were automatically extrapolated. Through these dimensions, Peterson's stress concentration factors [3] were determined to account for the presence of the screw hole. A fatigue limit equal to  $0.5\sigma_{UTS}$  [4] was applied for all bone plates. The Goodman and Gerber failure criteria [5] were implemented to calculate the mean stress effect due to an  $R$ -ratio equal to 0.1 (the minimum of the sinusoidal waveform was computed as 10% of the maximum stress), as required by the standard for the testing condition. The maximum bending moment was calculated for each bone plate using both failure criteria, defining the range of the runout moment prediction. Stress-life (S-N) diagrams were therefore estimated to additionally compare the experimental loads above the runout with the analytical prediction; Basquin's equation [5] was applied to calculate the alternating stress from the experimental number of cycles. The resulting moments were finally categorized into three intervals: (a) plastic range, (b) elastic range, and (c) runout condition in order to verify the prediction accuracy of the analytical approach.

## Results

In the runout condition, most experimental values fall within the predicted range outlined by the Goodman and Gerber criteria (Figure 1). Maximum bending moments calculated with the Goodman approach were considered as the lower limit of the range prediction: eight out of eleven plates met this expectation. On the other hand, all tested bone plates showed a maximum bending moment below the limit estimated with the Gerber criterion.

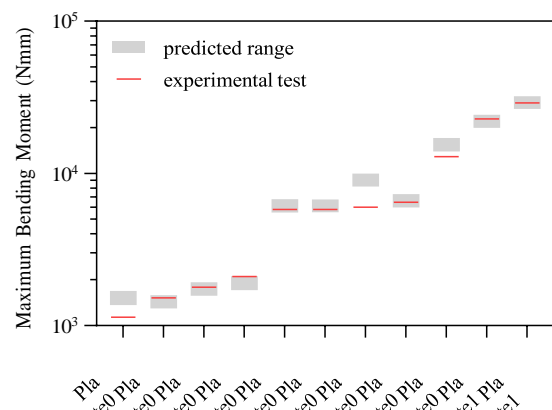


Figure 1: Experimental (red lines) and predicted (grey boxes) maximum bending moments for each bone plate.

Lastly, the predicted values were compared with experimental results (Table 1): while the predictive ability drastically decreased, as expected, when the yield strength of the material was exceeded, in the elastic range, as well as in the runout condition, the prediction performance has shown a significant improvement.

	Plastic	Elastic	Runout
Goodman	0.4089	0.9604	0.9694
Gerber	0.6183	0.9716	0.9549

Table 1:  $R^2$  coefficients in plastic, elastic, and runout conditions for the Goodman and Gerber criteria.

## Discussion

The developed analytical framework exhibited a promising predictive ability, with potential impact in reducing the experimental tests needed for the CE marking of bone plates and could represent a guideline to avoid the underestimation of the runout load.

## References

1. ASTM International, ASTM F382-17, 2017.
2. Terzini et al, GNB 2020, 186905:317-320, 2020.
3. Peterson, Stress concentration factors, Wiley, 1974.
4. Juvinal et al, Fundam of Mach Comp Des, Wiley, 2012.
5. Dowling et al, Fatigue Frac Eng Mat Str, 32:163-179, 2009.



# ANALYSING FIXATION LENGTH AS A RISK FAILURE FACTOR VIA A COMBINED MUSCULOSKELETAL AND FLEXIBLE BODY MODELING

Simone Borrelli (1,2), Giovanni Putame (1,2), Alberto L. Audenino (1,2), Mara Terzini (1,2)

1. Polito<sup>BIO</sup>Med Lab, Politecnico di Torino, Turin, Italy

2. Department of Mechanical and Aerospace Engineering, Politecnico di Torino, Turin, Italy.

## Introduction

The growing incidence of degenerative spine diseases necessitating a segment fixation is dramatically increasing. At present, reducing the number of fixed vertebral levels is topic of clinical debate, but long fixations are still preferred as more stabilizing, and in case of pedicle screw failure, permit a more conservative revision treatment [1]. This study explores, through a multi-level modeling, whether fixation length affects the loads exchanged in spine-implant construct, being a risk factor for the mechanical failure of the fixation itself.

## Methods

From 25 upper-body healthy male subject-specific musculoskeletal models [2], postoperative outcomes were designed in OpenSim, simulating a long (L1-L5, *L*) and a short (L2-L4, *S*) lumbar fixations, rigidly connecting the vertebrae involved in the surgical implant. The altered kinematics of postoperative models was returned by compensating the null contribution of the fixed levels on the cranial and caudal adjacent free levels (75% and 25%, respectively) [3]. The muscular activity of the erector spinae, transversospinalis, psoas major, and quadratus lumborum was recorded for 30° flexion and 15° axial left rotation for each configuration (Fig. 1A). Then, the surgical implants were built on a T12-S1 multibody validated model [4] which incorporated ligaments, intervertebral discs and facet joints, all characterized by non-linear constitutive laws.

Modal theory was used to return the flexibility of CFR-PEEK rods. Conversely, pedicle screws were modelled as flexible connectors whose stiffness was evaluated assuming the screws as beams with one fixed extremity (i.e., their insertion point), and the other subjected to the loads transmitted by the rod (Fig. 1B). The computed muscular loads were applied in terms of concentrated forces and moments and added to the multibody-FEM co-simulation in MSC Adams (Fig. 1C). For both *L* and *S*, the pull-out and shear forces at the anchorages were estimated, together with the Von Mises stresses along the rods. These loads were deemed the most hazardous for the construct mechanical failure.

## Results

The muscular recruitment in the T12-S1 region differed among the three configurations. At 30° flexion, the muscular compressive force acting on L5 was increased of +86% (*L*) and +48% (*S*) with respect to the intact model. Generally, at parity of task, *L* always resulted more loaded than *S*. Observing the reactions at the anchorages, during axial rotation the maximum shear force in *L* occurred in L1 and was 3.5 times higher than the maximum in *S* (Fig. 1D); moreover, bending moment reached 10Nm in L3, significantly stressing the whole construct. In flexion, cranial anchorages were subjected to pull out forces, and short rods limited them of 72% (~125N in *L*). Finally, *S* revealed more uniform Von Mises stresses, avoiding the load shielding emerged in the central anchorages of long rods.

## Discussion

The impact of fixations on intervertebral joints has been extensively explored in literature, yet the stress that implants must endure during daily tasks is often overlooked. Delving in this direction, a significant dependency with fixation length emerged: long fixation appeared as hyperstatic construct and its altered kinematics provoked greater muscular recruitment and the production of heightened and severe reactions at the implant anchorages which could accelerate the dislodgment or the early fatigue of the screws. Then, the study suggests reconsidering lengthening fixation as a solution that risks to trigger the development of unfavorable loads, adverse for the implant lifetime.

## References

1. Li et al, Int J Clin Exp Med, 10(2): 1750-1762, 2017.
2. Anderson et al, Harvard Dataverse, V2, 2020.
3. Ebrahimkhani et al, Sci Rep, 11, 17892, 2021.
4. Borrelli et al, Ann Biomed Eng, 50(10):1243-1254, 2022.

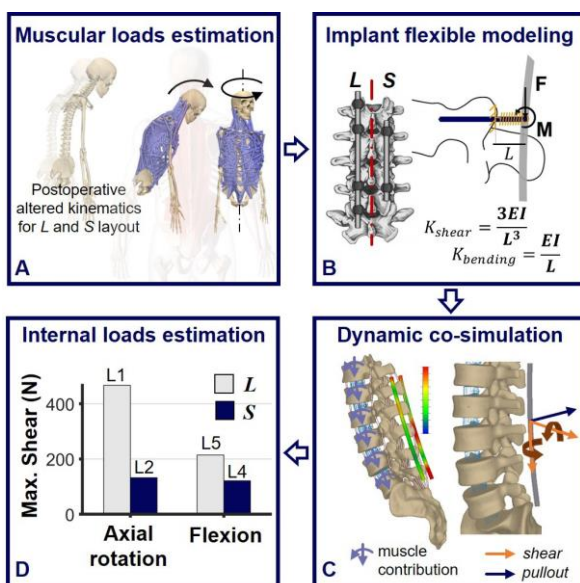


Figure 1: Workflow of this study



# BIOMECHANICS, KINEMATIC ANALYSIS OF ANKLE PROSTHES

Enrico Cecchini (2), Edoardo Bori (1), Alessandro Mengarelli (2), Bernardo Innocenti (1), Federica Verdini (2)

1. Université libre de Bruxelles, Belgium; 2. Università Politecnica delle Marche, Italy

## Introduction

Injuries and diseases affecting the ankle can cause significant discomfort and hinder regular activities, negatively impacting joint function and movement [1]. Various therapies have been developed to alleviate pain and restore mobility, including total ankle replacement (TAR), which is a promising option that is continuously evolving. To determine the effectiveness of different prosthetic designs, robotic simulators are commonly utilized to mimic natural ankle joint movements and compare the performance of various prosthetic designs [2]. Thus, the objective of this thesis was to develop a universal robotic simulator that could test both ankle and knee prostheses. In particular, the robot was utilized to assess the effectiveness of a PLA prototype ankle prosthesis during walking.

## Methods

Initially, the robot experienced multiple mechanical and electrical problems that had a significant impact on its functionality. Despite being a metal frame with four motors that offered four degrees of freedom, it was unable to move synchronously, with the axial motor being particularly affected. Nevertheless, the current advanced robotic system can accurately replicate natural ankle movements by executing a variety of synchronous instructions outlined in ISO 22622:2019. These instructions, such as Plantar/Dorsiflexion (P/D), Internal/External rotation (I/E), Anterior/Posterior displacement (A/P), and Axial load, are controlled by a C++ application that was developed as a part of this thesis.

In addition, motors calibration has been performed. To accomplish this, an Optoelectronic system from OptiTrack was utilized, consisting of three cameras aimed at the motion of three rigid bodies equipped with three markers each. Using this advanced system, the movement of each motor can be precisely controlled, enabling the evaluation of motor performance one at a time.

Tekscan 4000 Pressure sensor was used to acquire data on the contact area and force applied over two tests. Comparative research was performed over ten different configurations of the Tibial and Talar interface, including changes to the Tibial part's position angle with respect to the Transverse Plane [ $0^\circ, 6^\circ, 10^\circ$ ] and the use of a mobile bearing. Afterward, a repeatability test checked the robot's ability to replicate the same gait cycle multiple times with the same characteristics, seven cycles were performed on the TAR configuration with 0-degree Eversion and mobile bearing.

## Results

Regardless of using only half the axial load specified in the ISO standard, the 3D-printed PLA part did not perform well under testing, causing failure after prolonged use.

Calibration indicate that motors have high accuracy and minimal error, with maximum errors of  $1.25^\circ$ ,  $0.94^\circ$ , and  $1.13$  mm for P/D, I/E, and A/P, respectively.

Moreover, from comparative research, the best configuration was found to be a neutral position of 0 degrees with a mobile bearing, showing higher values of the contact area, as shown in Figure 1.

Finally, from the repeatability test standard deviation was calculated over cycles, showing a good repeatability, as reported in Table 1.

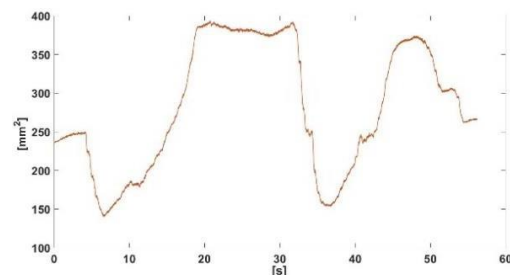


Figure 1: Area of contact data coming from the repeatability test with their standard deviations.

Cycle	1	2	3	4	5	6	7
Std	0.17	0.10	0.13	0.07	0.11	0.13	0.12

Table 1: Mean standard deviation for each cycle during the repeatability test.

## Discussion

Despite mechanical issues, solutions were developed, and the robot performed well during testing. Calibration and repeatability tests confirmed its high accuracy and repeatability.

On the other hand, this study is anticipated to make a valuable contribution to ankle prosthetics and establish the foundation for future advancements.

## References

1. Bonasia, Davide Edoardo, et al. "Total ankle replacement: why, when and how?." The Iowa orthopaedic journal 30 (2010): 119.
2. Natsakis, Tassos, et al. "Foot-ankle simulators: A tool to advance biomechanical understanding of a complex anatomical structure." Proceedings of the Institution of Mechanical Engineers, Part H: Journal of Engineering in Medicine 230.5 (2016): 440-449.



# EXPERIMENTAL ASSESSMENT OF PELVIS SLIPPING DURING POSTLESS TRACTION FOR ORTHOPEDIC APPLICATIONS

Marco Daghero (1,3), Taian M. Vieira (2,3), Simone Borrelli (1,3), Francesco Cannito (1,3), Sara Belfiore (4), Alessandro Aprato (4), Mara Terzini (1,3), Cristina Bignardi (1,3)

1. Department of Mechanical and Aerospace Engineering, Politecnico di Torino, Turin, Italy; 2. LISiN-Department of Electronics and Telecommunications, Politecnico di Torino, Turin, Italy; 3. Polito<sup>BIO</sup>Med Lab, Politecnico di Torino, Turin, Italy; 4. Department of Orthopedic and Traumatology, University of Turin, Turin, Italy

## Introduction

Common orthopedic surgeries, such as hip arthroscopy and proximal femoral fracture reduction, require the traction of the patient's lower limb with a perineal post. Pressure in the perineal region has been reported to cause groin-related complications, including soft tissue damage and neuropraxia [1]. To contend with these issues, the use of high friction conformable pads was recently introduced [2]. However, whether these pads provide sufficient adherence remains undocumented. In this study we thus evaluate the relative displacement of a single subject lying on high-friction pads.

## Methods

In this single-case study, the healthy, male subject (73 kg, 177 cm) was tested on a padded bed, in supine and in two Trendelenburg positions ( $\alpha$ : 5° and 10°). Tensile forces of progressively greater magnitude were applied coaxially to the longitudinal axis of the right leg through a customised, boot-pulley system (Figure 1).

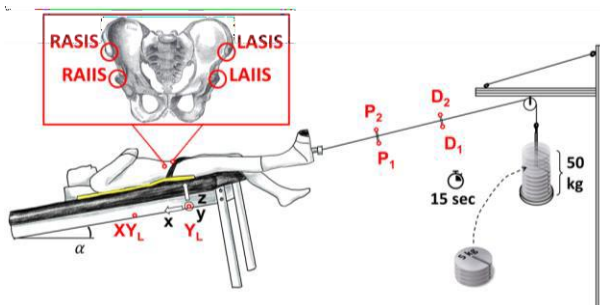


Figure 1: Representation of the experimental set up.

Ten load disks (5 kg) were dropped at 15 s intervals, each at a time, increasing gradually the tensile load from 2 kg to 52 kg. Movement of the pelvis was measured through a 12-camera motion capture system. Four markers were used to define the bed plane, with respect to which the pelvis displacement was measured using a four-marker protocol [3]. Two pairs of markers were placed on the steel cable to assess the traction direction. Nine trials were applied, three inclinations and three commercial pads: PinkPad by Xodus Medical, CarePad by Ab Medica and an antislip pad by BioMatrix.

## Results

Figure 2 shows that all pads were able to limit x-axis pelvis displacement to values lower than 75 mm. Comparing pads, seemingly, the BioMatrix pad was the

one causing larger displacements at higher loads. Surprisingly, no clear trend between bed inclination and pelvis displacement was observed; conversely, the cable inclination with respect to the bed appeared to affect the pelvis slipping: higher inclinations resulted in higher displacements. Lastly, rotation of the pelvis lower than 5° over the three axis was observed for all pads tested.

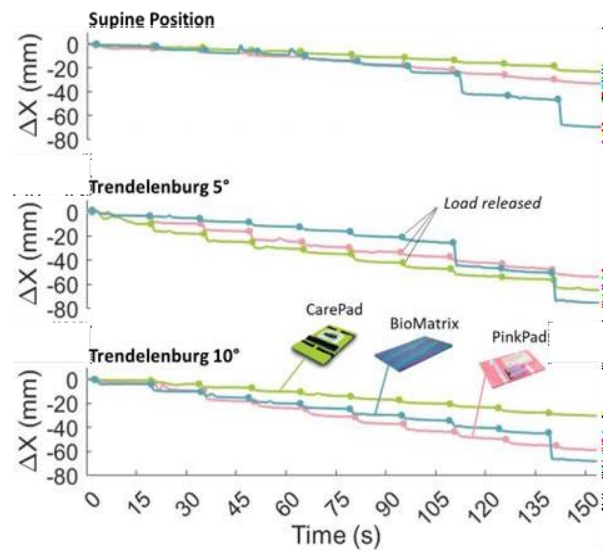


Figure 2: Pelvis displacement along the x axis with respect to the initial stance.

## Discussion

The weak relationship between Trendelenburg angle and pelvis slipping could be due to other factors, such as the cable inclination in relation to the bed plane. Results obtained for a single subject encourage furthering this study on a participant pool, as we are actively enlisting subjects. If confirmed for a larger cohort with different body compositions, the use of high-friction pads would be advised when perineal pressure resulting from the conventional procedure is to be suppressed.

## References

1. Topliss et al, Injury, 32: 689-691, 2001.
2. Aprato et al, Tech Orthop, 36(2): 205-208, 2021.
3. van Hellemond et al, Clin Orthop Relat Res, 405: 287-293, 2002.

## Acknowledgements

The authors acknowledge NUOVA BN S.r.l. for providing materials utilized in the experiments.



# DEVELOPMENT OF A MARKOV CHAIN MONTE CARLO ALGORITHM TO PREDICT HIP FRACTURES IN POSTMENOPAUSAL WOMEN

Giacomo Savelli (1,2), Antonino A La Mattina (1,2), Sara Oliviero (1,2), Marco Viceconti (1,2)

1. Department of Industrial Engineering, Alma Mater Studiorum - University of Bologna, Italy;

2. Medical Technology Lab, IRCCS Istituto Ortopedico Rizzoli, Bologna, Italy

## Introduction

Fragility hip fractures associated with osteoporosis (OP) represent a significant social burden as they lead to reduced quality of life, high mortality (17-32%) and healthcare costs. These injuries are particularly common in postmenopausal women [1].

Intervention clinical trials for the development of OP treatments are associated with high costs due to the need for large sample sizes and lengthy follow-up periods. Therefore, there is a need for more efficient methods to evaluate the effectiveness of OP interventions, and computational models could be used to improve drug development (In Silico Clinical Trials) (ISCT).

Finite Element (FE) models of the femur have been extensively validated for the prediction of failure load in a sideways-fall configuration [2] and can be applied in this framework.

The aim of this study was to develop an ISCT method based on a Markov Chain Monte Carlo algorithm to simulate clinical trials for OP treatments and predict fracture incidence in a virtual cohort.

## Materials and methods

1089 virtual patients were generated by sampling a statistical atlas obtained from a set of 94 subject-specific CT-based proximal femur FE models of postmenopausal women [3]. Baseline characteristics matched the population recruited in a previous clinical trial [4] ( $aBMD = 0.722 \pm 0.096 \text{ g/cm}^3$ ). The synthetic models consisted of quadratic tetrahedral elements (average mesh size = 3 mm) with isotropic linear elastic material properties.

At each simulated follow up year, 3 in total, the occurrence of falls was randomly determined from the probability density function of falls in the population of interest [5]. For each fall, impact direction is determined stochastically from the relative probability distribution. Failure load in the corresponding direction is obtained using a well-established FE procedure [2].

The impact force associated with each fall is obtained stochastically with a multiscale model, considering subject-specific height and weight, attenuation parameters and kinematic of fall [6]. We assumed the effect of muscle co-contraction was negligible due to the increased reaction time associated with aging [7].

At each fall, if impact load exceeds the failure load, a patient is considered fractured and excluded from the virtual cohort.

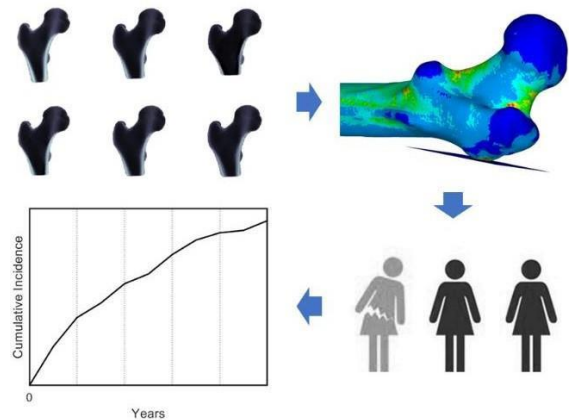


Figure 1: Workflow of the Markov Chain Monte Carlo algorithm.

## Results

Preliminary results showed that in 3 years of simulated follow up, 37 of hip fractures occurred among the cohort, which is in the same order, although slightly overestimating) with data reported for the placebo group of a concluded clinical trial, where a total of 14 hip fractures was reported [4].

## Discussion

The present study shows the ability of this Markov Chain Monte Carlo algorithm to predict the number of hip fractures as consequence of falls in a population of postmenopausal women. Future work will be focused on calibration of the stochastic parameters to reproduce the specific features of the population of interest, and on validation of the model using clinical data. The potential of *In Silico Clinical Trials* is to improve time- and cost-effectiveness of the drug development process.

## References

1. Borgstorm et al, Arch Osteoporos, 15(1):59, 2020
2. Schileo et al, J Biomech.,47(14): 3531-3538, 2014
3. La Mattina et al, Ann Biomed Eng,51(1):117-124, 2023
4. Cummings et al, N Engl J Med,359(7):697-708, 2008
5. Gillespie et al, Cochrane Database of Syst rev, 2012
6. Bhattacharya et al, Biomech Model Mechanobiol, 18(2): 301-318, 2019
7. Woods et al, Front Hum Neurosci,9, 215

## Acknowledgements

This study was supported by the European Commission through the H2020 project “In Silico World: Lowering barriers to ubiquitous adoption of In Silico Trials” (topic SC1-DTH-06-2020, grant ID 101016503).



# IN SILICO SIMULATIONS OF LUNG RECRUITMENT IN PATIENTS VENTILATED WITH AN INNOVATIVE DEVICE FOR CPAP THERAPY

A. Formaggio<sup>1,2</sup>, M. De Luca<sup>1,2</sup>, G. Putame<sup>1,2</sup>, S. Borrelli<sup>1,2</sup>, A. L. Audenino<sup>1,2</sup> and M. Terzini<sup>1,2</sup>

1. Department of Mechanical and Aerospace Engineering, Politecnico di Torino, Torino (Italy)

2. Polito<sup>BIO</sup>Med Lab, Politecnico di Torino, Torino (Italy)

## Introduction

CPAP (continuous positive airway pressure) therapy, widely used during the COVID-19 pandemic, is traditionally delivered in an open-configuration, to treat patient with hypoxemic respiratory failure. Recently, a new non-invasive ventilation system was proposed [1], exploiting a closed-loop circuit, able to reduce the oxygen consumption and the viral load dispersion in the environment. In acute respiratory distress syndrome (ARDS), typical complication of COVID-19 disease, CPAP promotes the recruitment of non-aerated alveoli and improves arterial oxygenation [2]. In this study, an *in silico* model was developed and experimentally validated, to analyse the effect of different CPAP levels on lung recruitment, with the final aim of selecting the most effective therapeutic pressure for the patient.

## Methods

The patient and the ventilation systems were reproduced as a lumped model (Figure 1) in Simscape (Mathworks).

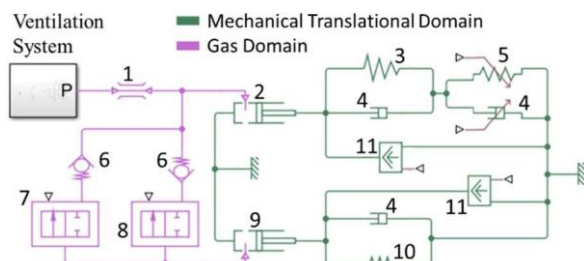


Figure 1: Schematics of the patient model 1) Airways; 2) Lung; 3) Non-linear lung compliance; 4) Tissues damping; 5) Variable compliance of recruitable alveoli; 6) Check valves; 7) Recruitment valve; 8) Collapse valve; 9) Collapsed alveoli; 10) Recruitment/collapse compliance; 11) Respiratory muscles.

Two conditions were evaluated, one involving external ventilation of a patient in apnoea, and the other involving treatment of a breathing patient using various CPAP levels in a closed-loop circuit. In this latter case, the device imposes CPAP at the patient's airway entrance, while a simulated muscles contraction generates the patient breathing. The recruitment valve opens when the alveolar pressure rises above a threshold ( $P_{rec}$ ), to allow the recruitment of non-aerated alveoli and the increment of the variable compliance. The opposite mechanism occurs when the alveolar pressure drops below the collapse pressure ( $P_{col}$ ). To validate the model, the ventilation systems were assembled *in vitro* using commercial components and connected to a lung simulator (TestChest® V3). Lung collapse and

recruitable alveoli index (R/I) were set at 50% and 0.5, respectively [3]. The lung volume and the alveolar pressure were recorded and compared, computing the  $R^2$  coefficient through regression with the 45-degline.

## Results

In both passive and active patient conditions (Figure 2) the *in silico* model was able to capture the *in vitro* behaviour ( $R^2 = 0.97$  and  $R^2 = 0.95$ , respectively). The *in silico* model allowed to analyse the effect of CPAP on aerated and collapsed alveoli separately (Table 1), estimating the efficacy of the therapy ( $\Delta V_{lung\ eff}$ ) as the lung recruited volume divided by the functional residual capacity increment ( $\Delta FRC$ ). Indeed, a high positive pressure limits the muscles work, reducing the tidal volume ( $\Delta V_{tidal}$ ); however, the alveolar recruitment increases the lung compliance, contrasting that effect.

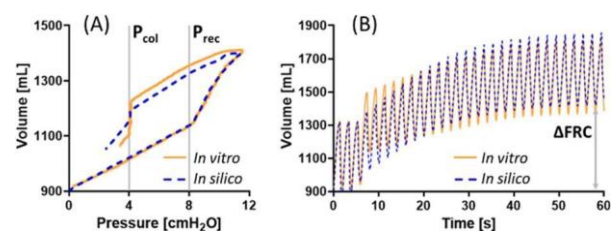


Figure 2: Pressure-Volume and Time-Volume curves for passive (A) and active (CPAP at 6 cmH<sub>2</sub>O) (B) patients.

CPAP level	Recruitment	$\Delta V_{lung\ eff}$	$\Delta V_{tidal}$
4 cmH <sub>2</sub> O	0 %	0 %	-11.9 %
6 cmH <sub>2</sub> O	19.2 %	50.3 %	8.4 %
8 cmH <sub>2</sub> O	37.5 %	54.1 %	21.9 %
10 cmH <sub>2</sub> O	40.9 %	50.9 %	23.3 %
12 cmH <sub>2</sub> O	43.2 %	47.8 %	21.7 %

Table 1: Comparison of the lung recruitment.

## Discussion

This study introduces a novel *in silico* lumped model able to replicate the dynamics of alveolar recruitment during non-invasive ventilation. This innovative feature makes the model a viable tool to understand the most effective CPAP therapy for different types of patients.

## References

1. M. Cavaglià et al. Artif. Organs, 45(7): 754-761, 2021.
2. A. Pagano et al. Respir Physiol Neurobiol, 280, 2020.
3. F. M. Beloncle et al, Ann. Intensive Care, 10(55), 2020.

## Acknowledgements

This work is part of the NODES project (MUR – M4C2 1.5 of PNRR, grant agreement no. ECS00000036)



# EXPERIMENTAL PRESSURE COMPARISON OF COMMERCIAL CPAP DEVICES: PRELIMINARY INVESTIGATION OF TARGET PERFORMANCE

Margherita De Luca (1,2), Andrea Formaggio (1,2), Giovanni Putame (1,2), Simone Borrelli (1,2), Alberto L. Audenino (1,2) and Mara Terzini (1,2)

1. Department of Mechanical and Aerospace Engineering, Politecnico di Torino, Torino (Italy)  
2. Polito<sup>BIO</sup>Med Lab, Politecnico di Torino, Torino (Italy)

## Introduction

CPAP (continuous positive airway pressure) therapy improves the treatment of patients with obstructive sleep apnoea syndrome and is widely used to treat patients with hypoxemic respiratory failure to avoid the necessity of intensive care. The traditional CPAP devices work in an open configuration with some disadvantages such as high daily oxygen consumption, viral air contamination and high noise [1]. An alternative solution lies in an innovative system able to deliver CPAP therapy with a closed-loop breathing circuit [2]. The aim of this study is to analyse the pressure performance of commercial devices able to deliver CPAP therapy according to their normal use configuration and evaluate performance variations when the devices were tested under the normal usage configurations of the innovative closed-loop concept.

## Methods

Two devices able to deliver CPAP therapy were tested: AirSense 10, ResMed (AS) and iSleep, Breas Medical (iS). Devices were tested in four configurations: in an open circuit with a full-face mask as an interface (MOP – standard configuration) or an helmet (HOP); in a closed-loop circuit with a full-face mask (MCL) or an helmet (HCL). The CPAP devices were connected via a circuit to a lung simulator (TestChest V3, Organix GmbH) and a flow analyser (FlowAnalyser Pro, IMT Analytics), and the therapy was delivered to a head phantom through the patient interface. All tests were performed using CPAP levels at 5, 7.5 and 10 cmH<sub>2</sub>O, simulating different conditions normally treated with CPAP therapy: a healthy subject (typical for obstructive sleep apnoea patient), a post-surgery patient and an acute respiratory distress syndrome (ARDS) patient. Thirty-six tests were performed in total, measuring the pressure at the patient connection port. Parameters for pressure performance evaluation are shown in Figure 1.

## Results

The maximum deviation of  $P_{mean}$  (i.e., mean static pressure measured with the patient in apnoea) from the set CPAP level is 18% in the MCL configuration with iS. Differences between expiratory and inspiratory peaks ( $\Delta P$ ), results smaller with AS in all the tested configurations (Figure 2). Compared to a mask interface, using a helmet reduces pressure fluctuations. Minimum oscillations are obtained with AS at a CPAP level of 5 cmH<sub>2</sub>O ( $\Delta P = 3$  cmH<sub>2</sub>O in HOP with ARDS

patient). Closing the breathing circuit always produces a  $\Delta P$  increase.

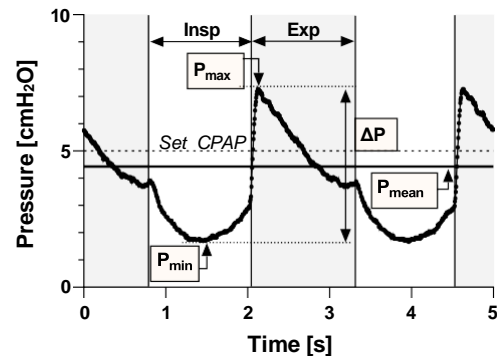


Figure 1: Pressure performance parameters depicted on a post-surgery patient (CPAP 5 cmH<sub>2</sub>O).

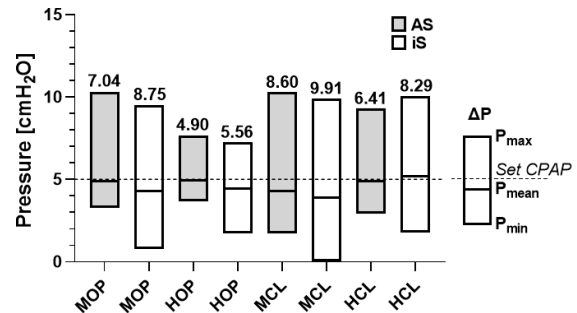


Figure 2: Performance comparison in all configurations for post-surgery patient (CPAP 5 cmH<sub>2</sub>O).

## Discussion

Initial findings indicate that AS device is more effective in maintaining  $P_{mean}$ , particularly when used in its standard configuration (MOP), likely due to a better-performing pressure control. Furthermore, the use of a helmet interface instead of a mask helps in stabilizing pressure fluctuations due to its larger internal volume. While closing the breathing circuit can solve issues related to oxygen consumption and viral load dispersion, it can also lead to increased pressure instability, possibly because the exhaled gas is retained within the circuit.

## References

1. Lucchini et al. Dimens Crit Care Nurs, 9(4):194-202,2020
2. Cavaglia et al. Artif. Organs, 45(7):754-761, 2021

## Acknowledgements

This work is part of the project NODES which has received funding from the MUR – M4C2 1.5 of PNRR with grant agreement no. ECS00000036



# INVESTIGATING THE INTERVERTEBRAL DISC'S CREEP BEHAVIOUR THROUGH MATHEMATICAL MODEL. AN IN VITRO STUDY

Vincenza Sciortino (1,2), Jan Ulrich Jansen (1), Donatella Cerniglia (2), Hans-Joachim Wilke (1)

1. Institute of Orthopaedic Research and Biomechanics, Ulm University, Germany; 2. University of Palermo, Department of Engineering, Italy

## Introduction

The intervertebral disc (IVD) is a complex biological structure due to its biphasic and viscoelastic properties that acts as a shock absorber allowing high loads and maintaining the spine mobility and flexibility. This involves relationships between external loads and the disc mechanobiology [1]. Nevertheless, although the viscoelastic properties of the IVD are a discussed topic, they are still not fully understood today. [2]. New insights are researched by modelling the IVD creep behavior. Investigating the biomechanical response of IVD to long-term loads is critical since it influences nutrient and water transport, i.e., hydration. The aim of this *in vitro* study is to describe the intermediate characteristics between solid and fluid of the IVD by using different mechanical constitutive models.

## Methods

Eight human frozen lumbar segments (L4-5) with an average age of 48 years (range: 38-58) and with no signs of degeneration were used. The specimens were prepared and embedded in PMMA and then fixed in a universal spine tester [4]. A creep test was performed with an axial compression load of 500 N for 15 minutes. The disc height reduction (DHR) was evaluated by using different rheological models and Nutting's power law (Fig. 1) (Wolfram Mathematica v13.). A correlation analysis was performed between the model parameters and the maximum value of DHR (RStudio).

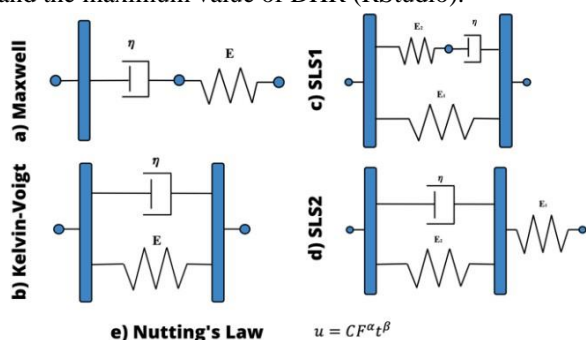


Figure 1. a) Maxwell: spring in series with dashpot; b) Kelvin-Voigt: spring in parallel with dashpot; c) SLS1: Kelvin-Voigt in series with spring; d) SLS2: Maxwell in parallel with spring; e) Nutting's Law

## Results

An immediate reduction in IVD height from the initial values (mean value 0.94 mm) was observed from the creep curves. After 15 minutes of creep, the disc height decreased by an average of 1.14 mm (min: 0.91 mm and max: 1.44 mm). By fitting the data, it was found that the

Maxwell and Kelvin-Voigt models do not fit the data, while the SLS1, SLS2 ones and Nutting's law seems to be the better fit (Fig. 2). Correlation matrices were calculated, identifying Pearson's significant values ( $r$ ,  $p < 0.05$ ). An important finding is the linear regression identified between stiffness and the maximum value of the DHR for the SLS1 model ( $r = -0.93$ , with  $R^2 = 0.84$ ) and for the SLS2 ( $r = -0.93$ , with  $R^2 = 0.97$ ).

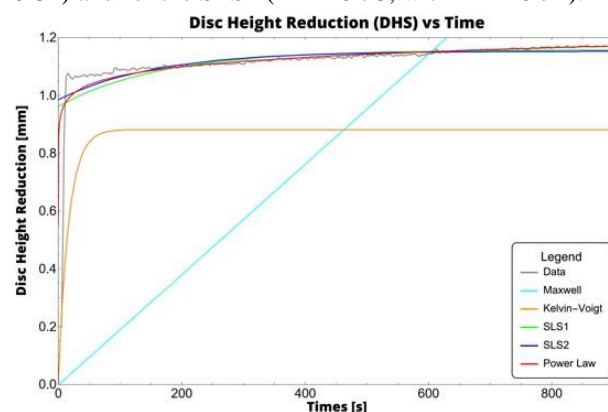


Figure 2. Example of fitting the creep curve. Legend: Raw data in Gray; Maxwell in Cyan; Kelvin-Voigt in Orange; SLS1 in Green curve; SLS2 in Blue; Nutting's Power law in Red.

## Discussion

From the creep curves modelled with the rheological models and Nutting's law, it is clear that the link between DHR and time is not linear. SLS1 and SLS2 capture well the regime trend of data but not the upward ramp. The Nutting's law seems to be the best fitting because it captures the total creep curve, and its formulation considers the biphasic properties of IVD. However, the fitting is not always successful. Hence, a biphasic model should be designed considering the direct link between external loads and the mechanobiology of IVD. Limitations include the creep time, the lack of a histological study to assess the water content, and that these mathematical models do not consider the cellular aspects. This *in vitro* study shows how necessary it is to find a mathematical model for the creep behavior of the IVD so that its mathematical and mechanical link between the macroscopic and cellular levels can be assessed.

## References

1. Neidlinger-Wilke, C., et al; European Spine J., 23, 333-343, (2014)
2. Sciortino, V., et al, In EWASHM (pp. 915-925), (2022)
3. Race, A., et al, Spine, 25(6), 662-669, (2000)
4. Wilke, H. J., et al European Spine J., 3, 91-97, (1994)



# ESB-ITA Master Thesis Award 2023

## *Finalists*

Torino, 19 September 2023



**TERESA BALDISSERA***Politecnico di Milano, Italy*DESIGN AND CHARACTERIZATION OF A 3D MICROSTRUCTURED TOOL  
FOR IMMUNOMODULATION THERAPY AND IMPLANT INTEGRATION**FRANCESCA DELL'AGNELLO***Fondazione Toscana G. Monasterio; Università di Pisa, Italy*DEVELOPMENT AND IMPLEMENTATION OF A COMBINED CFD AND  
MESH MORPHING TECHNIQUE FOR THE THORACIC AORTA**ALESSANDRO MASTROFINI***Università degli Studi di Roma Tor Vergata, Italy*THE IMPACT OF RESIDUAL STRAINS ON THE STRESS ANALYSIS OF  
ATHEROSCLEROTIC CAROTID VESSEL: PREDICTION BASED ON THE  
HOMOGENOUS STRESS HYPOTHESIS

# ESB-ITA 2023 Awards Winners

Torino, 18-19 September 2023



**ESB-ITA 2023 Awards Winners**

**ESB-ITA 2023 Best Oral Presentation in Integrative Biomechanics**

**Marco Bellotti**

*Università di Pavia*

NUMERICAL SIMULATION OF THE FORMATION PROCESS OF NANOPARTICLE

**ESB-ITA 2023 Best Poster Presentation in Integrative Biomechanics**

**Giulia Fraterrigo**

*Istituto Ortopedico Rizzoli*

FINITE ELEMENT ANALYSIS OF HEMIPELVIC CUSTOM-MADE RECONSTRUCTIONS IN THE LONG-TERM FOLLOW-UP

**ESB-ITA 2023 Best Oral Presentation**

**Valentina Mazzi**

*Politecnico di Torino*

VORTICITY TRANSPORT IN ABDOMINAL AORTIC ANEURYSM WITH FOLLOW UP

**ESB-ITA 2023 Best Poster Presentation**

**Federica Ninno**

*University College London*

IMPACT OF DIFFERENT PATIENT-SPECIFIC BOUNDARY CONDITIONS ON HEMODYNAMIC MARKERS IN PERIPHERAL ARTERIAL DISEASE

**ESB-ITA Master Thesis Award 2023 Winner**

**Francesca Dell'Agnello**

*Fondazione Toscana G. Monasterio, Università di Pisa*

DEVELOPMENT AND IMPLEMENTATION OF A COMBINED CFD AND MESH MORPHING TECHNIQUE FOR THE THORACIC AORTA

### Sponsors' Awards Winners

#### **Benedetta Fantaci**

*University of Zaragoza*

SATISFACTORY MODELLING COMPLEXITY  
FOR PRK IN-SILICO SIMULATION: AN  
OPTO-MECHANICAL ANALYSIS

**RECORNEA**  
securing your vision

#### **Michela Astore**

*Università di Roma Tor Vergata*

EXPERIMENTAL AND MODELLING  
ANALYSES FOR UNDERSTANDING OF THE  
STRUCTURE-MECHANICS RELATIONSHIP  
OF ARTIC TISSUE

**OPTICS** life

#### **Francesco De Gaetano**

*Politecnico di Milano*

BEYOND THE STANDARD: HOW DO THE  
CHARACTERISTIC OF THE AORTIC  
CONDUIT AFFECT THE PERFORMANCES  
OF HEART VALVES

#### **Margherita De Luca**

*Politecnico di Torino*

EXPERIMENTAL PRESSURE COMPARISON  
OF COMMERCIAL CPAP DEVICES:  
PRELIMINARY INVESTIGATION OF  
TARGET PERFORMANCE

**3B**  
3B SRL  
DEALER IN HEALTHCARE

#### **Federica Bianconi**

*Università Campus Bio-Medico di Roma*

OPTIMIZATION OF PHOTOTHERMAL  
LASER ABLATION USING AN  
EXPERIMENTAL-NUMERICAL APPROACH  
ON AGAROSE PHANTOM

#### **Maria Ghirardi**

*Università di Padova*

BIOMECHANICAL CHARACTERIZATION  
OF THE HUMAN FASCIA

**dipromed**  
Dipro Medical Devices



#### **Michela Bozzetto**

*Istituto di Ricerche Farmacologiche Mario Negri IRCCS*

VASCULAR WALL VIBRATIONS IN THE ARTERIOVENOUS FISTULA: A NOVEL  
MECHANOBIOLOGICAL STIMULUS?

#### **Stefano Gabetti**

*Politecnico di Torino*

CHARACTERIZATION OF PANCREATIC DUCTAL ADENOCARCINOMA CELL MIGRATION AND  
TRACTION FORCE ON STIFFNESS-TUNABLE SUBSTRATES

#### **Michele Marino**

*Università di Roma Tor Vergata*

MODELLING VASCULAR TONE REGULATION: AN INTEGRATIVE APPROACH FROM MOLECULAR  
TO SYSTEMIC LEVEL

# ESB - ITA 2023

XII Annual Meeting of the ESB-ITA



Venue: Aule R, Politecnico di Torino, Italy

